3. SITE 998[1]

Shipboard Scientific Party[2]

HOLE 998A

Position: 19°29.377′N, 82°56.166′W (Cayman Rise)

Date occupied: 0215 hr, 24 December 1995

Date departed: 1715 hr, 28 December 1995

Time on hole: 111.0 hr (4 days, 15 hr)

Seafloor depth (drill-pipe measurement from rig floor, mbrf): 3190.7

Total depth (drill-pipe measurement from rig floor, mbrf): 3828.3

Distance between rig floor and sea level (m): 10.8

Water depth (drill-pipe measurement from sea level, m): 3179.9

Penetration (mbsf): 637.6

Coring totals:
Type: APC; No: 17; Cored: 160.8 m; Recovered: 165.9 m (103.2%)
Type: XCB; No: 50; Cored: 476.8 m; Recovered: 275.0 m (57.7%)
Total: No: 67; Cored: 637.6 m; Recovered 440.9 m (69.1%)

Formation:
Nannofossil ooze/chalk, nannofossil mixed sediments, and clays interbedded with carbonate turbidites and volcanic ash layers

Oldest sediment cored:
Depth (mbsf): 637.6
Nature: Nannofossil chalk
Age: late Eocene

HOLE 998B

Position: 19°29.387′N, 82°56.160′W (Cayman Rise)

Date occupied: 1715 hr, 28 December 1995

Date departed: 2015 hr, 3 January 1996

Time on hole: 147 hr (6 days, 3 hr)

Seafloor depth (drill-pipe measurement from rig floor, mbrf): 3190.7

Total depth (drill-pipe measurement from rig floor, m): 4095.5

Distance between rig floor and sea level (m): 10.9

Water depth (drill-pipe measurement from sea level, m): 3179.8

Penetration (m): 904.8

Coring totals:
Type: RCB; No. 37; Cored: 346.5 m; Recovered: 287.9 m (83.1%)

Formation:
Nannofossil chalk, altered volcanic ash, calcareous volcaniclastic mixed sedimentary rock, and limestone

Oldest sediment cored:
Depth (mbsf): 904.8
Nature: Calcareous volcaniclastic mixed sedimentary rock
Age: early Eocene

Comments: Drilled from 0.0 to 558.3 mbsf

Principal results: Site 998 is located on the Cayman Rise, between the Yucatan Basin to the north and the Cayman Ridge and Cayman Trough to the south. This site was targeted for recovery of a continuous Cenozoic section to record the evolution of Caribbean ocean circulation, a Cretaceous/Tertiary boundary section relatively proximal to the Chicxulub impact site, and basement. Owing to the thickness of the sedimentary section and the very slow rate of penetration, the two deeper objectives could not be met within the time constraints of the leg.

A largely complete sedimentary section spanning the lower Eocene (nannofossil Zone CP10) to Pleistocene was cored in two holes at Site 998. Hole 998A was cored with the APC to a depth of 160.8 mbsf (upper Miocene) with 103.1% recovery, and then cored with the XCB to a depth of 637.6 mbsf with 57.7% recovery. Hole 998A terminated in upper Eocene nannofossil chalk. A free-fall funnel was deployed but was too deeply buried in soft sediment to reenter successfully with the RCB, so a second hole was drilled. Hole 998B was drilled ahead to 567.9 mbsf before resuming coring operations to a total depth of 904.8 mbsf. Recovery with the RCB was very good, with 83.1% of the drilled interval recovered. Hole 998B terminated in lower Eocene calcareous volcaniclastic mixed sedimentary rock.

Four lithologic units were recognized at Site 998. Unit I (0.0–94.3 mbsf; Pleistocene–lower Pliocene) consists of nannofossil ooze with foraminifers and clays interbedded with graded foraminiferal ooze and ash layers. Unit II (94.3–161.0 mbsf; basal Pliocene–uppermost middle Miocene) is divided into three subunits, all of which have interbedded turbidites and ash layers. The dominant lithologies in Unit II are clayey nannofossil mixed sediment, nannofossil ooze with foraminifers and clays, and clay with nannofossils. Unit III (161.0–766.0 mbsf; middle Miocene–middle Eocene) consists of nannofossil chalks that grade with depth into limestone with clay. The dominant lithologies of Unit IV (766.0–904.8 mbsf; middle–lower Eocene) are limestone with clay and calcareous volcaniclastic mixed sedimentary rock, with interbedded altered volcanic ash and volcaniclastic turbidites.

A seismic reflection at 5.15 s two-way traveltime is interpreted as acoustic basement, which we suggest is the top of a volcanic arc of unknown age. Based on logging and physical properties velocities obtained at the site, the depth to basement is estimated to be 1100–1130 mbsf at the location of Site 998. Thus, about 210 m of the sedimentary section above basement was not cored.

Shipboard biostratigraphy and magnetostratigraphy suggest that the cored section is virtually complete. Sedimentation rates averaged between 15 and 24 m/m.y. in the lower Eocene to middle Miocene interval, 8 m/m.y. in the upper Miocene, and nearly 19 m/m.y. for the Pliocene–Pleistocene; the highest rates are recorded for the Oligocene interval of nannofossil chalk where there are fewer turbidites and discrete ash layers. A shipboard magnetostratigraphy was established for the uppermost 200 m of Hole 998A (Pleistocene–middle Miocene) and all of Hole 998B (basal Oligocene–lower Eocene). A strong drill-string overprint and the nature of core quality in the middle Miocene–Oligocene XCB cores of Hole 998A contributed to an absence of interpretable paleomagnetic data through the middle part of the cored section at Site 998.

The sedimentary section at Site 998 yielded several unexpected results, including numerous pelagic turbidites and thick ash fall deposits in the Miocene, and thinner but much more frequent volcaniclastic turbidites in the lower to middle Eocene. The bases of these older turbidites consist of foraminifers in a matrix of redeposited volcanic ash. The Miocene ash-

[1]Sigurdsson, H., Leckie, R.M., Acton, G.D., et al., 1997. *Proc. ODP, Init. Repts.*, 165: College Station, TX (Ocean Drilling Program).
[2]Shipboard Scientific Party is given in the list preceding the Table of Contents.

es are rhyolitic fallout layers, which were probably derived from distant silicic volcanoes in Central America, whereas the Eocene volcaniclastic turbidites and associated ash falls were derived from a proximal island arc source, probably the nearby Cayman Ridge. More than 500 ash layers were described at Site 998. Turbidite frequency at this site may have been linked closely with spreading activity in the Cayman Trough and strike-slip motion along the fault zone that defines the northern boundary of the Caribbean Plate.

Concentrations of total organic carbon are extremely low in sediments recovered from Holes 998A and 998B, and most measurements were below analytical resolution. Similarly, methane was found to occur at only trace levels and additional hydrocarbon gases were not observed. The chemical composition of pore waters in the sediments displays a large range that varies systematically with depth and lithology. A downcore decrease in sulfate in the uppermost 50 m of the sediment and an increase in Fe are associated with redox conditions typical for deep-marine suboxic diagenesis.

Marked increases in pore-water Ca and Sr with depth most likely are related to dissolution of carbonate and weathering reactions of the volcanic ash and basement. The decrease in Mg with depth probably reflects the alteration of volcanic ashes to tri-octahedral smectite, which creates a sink for Mg as well as dolomite precipitation. A number of pore-water constituents (notably silica, Rb, K, and alkalinity) show downcore variations that strongly parallel the abundance trends for the Miocene silicic volcanic ash layers in the sediments, and the peak abundance in these dissolved components is thought to reflect their release during the initial stages of alteration of volcanic glass in the ash layers. The solid phase geochemistry of the sediments reflects the deposition of three principal components at Site 998: biogenic calcium carbonate, terrigenous detrital material, and dispersed volcanic ash. Using refractory elemental ratios such as Ti/Zr as discriminants of terrigenous and volcanic ash sources, we find that terrigenous material represents about 9%–10% of the total sediment, with a marked peak abundance in the top 120 m of the core, where it approaches concentrations of about 15%–20%. The total dispersed ash abundance is about 7% in the cored sediment, but shows a peak up to 30% at the 150-m level, where ash fall layers are also most common.

An important discovery at Site 998 is a marked reduction in pelagic carbonate deposition that occurred during the time of the middle/late Miocene boundary interval about 10.5–12.5 Ma. This oceanographic event is well developed in the upper Miocene sequences of the central and eastern equatorial Pacific, but it has not been previously documented in the tropical Atlantic or Caribbean Sea. Tectonic activity associated with the closing of the Central American Seaway during the late Neogene is suspected to have been an important variable in the evolution of Northern Hemisphere climate and ocean circulation. The signature of strong carbonate dissolution on both sides of the present-day Isthmus of Panama has important tectonic and paleoceanographic implications for the cause and extent of the late Miocene "carbonate crash."

BACKGROUND AND OBJECTIVES

Site 998 on the Cayman Rise is the northernmost site drilled during Leg 165 and is the most proximal to the Chicxulub impact crater on the northern Yucatan Peninsula. The objectives at this site were to include (1) impact-related depositional processes at a Cretaceous/Tertiary (K/T) boundary sequence relatively close to the Yucatan Peninsula impact site; (2) Late Cretaceous(?) and Paleogene tropical ocean and climate history with particular emphasis on times of moderate to extreme global warmth and of rapid change in the ocean-climate system; (3) timing of late Eocene impact events and the distribution and character of microtektites; (4) regional paleoceanographic conditions before and after partial foundering of an extensive carbonate megabank across the northern Nicaraguan Rise (NNR) during Oligocene–Miocene time, including the history of the Caribbean Current; 5) Neogene history of intermediate waters in the Yucatan Basin; and (6) age and nature of Cayman Rise basement rocks.

The discovery of numerous turbidites and rhyolitic volcanic ash layers, particularly in the Miocene and middle to lower Eocene part of the section, resulted in some additional research goals, as well as some modification to the sampling strategy for the high-resolution ocean and climate history objectives. For example, the spreading history of the Cayman Trough may be closely tied to the segmentation and partial drowning of the carbonate platform that extended along the length of the NNR, and may have led to earthquake-induced turbidite deposition on the Cayman Rise. Therefore, turbidite frequency has important implications for constraining the timing of plate interactions across the northern Caribbean. In addition, the source, chemistry, and circulation of water masses through the Caribbean were closely linked with changing sill depths of gateways into and out of the Caribbean. The spectacular record of explosive ash deposition recovered at this site has a bearing on the timing, nature, and volume of subduction-related volcanism in Central America during the Miocene whereas the volcaniclastic turbidites in the lower–middle Eocene suggest a more proximal source.

The seismic profiles and the *P*-wave velocities from logging at Site 998 indicate that basement is at about 1100–1130 mbsf. Because of the very slow rate of penetration and our tight time schedule, drilling was terminated at this site in lower Eocene sediments that occur at a depth of 904.8 mbsf. Thus, neither the K/T boundary nor basement were reached.

SEISMIC STRATIGRAPHY

Site 998 is located at 19°29.377′N and 82°56.166′W on the Cayman Rise, about 100 km northeast of Misteriosa Bank and 170 km west of the Cayman Islands (Fig. 1). The Cayman Rise is flanked by the Cayman Ridge and the Cayman Trough to the south and the Yucatan Basin abyssal plain to the north. Geophysical characteristics of the Cayman Rise include a region with a high positive magnetic anomaly on the order of 100 to 200 nT, and a free air gravity high of 50 to 100 mGal (Westbrook, 1990). Both of these anomalies follow the east northeast–west southwest physiographic trend of the ridge.

Site selection for Site 998 was based on the grid of single channel seismic (SCS) data acquired during an *Ewing Cruise* (EW9417) described in the "Explanatory Notes" chapter (this volume). The site is at a water depth of 3180 m (drill string corrected to sea level) and is situated on shotpoint 350 on the northwest-trending SCS Line EW9417-13, about 0.76 km northwest of the crossing with the SCS

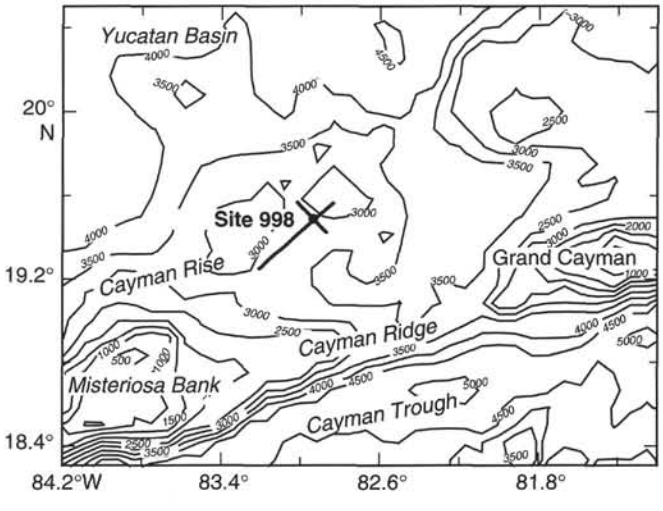

Figure 1. Bathymetric map (500-m contour interval) showing the location of Site 998 and the surrounding large-scale physiographic features of the area. Site 998 is located northwest of the intersection of EW9417 SCS Lines 13 and 16 (solid straight lines).

Line EW9417-16 (Fig. 2). The site is located 11 km southwest of multichannel seismic Line (MCS) GT2-52G collected by the *Ida Green* (IG2401) in 1977. Within the surveyed region, the acoustic basement appears as a high-amplitude, fairly continuous reflection with numerous diffractions beneath a thick (up to 1 s two-way traveltime; s TWT) sedimentary section. At Site 998 on SCS Line E9417-13 (Fig. 3), acoustic basement lies at 5.15 s TWT. Acoustic basement displays irregular relief and varies in depth by up to 300 ms in the vicinity of the site. Predrilling estimates of interval velocities, ranging from 1.6 to 2.5 km/s, indicated a total sediment thickness of approximately 1000 m.

Four main reflectors within the sedimentary section exhibit good lateral continuity (Fig. 3). The intervals between the main reflectors generally remain uniform in thickness in the upper half of the sedimentary section, whereas the thickness of the lower half of the section varies, smoothing the original relief of the acoustic basement. A number of vertical or high-angle discontinuities appear to cross-cut the entire sedimentary section and are interpreted to be faults or fluid-escape structures that typically occur at intervals of approximately 20 km. Some of these features are localized within the sedimentary section overlying basement highs and may be compaction-related faults. It is unclear whether or not these structures extend into basement and/or are related to the east-northeast-trending horst-and-graben tectonic fabric of the Cayman Rise (Rosencrantz, 1990). Site 998 was located in a region of undisturbed seismic reflections between two such structures in an attempt to avoid potential lithologic disturbances.

The lowermost seismic interval (seismic Unit C) from 5.15 to 4.94 s TWT consists of relatively high-amplitude, low-frequency, moderately continuous, subparallel reflections. Reflections within this unit are thickest over basement depressions and thin over or onlap onto basement highs. Reflector 4 (Fig. 3) within this package at 4.94 s TWT is identified as a high-amplitude, continuous reflection except in those areas where it onlaps basement.

Seismic Unit B, extending from 4.94 to 4.72 s TWT, has moderate amplitude, variable to poor continuity, subparallel to slightly divergent reflections. Reflector 3 (Fig. 3) at 4.72 s TWT is characterized by a high-amplitude, continuous reflection that can be correlated throughout most of the EW9417 survey area.

The interval from 4.72 to 4.18 s TWT defines seismic Unit A and consists primarily of low-amplitude, low to moderate continuity, parallel reflections. It does contain several high-amplitude reflections or sets of reflections. Reflector 2 (Fig. 3) is a high-amplitude, moderate to highly continuous reflector at 4.47 s TWT and is the major reflection within this unit that is mappable around Site 998. A series of high-amplitude, high continuity, parallel reflections (top marked by Reflector 1; Fig. 3) between 4.39 to 4.32 s TWT can also be correlated throughout the survey area.

Correlations between seismic stratigraphy and lithology at Site 998 are discussed in the "Summary and Conclusions" section (this chapter).

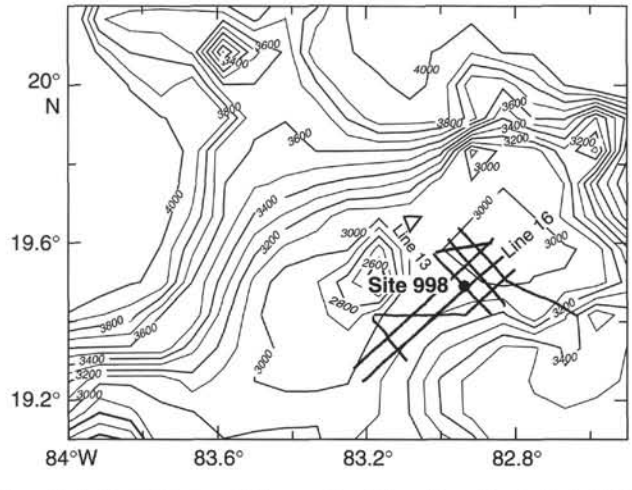

Figure 2. Bathymetric map (100-m contour interval) and track chart of SCS lines acquired during EW9417. Site 998 is located on EW9417 Line 13 approximately 0.76 km northwest of its intersection with EW9417 Line 16. A portion of EW9417 Line 13 is displayed in Figure 3.

OPERATIONS

The 585-nmi transit from Miami was uneventful owing to calm seas and favorable currents. We proceeded at an average speed of 11.0 kt and experienced only a slightly lower speed of 8.25 kt while heading into the Gulf Stream current.

Hole 998A

At Hole 998A, core recovery with the advanced piston coring (APC) system was excellent (100%–107%). The extended core barrel (XCB) coring system achieved good recovery (typically 60%–100%) and rate of penetration until the cutting shoe began to jam. Core quality also deteriorated with depth, though hole conditions remained excellent throughout the drilling (see Table 1).

A free-fall funnel was deployed so that the hole could be reentered after changing to the rotary core barrel (RCB) coring system. Upon attempting to reenter the hole, a large crater (roughly 10 m in diameter) was identified on the seafloor, but the funnel and tethered glass balls were not visible. After one failed attempt to reenter the hole by spudding into the crater, Hole 998A was abandoned.

Hole 998B

Drilling at Hole 998B was initiated 20 m to the northeast of Hole 998A. The hole was drilled down to 558.5 mbsf with the RCB and center-bit combination before attempting core recovery. This depth was selected to allow about 80 m overlap of the lower, poorly recovered section of the formation in Hole 998A. The RCB system exceeded the recovery of the XCB system throughout this overlap interval and provided superior core quality (see Table 1).

Core recovery with the RCB was exceptionally good, averaging 83.1% for the hole. The rate of penetration through the drilled section of the hole averaged 37.2 m/hr. In the cored intervals, it ranged from a high of 30.3 m/hr in the upper section to a low of 4.5 m/hr at the bottom (as averaged over approximate 100-m intervals).

Hole stability was generally good; however, a rise in pump pressure, coupled with higher torque, was noticed when picking up the drill string in each of the last three cores. Sepiolite mud pills of 15 bbls were required after cutting each of these cores. In addition, we conducted a wiper trip to prepare the hole for logging, after which 5 m of fill was found on bottom and subsequently circulated out.

Four suites of logging tools were deployed in the hole: The first two runs, with the Quad combination tool and the geochemical logging tool, reached the bottom of the hole without incident and logged from 904 to 172 mbsf. Approximately 35 m of hole near the bottom (709–744 mbsf) was found to be at least 47 cm in diameter (maximum caliper extension). Collapse of this section apparently was the source of the increased torque and pump pressure observed after cutting the last three RCB cores. Owing to an obstruction in the hole, the third and fourth runs, with the Formation MicroScanner and geological high-sensitivity magnetic tool, only reached a total depth of 430 mbsf and logged up to 172 mbsf.

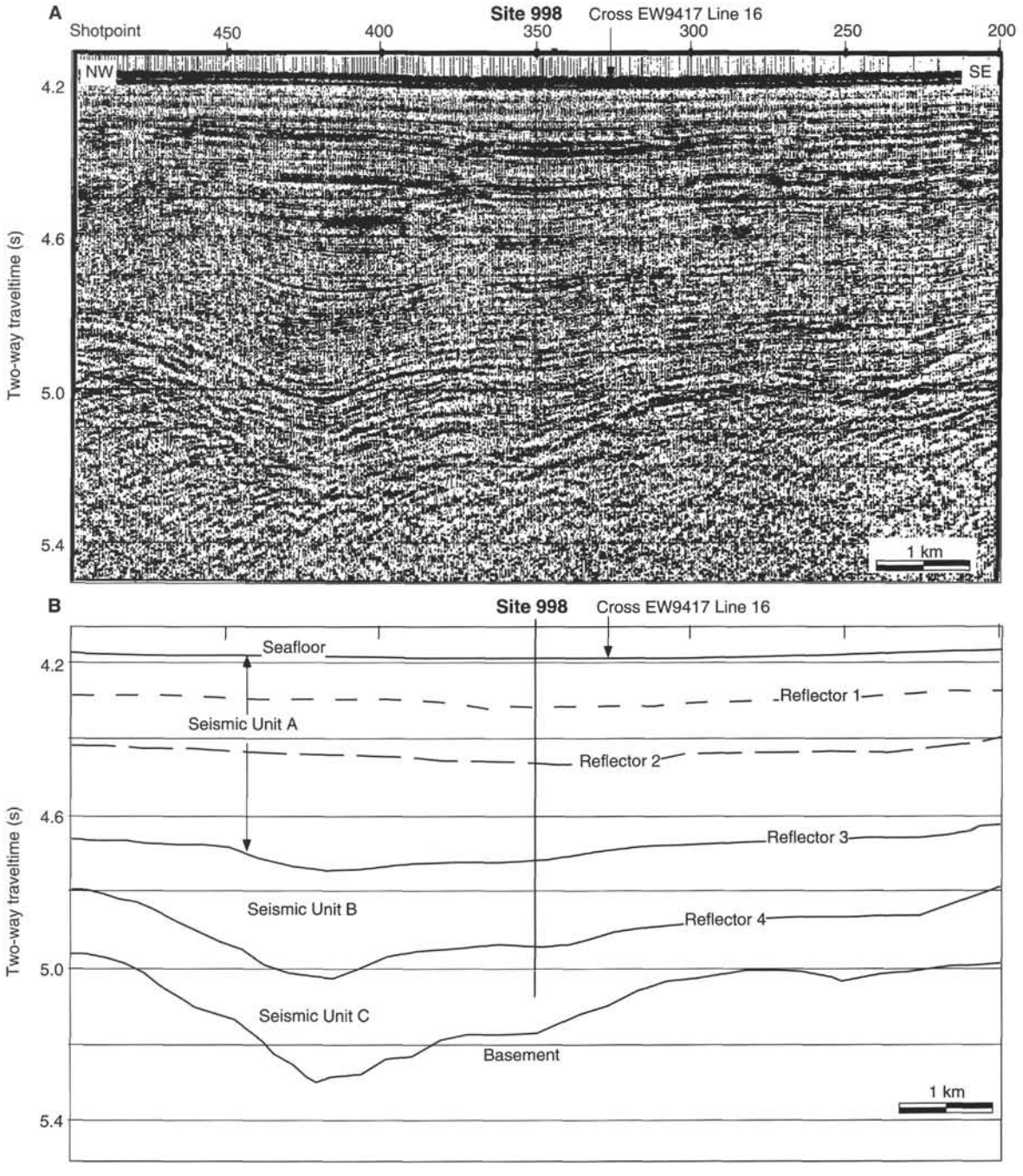

Figure 3. **A.** EW9417 Line 13 SCS profile showing location of Site 998 (shotpoint 350) and the intersection with EW9417 Line 16 less than 1 km southwest of Site 998. **B.** Interpreted seismic stratigraphic correlation of Figure 3A.

LITHOSTRATIGRAPHY

Introduction

The 904.8-m-thick sedimentary sequence, recovered in Hole 998A by means of APC and XCB coring, and in Hole 998B by RCB drilling, ranges in age from early Eocene to recent and consists of dominantly pelagic sediments with clays, volcanic ash layers, pelagic turbidites, and volcaniclastic turbidites. The main lithologies at Site 998 consist of nannofossil and foraminifer oozes with clays in the upper part of the sequence, grading downhole into chalks with clays and calcareous limestones with clays. Correlations between Holes 998A and 998B are based on biostratigraphy, continuously measured color reflectance, and MST data (Figs. 4, 5), as well as on the basis of such sedimentological features as thickness and stacking patterns of ash layers and slump beds (see lithologic Unit III below). High-density measurements (5-cm-spaced sample interval) of color reflectance (see Appendix tables on CD-ROM, back pocket, this volume, for complete data set) and magnetic susceptibility, in addition to a limited number of $\%CaCO_3$ content measurements, together with sedimentological criteria (percentages of microfossils and minerals in smear slides, depositional textures, sedimentary structures, XRD bulk fraction analyses), form the basis for dividing the recovered sequence into four lithologic units: Units I, II, III, and IV. Lithologic

Table 1. Coring summary, Site 998.

Core no.	Date (1995–1996)	Time (UTC)	Depth (mbsf)	Cored (m)	Recovered (m)	Recovery (%)
165-998A-						
1H	24 Dec	1530	0.0–8.8	8.8	8.80	100.0
2H	24 Dec	1615	8.8–18.3	9.5	9.90	104.0
3H	24 Dec	1715	18.3–27.8	9.5	9.70	102.0
4H	24 Dec	1800	27.8–37.3	9.5	9.81	103.0
5H	24 Dec	1855	37.3–46.8	9.5	9.81	103.0
6H	24 Dec	1945	46.8–56.3	9.5	9.76	103.0
7H	24 Dec	2030	56.3–65.8	9.5	9.74	102.0
8H	24 Dec	2120	65.8–75.3	9.5	9.79	103.0
9H	24 Dec	2220	75.3–84.8	9.5	9.93	104.0
10H	24 Dec	2310	84.8–94.3	9.5	9.77	103.0
11H	25 Dec	0010	94.3–103.8	9.5	9.83	103.0
12H	25 Dec	0110	103.8–113.3	9.5	10.15	106.8
13H	25 Dec	0210	113.3–122.8	9.5	10.09	106.2
14H	25 Dec	0305	122.8–132.3	9.5	9.56	100.0
15H	25 Dec	0350	132.3–141.8	9.5	9.58	101.0
16H	25 Dec	0455	141.8–151.3	9.5	10.12	106.5
17H	25 Dec	0545	151.3–160.8	9.5	9.52	100.0
18X	25 Dec	0720	160.8–166.2	5.4	5.10	94.4
19X	25 Dec	0820	166.2–175.9	9.7	9.69	99.9
20X	25 Dec	0920	175.9–185.5	9.6	7.80	81.2
21X	25 Dec	1030	185.5–195.1	9.6	6.80	70.8
22X	25 Dec	1130	195.1–204.8	9.7	8.73	90.0
23X	25 Dec	1225	204.8–214.4	9.6	7.80	81.2
24X	25 Dec	1300	214.4–224.0	9.6	9.14	95.2
25X	25 Dec	1350	224.0–233.6	9.6	5.78	60.2
26X	25 Dec	1440	233.6–243.2	9.6	7.32	76.2
27X	25 Dec	1545	243.2–252.9	9.7	7.37	76.0
28X	25 Dec	1700	252.9–262.5	9.6	6.79	70.7
29X	25 Dec	1800	262.5–272.1	9.6	8.25	85.9
30X	25 Dec	1910	272.1–281.7	9.6	0.01	0.1
31X	25 Dec	2050	281.7–291.3	9.6	7.19	74.9
32X	25 Dec	2230	291.3–300.9	9.6	4.67	48.6
33X	26 Dec	0045	300.9–310.5	9.6	1.73	18.0
34X	26 Dec	0215	310.5–320.2	9.7	7.00	72.1
35X	26 Dec	0330	320.2–329.8	9.6	9.01	93.8
36X	26 Dec	0450	329.8–339.4	9.6	6.05	63.0
37X	26 Dec	0630	339.4–349.0	9.6	6.23	64.9
38X	26 Dec	0730	349.0–358.6	9.6	2.49	25.9
39X	26 Dec	0850	358.6–368.2	9.6	3.10	32.3
40X	26 Dec	1000	368.2–377.9	9.7	8.40	86.6
41X	26 Dec	1130	377.9–387.6	9.7	6.40	66.0
42X	26 Dec	1245	387.6–397.2	9.6	6.86	71.4
43X	26 Dec	1400	397.2–406.8	9.6	3.63	37.8
44X	26 Dec	1520	406.8–416.4	9.6	4.87	50.7
45X	26 Dec	1640	416.4–426.0	9.6	5.38	56.0
46X	26 Dec	1800	426.0–435.7	9.7	4.71	48.5
47X	26 Dec	1920	435.7–445.3	9.6	2.55	26.5
48X	26 Dec	2045	445.3–454.9	9.6	4.06	42.3
49X	26 Dec	2215	454.9–464.5	9.6	5.41	56.3
50X	26 Dec	2340	464.5–474.1	9.6	6.10	63.5
51X	27 Dec	0100	474.1–483.7	9.6	3.78	39.4
52X	27 Dec	0205	483.7–493.3	9.6	6.76	70.4
53X	27 Dec	0330	493.3–502.9	9.6	5.18	53.9
54X	27 Dec	0450	502.9–512.5	9.6	5.76	60.0
55X	27 Dec	0600	512.5–522.1	9.6	4.86	50.6
56X	27 Dec	0720	522.1–531.8	9.7	4.54	46.8
57X	27 Dec	0840	531.8–541.4	9.6	5.55	57.8
58X	27 Dec	1000	541.4–551.1	9.7	4.62	47.6
59X	27 Dec	1130	551.1–560.7	9.6	7.11	74.0
60X	27 Dec	1300	560.7–570.3	9.6	8.28	86.2
61X	27 Dec	1430	570.3–579.9	9.6	7.50	78.1
62X	27 Dec	1600	579.9–589.5	9.6	6.49	67.6
63X	27 Dec	1750	589.5–599.1	9.6	1.13	11.8
64X	27 Dec	1930	599.1–608.7	9.6	0.77	8.0
65X	27 Dec	2145	608.7–618.3	9.6	1.19	12.4
66X	27 Dec	2345	618.3–628.0	9.7	4.12	42.5
67X	28 Dec	0200	628.0–637.6	9.6	0.96	10.0
Coring totals				637.6	440.88	69.1
165-998B-						
*****Drilled from 0.0 to 558.3 mbsf*****						
1R	29 Dec	1700	558.3–567.9	9.6	9.27	96.5
2R	29 Dec	1830	567.9–577.5	9.6	9.07	94.5
3R	29 Dec	1945	577.5–587.1	9.6	8.94	93.1
4R	29 Dec	2100	587.1–596.8	9.7	8.10	83.5
5R	29 Dec	2230	596.8–606.3	9.5	8.57	90.2
6R	29 Dec	2355	606.3–616.0	9.7	9.57	98.6
7R	30 Dec	0115	616.0–625.6	9.6	6.75	70.3
8R	30 Dec	0255	625.6–635.2	9.6	7.00	72.9
9R	30 Dec	0425	635.2–644.8	9.6	8.64	90.0
10R	30 Dec	0600	644.8–654.5	9.7	8.51	87.7
11R	30 Dec	0725	654.5–664.1	9.6	4.71	49.0
12R	30 Dec	0840	664.1–673.8	9.7	5.44	56.1
13R	30 Dec	1010	673.8–683.5	9.7	7.48	77.1
14R	30 Dec	1130	683.5–693.1	9.6	4.94	51.4
15R	30 Dec	1330	693.1–702.7	9.6	5.77	60.1
16R	30 Dec	1500	702.7–712.3	9.6	5.32	55.4
17R	30 Dec	1650	712.3–722.0	9.7	6.01	61.9
18R	30 Dec	1820	722.0–731.6	9.6	8.98	93.5
19R	30 Dec	1955	731.6–741.2	9.6	9.18	95.6
20R	30 Dec	2140	741.2–750.8	9.6	5.03	52.4
21R	30 Dec	2315	750.8–760.5	9.7	8.02	82.7
22R	31 Dec	0120	760.5–770.1	9.6	8.48	88.3
23R	31 Dec	0340	770.1–777.1	7.0	6.49	92.7
24R	31 Dec	0525	777.1–779.8	2.7	1.69	62.6
25R	31 Dec	0830	779.8–789.4	9.6	9.49	98.8
26R	31 Dec	1145	789.4–798.9	9.5	8.59	90.4
27R	31 Dec	1515	798.9–808.5	9.6	9.11	94.9
28R	31 Dec	1900	808.5–818.2	9.7	9.55	98.4
29R	31 Dec	2320	818.2–827.8	9.6	7.28	75.8
30R	1 Jan	0500	827.8–837.5	9.7	9.87	102.0
31R	1 Jan	0720	837.5–847.1	9.6	9.63	100.0
32R	1 Jan	1030	847.1–856.7	9.6	9.31	97.0
33R	1 Jan	1250	856.7–866.3	9.6	8.44	87.9
34R	1 Jan	1545	866.3–875.9	9.6	9.24	96.2
35R	1 Jan	1830	875.9–885.5	9.6	8.97	93.4
36R	1 Jan	2130	885.5–895.1	9.6	8.26	86.0
37R	2 Jan	0140	895.1–904.8	9.7	8.18	84.3
Coring totals				346.5	287.88	83.1
Drilled				558.3		
Total				904.8		

Note: An expanded version of this coring summary table that includes lengths and depths of sections, location of whole-round samples, and comments on sampling disturbance is included on CD-ROM in the back pocket of this volume.

Unit II is further divided into three subunits: Subunits IIA, IIB, and IIC. The stratigraphic distribution of the units and subunits is summarized in Figure 4.

Description of Lithologic Units

Lithologic Unit I

Intervals: Cores 165-998A-1H through 10H
Age: Pleistocene to early Pliocene
Depth: 0.0–94.3 mbsf, Hole 998A

Unit I, early Pliocene to Pleistocene in age and 94.3 m thick, is composed of pelagic biogenic ooze with clays. Carbonate content values in Unit I range from 62% to 85.5% (average 76%), and magnetic susceptibility values are intermediate between those for Units II and III (see Fig. 4). Based upon the different proportions of foraminifers, nannofossils, and clays, these sediments are classified as nannofossil ooze with foraminifers and clays, clayey nannofossil ooze, and foraminiferal ooze. However, the dominant lithology is a nannofossil ooze with foraminifers and clays, interbedded with redeposited graded layers of foraminiferal ooze fining upward into clayey nannofossil ooze and a few scattered volcanic ash layers.

Based upon smear-slide estimates and XRD data interpretation, the dominant sediment component of Unit I consists of a mixture of biogenic grains (coccolith plates, foraminifer whole tests and fragments, sponge spicule debris), siliciclastic detrital particles (some quartz, clay minerals), and occasional traces of dolomite. Pteropod shell fragments are restricted to the uppermost two sections (165-998A-1H-1 and 2) of Site 998. The unit displays a wide variety of colors from brown-pale brown (10YR 5/3-5/4), light olive brown–light yellowish brown–pale yellow (2.5Y 5/4-6/4-7/4) to light yellowish–light brownish gray–light gray (2.5Y 6/4–6/2-7/2). This wide range of colors correlates with the most highly variable ratios of color reflectance in the red/blue (680/420 nm) wavelengths found in the entire Site 998. Unit I is generally homogeneous with occasional mottling and displays light to moderate bioturbation, with only rare inter-

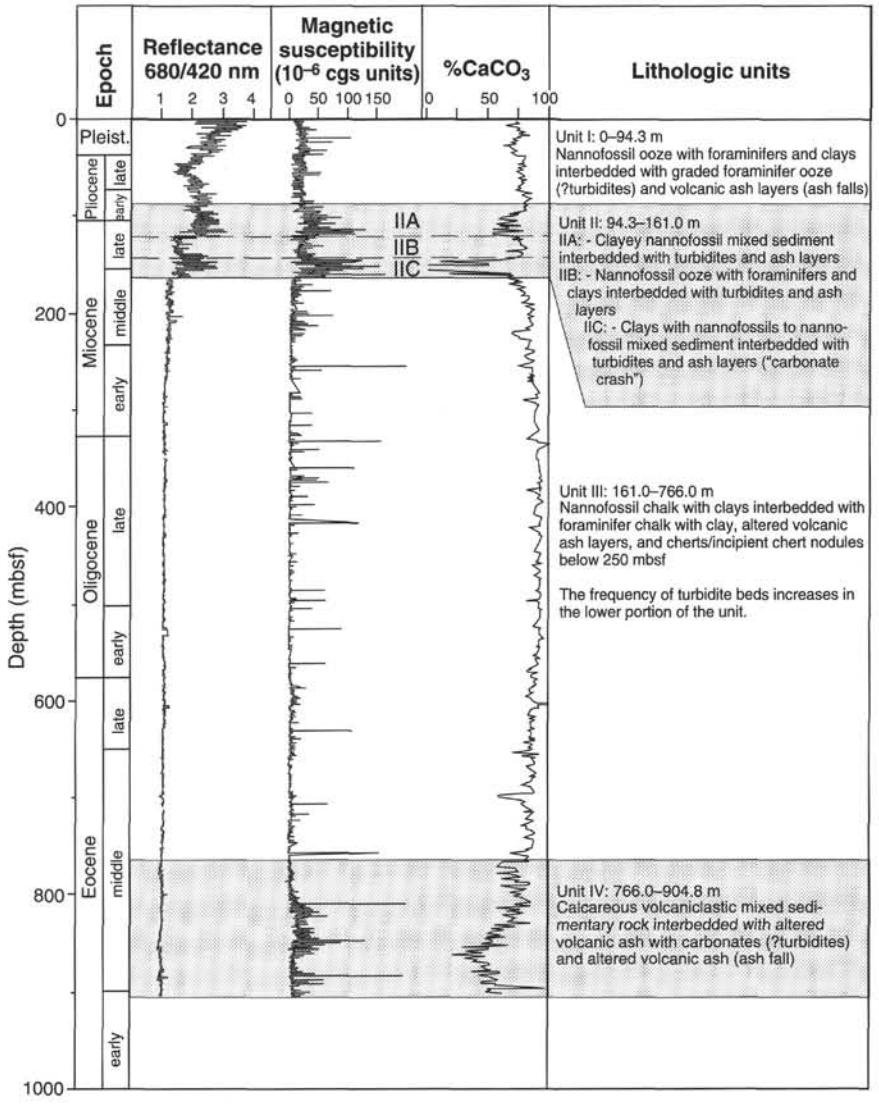

Figure 4. Composite summary of color reflectance, magnetic susceptibility, and $\%CaCO_3$ data used to define the lithologic units at Site 998.

vals characterized by intense bioturbation. Pyrite occurs occasionally in burrows.

Graded foraminifer silt to sand layers, usually overlain by clayey nannofossil ooze, are interbedded within the nannofossil ooze with foraminifers and clays (Unit I dominant lithology), and are interpreted as redeposited pelagic sediments or turbidites. These redeposited sediments consist of very pale brown (10YR 7/3) graded layers. No color variations occur in relation to compositional changes within the layers. The boundary with the underlying units is generally sharp and erosive with up to 1.5 cm of erosional relief, whereas the boundary with the overlying sediment is usually gradational and overprinted by bioturbation. The sand to silt bases are generally massive (possibly because soupy texture of sediment does not preserve depositional structures) and rarely parallel laminated. Smear-slide data show that the basal silt/sand units consist primarily of foraminifer tests and fragments, and minor nannofossil mixed sediment with clays. The foraminiferal oozes at discrete intervals and below the level at Section 165-998A-9H-1 to 120 cm are partially lithified. Discrete intervals with sharp boundaries within the sand- and silt-sized fraction contain foraminifer tests encrusted by a black mineral of uncertain nature (possibly pyrite and/or Fe-oxides). The high concentrations of these blackened foraminifers give a "salt and pepper sand" appearance to some intervals. The transition between the basal silt/sand and the upper clayey part may be gradational or sharp. The upper part is typically slightly to moderately bioturbated. These layers average 17 cm thickness in Unit I and can reach up to 120 cm thick. Detailed tabulation and discussion of the frequency and thickness of these layers (turbidites) is presented below.

Thin volcanic ash layers, a minor, but important lithology occurring throughout Unit I, are derived from eolian transport of pyroclastic material from explosive eruptions (Fig. 6; Section 165-998A-10H-4). They can be recognized by their greenish to brownish color and distinctive lithology. These horizons occur as (1) discrete layers; (2) bioturbated, but visible patches; and (3) dispersed ash in the clayey nannofossil ooze. Discrete layers have a sharp base and a bioturbated top; they are well sorted.

Lithologic Unit II

Intervals: Core 165-998A-11H through Section 165-998A-18X-1, 20 cm
Age: early Pliocene to late middle Miocene
Depth: 94.3–161.0 mbsf, Hole 998A

Unit II at Site 998 consists of sediments that range in composition from pelagic oozes to nearly pure clays as end-members. The top of Unit II is marked by the first downhole appearance of mixed sedi-

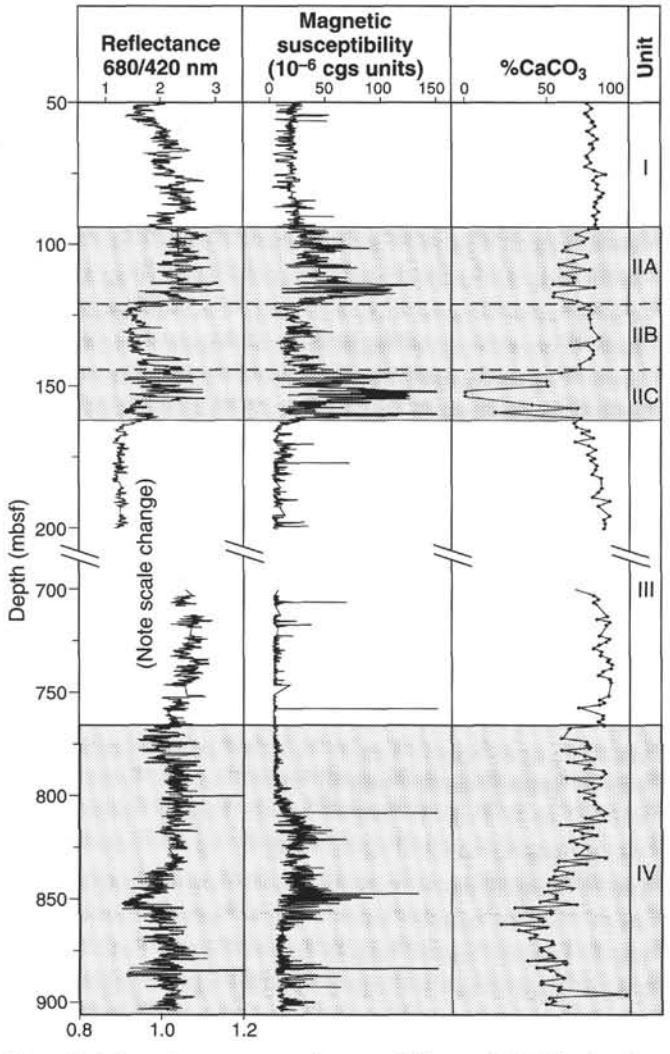

Figure 5. Color reflectance, magnetic susceptibility, and $\%CaCO_3$ data from 50 to 200 mbsf and from 700 to 903.3 mbsf. Note the change in scale for the color reflectance data between the upper and lower parts of the plot.

ment, with carbonate contents dropping below 80% and remaining at levels below this for the entire stratigraphic extent of the unit. The lower boundary of the unit is defined by a return to higher carbonate concentrations and the first consistent appearance of sediments lithified enough to be called chalks. Based upon differing proportions of foraminifers, nannofossils, and clays, the sediments of Unit II can be classified as foraminiferal ooze with nannofossils and clays, nannofossil ooze with clays and foraminifers, nannofossil ooze with clays, clayey nannofossil ooze with foraminifers, clayey nannofossil mixed sediment, nannofossil clayey mixed sediment, and clay. At a few discrete levels, incipient lithification has converted foraminiferal oozes into chalks. Silicic volcanic ash layers and turbidites are relatively common and distributed throughout the section.

Unit II is divided into three subunits (IIA, IIB, and IIC), based upon variations in carbonate content as well as upon distinct patterns in magnetic susceptibility and color reflectance data (see Figs. 4, 5). The entire unit ranges from late middle Miocene to early Pliocene in age.

Subunit IIA

Intervals: Cores 165-998A-11H through 165-998A-13H-5, 70 cm
Age: early Pliocene to late Miocene
Depth: 94.3 to 120.0 mbsf, Hole 998A

Sediments of Subunit IIA consist predominantly of clayey nannofossil mixed sediment with interbedded turbidites and volcanic ash layers. XRD data indicate the presence of minor quartz and traces of dolomite and the mineral phases illite and chlorite in the mixed sediment (Fig. 7; Table 2). The top and base of the subunit are defined by relatively abrupt changes in carbonate content and magnetic susceptibility. Low carbonate values and high susceptibility values typify the subunit. The average carbonate content of Subunit IIA is about 65%, but values as low as 50% were measured. The base of the subunit is marked by a sharp drop in the ratio of color reflectance within the red/blue wavelengths (680/420 nm), but lithologic changes at the top of the subunit are apparently insufficient to produce a similar response in the reflectance data.

The clayey nannofossil mixed sediment that dominates Subunit IIA ranges in color from light yellowish brown (2.5Y 6/4) and light brownish gray (2.5Y 6/2) to dark olive brown (2.5Y 3/4) depending upon carbonate content. Interbedded throughout these moderately bioturbated pelagic sediments are relatively thin volcanic ash layers and an abundance of coarser turbidites that consist of redeposited pelagic carbonate (Fig. 8). The latter are usually light gray (2.5Y 7/2) with sharp bases and are lithologically described as foraminiferal oozes and chalks with nannofossils and clays that fine upward into clayey nannofossil oozes with foraminifers. At a number of levels, incipient lithification has begun to transform the coarser foraminifer-rich bases into weakly indurated chalks. The absence in smear slides of obvious shallow-water components suggests that the turbidites in this interval are derived from locally higher topography on the Cayman Ridge to the south of Site 998 or from a small unnamed escarpment to the west. The origin and character of the ash layers are discussed further in the "Igneous Petrology and Volcanology" section (this chapter).

Subunit IIB

Intervals: Sections 165-998A-13H-5, 70 cm, through 165-998A-16H-3, 20 cm
Age: late Miocene
Depth: 120.0 to 145.0 mbsf, Hole 998A

Sediments of Subunit IIB largely consist of nannofossil oozes with varying proportions of clays and foraminifers as minor components. The transition downhole between Subunits IIA and IIB is marked by an abrupt rise in carbonate content, a corresponding decrease in magnetic susceptibility, and a sharp drop in the ratio of color reflectance in the red/blue (680/420 nm) wavelengths. Relative carbonate contents appear to average about 75% in this subunit based on a limited number of analyses (Figs. 4, 5).

The nannofossil oozes of Subunit IIB are typically light gray (2.5Y 7/2) or light brownish gray (2.5Y 6/2) to dark yellowish brown (10YR 4/2) in color, and are mottled by moderate bioturbation throughout. Minor quartz, traces of feldspar, and clays (chlorite/kaolinite? and some illite) occur throughout these cores (Table 2). Turbidites consisting of redeposited carbonate are again common in this subunit, with sharp and erosive basal contacts and upward grading from light gray (2.5Y 7/2) foraminiferal ooze with clay to nannofossil ooze with clay. Thin (<1 cm) turbidite layers are often grouped in bundles of two or more beds, and distinguishing between discrete events can be difficult. The carbonate contents of turbidites in this subunit are not significantly different from the already high values recorded by the pelagic oozes. Volcanic ash layers are preserved at various levels within Subunit IIB with a frequency (i.e., a few per core) comparable to that found in the overlying subunit.

Subunit IIC

Intervals: Sections 165-998A-16H-3, 20 cm, through 165-998A-18X-1, 20 cm
Age: early late Miocene to late middle Miocene
Depth: 145.0 to 161.0 mbsf, Hole 998A

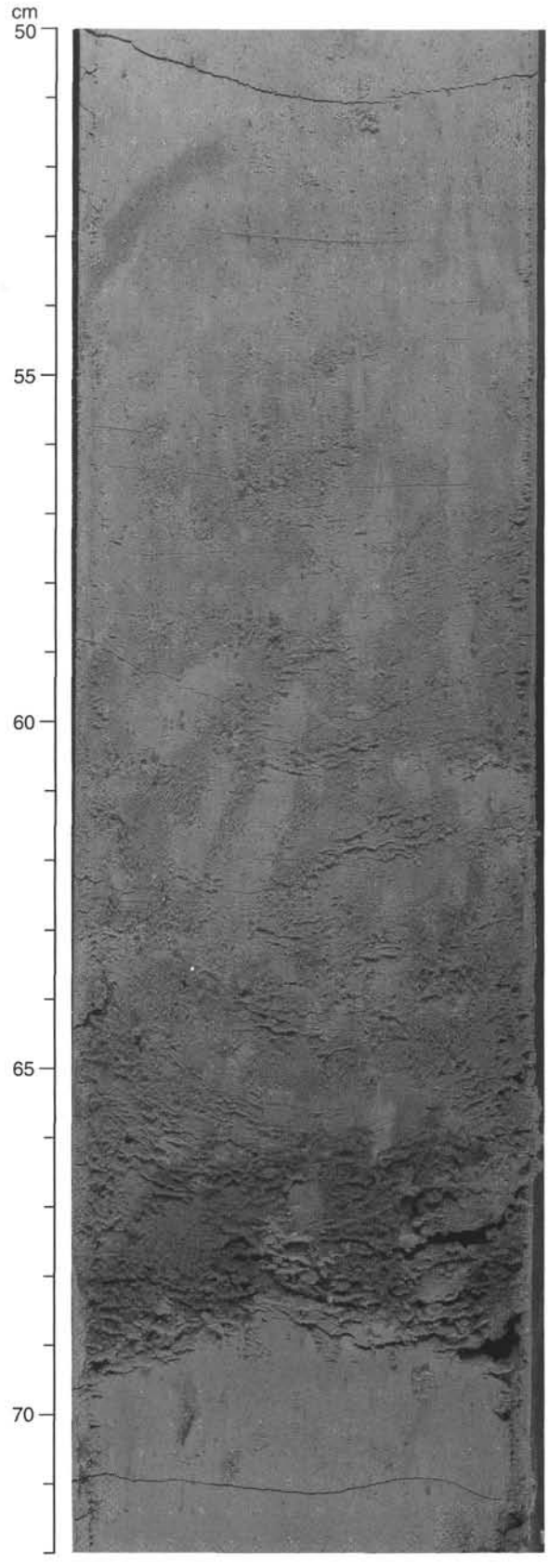

Figure 6. Volcanic ash layer with a sharp base and transitional top, reworked by bioturbation. Closeup photo, interval 165-998A-10H-4, 50–72 cm.

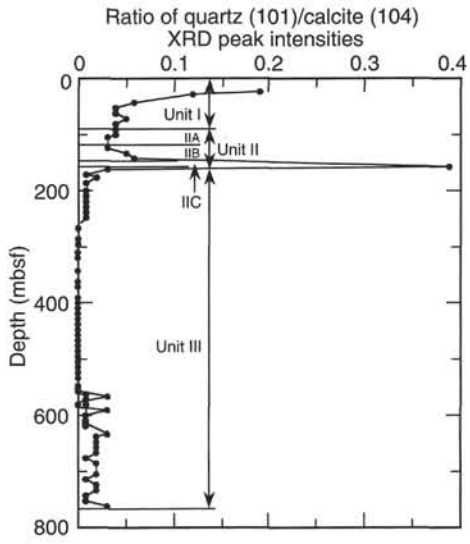

Figure 7. Ratio of relative quartz/calcite XRD peak intensities for lithologic Units I through III.

Subunit IIC consists of a 16-m-thick sequence of nannofossil mixed sediment and clay of the middle/late Miocene boundary interval. The subunit stands out from the rest of the section drilled at Site 998 in that carbonate contents drop to near zero in the middle of the sequence, indicating a shoaling of the early late Miocene carbonate compensation depth (CCD) to a position above or very close to the paleodepth of this site (Fig. 9). This event, similarly recognized in Ocean Drilling Program (ODP) Leg 138 sites on the western side of the Central American Isthmus, has been referred to as the late Miocene "carbonate crash" (Lyle et al., 1995) and is discussed in more detail at the end of this section.

The transition from Subunit IIB to IIC is distinguished by a sharp drop in carbonate content, a sharp rise in magnetic susceptibility values, a major shift in the ratio of reflectance at red to blue wavelengths (Figs. 4, 5), and a sharp rise in the quartz/calcite ratio (Fig. 7). Though carbonate values drop close to zero over selected intervals of the subunit, the average carbonate content of the sediments seems to be closer to about 30%. The sediments of Subunit IIC range in color from light to pinkish gray (2.5Y 7/2 to 7.5YR 6/2) when carbonate is present, to dark yellowish brown (10YR 3/4) when carbonate contents are very low. Mineral phases identified from XRD data include quartz, traces of zeolites (clinoptilolite?) and the clay mineral smectite, possibly derived from altered volcanic ash deposits. Trace quantities of other clay group minerals include kaolinite or chlorite (?) and possibly illite. Mixing of the sediments by bioturbation is evident throughout.

Minor lithologies in this subunit are similar to those observed in Subunits IIA and IIB and include graded turbidites and volcanic ash layers. Compared to the carbonate-poor host sediment, the turbidites consist largely of displaced foraminifers and nannofossils that were apparently buried quickly enough to escape dissolution during a time interval when the CCD was clearly very shallow (Fig. 10). The majority of ash layers are a few centimeters thick at most, with the notable exception of one near the very top of the subunit that spans almost a meter of Section 165-998A-16H-4. This thick ash layer is made more prominent by its fresh appearance and bright red color (10R 5/4).

Lithologic Unit III

Intervals: Section 165-998A-18X-1, 20 cm, to Core 165-998A-67X; Core 165-998B-1R to Section 165-998B-22R-4, 90 cm
Age: middle Miocene to middle Eocene
Depth: 161.0–637.6 mbsf, Hole 998A; 558.3–766. 0 mbsf, Hole 998B

Table 2. XRD bulk mineralogical analyses for Site 998.

Unit	Subunit	Hole, core, section, interval (cm)	Depth (mbsf)	Mineralogy									Ratio of quartz/calcite XRD peak intensities
									Clays				
				Calcite	Feldspar	Quartz	Dolomite	Zeolites (clinoptilolite?)	Presence/ absence	Chlorite/ kaolinite?	Illite	Smectite	
I		998A-3H-4, 24–25	23.04	P		P			P	Tr?		P	0.19259
		998A-3H-6, 112–113	26.92	P		P	P		P	Tr	Tr?		0.12331
		998A-5H-4, 50–52	42.32	P		P			P	Tr	Tr		0.06259
		998A-6H-4, 50–51	51.8	P		P			P	Tr			0.04151
		998A-7H-4, 50–52	61.3	P		P			P	Tr			0.04190
		998A-8H-3, 38–40	69.18	P		P	P		P	Tr			0.05250
		998A-9H-3, 50–52	78.8	P		P			P	Tr			0.04185
		998A-10H-4, 109–111	90.39	P		P	P		P	Tr			0.04151
II	A	998A-11H-3, 111–112	98.41	P		P	P?		P	Tr			0.04190
		998A-12H-2, 133–134	106.63	P		P			P	Tr			0.03159
		998A-13H-3, 28–30*				Tr			P			P	
	B	998A-14H-3, 34–37	126.14	P	Tr	P			P	Tr?			0.03121
		998A-15H-3, 33–35	135.63	P	Tr	P			P	Tr?	Tr		0.05182
		998A-16H-3, 28–30	145.08	P		P			P	Tr?			0.06231
	C	998A-16H-4, 145–146*				Tr			P			P	
		998A-17H-3, 110–112	155.4	P		P		Tr	P			P	0.39566
III		998A-18X-1, 14–15	160.94	P		P			P				0.03110
		998A-19X-5, 8–10	172.28	P		Tr		Tr	Tr		Tr?		0.0167
		998A-20X-2, 51–53	177.91	P		Tr			Tr				0.0294
		998A-21X-1, 107–108	186.57	P		Tr			Tr				0.0141
		998A-22X-5, 59–60	201.69	P		Tr			Tr				0.0140
		998A-23X, 65–66	211.45	P		Tr			Tr				0.0145
		998A-24X-5, 64–65	221.04	P		Tr?			Tr?				0.0146
		998A-25X-2, 73–74	226.23	P		Tr			Tr?				0.0152
		998A-26X-3, 73–75	237.33	P		Tr			Tr				0.0146
		998A-27X-4, 74–77	248.44	P		Tr?			Tr				0.0141
		998A-29X-4, 41–42	267.41	P		Tr?			Tr				0.0027
		998A-31X-4, 58–59	286.78	P		Tr?			Tr?				0.0019
		998A-32X-3, 54–56	294.84	P					Tr?				0.00
		998A-34X-1, 90–92	311.4	P				Tr?	Tr?				0.00
		998A-35X-1, 101–102	321.21	P									0.00
		998A-37X-2, 110–111	342	P				Tr	Tr				0.00
		998A-39X-2, 108–109	361.18	P				Tr					0.00
		998A-40X-2, 71–72	370.41	P				Tr					0.00
		998A-42X-2, 74–75	389.84	P	Tr			Tr					0.00
		998A-43X-2, 23–24	398.93	P				Tr					0.00
		998A-44X-2, 76–78	409.06	P				Tr					0.00
		998A-45X-3, 72–74	420.12	P				Tr					0.00
		998A-46X-3, 17–19	429.17	P				P					0.00
		998A-47X-1, 107–109	436.77	P				Tr					0.00
		998A-48X-2, 75–76	447.55	P				Tr					0.00
		998A-49X-3, 83–85	458.73	P				Tr					0.00
		998A-50X-3, 63–64	468.13	P				Tr					0.00
		998A-51X-1, 25–26	474.35	P				Tr			Tr		0.00
		998A-51X-3, 43–45	477.53	P				Tr					0.00
		998A-52X-3, 130–132	488	P				Tr					0.00
		998A-53X-3, 17–19	496.47	P				Tr					0.00
		998A-54X-1, 16–17	503.06	P				Tr					0.00
		998A-55X-3, 109–110	516.59	P				Tr					0.00
		998A-56X-2, 16–17	523.76	P				Tr					0.00
		998A-57X-2, 19–31	533.49	P				Tr					0.00
		998A-58X-3, 88–89	545.28	P				Tr					0.00
		998A-59X-3, 43–44	554.53	P				Tr					0.00
		998A-60X-4, 88–89	566.08	P		Tr		Tr					0.03139
		998A-61X-1, 125–126*	571.55	Tr		Tr?			P			P	
		998A-62X-3, 31–33	583.21	P									0.00
		998A-63X-1, 68–69	590.18	P		Tr		Tr					0.03112
		998A-64X-1, 11–12	599.21	P		Tr		Tr					0.0174
		998A-65X-1, 31–32	609.01	P		Tr		Tr					0.0185
		998A-66X-2, 15–17	619.95	P		Tr		Tr					0.0181
		998B-1R-1, 79–80	559.09	P		Tr?		Tr?					0.0021
		998B-1R-4, 66–67	563.46	P		Tr?		P			P		0.0156
		998B-2R-3, 126–127	572.16	P		Tr?		Tr					0.0132
		998B-3R-4, 85–87	582.85	P		Tr?		Tr					0.0127
		998B-5R-4, 73–75	602.03	P		Tr		Tr?					0.0138
		998B-6R-3, 58–59	609.88	P		Tr							0.0149
		998B-7R-1, 24–25	616.24	P		Tr		Tr					0.0159
		998B-8R-5, 55–57	632.15	P		Tr		P			P		0.03139
		998B-9R-3, 117–118	639.37	P		Tr		Tr					0.02100
		998B-10R-2, 2–3	646.32	P		Tr		Tr					0.02121
		998B-11R-1, 65–66	655.15	P		Tr		Tr					0.02128
		998B-12R-3, 117–118	668.27	P		Tr		Tr					0.02102
		998B-13R-3, 132–133	678.12	P		Tr		Tr					0.0176
		998B-14R-3, 50–52	687	P		Tr		Tr					0.0298
		998B-15R-4, 38–39*	697.68	Tr		Tr		Tr	P			P	
		998B-16R-3, 97–98	706.67	P		Tr		Tr					0.02104
		998B-17R-1, 68–69	712.98	P		Tr		Tr					0.0150
		998B-18R-3, 96–98	725.96	P		Tr		Tr					0.0290
		998B-19R-3, 102–104	735.62	P		Tr		Tr					0.02119
		998B-20R-2, 48–50	743.18	P		Tr		Tr					0.0171
		998B-21R-1, 86–88	751.6	P		Tr		Tr					0.0166

Table 2 (continued).

Unit	Subunit	Hole, core, section, interval (cm)	Depth (mbsf)	Mineralogy									
				Calcite	Feldspar	Quartz	Dolomite	Zeolites (clinoptilolite?)	Clays: Presence/ absence	Clays: Chlorite/ kaolinite?	Clays: Illite	Clays: Smectite	Ratio of quartz/calcite XRD peak intensities
		998B-22R-2, 8–10	762.08	P		Tr		Tr					0.03142

Notes: The precise identification of chlorite and kaolinite is not possible due to the low intensities of diagnostic peak reflections. Sample intervals with asterisks are volcanic ashes. P = present, Tr = trace quantities, and Tr? = presence of mineral uncertain.

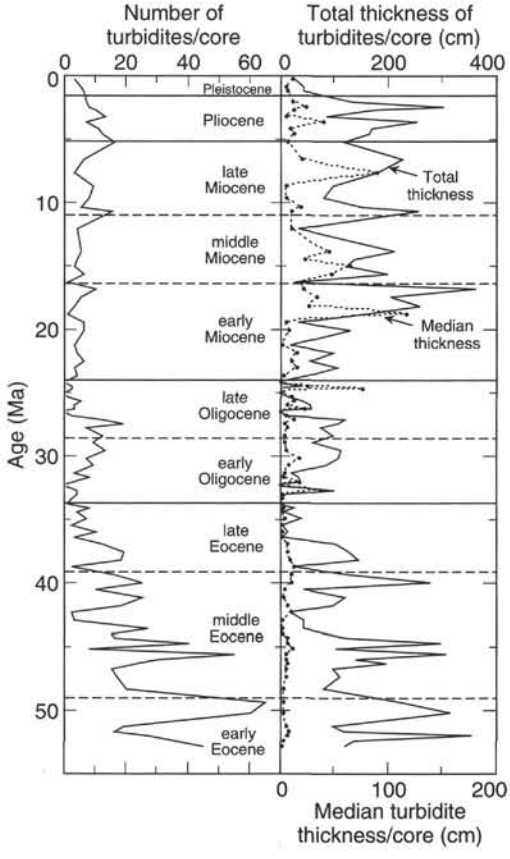

Figure 8. Plot of turbidite frequency and the median and total bed thicknesses vs. age.

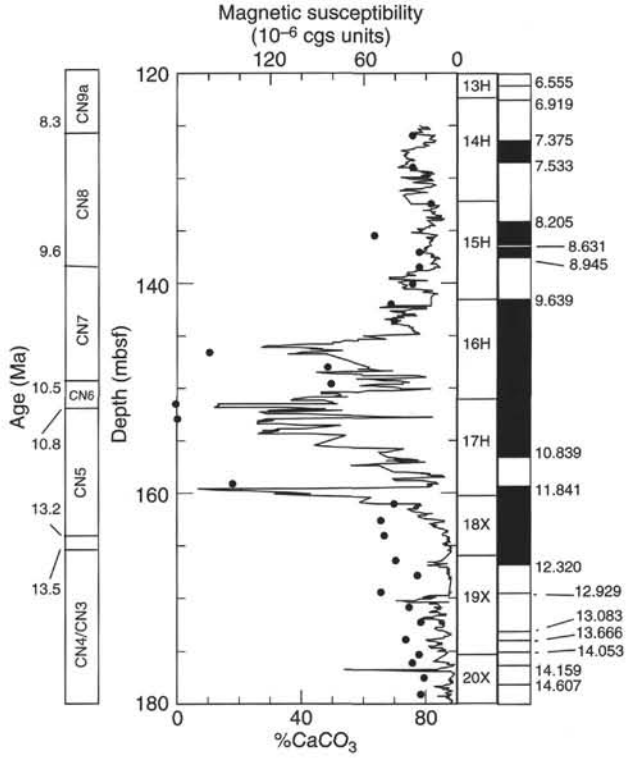

Figure 9. Summary chart showing correlation between $\%CaCO_3$ (solid circles) and magnetic susceptibility (solid line) data for pelagic carbonates (values from redeposited beds and ash layers have been omitted) from 120 to 180 mbsf. Ages from nannofossil zonal distribution and magnetic polarity data given in right and left hand columns.

Unit III is 605.2 m thick and consists of light gray (5GY 7/1) to greenish gray (5GY 6/1) nannofossil chalk mixed with varying amounts of clays and foraminifers. This lithology grades with depth into dark greenish gray (5GY 4/1) calcareous limestone with clay. There is a distinct decline downhole in the abundance of quartz and clay minerals, immediately below the Subunit IIC/Unit III boundary. XRD data indicate the presence of zeolites below Core 165-998A-36X. The boundary between chalk and limestone is transitional, probably occurring over tens of meters, but is complete by Core 165-998B-16R (~700 mbsf). The dominant background lithology is interbedded with redeposited layers of light gray to pinkish gray foraminifer chalk, grading upward into clayey nannofossil chalk, and with dark greenish gray volcaniclastic ash layers. Downhole, the background sediments become progressively darker because of the mixing with dark greenish gray clays derived from the alteration of volcanic ash. The measured carbonate content of the background sediment varies between 59% and 100%, although most of the unit contains more than 80% carbonate. The first occurrence downhole of chert nodules at Site 998 is within Unit III (Section 165-998A-27X-4, 122–126 cm), and they are present thereafter throughout Unit III. Incipient chert nodules, characterized by an inner core of chert and an outer core of silicified limestone and ranging up to 3 cm thick, are frequent. The distribution of chert and incipient chert nodules form a distinct trend downhole (Fig. 11). Slumped intervals with reverse grading and extensive soft-sediment deformation occur in Cores 165-998A-31X through 32X and 66X (Sections 1 and 2), and in Core 165-998B-8R (Sections 1 and 2). Correlation of thickness and relative spacing between three adjacent ash layers and slump intervals in Sections 165-998A-62X-3 and 165-998B-3R-4 confirmed the splicing of Holes 998A and 998B based on color data correlation.

Nannofossil chalk with clay and foraminifers and calcareous limestone with clay is light gray to greenish gray (10YR 7/2–5GY 6/1) in color. Bioturbation grades from slight to intense, and is most visible in adjacent lithologies with contrasting colors. Smear-slide data indicate that the sediment consists of a mixture of clay minerals, coccolith plates, and minor foraminifer fragments. Calcareous grains, probably derived from the recrystallization of nannofossils and foraminifers, appear in Core 165-998A-59X and become progressively more abundant downhole. Calcium carbonate data show

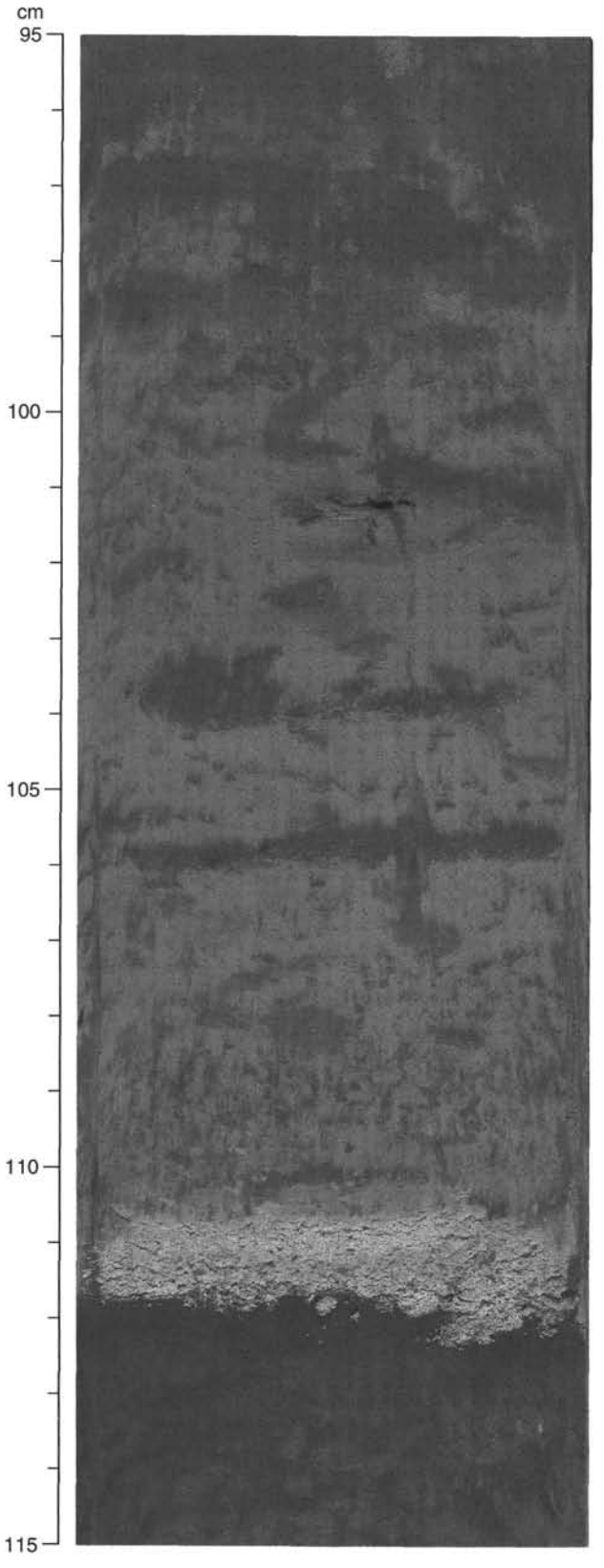

Figure 10. Redeposited layer composed of sand-sized foraminiferal chalk grading upward into a nannofossil chalk. The base of the layer is sharp and erosional, the top is transitional and reworked by bioturbation. Closeup photo, interval 165-998A-17H, 95–115 cm.

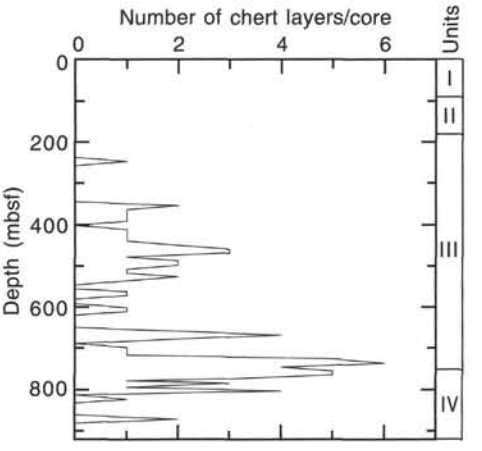

Figure 11. Number of chert nodules per core in Site 998 vs. depth.

that during deposition of Unit III the $CaCO_3$ content initially increased from 66 to 90 wt% and started to decrease after Core 165-998A-59X (Figs. 4, 5). Wispy dissolution seams initially become observable because of the accumulation of dark greenish gray (5GY 4/1) clay in Core 165-998A-57X, and they become progressively more abundant with depth.

Normally graded sediment layers are interpreted as turbidites. The lower part contains sand- to silt-sized light gray (10YR 7/2) to pinkish gray (5YR 7/2) foraminifer chalk, grading to an upper part with clay- or silt-clay-sized, light greenish gray (5GY 7/1) clayey nannofossil chalk. These layers range in thickness from 10 to 30 cm, but can reach up to 76 cm. The boundary with the underlying units is generally sharp and erosive, whereas the boundary with the overlying sediment is usually gradational and overprinted by bioturbation. The sand to silt bases are generally massive or parallel laminated. Starting with Core 165-998A-40X and below, some sand to silt layers show an alternation of parallel and cross laminations, suggesting reworking of the redeposited beds by contourite currents. Smear-slide data show that the basal silt/sand units consist primarily of intact and fragmented foraminifer tests and minor nannofossils mixed with clays. The transition between the basal silt/sand and the upper clayey part may be gradational or sharp. The upper part is typically slightly to moderately bioturbated.

Volcanic ash layers are an important lithology of Unit III. They occur in very thin- to medium-bedded layers and are derived from eolian transport of pyroclastic material from explosive eruptions. They can be recognized by their greenish color and distinctive lithology. This material occurs as (1) discrete layers, (2) bioturbated but visible patches, and (3) dispersed ash in the clay. Some ash was also reworked together with carbonate grains as turbidite layers.

Lithologic Unit IV

Intervals: Sections 165-998B-22R-4, 90 cm, to 37R-CC
Age: middle to early Eocene
Depth: 766.0–904.8 mbsf, Hole 998B

Unit IV is 137.3 m thick and is middle to early Eocene in age. The dominant lithologies are calcareous limestone, calcareous limestone with clay, and calcareous volcaniclastic mixed sedimentary rock interbedded with foraminiferal limestone, altered volcanic ash, altered volcanic ash with carbonate, and minor chert. This unit is distinguished from Unit III by (1) a sharp increase in the frequency of graded foraminifer limestone, altered volcanic ash, and altered volcanic ash with carbonate (turbidites, Fig. 8); (2) a decrease in carbonate content, and (3) a slight increase in the variability of color reflectance (Figs. 4, 5).

Light greenish gray (5GY 7/1) calcareous limestone and calcareous limestone with clay occur as thick-bedded sequences that appear relatively homogeneous with occasional mottling and slight to moderate bioturbation. With increasing depth in Unit IV, the dominant lithology shifts to calcareous volcaniclastic mixed sedimentary rock. This shift can be seen as an overall decrease in carbonate content and an increase in magnetic susceptibility with depth (Figs. 4, 5). The mixed sedimentary rocks are also thick-bedded but less bioturbated. They often exhibit fine-scale parallel laminations on the order of 1–5 mm.

The dominant lithologies are interbedded with numerous thin- to medium-bedded layers of normally graded foraminifer limestone and altered volcanic ash with carbonate. Foraminiferal limestone beds commonly have a sharp base, are normally graded, and have a fine-grained, bioturbated top. In many of the beds, the coarse bases show parallel and cross laminations. These beds are interpreted as turbidity current deposits or intervals reworked by bottom currents and are most common in the upper part of Unit IV (Cores 165-998B-21R through 30R).

Beginning at Core 165-998B-30R, there is a marked increase in the abundance of altered volcanic ash with carbonate. It occurs as greenish gray to dark greenish gray, thin- to medium-bedded layers with sharp bases and bioturbated tops (Fig. 12). A distinctive feature of these layers is a gradation in color from light gray (10YR 7/2) at the base to greenish gray (5GY 6/1) at the top. The color change is caused by an enrichment in foraminifer fragments at the base and a gradational increase in the proportion of altered volcanic ash toward the tops of the layers. Most of the layers have bases that are planar to cross-laminated and are likely the result of turbidity current deposition, with perhaps some reworking by bottom currents. The frequency of the altered volcanic ash with carbonate layers goes through a maximum in Core 165-998-32R, causing a lowering in the carbonate vs. depth curve at about 860 mbsf (Fig. 5). With increasing depth, the trend then moves toward an overall increasing carbonate content and a return to limestone lithologies at the base of the hole.

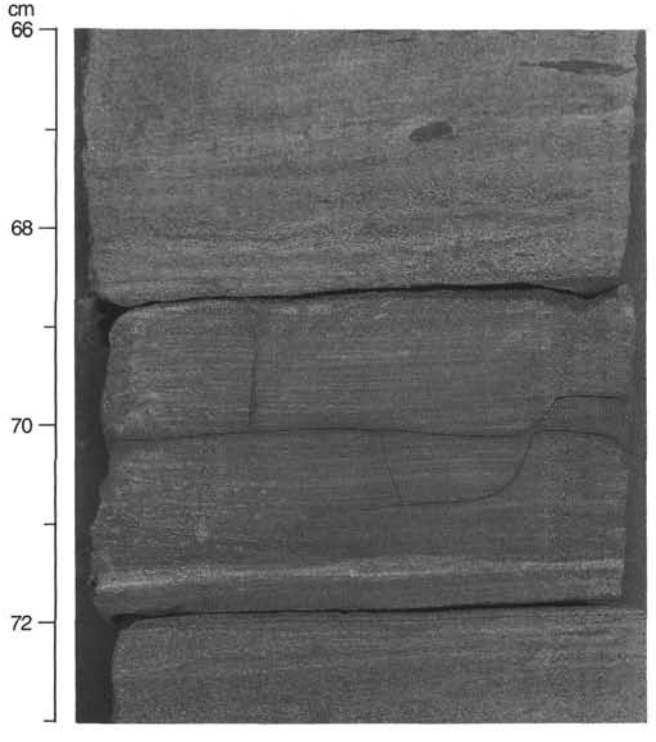

Figure 12. Redeposited layer composed of volcaniclastic sand mixed with foraminifers. The sand shows an alternation of parallel and cross lamination, suggesting a reworking of the turbidite bed by contour currents. Closeup photo, interval 165-998B-35R-4, 66–73 cm.

Many cores from Unit IV contain bioturbated intervals 1 to 10 cm thick that are darker green in color than the dominant lithology and have been described as "wispy" laminations because of their undulatory and disseminated nature. The color of these intervals is quite similar to discrete layers of altered volcanic ash, and their common association with volcanic ash beds suggest that they represent altered zones of dispersed volcanic ash within the background sediment. Carbonate concentrations in these zones are typically lower than the surrounding sediment, indicating dilution of the pelagic carbonate fraction with the alteration products of volcanic ash.

Greenish gray (5GY 6/1), altered volcanic ash also occurs as thin bedded layers with sharp bases and bioturbated tops (e.g., Core 165-998B-37R). However, these are far less common than the altered ash with carbonate layers and lack the basal planar and cross laminations. The occurrence of normal grading, lack of tractional sedimentary structures, and low carbonate content of these layers suggest that they represent volcanic ash fall layers produced by individual explosive eruptions. In Sections 165-998B-21R-5 to 21R-CC and Sections 165-998B-26R-2 through 26R-4, there are intervals of disturbed sediments in which bedding contacts are inclined or deformed and the units have been fractured. These features suggest that the stratigraphy has been disrupted by minor slumping. These intervals are found just above the commonly graded foraminiferal limestone beds (turbidites) in Unit IV.

A minor but significant lithology of Unit IV are zones of incipient silicification of limestones. These zones are found in Sections 165-998B-22R-1 to 22R-4 and in Sections 165-998B-23R-2 to 23R-CC and are usually a few centimeters in thickness or diameter (Fig. 11). They typically have smooth undulating boundaries that transect lithologic contacts.

Relationship of Lithology to Color Reflectance and Magnetic Susceptibility

Magnetic susceptibility and color reflectance measurements were used to define lithologic units at Site 998 in conjunction with results from carbonate analyses and visual core descriptions. Because of the much closer sample spacing between measurements (5 cm), magnetic susceptibility and color reflectance data show variability at a much higher frequency than other lithologic parameters examined. At sites where multiple holes were drilled, the high-resolution records provided by magnetic susceptibility and digital color measurements were often the primary data used to make between-hole correlations and to construct composite stratigraphic sections. Though not essential at Site 998 because of the minimal overlap between holes, it is still useful to examine the relationships between sediment lithology, susceptibility, and reflectance.

To a first approximation, variations in magnetic susceptibility and color reflectance are generally assumed to reflect the changing proportions of carbonate to lithogenic materials. The relationships between carbonate, magnetic susceptibility, and the ratio of reflectance at the red and blue wavelengths (680/420 nm) for sediments in Hole 998A are shown in Figure 13. Data pairs plotted in this figure represent measurements of color and susceptibility directly associated with discrete samples from Hole 998A that were analyzed for their carbonate content. As carbonate samples were primarily selected to avoid turbidites and visible ash layers, the relationships indicated in Figure 13 can be assumed to apply only to the dominant pelagic component of the sediments.

Magnetic susceptibility exhibits a high linear correlation with carbonate content ($r = 0.87$), with higher values corresponding to low carbonate concentrations. This is consistent with the hypothesis that the susceptibility magnitude is determined by the relative concentrations of carbonate and clay minerals in the pelagic fraction. The

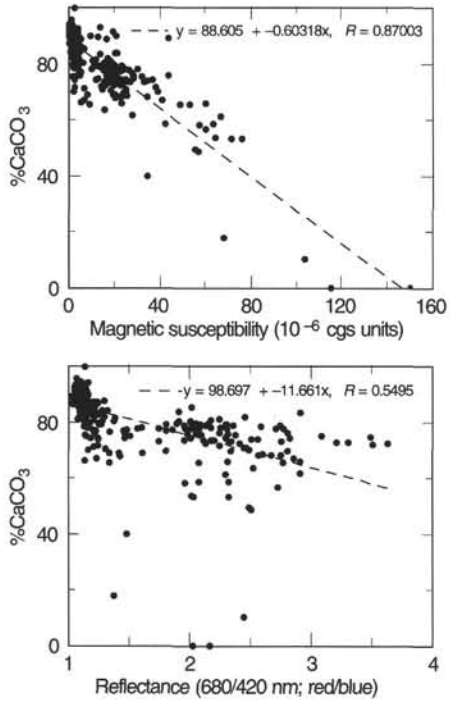

Figure 13. Relationship between carbonate content and magnetic susceptibility (top) and color reflectance (bottom) in sediments from Hole 998A. Magnetic susceptibility and reflectance values correspond to discrete samples where carbonate contents were directly measured.

strength of this relationship suggests that magnetic susceptibility has potential as a means of indirectly estimating sedimentary carbonate contents for purposes of carbonate accumulation and dissolution studies. This potential will be further evaluated in more detailed postcruise studies.

Analysis of the complete magnetic susceptibility record (Fig. 13) indicates numerous individual measurements that rise far above the general range of background variability. Comparison of these peaks to the actual lithologies suggests that the majority of these measurements fall within volcanic ash layers and/or turbidites (which are themselves often volcaniclastic). In general, the relationship between ash content, the degree of ash alteration, and susceptibility is likely to be complicated at Site 998, especially in the deeper sections where the volcanic contribution is high. In Unit IV, for example, there is clearly an offset between the interval of minimum carbonate values and the interval of maximum susceptibility (Fig. 13). Such observations suggest that variations in the nature of the noncarbonate component will need to be considered before magnetic susceptibility can be used to estimate carbonate concentrations at high resolution.

Color reflectance data have also been shown to exhibit a first-order relationship with carbonate content in open-marine settings (e.g., Mix et al., 1992; Curry, Shackleton, Richter, et al., 1995). At Site 998, where the carbonate contents of sediments are generally quite high (>80%), we found that examination of downhole patterns of reflectance variability over individual wavelengths was not particularly useful in terms of helping to define lithologic units. Color spectra were also found not to be especially diagnostic of the changing lithologies. As Figure 14 shows, spectra representative of individual units are fairly similar, with most of the differences related to overall levels of reflectance across the complete range of wavelengths measured. Contrasts between units are most evident when looking at relative reflectance at the ends of the visible spectrum. For that reason, we chose at this site to emphasize the ratio of reflectance values in the "red" and "blue" bands, or at 680 and 420 nm, respectively.

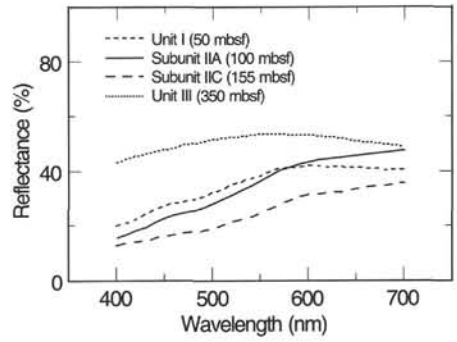

Figure 14. Color reflectance spectra for representative lithologies in Hole 998A. Reflectance was measured over 10-nm intervals between visible wavelengths of 400 and 700 nm.

As already noted in the discussion of lithologic units, the 680/420 nm ratio is most variable in sediments of Units I and II. Higher ratios above 161.0 mbsf in Hole 998A are taken to indicate a greater proportion of oxidized iron in the sediment. Below 161.0 mbsf, in Units III and IV, the red to blue ratio is centered around a value of 1.0, indicating maximum reflectance at about 550 nm (or "green") in the visible spectrum. We interpret sediments below this level to have been affected by reducing conditions. This change is consistent with sedimentological descriptions of sediments changing from dominant shades of pale and light yellowish brown to light gray to greenish gray near the Unit II/III transition.

Figure 14 shows the relationship between percent carbonate and the 680/420 nm reflectance ratio for paired samples in Hole 998A. The degree of correlation between carbonate and color is much less robust ($r = 0.55$) than it is for magnetic susceptibility, with the scatter particularly severe at low carbonate values. Hence, color reflectance data (or at least the ratio looked at here) would appear to have less value as a potential predictor of sedimentary carbonate content.

Turbidite Frequency and Character at Site 998

Deposition of sediment by turbidity currents had a major impact on the lithologic character of Site 998. A total of 1069 turbidite layers with an aggregate thickness of 106.9 m (normalized for core recovery) and representing 12% of the sedimentary sequence of Site 998 were identified based on visual core description. These values are most likely minima owing to the difficulty in recognizing turbidite deposits in intervals cored with the XCB and RCB and in low recovery cores.

The frequency of turbidites at Site 998 was assessed by tabulating the number of turbidites per core and then normalizing for core recovery. There are large variations in the frequency of turbidites downcore (Fig. 8). Two distinct peaks in frequency (~16 turbidites/core) are found near the Miocene/Pliocene and late to middle Miocene boundaries within Units I and II. A third peak (18 turbidites/core) is found within Unit III near the early/late Oligocene boundary. The highest turbidite frequency occurs in the early Eocene and drops off dramatically through the middle Eocene within Unit IV.

The total thickness contribution of turbidite deposits shows two broad maxima in the Pliocene to late early Miocene and in the late to early Eocene (Fig. 8). These maxima are roughly similar in magnitude, despite large contrasts in the frequency of turbidites during these intervals (Fig. 8). This results from a major difference in the scale of turbidites being emplaced during the two intervals. From the Pliocene to the late early Miocene, the turbidite deposits have had a higher median and maximum thickness per core compared with the deposits of the late Oligocene to early Eocene (Fig. 8). Thus, the first maximum was produced by an accumulation of relatively thick tur-

bidites whereas the second maximum was generated by much more frequent, yet smaller turbidites.

The two broad maxima reflect fundamentally different types of sediment being delivered by turbidity currents to the site. The frequent, thinner turbidites of the early to middle Eocene consist of altered volcanic ash with carbonate and thus represent a mixture of sediment from a volcanic and pelagic carbonate source. In contrast, the less frequent but thicker turbidites of the Pliocene to late early Miocene maximum consist almost exclusively of redeposited pelagic, carbonate-rich material with little volcanic component.

The almost exclusive occurrence of planktonic and bathyal benthic foraminifers (see "Biostratigraphy" section, this chapter) in the sandy to silty bases of representative turbidites throughout the Site 998 sedimentary succession indicates that the source of the carbonate fraction is most likely from a deep-water environment.

Discussion

The sedimentary sequence of Site 998 reflects significant variations in the contributions of pelagic (carbonate), detrital, and volcanogenic components. The oldest sediments recovered are early Eocene in age (52–53 Ma, Unit IV). At this time, large amounts of volcaniclastic material was deposited as turbidites mixed with carbonate and minor ash falls. The great abundance of turbidite units and their mixed carbonate-volcaniclastic lithology suggests a source from an adjacent island-arc complex, where explosive volcanism generated large quantities of vitric and crystal-rich volcaniclastic material that was mixed with carbonate sediment and redeposited in a deep-water environment. Grain size and bed thicknesses of the turbidites are similar to volcaniclastic facies found in modern-day forearc and backarc basins. Significant quantities of volcaniclastic material are also present in the background sediment (volcaniclastic mixed sedimentary rock) and were most likely deposited under hemipelagic conditions. The source of this material was likely to be an active volcanic arc complex developed along the Cayman Ridge.

During the middle Eocene, the influx of volcaniclastic material was significantly reduced and turbidite influx to the site carried predominantly carbonate sediment. These carbonate turbidites progressively decreased in frequency, marking the beginning of a long interval from the middle Eocene through the middle Miocene (Unit III) when pelagic sedimentation was generally stable and produced a thick sequence of homogeneous calcareous limestones and nannofossil chalks. The pelagic sedimentation was intermittently interrupted by deposition of carbonate turbidites and volcanic ash fallout, but no volcaniclastic material was deposited by turbidity currents. During the mid-Oligocene, there was a period of more frequent carbonate turbidites.

At the transition from the middle to the late Miocene, the carbonate content in the pelagic sediments began a gradual decline. The first sharp reduction in $\%CaCO_3$ is recorded at approximately 11.8–12.3 Ma (Fig. 9). At that time, the fraction of carbonate preserved in the pelagic sediments of Site 998 (with the exclusion of redeposited sediment and ash layers) dropped precipitously, with carbonate deposition appearing to have virtually ceased in an interval tentatively centered on about 10.5 Ma (within calcareous nannofossil Zones CN5 to CN7; see "Biostratigraphy" section, this chapter). Poor preservation of calcareous microfossils observed in smear slides and planktonic foraminifers in washed samples (see "Biostratigraphy" section, this chapter) as well as lower sedimentation rates during this interval (see "Sedimentation Rates" section, this chapter) suggest that carbonate dissolution and a sudden shoaling of the CCD were responsible for the accumulation of nearly pure clays on the top of the Cayman Rise during the middle/late Miocene boundary interval. Leg 138 results from the eastern equatorial Pacific have identified a similarly profound change in carbonate depositional patterns within the same calcareous nannofossil zones (i.e., CN6/CN7) at Site 846 from the northern part of the Peru Basin (Mayer, Pisias, Janecek, et al., 1992). This interval has been referred to as the late Miocene carbonate crash (Lyle et al., 1995; Farrell et al., 1995). Lyle et al. (1995) offered two possible mechanisms for what they inferred to represent a rapid change in the deep-water chemistry of the eastern Pacific. Their first and favored mechanism involved the increasing constriction of the Panama Gateway and the resulting diminution of the flow of high CO_3^{2-} deep water from the Atlantic to the Pacific. The second mechanism invoked the onset of North Atlantic Deep Water (NADW) flow and its effects on interbasinal chemistry and circulation. Our observation at Site 998 that the carbonate crash is recorded on the Atlantic side of the Central American Seaway and more specifically near the Yucatan Basin, a basin along the pathway of the surface- and intermediate-water return flow of the NADW, should allow us to place important constraints on the processes responsible for this major Neogene event.

Carbonate accumulation rebounded abruptly in the late Miocene (Subunit IIB) but then decreased again (Subunit IA) with the production of nannofossil mixed sediment. Throughout these intervals, pelagic sedimentation was interrupted by carbonate turbidites and volcanic ash deposition. Turbidite deposition reached a maximum around the early Pliocene. Influx of volcanic ash by fallout was especially intense during the early and middle Miocene and was most likely derived from large-scale explosive volcanic eruptions in Central America (see "Igneous Petrology and Volcanology" section, this chapter).

From the early Pliocene to the recent, sediments recovered at Site 998 record the accumulation of nannofossil oozes of relatively uniform composition, foraminiferal turbidites, and rare volcanic ash falls. An increase in the quartz to carbonate ratio during this interval may be related to the enhanced influx of continental material associated with the onset of Northern Hemisphere glaciation.

BIOSTRATIGRAPHY

Calcareous Nannofossils

The Cenozoic section recovered at Site 998 appears to be largely complete, at least to within nannofossil biostratigraphic resolution. Minor unconformities can be detected in the upper Neogene section. We prepared standard smear slides in every core section recovered, but concentrated on determining, as precisely as possible, standard nannofossil datums (see Table 2, "Explanatory Notes" chapter, this volume). Extreme care was taken in the entire section to avoid sampling turbidites; as a result, only minor reworking was observed in a few samples. The nannofossil datums determined at Site 998 are compiled in Table 3, and the zonal boundaries of Okada and Bukry (1980) are illustrated in Figure 62.

Pleistocene and Neogene

The Pleistocene and Neogene section recovered at Site 998 is almost complete, although the presence of minor unconformities or condensed intervals is suggested by a clustering of nannofossil datums (Table 3). Calcareous nannofossils are abundant throughout the core. Preservation is good from the Pleistocene to middle Miocene and generally moderate below the lower Miocene. Intervals of somewhat poorer preservation characterize the lower part of the upper Miocene (Cores 165-998A-16X and 17X) and the lower Miocene. Nannofossils become somewhat overgrown in the lowest part of the Miocene.

All of the Pleistocene nannofossil zones and subzones can be defined in the uppermost part of Hole 998A (Table 3; Fig. 62). Some of the additional Pleistocene nannofossil datums proposed by Takayama and Sato (1987) and Sato et al. (1991) can be also detected. Samples 165-998A-3H-4, 100 cm, and 3H-5, 100 cm, contain *Reticu-*

Table 3. Nannofossil datums, absolute ages, and depths at Site 998.

Event	Zone (base)	Age (Ma)	Core, section, interval (cm)	Depth (mbsf)
Hole 998A:				
B *Emiliania huxleyi*	CN15	0.248	1H-CC to 2H-1, 100	9.30
T *Pseudoemiliania lacunosa*	CN14b	0.408	2H-1, 100 to 2H-2, 100	10.55
T *Reticulofenestra asanoi*		0.88	3H-3, 100 to 3H-4, 100	23.05
B *Gephyrocapsa parallela*	CN14a	0.94	3H-5, 100 to 3H-6, 100	26.05
B *Reticulofenestra asanoi*		1.17	3H-5, 100 to 3H-6, 100	26.05
T Large *Gephyrocapsa* spp.		1.23	3H-CC to 4H-1, 100	28.40
T *Helicosphaera sellii*		1.26	3H-CC to 4H-1, 100	28.40
B Large *Gephyrocapsa* spp.		1.48	4H-1, 100 to 4H-2, 100	29.55
T *Calcidiscus macintyrei*		1.64	4H-4, 100 to 4H-5, 100	34.05
B *Gephyrocapsa caribbeanica*	CN13b	1.71	4H-5, 100 to 4H-6, 100	35.55
T *Discoaster brouweri*	CN13a	1.95	4H-6, 100 to 4H-7, 60	36.85
T *Discoaster pentaradiatus*	CN12d	2.36	4H-6, 100 to 4H-7, 60	36.85
T *Discoaster surculus*	CN12c	2.51	6H-4, 100 to 6H-5, 100	53.05
T *Discoaster tamalis*	CN12b	2.82	7H-3, 100 to 7H-4, 100	61.05
T *Sphenolithus* spp.	CN12a	3.62	8H-2, 100 to 8H-3, 100	69.05
T *R. pseudoumbilicus*	CN12a	3.83	8H-7, 60 to 8H-CC	75.50
T *Amaurolithus* spp.	CN11	4.50	10H-6, 100 to 10H-CC	93.94
B *Ceratolithus rugosus*	CN10c	5.046	10H-CC to 11H-1, 100	94.94
B *Ceratolithus acutus*	CN10b	5.089	11H-4, 100 to 11H-5, 100	100.55
T *Discoaster quinqueramus*	CN10a	5.537	11H-CC to 12H-1, 100	104.47
B *Amaurolithus* spp.	CN9b	7.392	13H-2, 100 to 13H-3, 100	116.55
B *Discoaster berggrenii*	CN9a	8.281	14H-2, 100 to 14H-3, 100	126.05
T *Discoaster hamatus*	CN8a	9.635	15H-4, 100 to 15H-5, 100	138.55
B *Discoaster hamatus*	CN7	10.476	16H-5, 100 to 16H-6, 100	149.58
B *Catinaster coalitus*	CN6	10.794	16H-CC to 17H-1, 100	152.12
T *Cyclicargolithus floridanus*		13.2	18X-2, 100 to 18X-3, 100	164.05
T *Sphenolithus heteromorphus*	CN5a	13.523	18X-3, 100 to 18X-4, 100	165.55
B *Sphenolithus heteromorphus*	CN3	18.2	26X-CC to 27X-1, 100	242.56
T *Sphenolithus belemnos*		18.3	27X-1, 100 to 27X-2, 100	244.95
B *Sphenolithus belemnos*	CN2	19.2	28X-3, 100 to 28X-4, 100	257.65
T *Sphenolithus delphix*		23.8	35X-CC to 36X-1, 100	330.01
T *Reticulofenestra bisecta*	CN1a	23.9	36X-2, 100 to 36X-3, 100	333.05
T *Sphenolithus ciperoensis*		25.5	40X-2, 100 to 40X-3, 100	371.45
T *Sphenolithus distentus*	CP19b	27.5	48X-2, 100 to 48X-3, 68	448.39
B *Sphenolithus ciperoensis*	CP19a	29.9	52X-2, 103 to 52X-3, 103	486.98
B *Sphenolithus distentus*	CP18	31.5	55X-1, 100 to 55X-2, 100	514.25
T *Reticulofenestra umbilicus*	CP17	32.3	60X-4, 100 to 60X-5, 100	566.95
T *Ericsonia formosa*	CP16c	32.8	61X-4, 100 to 61X-5, 100	576.55
T *Discoaster saipanensis*	CP16a	34.2	62X-4, 100 to 62X-5, 60	586.00
T *Discoaster barbadiensis*	CP16a	34.3	62X-4, 100 to 62X-5, 60	586.00
T *Chiasmolithus grandis*	CP15	37.1	Below base of section	
Hole 998B:				
T *Reticulofenestra umbilicus*	CP17	32.3	1R-5, 100 to 1R-6, 90	566.00
T *Ericsonia formosa*	CP16c	32.8	2R-3, 100 to 2R-4, 110	572.70
T *Discoaster saipanensis*	CP16a	34.2	4R-3, 110 to 4R-4, 110	591.95
T *Discoaster barbadiensis*	CP16a	34.3	4R-3, 110 to 4R-4, 110	591.95
T *Chiasmolithus grandis*	CP15	37.1	10R-5, 110 to 10R-4, 100	651.10
B *Reticulofenestra bisecta*		38.0	13R-4, 110 to 13R-CC	680.24
T *Chiasmolithus solitus*	CP14b	40.4	13R-3, 110 to 13R-4, 110	678.65
T *Nannotetrina fulgens*		43.1	19R-CC to 20R-1, 126	741.62
B *Reticulofenestra umbilicus*	CP14a	43.7	20R-CC to 21R-1, 110	749.07
T *Chiasmolithus gigas*	CP13c	44.5	25R-1, 100 to 25R-2, 100	781.55
B *Chiasmolithus gigas*	CP13b	46.1	28R-1, 125 to 28R-2, 120	810.48
B *Nannotetrina fulgens*	CP13a	47.3	30R-2, 129 to 30R-3, 92	831.16
B *Discoaster sublodoensis*	CP12	49.7	32R-6, 90 to 32R-CC	855.43
T *Tribrachiatus orthostylus*		50.6	33R-1, 123 to 33R-3, 100	859.20
B *Discoaster lodoensis*	CP10	52.0	Below base of section	

Notes: T = top of species range (last appearance datum), B = base of species range (first appearance datum). This entire table also appears on CD-ROM (back pocket).

lofenestra asanoi together with *Gephyrocapsa parallela,* suggesting an age between 0.88 and 0.94 Ma. Large *Gephyrocapsa* specimens and *Helicosphaera sellii* were observed in Sample 165-998A-4H-1, 100 cm. A few reworked specimens of *Discoaster* and *Sphenolithus,* possibly from the Miocene, were observed in Sample 165-998A-2H-CC.

The lowest occurrence of *Gephyrocapsa caribbeanica,* which defines the Subzone CN13b/CN13a and the Pliocene/Pleistocene boundaries, is placed between Samples 165-998A-4H-5, 100 cm, and 4H-6, 100 cm. Most of the Neogene zones and subzones of Okada and Bukry (1980) can be recognized except Subzone CN12d; the last occurrences (LOs) of *Discoaster brouweri* and *D. pentaradiatus* both lie between Samples 165-998A-4H-6, 100 cm, and 4H-7, 60 cm. The LO of *Reticulofenestra pseudoumbilicus* lies between Samples 165-998A-8H-7, 60 cm, and 8H-CC; and the LO of *Sphenolithus* spp. lies between Samples 165-998A-8H-2, 100 cm, and 8H-3, 100 cm. Thus, the LOs of these species do not coincide in Hole 998A as many authors have pointed out (e.g., Backman and Shackleton, 1983). We use the LO of *R. pseudoumbilicus* to define the CN12/CN11 boundary.

The Miocene/Pliocene boundary is thought to lie between the LO of *Discoaster quinqueramus* and the FO of *Ceratolithus acutus* (Samples 165-998A-11H-4, 100 cm, and 12H-1, 100 cm. We did not observe *Discoaster loeblichii,* the first occurrence (FO) of which defines the base of Subzone CN8b, and therefore could not divide Subzones CN8a and CN8b in Hole 998A. The base of Subzone CN5b could not be precisely determined because of the rarity of the marker taxon *Discoaster kugleri* and the presence of reworking in Core 165-998A-18X. Thus, Samples 165-998A-18X-3, 100 cm, down to 18X-CC were tentatively placed in Zone CN5 based on the absence of *Catinaster coalitus* and *Sphenolithus heteromorphus. Helicosphaera ampliaperta,* the LO of which defines the Zone CN3/CN4 boundary, is also absent in Hole 998A. *Discoaster druggii,* the FO of which de-

fines the boundary between Subzones CN1c and CN1b, was difficult to identify because common overgrowth in the lower Miocene interval tends to obscure specimens of *Discoaster.*

Paleogene

The Paleogene section ranges from Oligocene (Zone CN1) to lower Eocene (Zone CP10) and appears to be complete, at least to within biostratigraphic resolution. Preservation in the Oligocene, upper Eocene, and upper part of the middle Eocene section is moderate and nannofossils are abundant. A noticeable deterioration in preservation and decrease in relative abundance is noted in Cores 165-998B-13R to 17R (675–720 mbsf), and nannofossils in the lower part of the middle and lower Eocene are characterized by significant fragmentation, dissolution, and overgrowth. Preservation deteriorates further and abundance decreases dramatically below Core 165-998B-32R with a substantial increase in dolomite content. Cores 165-998B-33R to 37R contain rare, substantially etched nannofossils, but important markers are still present.

Almost all of the Paleogene zones and subzones of Okada and Bukry (1980) can be defined at Site 998 (Table 3; Fig. 62), although some more precisely than others. We are less confident about the precision of standard Oligocene datums (see Table 2, "Explanatory Notes" chapter, this volume) in Holes 988A than about those in the Neogene. We had considerable difficulty distinguishing consistently between *Sphenolithus ciperoensis, S. distentus,* and *S. predistentus* because of the considerable morphological overlap, even though we strictly applied guidelines outlined by Aubry (1989). Another taxon, *Zygrhablithus bijugatus,* is sparse in the later part of its range. We note that *Reticulofenestra bisectus* is considerably smaller in the uppermost part of its range than the standard size of this species (at least 10 µm in most definitions).We did not observe a pronounced acme of *Ericsonia subdisticha* and therefore could not determine the boundary between Subzones CP16a and CP16b. We did not observe the species *Coccolithus crassus,* the FO of which defines the base of Zone CP11. Sample 165-998B-34R-CC correlates with Zone CP10 based on the occurrence of *Discoaster multiradiatus,* which does not range above the lower part of the zone (e.g., Bralower and Mutterlose, 1995). Thus, we tentatively place the CP11/CP10 boundary between Cores 165-998B-33R and 34R.

Several datums lie in the Eocene/Oligocene boundary interval. The LOs of *Reticulofenestra umbilicus* and *Ericsonia formosa* have been determined with confidence. We are less confident about the placement of the LOs of *Discoaster barbadiensis* and *Cribrocentrum reticulatum* (the latter datum is placed between Samples 165-998A-62X-3, 90 cm, and 62X-4, 90 cm, and between Samples 165-998B-2R-5, 120 cm, and 2R-CC) due to the rarity of these taxa, and the LO of *D. saipanensis* due to overgrowth. However, the Eocene/Oligocene boundary lies between the LOs of *D. barbadiensis* and *E. formosa* (i.e., between Samples 165-998A-61X-4, 100 cm, and 62X-5, 60 cm, and between Samples 165-998B-2R-3, 100 cm, and 4R-4, 110 cm.

We could not determine the following Eocene nannofossil events: the FOs of *Cribrocentrum reticulatum* because this species is very rare in the lower part of its range, and *Blackites inflatus* because no specimens of this species were observed. We used minimum sizes of 10 and 14 µm to define *Reticulofenestra bisecta* and *R. umbilicus* (e.g., Backman and Hermelin, 1986), respectively, but note that slightly smaller specimens extend 10–20 m below the ranges determined here. The rarity of *Chiasmolithus solitus, Nannotetrina fulgens,* and *Tribrachiatus orthostylus* toward the ends of their ranges diminished the reliability of these events. We could determine events based on *Chiasmolithus grandis, C. gigas,* and *Discoaster sublodoensis* more precisely because of their higher abundances. Another event that can be detected with confidence is the LO of *Discoaster lodoensis* (between Samples 165-998B-30R-CC and 30R-5, 130 cm).

Planktonic Foraminifers

Planktonic foraminifer preservation deteriorates greatly in association with the middle Miocene carbonate crash. Zones N16, N15, and N14 are difficult to constrain through an interval in Cores 165-998A-16H, 17H, and 18X, where preservation is poor and some samples are barren of planktonic foraminifers. Some samples initially taken are located in turbidites (see Table 4 for identification of samples associated with disturbed intervals and for the location of constrained datums).

Pleistocene

The Pleistocene zonation of Bolli and Premoli Silva (1973) can be partly demarked in the sediments of Hole 998A (Fig. 62). The last occurrence (LO) of *Globorotalia tumida flexulosa* is probably between Samples 165-998A-1H-2, 40–42 cm, and 1H-4, 40–42 cm, as this morphotype is not found in the former sample, which was the highest examined. This datum marks the base of the *Globigerina bermudezi* Zone (N23 of Blow, 1969), which was assigned an absolute age of 80 ka based on work at Site 147 in the Cariaco Basin on Deep Sea Drilling Project (DSDP) Leg 15 (Edgar, Saunders, et al., 1973). The base of the *Globigerina calida calida* Zone, which is defined by the FO of the eponymous subspecies, is located between Samples 165-998A-2H-4, 40–42 cm, and 2H-CC, and is assigned an absolute age of 240,000 ka based on Site 147 (Edgar, Saunders, et al., 1973).

Pliocene

The Pleistocene/Pliocene boundary is approximated by the LO of *Globigerinoides fistulosus* (1.7 Ma), which is found between Sample 165-998A-4H-CC and 5H-2, 17–19 cm. The latter sample is located in a turbidite. The base of Zone N22, which is marked by the FO of *Truncorotalia truncatulinoides* (2.0 Ma), is found between Samples 165-998A-5H-2, 17–19 cm and 5H-2, 40–42 cm. The boundary event for the base of Zone N21, the FO of *Truncorotalia tosaensis,* cannot be constrained at Site 998 because the marker species occurs only sporadically. The base of Zone N21/N20 is also problematic. The overlapping ranges of *Menardella miocenica* and *M. pseudomiocenica* at this site make the identification of the FO of the former species difficult. Therefore, the LO of *Hirsutella margaritae* (3.6 Ma) is used to mark the base of this zone. This event is located between Samples 165-998A-8H-CC and 9H-2, 40–42 cm. Robust specimens that resemble *Hirsutella margaritae* are seen in Samples 165-998A-8H-2, 100–102 cm, and 9H-4, 40–42 cm. These are transitional forms toward *Hirsutella hirsuta* and are distinguished by their much larger size, less delicate, more opaque test wall, and more pronounced keel.

Miocene

The Pliocene/Miocene boundary (5.3 Ma) is approximated by the base of Zone N19, which is associated with the FO of *Sphaeroidinella dehiscens* (5.6 Ma). Specimens in the sample above (Sample 165-998A-11H-CC) at the FO have minute secondary apertures. Specimens in the sample below (Sample 165-998A-12H-2, 39–41 cm) have translucent areas where the secondary apertures will develop.

In Hole 998A, *Globorotalia tumida* is found in only one sample in the upper Pliocene (Sample 165-998A-5H-4, 40–42 cm) and two samples in the lower Pliocene (Samples 165-998A-11H-2, 40–42 cm, and 11H-4, 40–42 cm). This stratigraphic pattern resembles the

Table 4. Planktonic foraminifer datums, absolute ages, and depths at Site 998.

Event	Zone (base)	Age (Ma)	Core, section, interval (cm)	Depth (mbsf)
Hole 998A:				
LO *Globigerinoides fistulosus*		1.7	4H-CC to 5H-2, 17–19[a]	38.27
FO *Truncorotalia truncatulinoides*	N22	2.0	5H-2, 17–19[a] to 5H-2, 40–40	39.01
LO *Menardella miocenica*		2.3	5H-CC to 6H-2, 50–52	48.45
LO *Dentoglobigerina altispira*		3.0	7H-2, 40–42 to 7H-4, 40–42	59.71
FO *Globigerinoides fistulosus*		3.2	7H-4, 40–42 to 7H–CC	63.61
LO *Hirsutella margaritae*	(N21/N20)	3.6	8H-CC[b] to 9H-2, 40–42[a]	76.39
LO *Globoturborotalita nepenthes*		4.3	9H-CC to 10H-2, 40–42	85.96
FO *Menardella exilis*		4.5	10H-2, 40–42 to 10H-4, 40–42	88.21
FO *Truncorotalia crassaformis*		4.7	10H-2, 40–42 to 10H-4, 40–42	88.21
FO *Sphaeroidinella dehiscens*	N19	5.6	11H-CC[b] to 12H-2, 39–41	104.90
FO *Hirsutella margaritae*		6.0	12H-2, 39–41 to 12H-4, 40–42	107.20
FO *Globigerinoides conglobatus*		6.2	12H-2, 39–41 to 12H-4, 40–42	107.20
FO *Globigerinoides extremus*		8.0	15H-4, 37–39 to 15H-CC	139.52
FO *Candeina nitida*		8.0	15H-4, 37–39 to 15H-CC	139.52
FO *Globorotalia plesiotumida*	N18/N17	8.2	15H-CC to 16H-2, 40–42	142.21
LO *Paragloborotalia mayeri*	N16/N15	10.3	16H-5, 41–43 to 16H-6, 40–42	148.99
LO *Fohsella fohsi*	N14/N13	11.8	17H-CC[b] to 18X-1, 40–42	161.03
FO *Fohsella fohsi*	N12	12.7	20X-CC to 21X-CC	187.94
FO *Fohsella praefohsi*	N11	14.0	22X-CC[a] to 23X-CC	208.21
FO *Fohsella peripheroacuta*	N10	14.8	22X-CC[a] to 23X-CC	208.21
FO *Praeorbulina circularis*		16.0	23X-CC to 24X-CC	218.06
FO *Praeorbulina sicana*	N9/N8	16.4	24X-CC to 25X-CC	226.65
LO *Catapsydrax dissimilis*	N7	17.3	26X-CC to 27X-CC	245.74
FO *Globigerinatella insueta* s.l.	N6	18.8	26X-CC to 27X-CC	245.74
LO *Paragloborotalia kugleri*	N5	21.5	31X-CC to 32X-CC	280.49
FO *Paragloborotalia kugleri*	N4	23.8	36X-CC to 37X-CC	340.74
FO *Paragloborotalia pseudokugleri*		25.9	41X-CC to 42X-CC	389.38
LO *Paragloborotalia opima*	P22	27.1	47X-CC to 48X-CC	443.81
LO *Ch. cubensis* (common)	P21b	28.5	52X-CC to 53X-CC	494.47
FO *Globoturborotalita angulisuturalis*	P21a	29.4	53X-CC to 54X-CC	503.45
LO *Turborotalia ampliapertura*	P20	30.3	55X-CC to 56X-CC	522.00
FO *Paragloborotalia opima*		30.6	57X-CC to 58X-CC	541.69
LO *Pseudohastigerina* spp.	P19	32.0	59X-CC to 60X-CC	562.90
LO *Hantkenina* spp.		33.7	62X-CC to 63X-CC	588.51
LO *Turborotalia cerroazulensis*	P18	33.8	Taxon not observed	
LO *Turborotalia pomeroli*		35.3	66X-CC to 67X-CC	625.69
Hole 998B:				
LO *Pseudohastigerina* spp.	P19	32.0	Above 1R-CC	
LO *Hantkenina* spp.		33.7	3R-CC to 4R-CC	590.82
LO *Turborotalia cerroazulensis*	P18	33.8	3R-CC to 4R-CC	590.82
LO *Turborotalia pomeroli*		35.3	9R-CC to 10R-CC[a]	638.33
LO *Porticulasphaera semiinvoluta*		35.3	3R-CC to 4R-CC	590.82
LO *Acarinina collactea*		37.7	4R-CC to 5R-CC[a]	600.29
LO *Morozovella spinulosa*		38.1	3R-CC to 4R-CC	590.82
FO *Porticulasphaera semiinvoluta*	P15	38.4	4R-CC to 5R-CC[a]	600.29
LO *Planorotalites* spp.		38.5	4R-CC to 5R-CC[a]	600.29
LO *Acarinina* spp.		37.5–38.5	4R-CC to 5R-CC[a]	600.29
LO *Acarinina primitiva*		39.0	6R-CC to 7R-CC	619.31
LO *Globigerapsis beckmanni*	P14	40.1	6R-CC to 7R-CC	619.31
FO *Globogerapsis beckmanni*	P13	40.5	8R-CC to 9R-CC	648.58
FO *Turborotalia pomeroli*		42.4	14R-CC to 15R-CC	693.66
FO *Globigerapsis index*		42.9	25R-CC[c] to 26R-CC	793.64
LO *Morozovella aragonensis*	P12	43.6	19R-CC to 20R-CC	743.51
FO *Globigerapsis kugleri*	P11	45.8	27R-CC to 28R-CC	813.03
FO *Acarinina pentacamerata*		50.8	Below 37R-CC	
FO *Morozovella aragonensis*		52.3	Below 37R-CC	

Notes: FO = first occurrence, LO = last occurrence. This entire table also appears on CD-ROM (back pocket).
[a]Sample in a turbidite.
[b]Sample in mixed sediments (40%–50% clay).
[c]Sample in ash layer.

one observed at Ceara Rise in the western tropical Atlantic on ODP Leg 154 (Curry, Shackleton, Richter, et al., 1995). Consequently, the base of Zone N18 cannot be located at Site 998. However, *Globorotalia plesiotumida* is regularly present in the sediments of Hole 998A. Its FO, which marks the base of Zone N17/N18 (8.2 Ma), is located between Samples 165-998A-15H-CC and 16H-2, 40–42 cm.

Below this level, the delimitation of zonal boundaries becomes problematic because of the poor preservation of planktonic foraminifers. The base of Zone N16, which is marked by the FO of *Neogloboquadrina acostaensis* (10.0 Ma), is tentatively placed between Samples 165-998A-17H-4, 40–42 cm, and 17H-CC. The former sample is characterized by large, robust *N. acostaensis* that resemble *Paragloborotalia mayeri.* This sample is also noteworthy for the presence of *Globoconella conoidea,* a temperate to warm subtropical species (Kennett and Srinivasan, 1983). However, the sediment in Sample 165-998A-17H-4, 40–42 cm, is taken from a turbidite and also includes *Globigerinoides subquadratus,* which does not occur above the base of Zone N14 (Kennett and Srinivasan, 1983; Bolli and Saunders, 1985). The presence of *Hirsutella juanai,* which does not occur below the base of Zone N16, suggests that undisturbed sediments near this level are <10.0 Ma.

The base of Zone N15 is located between Samples 165-998A-18X-2, 38–40 cm, and 19X-2, 40–42 cm. (Sample 165-998A-18X-CC is composed entirely of volcanic glass and is barren.) The *Fohsella* group (*F. fohsi, F. peripheroacuta, F. praefohsi)* is encountered in Sample 165-998A-19H-4, 40–42 cm. The base of Zone N14/N13, which is defined by the LO of this group, is therefore placed between Sample 165-998A-19X-2, 40–42 cm, and 19X-4, 40–42 cm. No *F. fohsi robusta* or *F. fohsi lobata* are observed, which suggests that the interval between the FO of these morphotypes (13.5 Ma) and the extinction of the group (11.8 Ma) is between these two samples. Below this level in the hole only core catchers were examined. Zonal bases

are described as being in the cores above LOs and below FOs that are found in core catchers. The base of Zone N12, marked by the FO of *F. fohsi,* is located in Core 165-998A-21X. The bases of Zones N11 and N10, marked by the FOs of *F. praefohsi* and *F. peripheroacuta,* respectively, are both located in Core 165-998A-23X.

Orbulina universa is not found below Sample 165-998A-19X-4, 40–42 cm. Therefore, the base of Zone N9 is not delimited. However, the base of Zone N9/N8 is marked by the FO of *Praeorbulina sicana* and is found in Core 165-998A-25X. The bases of Zones N7 and N6, marked by the LO of *Catapsydrax dissimilis* and the FO of *Globigerinatella insueta* s.l., respectively, are located in Core 165-998A-27X. Specimens of *Globigerinatella insueta* s.s. (with areal apertures) are not found below Sample 165-998A-24X-CC.

The total range of *Paragloborotalia kugleri* delimits the bases of Zones N5 and N4. The LO of *P. kugleri* is in Core 165-998A-31X and the FO of this species, which also marks the Miocene/Oligocene boundary, is located in Core 165-998A-37X.

Oligocene

The base of Zone P22 is defined by the LO of *Paragloborotalia opima.* Because this taxon is distinguished from *Paragloborotalia nana* solely by its larger size, we have followed Bolli and Saunders (1985) and considered specimens >0.39 mm in test diameter to be *P. opima.* Given this definition, the LO of *P. opima* is between Samples 165-998A-47X-CC and 48X-CC. Following Leckie et al. (1993), we have identified the base of Subzone P21b by the LO of common *Chiloguembelina cubensis.* Given our abundance definitions (i.e., common = 15%–30% of the fauna), the LO of common *C. cubensis* is between Samples 165-998A-52X-CC and 53X-CC. In lower abundance, *C. cubensis* ranges as high as Samples 165-998A-44X-CC to 45X-CC.

The base of Subzone P21a is marked by the FO of *Globoturborotalita angulisuturalis;* this lies between Samples 165-998A-53X-CC and 54X-CC. The base of Zone P20, as marked by the LO of *Turborotalia ampliapertura,* is between Samples 165-998A-55X-CC and 56X-CC. The LO of the genus *Pseudohastigerina* marks the base of Zone P19 between Samples 165-998A-59X-CC and 60X-CC. As approximated by the LO of the genus *Hantkenina,* the Eocene/Oligocene boundary is between Samples 165-998B-3R-CC and 4R-CC. In Hole 998A, this datum lies between Samples 165-998A-62X-CC and 63X-CC, but this level is clearly Eocene based on the presence of the nannofossils *Discoaster barbadiensis* and *D. saipanensis.*

Eocene

Identification of Eocene planktonic foraminifer zones in Holes 998A and 998B is complicated by the rarity or absence of several taxa that are used as standard zonal markers. For example, the bases of Zones P17 and P16 are marked by the LOs of *Cribrohantkenina inflata* and *Turborotalia cunialensis,* respectively, neither of which was observed at this site. The rarity of such taxa may result in part from the strong lithification and consequent poor foraminiferal preservation throughout the Eocene interval of this site.

The LO of *Turborotalia cerroazulensis,* which marks the base of Zone P18, approximately coincides with the LO of *Hantkenina* at Hole 998B (between Samples 165-998B-3R-CC and 4R-CC). It also coincides with the only observation of *Porticulasphaera semiinvoluta* at Hole 998B. Because the bases of Zones P15 and P16 are defined by the FO and LO of *P. semiinvoluta,* respectively, the coincidence of these datums indicates that at this site either Zones P16 and P17 are greatly abbreviated or reworking has rendered Zones P15 through P17 inseparable. In either case, the short interval attributable to Zones P14 through P17 suggests that, based on the foraminiferal evidence, mean late Eocene sediment accumulation rates were unusually low at Site 998.

The base of Zone P14, defined by the LO of *Globigerapsis beckmanni,* occurs between Samples 165-998B-6R-CC and 7R-CC. The base of Zone P13, marked by the FO of the same taxon, is between Samples 165-998B-8R-CC and 9R-CC. The LO of *Morozovella aragonensis* marks the base of Zone P12 between Samples 165-998B-19R-CC and 20R-CC, whereas the FO of *Globigerapsis kugleri* places the base of Zone P11 between Samples 165-998B-27R-CC and 28R-CC. The presence of *M. aragonensis* and *Acarinina pentacamerata* Sample in 165-998B-37R-CC suggests that the oldest sediments cored at this site are no younger than Zone P10 and no older than Zone P8.

Preservation

The preservational state of planktonic foraminifers is described by assignment to one of six classes (poor to very good; see "Explanatory Notes" chapter, this volume). Figure 15 shows the preservational state, where preservational classes have been converted to numerical values (poor = 1 and very good = 6) vs. depth in Hole 998A. Preservation of planktonic foraminiferal tests is very good to good in the Pleistocene and Pliocene. In the lower Pliocene, preservation declines steeply to generally moderately in the upper Miocene before a series of samples near 150 mbsf that are consistently poorly preserved or barren. These samples coincide with the carbonate crash observed in other records (see "Lithostratigraphy" and "Geochemistry" sections, this chapter).

A general trend toward better preservation can be discerned between ~200 and 300 mbsf. The condition of planktonic foraminifers then alternates between poor and moderate through much of the Oligocene, although a small number of moderately well-preserved samples are encountered in the lower Oligocene. Due to increased lithifi-

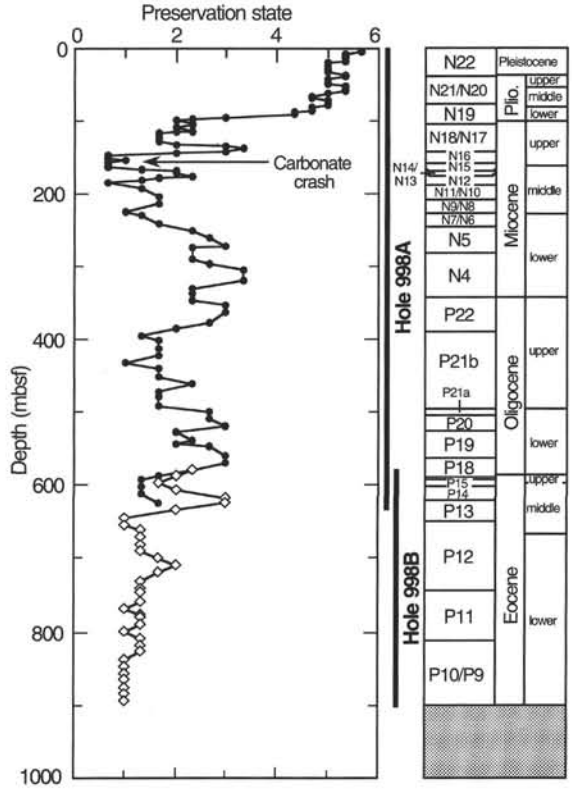

Figure 15. Planktonic foraminifer preservation in Holes 998A and 998B. Preservational classes have been converted to numerical values (poor = 1 and very good = 6).

Table 5. Benthic foraminifers in turbidites at Site 998.

Core, section, interval (cm)	Age (zone)	Approximate paleodepth	Reworked planktonics (age)	Additional comments
165-998A-				
5H-2, 17–19	late Pliocene (CN12c)	Bathyal	Yes (middle Pliocene)	Rare benthic foraminifers; very rare ostracodes, echinoderm spines
8H-2, 33–35	e.-l. Pliocene (CN12a)	Bathyal	No	Rare benthic foraminifers
13H-2, 59–61	late Miocene (CN9b)	Bathyal	No	Few benthic foraminifers; very rare echinoderm spines, ostracodes, and fish teeth
16H-4, 19–21	late Miocene (CN7))	Mix of neritic and bathyal	Yes (Eocene)	Few benthic foraminifers; sorted foraminifer shells (<250 µm)
17H-5, 40–42	m.-l. Miocene (CN5)	Mix of neritic and bathyal	Yes (Eocene–early Miocene)	Few benthic foraminifers; sorted foraminifer shells (<250 µm)
42X-3, 31–34	late Oligocene (CP19b)	Bathyal	Yes (Eocene)	Rare/few benthic foraminifers; very rare echinoderm spines, fish teeth, and grains of mica schist and quartzite
58X-1, 29–31	early Oligocene (CP17)	Outer Neritic? and bathyal	Yes (Eocene)	Rare benthic foraminifers; very rare sponge spicules; sorted foraminifer shells (<250 µm)
165-998B-				
5R-CC	late Eocene (CP15)	Mix of neritic (carbonate platform) and bathyal	Yes (late Paleocene; P4)	Abundant benthic foraminifers; few echinoderm spines
31R-2, 12–13 (TS)	e.-m. Eocene (CP12)	Neritic (carbonate platform)?	Not determined	Layers with abundant planktonic foraminifers, but only rare benthic foraminifers; two suspected ghosts of dissolved larger benthic foraminifers; few radiolarians
31R-6, 70–72 (TS)	e.-m. Eocene (CP12)	Not determined	Not determined	Layers with abundant planktonic foraminifers; very rare benthic foraminifers (no obvious larger benthic foraminifers); rare radiolarians
33R-4, 56–57 (TS)	early Eocene (CP10)	Not determined	Not determined	Rare to few planktonic foraminifers and rare benthic foraminifers (no obvious larger benthic foraminifers); abundant ghosts of radiolarians

Note: e.-l. = early to late, e.-m. = early to middle, m.-l. = middle to late, TS = thin section.

cation, preservation in the Eocene is almost uniformly poor in both Holes 998A and 998B.

Benthic Foraminifers

Benthic foraminifers were examined from 11 turbidite horizons in Holes 998A and 998B. Approximate paleodepth and/or source of origin for the turbidites was determined based on a genus-level evaluation of the benthic foraminifer assemblages from the lower Eocene to Pleistocene section at Site 998 (Table 5). There are two distinct types of turbidites (see "Lithostratigraphy," this chapter): the Neogene and Oligocene part of the section is characterized by pelagic turbidites (foraminiferal sands grading upward into nannofossil ooze), whereas the Eocene contains numerous volcaniclastic turbidites (foraminiferal or radiolarian sands and redeposited ash). The Neogene and Oligocene turbidites are mostly characterized by bathyal benthic foraminifers (e.g., *Planulina, Cibicides, Cibicidoides, Globocassidulina, Stilostomella, Melonis, Gyroidina, Anomalinoides, Laticarinina, Pleurostomella,* and *Bulimina*), suggesting a deep-water source for many of these deposits. Two obvious exceptions are Samples 998A-16H-4, 19–21 cm, and 17H-5, 40–42 cm, which contain a mixture of neritic and bathyal taxa including *Elphidium, Nonionella, Cassidulinoides, Lenticulina, Bolivina (Brizalina), Plectofrondicularia, Planulina, Pleurostomella, Nuttalides*(?), *Oridorsalis, Oolina, Fissurina, Lagena, Dentalina, Nodosaria, Melonis,* and *Stilostomella.* These particular samples are also distinguished from the other Neogene samples by their stratigraphic position within the interval of the carbonate crash and their distinct size sorting (very few specimens exceed 125 µm).

Sample 165-998B-5R-CC (upper Eocene) contains abundant benthic foraminifers of mixed bathyal and neritic affinities, including numerous broken specimens of one or more species of larger benthic foraminifer. This latter taxon (taxa?) is characterized by multiple small chamberlets suggestive of a carbonate platform dweller with photosymbionts. The three middle to lower Eocene samples are thin sections, and these contain few benthic foraminifers. The samples did, however, contain layers with abundant planktonic foraminifers (samples from Core 165-998B-31R) or radiolarians (Sample 165-998B-33R-4), indicating a pelagic source. Sample 165-998B-31R-2, 12–13 cm contains two specimens that appear to be the recrystallized ghosts of disk-shaped larger foraminifers, which would imply a shallow-water origin.

PALEOMAGNETISM

Introduction

Two problems were encountered in obtaining a reliable magnetostratigraphy from the sediments of Site 998. The first involved removal of a large vertical overprint that is imparted to the cores by remagnetization in the strong magnetic fields present in the drilling pipe. The vertical overprint was mostly removed from samples with finer grained magnetic mineral assemblages by alternating-field (AF) demagnetization with peak fields of 20 mT (Fig. 16A; paleomagnetic data for discrete samples are given in Appendix tables on CD-ROM in the back pocket of this volume). It was not always possible, however, to remove the vertical overprint completely and isolate a stable primary remanence from other samples, which are likely composed of coarser grained magnetic mineral assemblages (Fig. 16B). The inability to remove the vertical overprint from these samples posed a significant problem because of the abundance of coarse-grained ash and turbidite layers found at Site 998.

A second problem encountered in this study involved the presence of a significant magnetic field in the sensor region of the shipboard cryogenic magnetometer. The magnitude of this magnetic field could be dependent on the orientation of the ship and the magnetometer relative to Earth's magnetic field. Because the magnetometer is oriented along the long axis of the ship, a larger magnitude field should occur when the long axis of the ship is in a north-south orientation (i.e., parallel to the flux lines of the ambient field), and a lower magnitude occurs when the long axis of the ship is oriented east-west (i.e., perpendicular to the flux lines of the ambient field). The orientation is probably important because the magnetometer's µ-metal shield functions best in the east-west direction. The Pb superconducting shield, how-

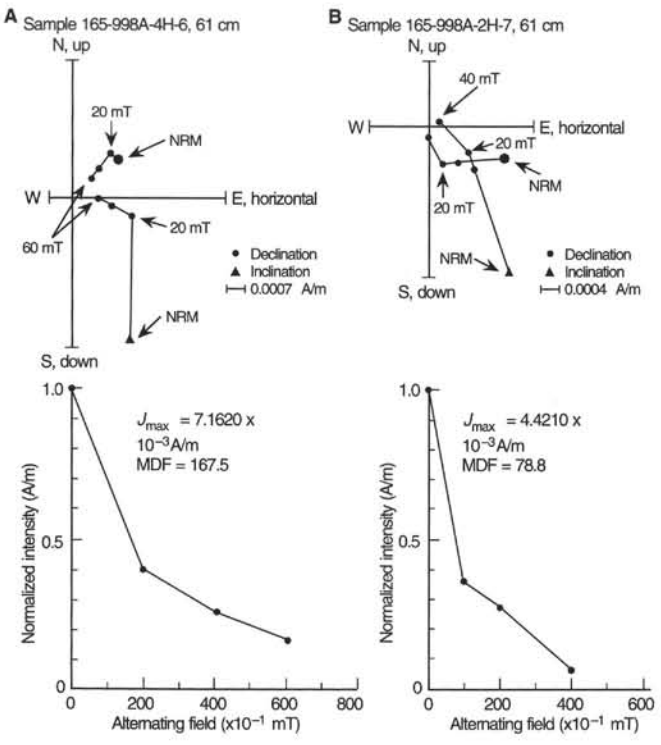

Figure 16. Vector demagnetization diagrams (top) and intensity decay diagrams (bottom) for (**A**) Samples 165-998A-4H-6, 61 cm, and (**B**) 2H-7, 61 cm. Note the steep inclination that is mostly removed for Sample 165-998A-4H-6, 61 cm, after AF demagnetization to 20 mT (the peak field used for most split-core measurements), whereas the steep component for the other sample is still being removed up to 40 mT.

ever, works best in the north-south orientation (W. Goree, pers. comm., 1996), and so the orientation of the ship may not be significant. In any case, we note that the *JOIDES Resolution* maintained a bearing of nearly due south throughout drilling at Site 998 because of the prevailing wind and current direction.

A significant magnetic field in the sensor region of the cryogenic magnetometer will cause an induced magnetization in a sample that will be superimposed on the sample's natural remanent magnetization (NRM). Studies of the blank sample holder indicated that the induced magnetization only affected the X and Z components of the magnetization, which again could be related to the ship's orientation. The declination values were observed to cluster around the north direction owing to the large X component of the induced magnetization, whereas the inclinations were oversteepened in the positive direction owing to a large induced Z component. As discussed in the "Explanatory Notes" chapter (this volume), this bias could result from a radial drilling-induced magnetization relative to the core rather than an induced magnetization.

It is difficult to remove uniquely the secondary magnetization from the data and isolate the primary component of remanence. We attempted, however, to remove mathematically the secondary magnetization by assuming it is an induced magnetization and by using our observations of the magnitude of the effect on repeated measurements of the empty sample holder. The method simply assumes a percentage of the total magnetization results from the addition of an induced vector component. The direction of that component is computed from the International Geomagnetic Reference Field coefficients for the location of Site 998. The size of the component is estimated iteratively until the corrected inclinations are symmetrically distributed about zero inclination (Fig. 17).

We attempted this mathematical treatment only for the upper 150 m of the sediment column in Hole 998A because of the strong NRM

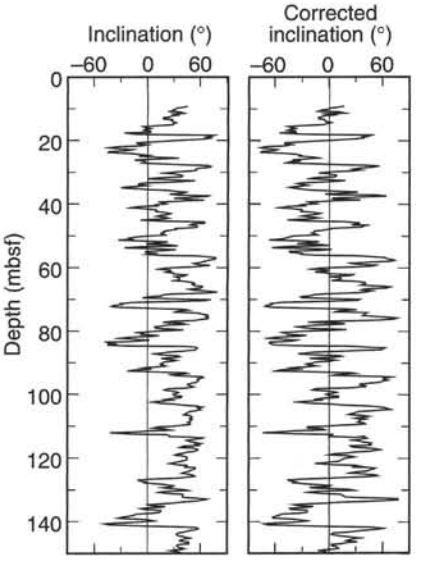

Figure 17. Inclinations measured on split-core sections from Hole 998A after AF demagnetization to 20 mT. The inclinations on the left are the raw measurements, which show a strong bias toward positive values. After subtracting an induced component that is 67% the size of the measured magnetization and has an orientation equivalent to the ambient geomagnetic field (inclination = 50° and declination = 359°), the corrected inclinations on the right are symmetric about zero inclination.

values and the continuous sedimentary record in this interval. We found that an induced component two-thirds the size of the measured remanent magnetization was needed to remove the strong bias in the inclination. Because we cannot determine uniquely the source of the biasing field, other magnetization components may be important.

Results

Remanence Intensity and Low-Field Magnetic Susceptibility

A comparison between remanence intensity and low-field magnetic susceptibility (Fig. 18) indicates a first-order correspondence between these parameters and the lithologic units identified at Site 998. Magnetic intensity and susceptibility are relatively high in Units I and II, which contain a larger component of noncarbonate material. Both of these parameters decrease in Unit III in conjunction with increasing carbonate, and they increase again in Unit IV as carbonate decreases.

Paleomagnetic Directions

The uppermost 200 m of Hole 998A and the entire sequence of Hole 998B provided results that are interpretable for magnetostratigraphic dating of the section. The interpretations are based primarily on variations in the inclination values because the induced magnetization along the X axis made it very difficult to correct the declination values. The tensor tool was deployed for the APC cores, though declination values were not corrected owing to time constraints.

Magnetostratigraphic Synthesis

The magnetostratigraphic interpretation was constrained by the nannofossil biostratigraphy, so first-order agreement with the biostratigraphy is imposed on the magnetostratigraphy. Using this approach, we were able to interpret the magnetostratigraphy of Hole 998A back to 16 Ma, and correlate the magnetozones with the magnetic polarity time scale (Table 6). The results from Hole 998B were superior to those from Hole 998A; we were able to correlate the entire

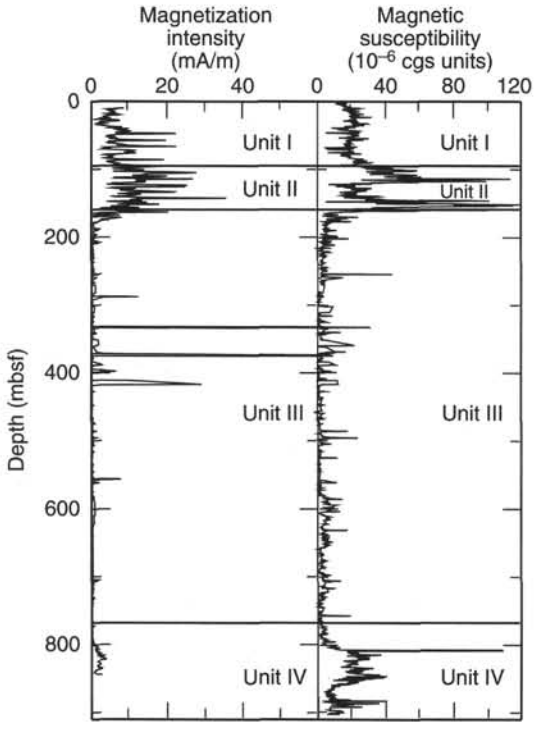

Figure 18. Comparison of magnetization intensity values after AF demagnetization to 20 mT to MST susceptibility values. Also shown are the unit boundaries defined in the "Lithostratigraphy" section (this chapter).

section with the magnetic polarity time scale for the interval from 33 to 51 Ma (Table 7). Even so, these correlations should be considered tentative and highly dependent upon the biostratigraphy.

SEDIMENTATION RATES AND MASS ACCUMULATION RATES

Sedimentation rates obtained from major planktonic foraminiferal and calcareous nannofossil datums (Tables 3, 4) and from magnetostratigraphic polarity zone boundaries (Table 6) are illustrated in the slopes of age-depth plots (Figs. 19, 20). Variations in the sedimentation rates through time are also directly estimated in two ways. In the first method, select nannofossil datums are used (Fig. 21), whereas in the second method, the rates are calculated from foraminiferal and nannofossil datums using a weighted (center datum has twice the weight as bounding data), three-point moving average (Fig. 22). Such smoothing tends to dampen large fluctuations but may also attenuate genuine intervals with very slow or very fast rates.

Uncertainties in the rates are relatively minor in the Neogene where our sample density is highest (one sample per section for nannofossils, three samples per core for foraminifers), but increase significantly in the Paleogene, where we have examined fewer samples and where carbonate microfossil preservation deteriorates. Because nannofossil age control was used to interpret the magnetostratigraphy, agreement between the two age-depth curves is imposed. Minor differences in the age-depth plots between nannofossils and foraminifers are observed in the middle Miocene, mid-Oligocene, and the middle to upper Eocene.

Age-depth plots illustrate largely continuous sedimentation at Site 998 for the past 50 m.y. (Fig. 19), but with rates varying by more than a factor of 3. The sedimentation rate history at Site 998 can be divided into five separate parts: from the early to middle Eocene, rates averaged 15 m/m.y.; rates increased to 24 m/m.y. for the late

Table 6. Preliminary reversal boundary depths and ages from Hole 998A.

Magnetochron	Depth (mbsf)	Age (Ma)
C1n (o)	15.35	0.780
C1r.1n (t)	18.35	0.990
C1r.1n (o)	20.25	1.070
C2n (t)	27.60	1.770
C2n (o)	31.40	1.950
C2n.1n (t)	32.60	2.140
C2n.1n (o)	32.90	2.150
C2An.1n (t)	35.90	2.600
C2An.1r (t)	40.65	3.040
C2An.1r (o)	45.45	3.110
C2An.2r (t)	50.15	3.220
C2An.2r (o)	55.85	3.330
C2Ar (t)	68.80	3.580
C3n.1n (t)	73.15	4.180
C3n.1n (o)	78.45	4.290
C3n.2n (t)	84.85	4.480
C3n.2n (o)	91.45	4.620
C3n.3n (t)	93.10	4.800
C3n.3n (o)	101.10	4.890
C3n.4n (t)	103.00	4.980
C3n.4n (o)	110.05	5.230
C3An (t)	113.00	5.875
C3An (o)	121.20	6.555
C3Bn (t)	122.40	6.919
C3Br.2n (o)	126.35	7.375
C4n (t)	128.45	7.533
C4n (o)	134.15	8.205
C4An (t)	136.40	8.631
C4An (o)	137.30	8.945
C5n (t)	141.50	9.639
C5n (o)	156.63	10.839
C5An (t)	159.33	11.841
C5An (o)	166.95	12.320
C5AAn (t)	169.65	12.929
C5AAn (o)	173.10	13.083
C5ACn (t)	174.00	13.666
C5ACn (o)	175.05	14.053
C5ADn (t)	176.35	14.159
C5ADn (o)	179.20	14.607
C5Cn (t)	203.50	16.014

Note: (t) = termination, (o) = onset.

Table 7. Preliminary reversal boundary depths and ages from Hole 998B.

Magnetochron	Depth (mbsf)	Age (Ma)
C12r (o)	581.35	33.058
C13n (o)	583.95	33.545
C13r (o)	598.95	34.655
C15n (o)	602.15	34.940
C15r (o)	603.35	35.343
C16n.1n (o)	604.65	35.526
C16n.1r (o)	607.80	35.685
C16n.2n (o)	616.90	36.341
C16r (o)	618.00	36.618
C17n.1n (o)	632.20	37.473
C17n.1r (o)	637.60	37.604
C17n.2n–3n (o)	657.20	38.113
C17r (o)	666.05	38.426
C18n (o)	703.50	40.130
C18r (o)	722.70	41.257
C19n (o)	730.95	41.521
C19r (o)	736.95	42.536
C20n (o)	761.55	43.789
C20r (o)	814.95	46.264
C21n (o)	842.35	47.906
C21r (o)	850.80	49.037
C22n (o)	854.80	49.714
C22r (o)	857.70	50.778
C23n.1n (o)	888.95	50.946
C23n.1r (o)	891.50	51.047

Note: (o) = onset.

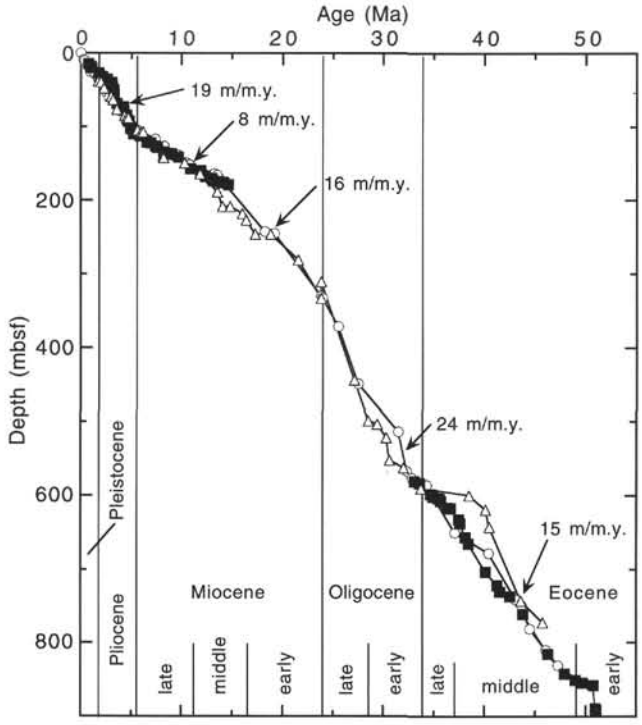

Figure 19. Age-depth plots for planktonic foraminifers (open triangles), calcareous nannofossils (open circles), and magnetostratigraphy (solid squares) for the interval from 0 to 50 Ma at Site 998.

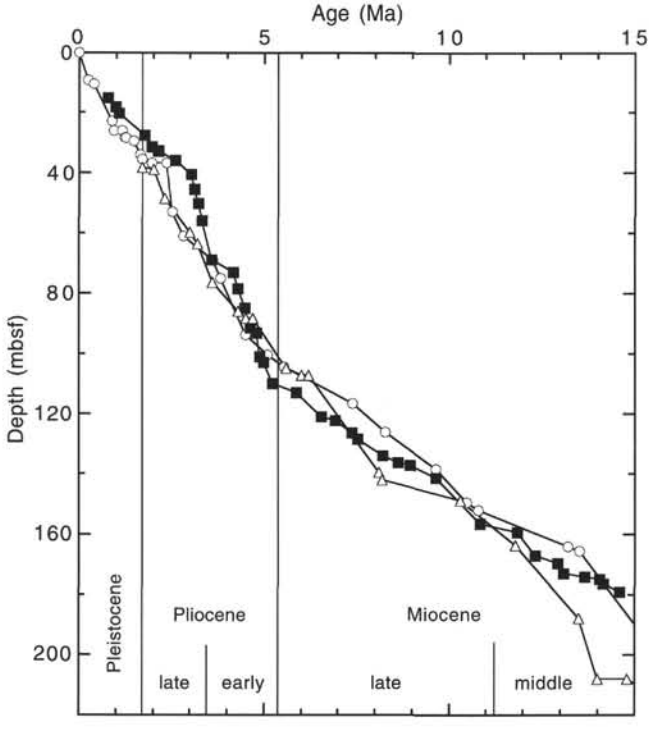

Figure 20. Age-depth plots for planktonic foraminifers (open triangles), calcareous nannofossils (open circles), and magnetostratigraphy (solid squares) for the interval from 0 to 15 Ma at Site 998.

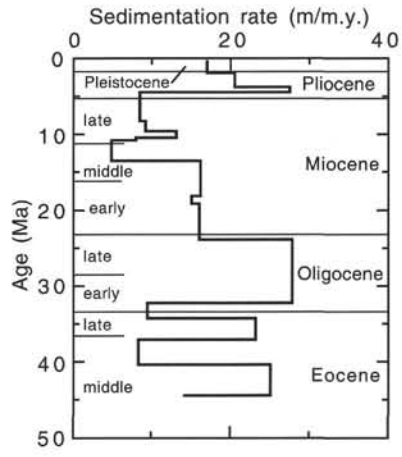

Figure 21. Sedimentation rates calculated from selected nannofossil datums vs. age.

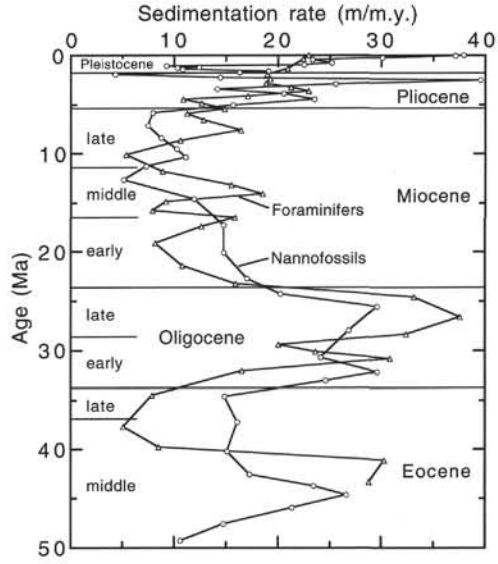

Figure 22. Sedimentation rates vs. age for planktonic foraminifers and calcareous nannofossils for the interval from 0 to 50 Ma at Site 998. Sedimentation rates are estimated using a three-point weighted moving average.

Eocene through Oligocene; and rates then decreased to 16 m/m.y. in the early to middle Miocene. Sedimentation rates averaged about 8 m/m.y. through the middle and late Miocene. This interval includes the carbonate crash (see "Lithostratigraphy" section, this chapter) between 145 and 160 mbsf in which nannofossil and planktonic foraminiferal preservation reflect intense dissolution. Further work will be required to determine whether the entire 5- to 20-Ma interval includes several minor breaks in sedimentation or merely condensed sedimentation. Finally, in the Pliocene to recent interval, rates averaged about 19 m/m.y. but are quite variable (Fig. 21).

The increase in sedimentation rates at about 5.5 Ma corresponds to a marked upcore increase in turbidite frequency (Fig. 8). Other rate changes further downcore, however, do not correspond to changes in turbidite or ash frequency. Therefore, we conclude that the interval of slow sedimentation in the middle and late Miocene reflects decreasing carbonate accumulation rates as a result of increasing dissolution and/or decreased carbonate productivity.

Mass accumulation rates for carbonate and noncarbonate fractions (Figs. 23, 24, 25, 26) were calculated from dry bulk density and

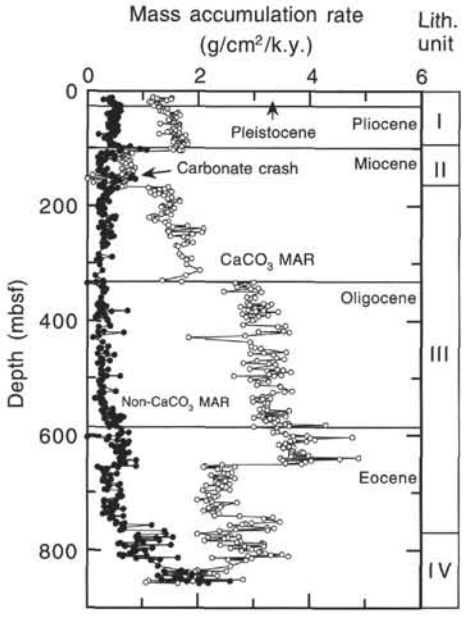

Figure 23. Mass accumulation rates for carbonate (open circles) and noncarbonate (solid circles) fractions vs. depth at Site 998. Lithologic unit boundaries are on the right (see "Lithostratigraphy" section, this chapter).

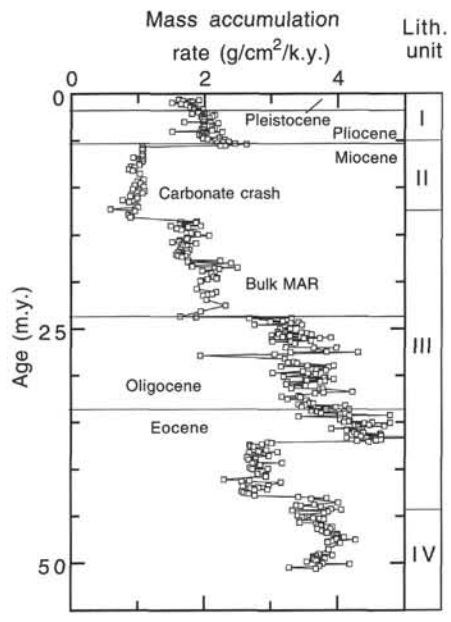

Figure 25. Bulk sediment mass accumulation rates vs. age at Site 998. Lithologic unit boundaries are on the right (see "Lithostratigraphy" section, this chapter).

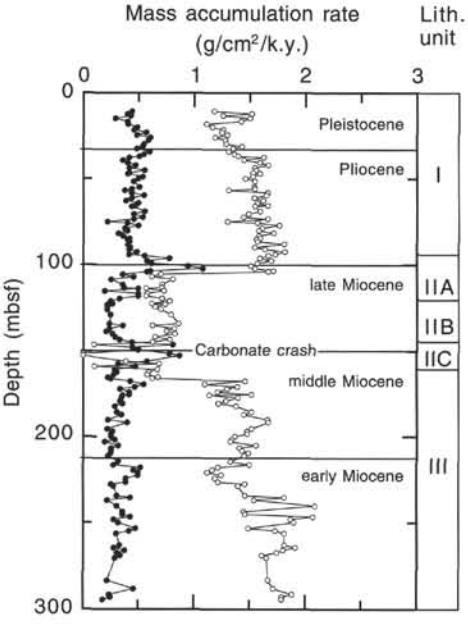

Figure 24. Mass accumulation rates for carbonate (open circles) and noncarbonate (solid circles) fractions through the upper 300 m of the section at Site 998. Note the increase in noncarbonate MAR in the interval of the carbonate crash.

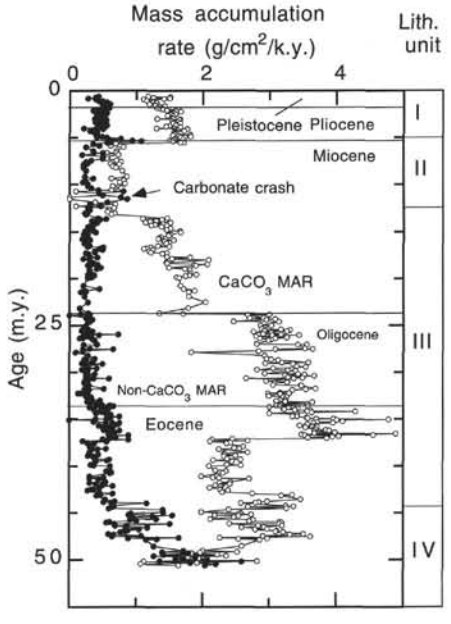

Figure 26. Mass accumulation rates for carbonate (open circles) and noncarbonate (solid circles) vs. age at Site 998. Lithologic unit boundaries are on the right (see "Lithostratigraphy" section, this chapter).

carbonate percentage data through five linear sedimentation rate segments (Table 8; see "Physical Properties" section, this chapter). The five segments are (1) 0.0–104.5 mbsf (Pliocene–Pleistocene), (2) 104.5–166.5 mbsf (upper Miocene), (3) 166.5–333.1 mbsf (lower–middle Miocene), (4) 333.1–651.1 mbsf (upper Eocene–Oligocene), and (5) 651.1–859.2 mbsf (lower–middle Eocene). These segments were chosen based on major changes in the sedimentation rate as shown in Figure 19. Mass accumulation rates of the detrital terrigenous and ash components of the bulk sediment are calculated from their absolute concentrations (see "Inorganic Geochemistry" section, this chapter) as well as from the dry bulk density and linear sedimentation rates (Fig. 27).

ORGANIC GEOCHEMISTRY

Introduction

Concentrations of inorganic carbon ($CaCO_3$) were measured coulometrically at a frequency of one sample per section (1.5 m) for each

Table 8. Interpolated ages and mass accumulation rate data from Site 998.

Core, section, interval (cm)	Depth (mbsf)	Age (Ma)	DBD (g/cm^3)	LSR (cm/k.y.)	Bulk MAR (g/cm^2/k.y.)	$CaCO_3$ (wt%)	$CaCO_3$ MAR (g/cm^2/k.y.)	Noncarbonate MAR (g/cm^2/k.y.)
165-998A-								
1H-2, 33–35	1.8		0.75			72.3		
1H-3, 29–31	3.3		0.82			74.9		
1H-4, 29–31	4.8		0.76			64.1		
1H-5, 29–31	6.3		0.80			71.3		
1H-6, 29–31	7.8		0.83			72.6		
2H-1, 28–30	9.1		0.86			75.1		
2H-2, 27–29	10.6	0.57	0.86	1.89	1.62	73.0	1.18	0.44
2H-3, 32–34	12.1	0.65	1.02	1.89	1.92	79.1	1.52	0.40
2H-4, 28–30	13.6	0.73	0.89	1.89	1.68	74.7	1.26	0.43
2H-5, 32–34	15.1	0.81	0.95	1.89	1.79	83.6	1.50	0.29

Note: DBD = dry-bulk density, LSR = linear sedimentation rate, MAR = mass accumulation rate.

Only part of this table is produced here. The entire table appears on CD-ROM (back pocket).

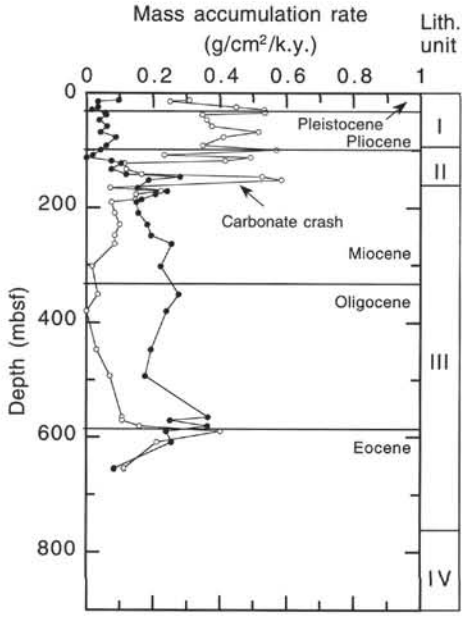

Figure 27. Mass accumulation rates for detrital terrigenous (solid circles) and ash (open circles) components as determined from trace element ratios (see "Inorganic Chemistry" section, this chapter). Note the relatively high ash MARs through the Oligocene–Miocene interval and the higher terrigenous MARs in the middle/upper Miocene boundary interval (carbonate crash) and through the Pliocene–Pleistocene.

core collected in Holes 998A and 998B (~500 total analyses). Concentrations of total organic carbon (TOC) were determined in one sample collected per core in Hole 998A to a depth of approximately 265 mbsf. At greater depths in Hole 998A and over the entirety of Hole 998B, TOC analyses were performed typically at a frequency of one sample per every other core. In conjunction with the measurement of TOC, additional data were generated for concentrations of total nitrogen (N_T) and sulfur (S_T). Finally, headspace gases were monitored routinely in compliance with drilling safety requirements (one sample/core). Analytical details are provided in the "Organic Geochemistry" section of the "Explanatory Notes" chapter (this volume).

Concentrations of Inorganic and Organic Carbon, Total Nitrogen, and Sulfur

Concentration trends for calcium-carbonate carbon are discussed and presented graphically in the "Lithostratigraphy" section of this chapter. These results, along with data for TOC, N_T, and S_T, also are provided in Table 9. Extremely low concentrations of TOC are the dominant organic-geochemical characteristic of Holes 998A and 998B. The majority of the TOC concentrations are below analytical resolution and are expressed as null values in Table 9. Nonzero values for TOC are typically on the order of only a few hundredths of a weight percent. The highest values of TOC, in slight excess of 0.1 wt%, are found over an interval of approximately 10 to 20 m centered at ~160 mbsf. This very subtle enrichment coincides with a pronounced minimum in concentrations of calcium carbonate and, consequently, records diminished dilution. The observed trend of low levels of organic matter (OM), as recorded in TOC and N_T, reflect the combined effects of oxic degradation within the water column and at the sediment-water interface, calcium-carbonate dilution, and comparatively low rates of OM primary production. The low concentrations of N_T are consistent with the extreme depletions in TOC. Given the low values of organic phases, no effort was made to characterize the organic matter further using either Rock-Eval pyrolysis or C/N ratios.

The low levels of TOC dictate the diagenetic pathways that dominate the coupled organic-inorganic regime at Site 998. As predicted from the concentrations of TOC and as discussed in the "Inorganic Chemistry" section of this chapter, degrees of bacterial sulfate reduction are minimal and likely associated with microenvironments. Consequently, production of hydrogen sulfide and, ultimately, precipitation of iron sulfides occur at minimal levels. As with TOC, the highest values of S_T coincide commonly with the lowest values of $CaCO_3$, once again highlighting the effects of dilution by carbonate sediment. Total sulfur is assumed to be present as FeS_2, although this assump-

Table 9. Concentrations of inorganic carbon, calcium carbonate, total carbon, total organic carbon, total nitrogen, and total sulfur, Holes 998A and 998B.

Core, section, interval (cm)	Depth (mbsf)	C_{inorg} (wt%)	$CaCO_3$ (wt%)	Total C (wt%)	TOC (wt%)	Total N (wt%)	Total S (wt%)
165-998A-							
1H-2, 33–34	1.83	8.68	72.3				
1H-3, 29–30	3.29	8.99	74.9	8.87	0.00	0.02	0.14
1H-4, 29–30	4.79	7.69	64.1				
1H-5, 29–30	6.29	8.56	71.3				
1H-6, 29–30	7.79	8.72	72.6				
2H-1, 28–29	9.08	9.02	75.1				
2H-2, 27–28	10.57	8.76	73.0				
2H-3, 32–33	12.12	9.49	79.1	9.51	0.02	0.02	0.00
2H-4, 28–29	13.58	8.97	74.7				
2H-5, 32–33	15.12	10.03	83.5				

Notes: Data are reported as weight percent (wt%). C_{inorg} = inorganic carbon, $CaCO_3$ = calcium carbonate, TOC = total organic carbon.

Only part of this table is produced here. The entire table appears on CD-ROM (back pocket).

Table 10. Interstitial water composition, Hole 998A.

Core, section, interval (cm)	Depth (mbsf)	pH	Alkalinity (mM)	Salinity (g/kg)	Cl^- (mM)	Na^+ (mM)	Mg^{2+} (mM)	Ca^{2+} (mM)	SO_4^{2-} (mM)	PO_4^{3-} (µM)	NH_4^+ (µM)	$Si(OH)_4$ (µM)	K^+ (mM)
165-998A-													
1H-3, 145-150	4.5	7.64	3.79	34	569	463	51.41	10.72	27.29	2		151	11.20
3H-3, 145–150	22.8	7.64	4.73	34	570	487	51.46	10.91	28.30	2	270	211	11.78
6H-3, 145–150	51.3	7.55	2.96	34	573	478	48.21	12.92	27.12	1	577	149	11.45
9H-3, 145–150	79.8	7.48	3.36	34	576	476	45.61	14.34	27.03	2	494	153	11.58
12H-3, 145–150	108.3	7.48	3.70	34	576	465	40.37	15.58	23.87	2	546	236	11.90
15H-3, 145–150	136.8	7.67	4.67	34	577	497	38.41	18.65	24.70	2	728	420	13.11
18X-2, 145–150	163.8	7.67	5.08	34	569	488	36.15	20.49	26.00	5	193	954	12.33
21X-3, 145–150	190.0	7.27	5.57	34	575	484	33.64	21.98	23.77	3	927	840	14.11
24X-3, 145–150	218.9	7.24	5.78	34	577	504	33.04	22.48	24.12	4	71	1176	13.31
27X-3, 145–150	247.7	7.51	5.78	34	564	497	31.69	23.45	23.36	4	625	1111	13.63
31X-3, 145–150	286.2	7.40	4.22	34	571	496	30.95	23.08	23.65	3	521	914	12.28
34X-3, 145–150	315.0	7.44	5.45	34	581	495	32.44	22.17	23.93	3	119	1118	12.14
37X-3, 145–150	343.9	7.40	3.03	34	579	492	30.70	22.79	21.77	3	162	822	12.36
40X-3, 145–150	372.9	7.30	4.37	34	576	494	30.16	23.76	22.08	2	184	782	10.97
44X-2, 145–150	409.8	7.34	3.05	34	576	624	34.74	22.73	22.36	2	191	699	14.57
48X-1, 145–150	446.8	7.43	2.44	34	581	497	29.94	24.54	21.49	2	667	540	9.66
52X-3, 145–150	488.2	7.57	3.21	34	575	515	29.11	25.43	20.97	2	284	679	8.72
55X-2, 145–150	515.5	7.57	2.43	34	579	508	29.96	24.80	21.80	2	295	753	8.72

Notes: BDL = below detection limit. This entire table also appears on CD-ROM (back pocket).

Table 10 (continued).

Core, section, interval (cm)	Depth (mbsf)	Fe (µM)	Mn (µM)	Sr (µM)	Rb (µM)	Li (µM)
165-998A-						
1H-3, 145-150	4.5	1	12.5	163	2.07	67
3H-3, 145–150	22.8	2	36.5	236	2.10	70
6H-3, 145–150	51.3	4	4.5	424	1.94	87
9H-3, 145–150	79.8	2	5.5	526	2.17	116
12H-3, 145–150	108.3	2	8.0	643	2.89	119
15H-3, 145–150	136.8	2	10.5	581	3.55	92
18X-2, 145–150	163.8	1	24.5	610	3.61	112
21X-3, 145–150	190.0	5	6.5	680	5.10	260
24X-3, 145–150	218.9	7	5.0	583	4.79	128
27X-3, 145–150	247.7	3	5.5	714	4.67	162
31X-3, 145–150	286.2	2	3.5	756	4.30	192
34X-3, 145–150	315.0	8	3.5	798	4.88	186
37X-3, 145–150	343.9	2	4.5	671	4.05	212
40X-3, 145–150	372.9	19	3.0	802	3.49	196
44X-2, 145–150	409.8	3	3.0	658	2.95	180
48X-1, 145–150	446.8	2	2.5	780	2.45	204
52X-3, 145–150	488.2	BDL	2.5	679	2.26	216
55X-2, 145–150	515.5	BDL	2.5	573	1.90	

tion was not tested by means of species-specific extractions. Total sulfur and TOC fail to show systematic trends downcore.

Volatile Hydrocarbons

As part of the shipboard safety and pollution monitoring program, hydrocarbon gases were measured continuously in the sediments of Holes 998A and 998B (one analysis/core) using the headspace technique. Consistent with the very low levels of organic carbon, methane was found to occur at only trace levels in all the samples collected from Hole 998A. Hole 998B contained methane at trace concentrations to a depth of ~773 mbsf; at greater depths, the levels typically ranged from 10 to 35 ppm. Additional hydrocarbon gases were not observed.

The gradual decrease in sulfate concentrations documented to a depth of ~520 mbsf in Hole 998A (the deepest available data for interstitial water) indicates low rates of bacterial sulfate reduction as a consequence of the low availability of reactive organic phases. A persistence in extremely low rates of sulfate reduction to the base of Hole 998B is indicated by the absence of significant concentrations of TOC and S_T. The observed paucity of methane is expected, given the likely persistence of sulfate over the entire lengths of both cores and the common observation that appreciable methanogenesis occurs only after sulfate is depleted and sulfate reduction essentially has reached completion (Martens and Berner, 1974). The slightly elevated levels of methane in the lower portions of Hole 998B reflect either production within organic-rich microenvironments or diffusion from below.

INORGANIC GEOCHEMISTRY

Interstitial Water Chemistry

Introduction

Seventeen interstitial water samples were collected at Site 998 at depths ranging from 4.5 to 515.5 mbsf (Table 10). Despite the persistence of adequate yields, pore-water sampling was suspended because of the proximity of the Oligocene/Eocene boundary, which had been identified as a critical sampling interval (see "Background and Objectives" section, this chapter). Analytical methods are detailed in the "Inorganic Geochemistry" section of the "Explanatory Notes" chapter (this volume).

Samples were analyzed for pH, salinity, chlorinity, alkalinity, sulfate, phosphate, ammonium, silica, Na^+, Fe, Mn, Mg^{2+}, Ca^{2+}, K, Sr, Rb, and Li. Pore-water profiles were not normalized to Cl^- concentrations because of the small (3% relative) variation in Cl^- abundance and because of uncertainty concerning the conservative behavior of this ion throughout the section. Data on volcanic ash thickness and frequency were used to evaluate the relationship between ash distributions and downcore geochemical trends. Reference seawater values are plotted as arrows on the axes of the various diagrams; these values are based on mean ocean bottom-water compositions as compiled by Millero and Sohn (1992). Substantial downhole lithologic variations, in particular, the frequent occurrence of ash layers of varying thickness (see "Lithostratigraphy" and "Igneous Petrology and Volcanology" sections, this chapter), create localized chemical effects that are manifested strongly in the pore-water profiles. Because diffusion has not totally obscured local-scale variations in pore-water compositions, inferences can be made regarding the relative rates of reaction and diffusion and the overall physical properties of the host lithologies. In many respects, the observed pore-water trends are in stark contrast to those commonly observed in carbonate-rich, deep-marine deposits, reflecting the significance of the ash component.

pH, Salinity, Chlorinity, and Sodium

The pH of pore waters ranged from 7.24 to 7.67 over the 500+ m of pore-water analyses, with a minimum near the center of the profile and a mean value of 7.48 ± 0.14 (1σ). All values are less than the average seawater value of 8.1. The narrow range of values reflects the strong buffering capacity of the abundant carbonate sediment. Salinity remained uniform throughout the profile, the value of 34 g/kg being indistinguishable from that of seawater. Chloride concentrations are all marginally above that of seawater (559 µmol/L) (Fig. 28). The profile shows a slight overall increase (only 3% relative) with depth, but numerous troughs are present that may indicate either nonconser-

vative behavior or sample contamination. Sodium shows a very slight increase with increasing depth, ranging from values very close to seawater to levels above 500 mM (Fig. 28). A prominent spike around 410 mbsf correlates with a large spike in K (see below), but the significance of this is not clear. The observation of smectite precipitation in the sediment section and the presence of zeolites in altered ash (see "Lithostratigraphy" section, this chapter, and discussions below) does not appear to have a significant effect on Na^+ abundance in interstitial waters.

Sulfate, Iron, and Manganese

Concentrations of dissolved sulfate decrease steadily, with some scatter, through the pore-water section (Fig. 29). Initial values are slightly less than the seawater value of 28.9 mM, but they decrease to 21–22 mM at the lowest depth of water retrieval. As expected from the low concentrations of total organic carbon (TOC; see "Organic Geochemistry" section, this chapter), degrees of sulfate reduction are minimal, with the bacterial process likely occurring within microenvironments. The small amounts of H_2S produced would react immediately with the available Fe-oxide phases, thus maintaining dissolved sulfide at essentially null levels that are undetectable by smell.

In the absence of appreciable concentrations of organic carbon, the redox conditions of the pore water are dominated by a classic deep-marine, suboxic, diagenetic regime (Froelich et al., 1979). Redox pathways show a sequence of microbially mediated reductive dissolution of Mn followed by reduction of Fe. This commonly observed hierarchy of reactions is manifested in the initial concentration increases displayed within the upper 50 mbsf, with the uppermost maximum for iron, although subtle, occurring slightly deeper than that for manganese. This relationship likely reflects the Fe- and Mn-oxides (oxyhydroxides) and perhaps Fe-rich clays present as detrital mineral phases. Again, the generally low concentrations of dissolved Fe and Mn are consistent with the paucity of organic carbon.

The dissolution of manganese in the upper tens of meters of burial is marked by a corresponding decrease in solid-phase Mn (Fig. 29), which documents the effective leaching of reactive Mn oxides. At greater depths, the profiles for both dissolved Fe and Mn show pronounced variability. The uppermost decreases in Fe and Mn record adsorption of both species on the abundant host carbonate sediment. With the exception of the maximum for Mn centered on ~150 mbsf, adsorption pathways appear to dominate the Mn profile at depth. The subsurface Mn maximum centered on ~150 mbsf corresponds in a general way with increased ash frequency but, most importantly, with a profound decrease in calcium carbonate concentration (see "Lithostratigraphy" section, this chapter). These effects are recorded in the solid-phase data presented in Figure 29. The observation that the maximum levels of Mn correspond precisely with the carbonate minimum suggests that carbonate dilution of the detritally delivered Mn component may be the critical control. The variability of dissolved Fe is more pronounced than that of Mn, suggesting an ash-related source or alteration effects. Finally, concomitant bicarbonate production (oxidation of organic carbon) during bacterial reduction of Fe and Mn, as well as sulfate reduction, may contribute to the downcore increase in alkalinity observed in the upper ~200 m of the pore-water profile.

Calcium, Magnesium, and Strontium

Calcium and magnesium show a strong antithetical relationship (Fig. 30). Concentrations of both these cations at the top of the sediment column approximate those of seawater, with Mg^{2+} concentrations decreasing and Ca^{2+} increasing with depth both by a factor of 2. Possible major influences on the relative abundances of these two elements include calcium carbonate dissolution and recrystallization, dolomite precipitation, weathering reactions involving ash in the sediment section, and weathering reactions involving the volcanic base-

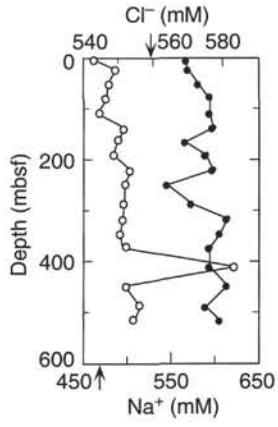

Figure 28. Depth profiles of Na^+ (open circles) and Cl^- (solid circles) in Site 998 interstitial waters. Mean ocean-bottom-water composition (arrows) taken from Millero and Sohn (1992).

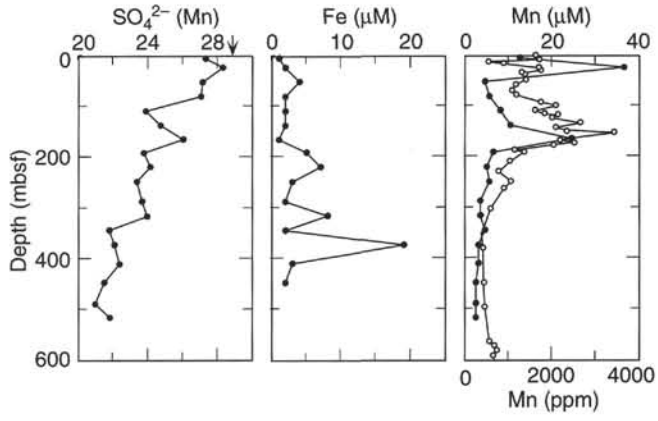

Figure 29. Depth profiles of sulfate, iron, and manganese in Site 998 interstitial waters. Mean ocean-bottom-water sulfate composition (arrow) taken from Millero and Sohn (1992). The complimentary sediment profile is also shown for Mn (open circles), in units of ppm.

ment that create a sink for Mg^{2+} and a source for Ca^{2+}. The formation of tri-octahedral smectite, which would sequester Mg^{2+} from solution, is perhaps the most significant reaction involving Mg^{2+}. The precipitation of a Mg-rich smectite is consistent with the available solid-phase data from altered ashes collected from the same stratigraphic level (see "Igneous Petrology and Volcanology" section, this chapter).

A fraction of the downcore decrease in dissolved Mg^{2+} (observed most readily in the upper 200 mbsf) is attributable to dolomite precipitation. Formation of dolomite is suggested by the decrease in alkalinity (Fig. 31) observed over the same range of depths and by the presence of dolomite recognized by X-ray diffraction (XRD; see "Lithostratigraphy" section, this chapter). If forming at the expense of a precursor calcite phase, dolomite precipitation may contribute to the concomitant increase in Ca^{2+} concentration. The dissolution and recrystallization of calcite, with high initial Sr concentrations, possibly exerts the dominant effect on the Sr concentration profile (Fig. 30). This conclusion is consistent with the observed downcore trend for Sr and its coherence with the Ca^{2+} profile. The highly variable Sr contents of the ashes (up to 600 ppm) make their effect difficult to quantify. The occurrence of calcium carbonate dissolution in the upper ~200–250 mbsf is paralleled by corresponding increases in the alkalinity and dissolved Ca^{2+}, although these trends also are linked to ash alteration. Dissolution of calcium carbonate may dominate the

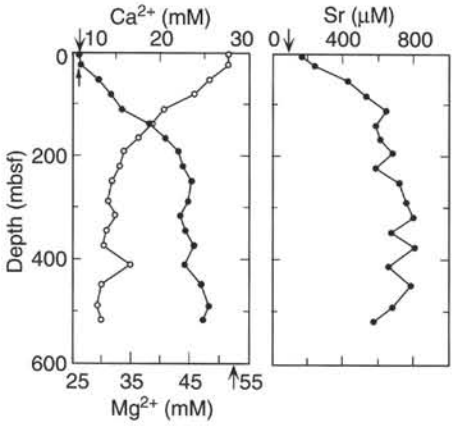

Figure 30. Depth profiles of Ca^{2+} (solid circles), Mg^{2+} (open circles), and Sr in Site 998 interstitial waters. Mean ocean-bottom-water composition (arrows) taken from Millero and Sohn (1992).

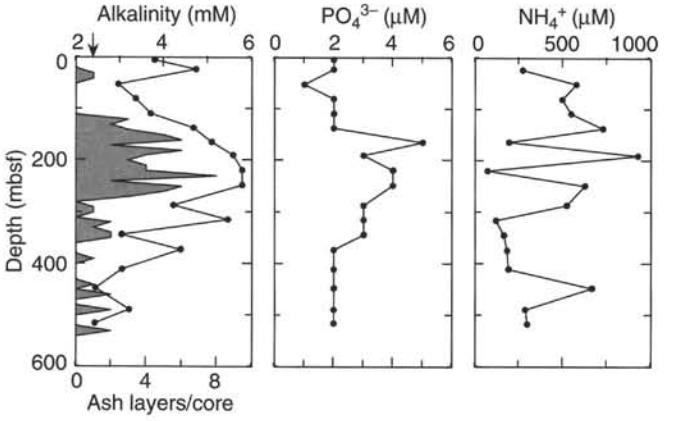

Figure 31. Depth profiles of alkalinity, phosphate, and ammonium in Site 998 interstitial waters. Ash layer distribution with depth (shaded area, in number of layers per core) is plotted to allow evaluation of their effect on pore-water chemistry. Mean ocean-bottom-water alkalinity value (arrow) taken from Millero and Sohn (1992).

upper 100 mbsf where ashes are minimal. The very low concentrations of organic carbon (see "Organic Geochemistry" section, this chapter) suggest that organic remineralization under aerobic conditions may not contribute significantly to conditions of calcium carbonate undersaturation (Emerson and Bender, 1981).

Alkalinity, Phosphate, and Ammonium

Alkalinity shows complex variation downsection (Fig. 31). Values at the top of the section are significantly higher than seawater, with the initial increase likely being related to organic matter degradation and calcium carbonate dissolution. This initial maximum also corresponds with the uppermost reported occurrence of ash beds. The alkalinity minimum at ~50 mbsf may be a consequence of the precipitation of the ~5%–10% dolomite observed in XRD samples from the upper section of the core (see "Lithostratigraphy" section, this chapter, and discussions above). A pronounced alkalinity maximum that appears between 150 and 300 mbsf correlates well with the main period of volcanic ash deposition. This alkalinity maximum, and the associated enhancement of cation concentrations, may be attributed to the effects of carbonate dissolution combined with weathering reactions and cation leaching linked to the alteration of glass and silicate components in the ash layers (e.g., smectite formation). The subsequent decline in alkalinity below the maximum may reflect removal of bicarbonate and cations from solution during silicate precipitation or reverse weathering. However, the decrease also may record the decrease in ash content below the alkalinity maximum. Consequently, the overall morphology of the alkalinity maximum represents, in part, diffusion away from an enriched source region.

Phosphate (Fig. 31) and ammonium in the upper sections of biogenic sequences are predominantly metabolic products of the decomposition of organic matter (Geiskes, 1983). The low TOC in sediments at Site 998, the irregular concentration profiles of these species, and their generally increased concentrations in association with increased ash abundance indicate that organic degradation is not a major influence on the profiles observed here, except perhaps in the very top of the section. Ammonium shows marked down-profile variability (Fig. 31). The multiple maxima and minima closely follow similar fluctuations in the K variability (Fig. 32). This trend may be a reflection of phosphate and ammonium liberation during weathering of K-feldspar and micas within the numerous silicic ash horizons found below 150 mbsf. Variability in the phosphate profile and the positive correlation with respect to the frequency of ash layers may reflect the comparatively high Fe contents of the associated sediment. Ferric-oxides have a strong capacity to scavenge phosphate. Consequently, the phosphate profile may be linked intimately to the redox cycling of Fe. The very low levels of dissolved phosphate above and below the ash maximum are maintained by effective adsorption of phosphate onto the surfaces of the carbonate sediment (Walter and Burton, 1986).

Rubidium, Potassium, and Lithium

In contrast to many oceanic sediment interstitial water profiles, K and Rb abundances from Site 998 show distinct maxima well below the sediment-water interface (Fig. 32). Rubidium levels of up to 5 μM are particularly enriched over normal seawater, with comparable values being reported only in interstitial waters associated with areas of pronounced hydrothermal activity (Geiskes, 1983). The well-defined Rb maximum between 180 and 350 mbsf coincides with the peak in ash frequency, indicating that the major source for pore-water Rb is glass-rich silicic ashes. Rubidium is liberated from the solid phase by leaching of volcanic glass and by weathering reactions that produce clays (e.g., smectites). Pore-water Rb levels decrease deeper downhole. This trend could be interpreted simply as reflecting a diminished source effect (a decreased flux of ash as well as increased dilution by the non-ash fraction). However, the distinct increase in solid phase Rb/Ti over this interval supports the notion that reverse weathering reactions occur that reincorporate cations from the aqueous phase (e.g., clay and/or zeolite precipitation). This diagenetic uptake continues downcore and is most intense in the region delineated by the high sedimentary Rb/Ti located slightly below the maximum in pore-water Rb. The sedimentary Rb/Ti maximum reflects the sequestering of the pore-water Rb and thus drives the diffusive gradient. Much the same rationale can be applied to the interpretation of the K distribution profile (and silica, as discussed below), that is, a dominantly volcanogenic source with the dominant sources and sinks controlled by reaction pathways of ash alteration.

In contrast, the Li profile does not mirror those of Rb and K in that it shows an overall linear increase with depth. A maxima of 250 μM is coincident with the zone of maximum ash abundance, suggesting a possible source effect; however, the continued steady increase implies no reincorporation during the reverse weathering reactions inferred for Rb and K. Furthermore, Li abundances do not appear to be significantly affected by silica precipitation within the chert horizons. The differing behavior of Li compared with the other alkali metals may be related to its substantially smaller ionic radius.

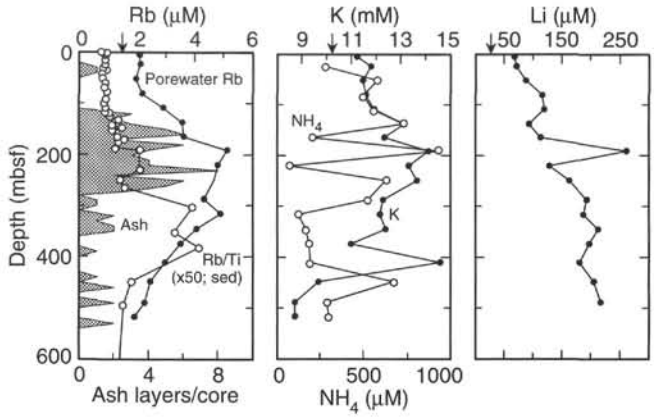

Figure 32. Depth profiles of Rb (solid circles), K (solid circles), and Li in Site 998 interstitial waters. Rb/Ti ratios (open circles) of sediment (×50 to accommodate plot scale) are also shown. Ammonium (open circles) plotted with K for comparison. Frequency of ash layers (shaded area, in number of layers per core) is also shown. Mean ocean-bottom-water composition (arrows) taken from Millero and Sohn (1992).

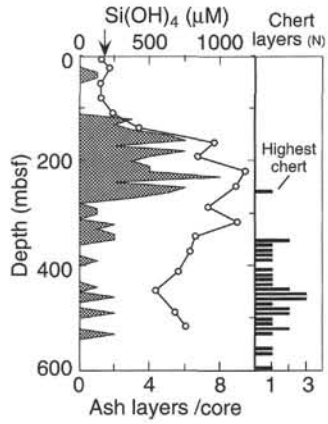

Figure 33. Depth profile of silica in Site 998 interstitial waters. Frequency of chert layers with depth indicated as histogram. Ash distribution (shaded area) also shown.

Silica

The dominant feature of silica variation in the interstitial water profile from Site 998 is a pronounced yet broad maximum from approximately 150–320 mbsf (Fig. 33). The initial downcore increase from approximate seawater values is thought to record silica release during the initial stages of ash alteration. This inference is supported by the dramatic increase in dissolved silica that is coincident with the first appreciable occurrence of ash layers. With the exception of a subtle concentration maximum in the uppermost 50 m interval, which corresponds with a minor occurrence of ash, concentrations of silica are comparatively invariant in the upper 100 m of core. This relationship further supports the role of Si-rich ash alteration (e.g., smectite precipitation) as a source of silica and corroborates independent sedimentologic observations that argue against biogenic inputs as a significant source of silica to these sediments.

The concentration profile for silica closely parallels those for K and Rb, suggesting that appreciable uptake of silica occurs as a consequence of silicate precipitation during a later phase of ash alteration and results in the eventual downcore decrease. In addition, decreasing concentrations of silica coincide with the first appearance and the progressive downcore presence of diagenetic chert, which is a sink for the dissolved silica (Fig. 33).

Interstitial Water Summary

A summary of the most significant chemical effects and possible causes seen in Site 998 interstitial waters is given in Table 11. The interstitial water chemistry largely reflects the influence of a prominent zone of Miocene silicic ash layers, superimposed upon the effects of carbonate dissolution and recrystallization reactions related to the carbonate-dominated host lithologies. These associations are corroborated independently by lithostratigraphic observations and produce downhole variations in the pore-water profiles that are coherent with solid-phase sediment chemistry. Pore-water redox conditions are characterized by typical deep-marine suboxic diagenesis. The influence of organic degradation and microbially mediated reactions appears restricted to the upper 50 m of sediment.

Sediment Chemistry

Introduction

Site 998 served as the pilot site for the Leg 165 shipboard sediment chemistry program (Tables 12, 13). Samples were initially acquired and processed at a rate of two per core, although this frequency soon proved unfeasible to maintain in terms of laboratory throughput. Therefore, Cores 165-998A-1H to 16H (~0–150 mbsf) were mostly analyzed at the two per core rate, whereas below this the sequence was sampled at a one per core rate until operations at the site were completed and the analytical program at this site discontinued. Discrete 10-cm^3 samples were taken from intervals that visually appeared representative and had no obvious marker beds (i.e., ash, turbidites, and other rapid or unusual events were avoided). The samples were analyzed as described in the "Explanatory Notes" chapter (this volume).

Quantifying Sedimentary Components (Terrigenous Material and Ash)

As evident from the "Lithostratigraphy" section of this chapter, the sediment at Site 998 can essentially be considered a three-component mixture of biogenic calcium carbonate, terrigenous detrital material, and volcanic ash. Although discrete ash layer frequency has been described elsewhere (see "Igneous Petrology and Volcanology" section, this chapter), the bulk sediment chemistry can be used to quantify the relative amounts of terrigenous material and ash dispersed through the sediment column. Quantifying the amount of dispersed ash is particularly important to better constrain diagenetic reactions and the sedimentologic nature of the recovered sequence. To this end, we consider the downcore behavior of several elemental ratios measured in the bulk sediment. Elemental ratios are generally more useful in quantifying components in the sediment column than individual concentrations because of the dilution of individual elements by a single dominant component (in this case, calcium carbonate).

At Site 998, the Ti/Zr (g/g) value was found to be a good component discriminant for a number of reasons. Both Ti and Zr are contained in stable, refractory phases of detrital components that are essentially unmodified by diagenesis. In the case of the glass-rich ashes, Ti and Zr most likely reside within the Si-rich glass or in refractory accessory minerals, and their immobility during low-temperature aqueous leaching and weathering reactions makes them a robust provenance indicator. In addition, in the system under consideration, Ti/Zr end-member ratios of terrigenous material and ash are distinct; in average clay Ti/Zr ~29 (Taylor and McLennan, 1985), compared to 7–9 in ash recovered at Site 998 (see "Igneous Petrology and Volcanology" section, this chapter). Even in heavily altered ash (MgO, ~5–7 wt%, 10% LOI), Ti/Zr (~10–13) remains distinct from that in average shale.

From 0 to 118 mbsf (Fig. 34), Ti/Zr is very close to that of average shale (Taylor and McLennan, 1985). This interval is coincident with

Table 11. Summary of diagenetic reactions occurring in sediment column, Hole 998A.

Lithologic unit	Process	Effect on pore-water chemistry	Remarks
I	Organic remineralization (minor, low TOC)	↓ SO_4 ↑ Fe and Mn ↑ Alkalinity	Low rates of bacterial sulfate reduction Bacterial reduction, suboxic diagenesis
II	Carbonate reactions		
	A. Dissolution	↑ Ca, Sr, and alkalinity	
	B. Dolomite precipitation	↑ Ca, ↓ Mg, and alkalinity	Uppermost 50 m; observed by XRD
	C. Adsorption onto $CaCO_3$	↓ PO_4, Mn, and Fe	
III	Leaching and weathering of ash layers	↑ K, Rb, Li, and NH_4 ↑ Alkalinity and silica ↓ Mg	Precipitation of Mg-rich smectite, glass dissolution Silica release dominant over biogenic source
IV	Extended ash alteration and chert precipitation	↓ Si, Rb, K, and alkalinity ↑ Li	Rb/Ti increases in solids, consistent with silicate precipitation

Table 12. Major element chemistry of bulk sediment at Site 998.

Core, section, interval (cm)	Depth (mbsf)	Ca (ppm)	Fe (ppm)	Mn (ppm)	P (ppm)	Ti (ppm)
165-998A-						
1H-2, 28–30	1.78	348393	15714	1599	449	1133
1H-6, 33–35	7.83	346877	16634	1676	337	1151
2H-3, 27–29	12.07	367571	8744	524	414	667
2H-5, 27–29	15.07	345199	13492	887	421	1031
3H-5, 33–35	24.63	345345	15596	1694	348	1080
4H-2, 27–29	29.57	324407	22776	1742	365	1603
4H-5, 27–29	34.07	332273	18675	1275	410	1307
5H-1, 27–29	37.57	357533	14162	1369	408	1018
6H-1, 28–30	47.08	365414	12220	1383	425	1052
7H-2, 50–51	58.30	359099	14556	1157	410	1016
8H-2, 110–112	68.40	345805	17787	1077	370	1252
9H-2, 37–39	77.17	355642	14498	1155	429	944
10H-5, 100–102	91.80	356347	14473	1720	360	924
11H-4, 28–30	99.08	342670	18140	2110	467	1187
12H-4, 26–28	108.56	339499	19992	1601	466	1270
13H-1, 27–29	113.57	305968	30377	1808	736	1933
13H-4, 27–29	118.12	307925	27774	2112	696	1748
14H-1, 26–28	123.06	355978	12899	1991	376	807
15H-1, 27–29	132.57	371492	9310	2647	327	601
16H-1, 27–29	142.07	352484	13506	2079	238	917
16H-4, 28–30	146.58	BDL	49575	2320	BDL	3065
17H-1, 26–28	151.56	BDL	52830	3436	BDL	3829
18X-4, 10–12	165.40	358827	11561	2150	441	568
19X-4, 28–30	170.98	369429	11191	2488	341	621
20X-1, 29–31	176.19	366343	11035	2008	373	581
21X-1, 40–42	185.90	352716	11354	1150	338	582
21X-4, 42–44	190.42	391034	3951	1357	138	241
23X-4, 31–33	209.61	377232	5451	1008	206	279
25X-4, 10–12	228.60	384750	4629	772	197	241
27X-4, 41–43	248.11	376379	6425	1055	210	350
29X-1, 27–29	262.77	372087	8027	878	255	350
33X-1, 54–56	301.44	397636	3187	587	144	89
38X-2, 62–64	351.12	394979	2222	375	155	76
41X-2, 99–100	380.39	399026	3240	412	215	85
48X-2, 49–51	447.29	399065	2079	422	114	112
53X-1, 27–29	493.57	390170	3340	456	150	197
60X-3, 62–64	564.32	380143	3929	562	248	173
61X-1, 45–47	570.75	382544	4296	658	198	231
62X-1, 65–67	580.55	374506	6580	702	296	294
63X-1, 0–2	589.50	363651	8408	642	288	489
65X-1, 28–30	608.98	372182	6273	697	196	398
165-998B-						
11R-1, 47–49	654.97	374942	4681	431	234	265

Notes: Data overspecified for calculation purposes. BDL = below detection limit. This entire table also appears on the CD-ROM (back pocket).

lithologic Unit I and Subunit IIA, in which the noncarbonate fraction is known, from observation, to be dominated by the terrigenous detrital component (see "Lithostratigraphy" section, this chapter). Ti/Zr subsequently decreases between 118 and 165 mbsf (to Section 165-998A-18X-4) to values comparable to the individual ash layers (see "Igneous Petrology and Volcanology" section, this chapter). This deeper interval is coincident with Subunits IIB and IIC. Below this depth, the data record very low Ti/Zr values throughout the upper portions of Unit III and increase toward the bottom of the sampled sequence (Core 165-998B-11R). Thus, the Ti/Zr record of the bulk sediment clearly indicates the transition from the upper ~120 m of sediment, where the noncarbonate component appears dominated by a detrital terrigenous signature, through a mixed zone from 120 to 190 mbsf, below which the noncarbonate component appears to be largely volcanogenic yet with a slight increase in the terrigenous component from ~500 to 700 mbsf.

Analogously, the Y/Zn value may also be used to assess the relative contribution of terrigenous detrital material and ash. In this case, the end-members are not as precisely defined because Zn is contained in both detrital terrigenous material and authigenic minerals forming at the expense of the ash. Nonetheless, Y/Zn in average shale equals ~0.32 (Taylor and McLennan, 1985) and is ~1 in the less altered ashes (low MgO, LOI <7 wt%).

Because the chemical behavior of the four different elements in the Ti/Zr and Y/Zn values are largely independent of each other, it is possible to construct a preliminary mass balance (or mixing) model and thus calculate the relative contributions of the detrital terrigenous and volcanogenic components. This is achieved by using the end-member ratios of average shale and average ash at this site, as described above. Sensitivity of the model to these different values will be discussed below.

For Ti/Zr, the mixing equation is as follows:

$$(\%\text{Terrigenous})(\text{Ti/Zr})_{\text{avg shale}} + (\%\text{Ash})(\text{Ti/Zr})_{\text{avg ash}} = (\text{Ti/Zr})_{\text{sample}},$$

which calculates the relative contribution of each component in the bulk sediment to the analyzed ratio. An analogous equation can be written for Y/Zn, and these equations can then be solved on a per sample basis for the amount of terrigenous material in a given sample. The equations were solved for the "% terrigenous" term, which was then used to calculate the "% ash" by difference from:

$$\%\text{Ash} = 100 - \%\text{CaCO}_3 - \%\text{Terrigenous}.$$

These calculations assume a three-component system, which is consistent with sedimentologic observations (see "Lithostratigraphy" section, this chapter). This method was chosen instead of recalculating the "%Ash" from the mixing model using the "%Terrigenous" output because of the expansion of uncertainty involved in calculating a small value (the "%Ash") from large values (the modeled "%Terrigenous"), which, although a factor in the calculation by difference, is particularly difficult to overcome in remodeling the "%Ash" value. Overall, because the "%Ash" values are relatively low (see below), the model is relatively insensitive to modest variations in ash end-member compositions.

The results of these calculations indicate that from ~0 to 120 mbsf the terrigenous detrital component accounts for ~15%–20% of the bulk sediment, whereas the ash maintains a constant ~3%–5% of the bulk (Fig. 34). From ~120 to 160 mbsf, a crossover between the amount of calculated ash and the amount of terrigenous detrital material occurs, with the ash becoming quantitatively more significant deeper downcore, and the terrigenous detrital load concomitantly less so. The pronounced carbonate minima at ~120–130 mbsf (Core 165-998A-13H) is compensated for by a disproportionately large increase in the terrigenous load (rather than by a coherent increase in both the

Table 13. Trace element chemistry of bulk sediment at Site 998.

Core, section, interval (cm)	Depth (mbsf)	Nb (ppm)	Zr (ppm)	Y (ppm)	Sr (ppm)	Rb (ppm)	Zn (ppm)	Cu (ppm)	Ni (ppm)	Cr (ppm)	V (ppm)	Ba (ppm)
165-998A-												
1H-2, 28–30	1.78	2.4	42	9	1032	18	50	45	32	22	35	158
1H-6, 33–35	7.83	2.5	46	9	1037	21	44	48	35	20	41	159
2H-3, 27–29	12.07	0.5	30	8	876	12	31	30	17	14	20	127
2H-5, 27–29	15.07	1.7	42	10	841	18	42	39	24	17	28	169
3H-5, 33–35	24.63	2.6	41	8	922	19	42	42	33	21	34	132
4H-2, 27–29	29.57	3.4	58	14	1094	27	55	75	47	34	57	235
4H-5, 27–29	34.07	2.6	51	11	963	24	50	63	35	26	39	220
5H-1, 27–29	37.57	1.4	42	8	1119	17	40	34	30	16	25	152
6H-1, 28–30	47.08	1.8	40	9	1139	17	38	242	30	21	48	141
7H-2, 50–51	58.30	1.3	42	8	1148	18	40	29	32	18	33	154
8H-2, 110–112	68.40	2.7	48	10	1096	22	43	36	36	24	33	152
9H-2, 37–39	77.17	1.2	40	9	1106	18	39	95	35	18	25	134
10H-5, 100–102	91.80	0.7	38	8	1023	17	37	50	34	19	20	126
11H-4, 28–30	99.08	1.9	44	12	1086	21	46	64	46	25	32	138
12H-4, 26–28	108.56	2.6	48	13	1151	23	52	37	48	28	41	177
13H-1, 27–29	113.57	3.3	67	20	1041	35	70	89	74	41	66	160
13H-4, 27–29	118.12	4.1	70	22	1064	36	65	60	56	36	45	231
14H-1, 26–28	123.06	1.9	50	11	1086	17	47	42	48	15	16	171
15H-1, 27–29	132.57	1.3	31	11	1008	16	33	25	28	12	19	169
16H-1, 27–29	142.07	1.6	53	11	1341	21	53	35	48	13	42	261
16H-4, 28–30	146.58	10.0	126	100	629	89	109	110	83	81	125	449
17H-1, 26–28	151.56	10.3	168	47	409	90	131	152	118	83	135	742
18X-4, 10–12	165.40	2.6	54	12	1335	15	56	26	45	12	31	523
19X-4, 28–30	170.98	1.5	43	11	1370	19	41	25	34	13	15	388
20X-1, 29–31	176.19	1.5	42	13	1260	16	43	30	38	9	26	476
21X-1, 40–42	185.90		40	11	1042	15	50	30	39	9	16	439
21X-4, 42–44	190.42		23	8	1009	10	24	19	13	4	6	210
23X-4, 31–33	209.61	0.5	25	5	936	8	33	19	21	5	9	272
25X-4, 10–12	228.60		27	7	834	10	420	21	19	4	6	293
27X-4, 41–43	248.11	0.5	38	9	1009	10	35	22	23	5	11	365
29X-1, 27–29	262.77	0.5	38	9	1207	11	36	26	28	7	8	506
33X-1, 54–56	301.44		22	5	1210	7	22	20	14	3	4	327
38X-2, 62–64	351.12		20	4	942	5	21	20	9	3	6	257
41X-2, 99–100	380.39		26	6	1316	7	22	24	12	4		372
48X-2, 49–51	447.29		20	3	1167	4	25	18	10			117
53X-1, 27–29	493.57	0.6	23	3	1155	6	21	17	14	3	6	128
60X-3, 62–64	564.32		23	4	1003	6	23	20	15	4		159
61X-1, 45–47	570.75	0.5	24	4	915	7	24	20	15	4	10	208
62X-1, 65–67	580.55	1.0	28	6	985	8	27	20	23	8	12	212
63X-1, 0–2	589.50		27	6	877	12	34	21	27	10	10	104
65X-1, 28–30	608.98		28	6	997	9	28	19	17	6	9	104
165-998B-												
11R-1, 47–49	654.97	0.7	16	4	588	7	23	27	12	4	5	155

Notes: Data overspecified for calculation purposes. No data indicates values <0.5 ppm. This entire table also appears on CD-ROM (back pocket).

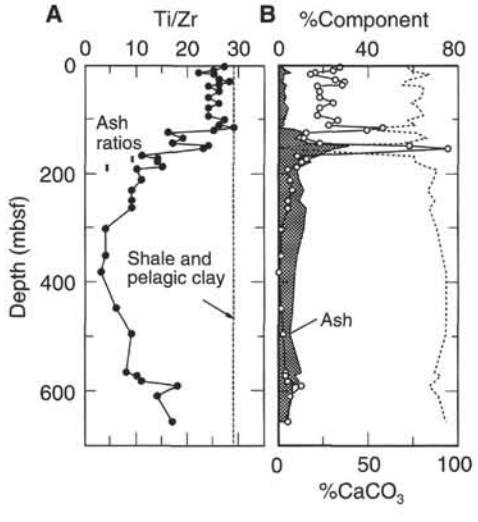

Figure 34. **A.** Downhole profile of Ti/Zr in bulk sediment, Holes 998A and 998B. Ash layer ratios in Samples 165-998A-19X-3, 54–57 cm, 20X-2, 9–11 cm, and 20X-CC, 32–33 cm, also shown by thick black bars. Average shale and pelagic clay from Taylor and McLennan (1985). **B.** Results of mass balance mixing model calculating the abundance of terrigenous detrital material (open circles), dispersed volcanic ash (shaded area, expressed as "%Component"), and $\%CaCO_3$ (dashed line).

terrigenous and ash components). The larger carbonate minima at ~145 mbsf (the middle/late Miocene carbonate crash; see "Lithostratigraphy" section, this chapter) is compensated for by only a modest increase in terrigenous material over ash. From 180 to 400 mbsf, the ash contribution remains at a constant ~10%, approximately twice that of the ash in the upper portions of the Site. The mixing model cannot resolve variations at the lowest concentration range (<5% of the bulk), and thus the contribution by the terrigenous component is imprecisely defined through this interval (although quantitatively minimal).

From 400 to 700 mbsf, both the absolute and relative contribution of the ash component decreases. This interval is characterized by extremely high concentrations of calcium carbonate (90%–95% $CaCO_3$), and therefore the total amount of noncarbonate material (i.e., ash and terrigenous material) is very low. Nonetheless, within this interval the model indicates that the amount of terrigenous material increases from essentially 0% to ~5%, with the ash decreasing from 10% to 5%. It is the increase in terrigenous material that also causes the Ti/Zr value to increase through this deepest interval.

We tested the mixing model using several methods. First, we calculated the abundance of the "%Terrigenous" component simply by normalizing to the abundance of Ti, according to the following formula:

$$(Ti_{sample}/Ti_{average\ shale}) \times 100 = \%\text{Terrigenous detrital material.}$$

This consciously neglects the contribution of ash to the total Ti load in the sediment (and thus will tend to overestimate the amount of terrigenous detrital material). Because the concentration of Ti in ash is relatively low (~1000 ppm) in comparison to that of average shale (~6000 ppm) and because the ash is a relatively small contributor to the bulk sediment through this uppermost sequence, the calculation remains a useful test of the mixing model. Unlike the model, the results from this calculation (because it is based exclusively on Ti abundances) are not forced by the difference subtraction into any restricted data range. Comparing this Ti-normative calculation of the terrigenous component to the mixing model confirms the pattern of deposition of terrigenous material (Fig. 35). Second, we tested the model by successively using Ti/Zr on the high and low ends of the observed range in the ashes at Site 998 (see "Igneous Petrology and Volcanology" section, this chapter); this was found to make only a negligible difference in the results. Finally, these observations are also fully consistent with XRD analysis of the relative amounts of quartz and calcite through the interval from 0 to 350 mbsf (see "Lithostratigraphy" section, this chapter).

In conclusion, the sediment chemistry successfully provides an assessment of the amount of dispersed ash and terrigenous detrital material in the bulk sediment. The chemical method is more quantitative than other standard physical methods (e.g., smear-slide determinations). Using reasonable end-member compositions and constrained by the sedimentologic descriptions of the sediment provided by other shipboard research groups, we have determined that the upper 120 mbsf of sediment contains ~20%–25% terrigenous detrital material and <5% dispersed ash, whereas from 200 to 350 mbsf the bulk sediment contains 0%–5% terrigenous detrital material and ~10% dispersed ash. In addition to this dispersed ash, an additional 2% of the section at Site 998 is composed of discrete ash layers (see "Igneous Petrology and Volcanology" section, this chapter). A minimum of ~0% terrigenous material is reached at ~400 mbsf. The amount of ash again decreases deeper in the core in the region of very high calcium carbonate, whereas terrigenous material increases to ~5%–10% of the bulk sediment.

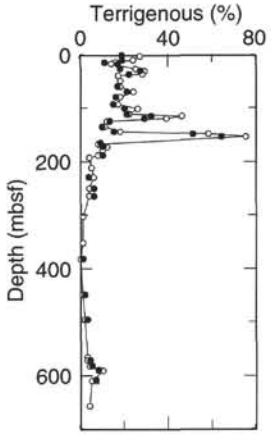

Figure 35. Downhole profiles of the terrigenous concentration in the bulk sediment, calculated by the two-ratio model (open circles) and by direct normative calculation (solid circles), assuming that all Ti is contained in the terrigenous component. The strong agreement between the two methods provides increased confidence in our assessments of the noncarbonate fraction in these sediments.

Chemical Proxies of Biogenic Production

Sedimentary calcium carbonate, opal, and organic carbon are diagenetically labile; therefore, it is difficult to directly link their respective final abundances in the sediment to variations in productivity of the overlying water. Because of this, much paleoceanographic research has focused on developing chemical proxies of biogenic production that are largely unaffected by diagenetic remobilization. When developing the shipboard sedimentary chemical methodology, particular effort was made to include Ba in the element menu because of its potential as a proxy of the organic carbon flux (Dehairs et al., 1980; Bishop, 1988; Dymond et al., 1992; Schmitz, 1987; Francois et al., 1995). Although many details of the biogeochemical linkages between Ba concentration and export production remain unclear, a basic observation is that in oceanic regions of high productivity, barite ($BaSO_4$) precipitates in close association with settling biogenic matter. The $BaSO_4$ is transported to the seafloor, and variations in its abundance (and, by inference, biogenic production) can be measured by the bulk chemical analysis of Ba through the sediment column. The Ba proxy is particularly useful in sequences such as Site 998 where sulfate reduction is minimal and $BaSO_4$ is unlikely to be altered significantly during diagenesis.

At Site 998, both the absolute concentration of Ba and the Ba/Ti value consistently indicate the low productivity of the overlying waters (Fig. 36). From 0 to 110 mbsf, Ba/Ti is essentially constant and remains very close to that of average shale (0.11; Taylor and McLennan, 1985). This value is low compared to areas of high biogenic productivity such as the eastern equatorial Pacific Ocean, where sedimentary Ba/Ti can range from 20 to 30. Similarly, concentrations of

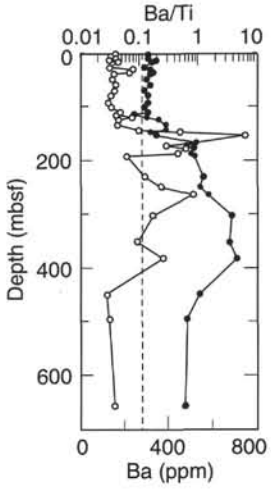

Figure 36. Downhole profiles of Ba concentrations (open circles) and Ba/Ti ratios (solid circles), Holes 998A and 998B. Ba/Ti in average shale (dashed line) from Taylor and McLennan (1985).

Ba itself are low throughout the entire sequence at Site 998, ranging from 150 to 400 ppm, whereas Ba at ODP sites in the eastern equatorial Pacific ranges from 1500 to 5000 ppm (R.W. Murray, unpubl. data, 1996). The increase in both Ba/Ti and Ba in the sediment depth profiles are coincident with the main ash occurrence. This spatial correlation, together with the high Ba concentrations of some ash layers, points to significant volcanogenic Ba input dispersed throughout this part of the sediment column.

Thus, the most significant result from our preliminary study of the behavior of the Ba proxy is that there have been no large-scale increases or decreases in biologic production at Site 998, at least through the intervals (and at the temporal resolution) sampled by the sediment chemistry program. It is clear from the overall pattern of Ba deposition that there have been no long-standing episodes (i.e., of several millions of years duration) of productivity variation recorded by the biogenic carbonate sediment.

IGNEOUS PETROLOGY AND VOLCANOLOGY

Introduction

The drilling of Site 998 has resulted in the discovery of a variety of volcanic sediments on the Cayman Rise, including abundant silicic volcanic ash fall layers of Miocene age, and Eocene volcaniclastic sediments of probable local origin, including both ash turbidites, and to a lesser extent, ash fall deposits. The Miocene ash fall layers provide a valuable record of explosive silicic volcanism in the Central American arc to the west of Site 998, and offer the first opportunity to date this important volcanic episode in the context of the detailed biostratigraphic marine record. Furthermore, they indicate that this volcanism was characterized by very large ignimbrite-forming eruptions. The Eocene volcaniclastic sediments were equally unexpected at this site. The petrography and abundance of volcaniclastic turbidites and ash fall layers in the Eocene sequence testifies to a local source, which leads us to propose that the Cayman Ridge was an active volcanic arc at this time. This finding has major implications for the volcano-tectonic setting of this part of the Caribbean region.

Ash Fall Layers

Volcanic ash fallout at Site 998 has produced both discrete ash fall layers and zones of dispersed ash. The distribution of ash layers in Holes 998A and 998B is shown in the Appendix tables on CD-ROM in the back pocket of this volume. Discrete ash fall beds are recognized by their sharp bases, bioturbated tops, normal grading, lack of tractional sedimentary structures, and high content of juvenile pyroclastic components (Fig. 37). Only two fall layers were recovered in the Pliocene–Pleistocene section at the site. A 12-cm-thick Pleistocene layer (165-998A-3H-4, 18–30 cm) is composed of 100–200 µm clear and fresh bubble-wall glass shards, with subhedral crystals of greenish to olive hornblende, 50–70 µm in diameter, and subhedral and twinned plagioclase 50–100 µm in size.

Ash fall layers are more abundant in the Miocene and range in thickness from 1 to 20 cm. One of the layers in Section 165-998A-14H-6 is composed of two light gray to gray, massive and normally graded units, with a total thickness of 96 cm. The basal contacts are sharp and the upper contact moderately bioturbated. The pale gray Miocene ash layers are dominated by colorless, platy to bubble-wall glass shards that range from 80% to 95% of the layer by volume. Carbonate is a very minor component of the layers, indicating rapid deposition with no admixing of secondary material. The delicate and unaltered glass shards are generally only a few micrometers in thickness, but they range from 50 to 350 µm in diameter (Fig. 38). Glass particles with a pipe-vesicle texture are also present but rare. The morphology of glass shards and massive, graded features of the Miocene layers is typical of distal fallout (co-ignimbrite ash) from major silicic ignimbrite eruptions.

The Miocene layers typically contain less than 10% of co-genetic phenocrysts. Biotite is a common constituent in most of the layers, occurring as olive green to brownish subhedral flakes, 100–300 µm in size (Fig. 39). Plagioclase is common as clear, euhedral to subhedral grains, 50–100 µm in size, with lamellar twinning. Quartz is a minor component, forming clear and typically angular grains or shardlike fragments, 50–200 µm in size. Amphibole is rare and occurs as subhedral greenish to olive, 50- to 70-µm grains (Fig. 40), probably of hornblende composition, associated with plagioclase (Samples 165-998A-3H, 26–28 cm, and 20X-1, 134 cm). Clinopyroxene is also rare and is present as yellowish, 50-µm anhedral grains in some layers (Sample 165-998A-14H-6, 18 cm).

Ash fall layers are relatively rare in the Oligocene of the section. They are principally composed of colorless silicic glass, but are much finer grained than the Miocene ashes (~50 µm) and generally show more signs of alteration of glass, especially beyond 400 mbsf (Fig. 41). Mineralogically, these layers are similar to the Eocene ashes be-

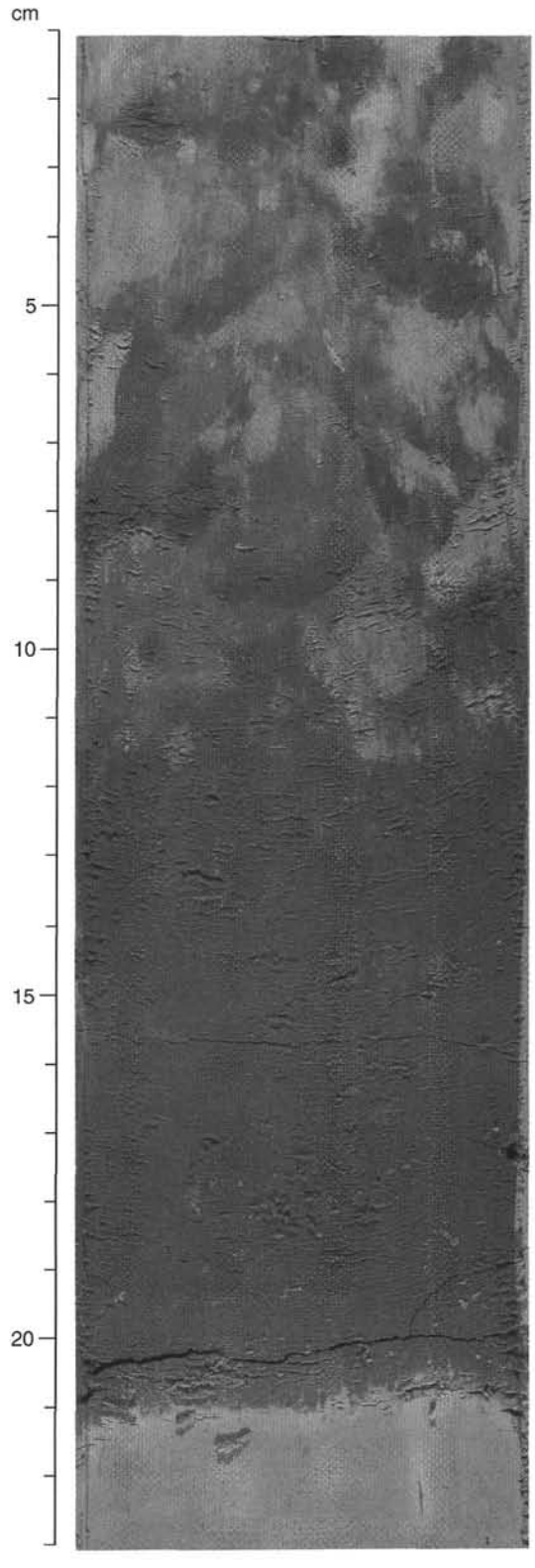

Figure 37. Volcanic ash fall layer in Section 165-998A-14H-6, 1–23 cm. Note the sharp basal contact and bioturbated upper zone.

Figure 38. Photomicrograph of typical rhyolitic glass shards in a 13.8-Ma volcanic ash fall layer in Section 165-998A-19X-3, 55–56 cm. The width of the field of view is 0.5 mm.

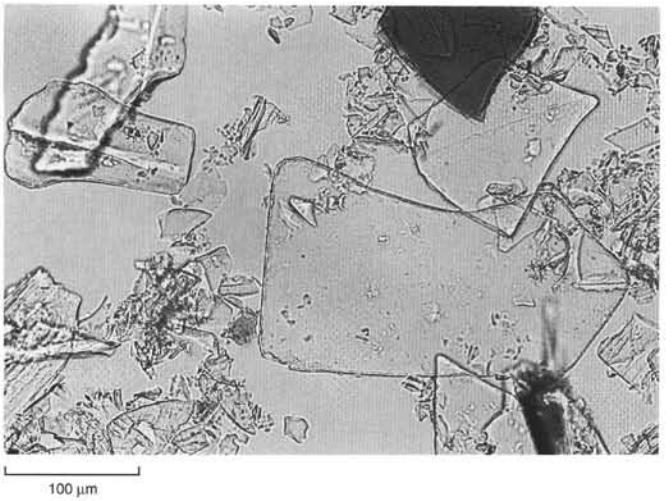

Figure 39. Photomicrograph of a biotite phenocryst and rhyolitic glass shards in a 14.4-Ma volcanic ash fall layer in Section 165-998A-20X-1, 134–135 cm. The width of the field of view is 0.5 mm.

low, with flakes of olive-brown biotite and small, rare laths of plagioclase.

The very abundant Eocene ash fall layers differ in several respects from the Miocene tephra. They are thin, typically in the 1- to 2-cm range (Fig. 42), finer grained, and greenish gray in color. Most of the glass has been altered to smectite and other clay minerals, rendering a dark greenish color to the layers. Relict glass occurs as clear, colorless, and angular shards, generally in the 20- to 50-µm-size range. Many of the layers are virtually crystal-free, whereas others contain minor olive biotite (50–100 µm), plagioclase laths, and angular fragments of quartz. A number of the Eocene ash fall layers are associated with volcaniclastic turbidites, as discussed in the "Lithostratigraphy" section (this chapter).

Ash Turbidites

An important change in the nature of volcaniclastic deposits takes place in the middle Eocene sequence of Site 998. Beginning at about 830 mbsf and extending to the base of the Hole 998B, the amount of

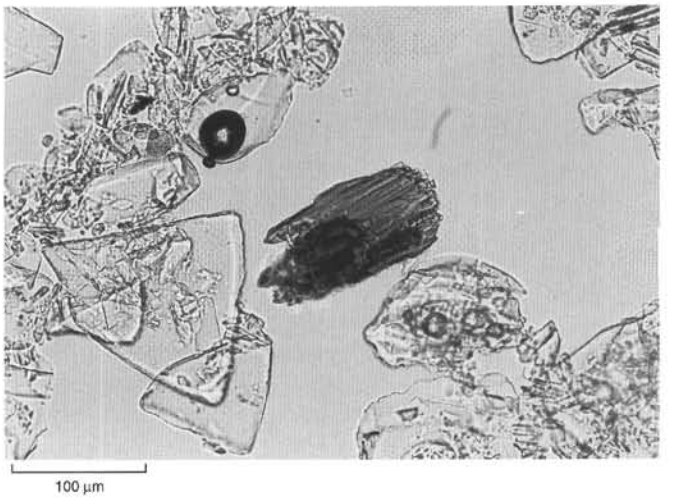

Figure 40. Photomicrograph of an amphibole phenocryst and typical fresh (clear) and altered (cloudy) glass shards in a 15-Ma volcanic ash fall layer in Section 165-998A-21X-3, 51–52 cm. The width of the field of view is 0.5 mm.

volcaniclastic material dramatically increases. Within this interval, volcaniclastic material is dominantly in the form of volcanic ash turbidites (Fig. 43). These turbidites contain a mixture of both pelagic (foraminifers and radiolarians) and volcaniclastic material. Foraminifers may include benthic shallow-water species (see "Biostratigraphy" section, this chapter), indicating that the source of at least some of the volcaniclastic turbidites is on the slope or shelf surrounding volcanic islands. The volcaniclastic component consists of smectite (altered volcanic glass), crystals of plagioclase, quartz, biotite and opaque minerals (~100 µm in diameter), and small igneous rock fragments with small laths of plagioclase (Fig. 44). XRD patterns of fine-grained units of the ash turbidites show that smectite is the dominant component, with traces of quartz, feldspar, and calcite. Total crystal contents can be quite high (up to 30%) in these layers compared with associated ash fall deposits. The presence of carbonate in these deposits indicates that they are produced by the mixing of sediment from at least two distinct sources.

Frequency of Ash Fall and Ash Turbidite Deposits

A total of 526 ash fall and ash turbidite layers were cored at Site 998, with an aggregate thickness of 19 m (normalized for core recovery). The stratigraphic distribution and number of volcanic ash layers observed per core, as well as the total thickness of ash observed per core in the drilled section is shown in Figure 45. The stratigraphic distribution and frequency of ash layers at Site 998 show two pronounced maxima: one in the Miocene and another in the early Eocene. These two volcanic episodes are characterized by fundamentally different transport processes and sources. The broad Miocene maximum actually contains a record of two major episodes, which, when taken together, represent a peak in the deposition of volcanic ash by fallout, with virtually no ash turbidites. In contrast, the massive influx of volcaniclastic material to Site 998 in the early Eocene was being delivered predominantly by turbidity currents that also carried carbonate sediment of both shallow- and deep-water origin. Some ash fallout occurred during this interval, but its volumetric contribution was minor compared with that being supplied by turbidites.

Geochemistry

The major and trace element composition of volcanic ash layers at Site 998 are shown in Table 14, based on shipboard X-ray fluores-

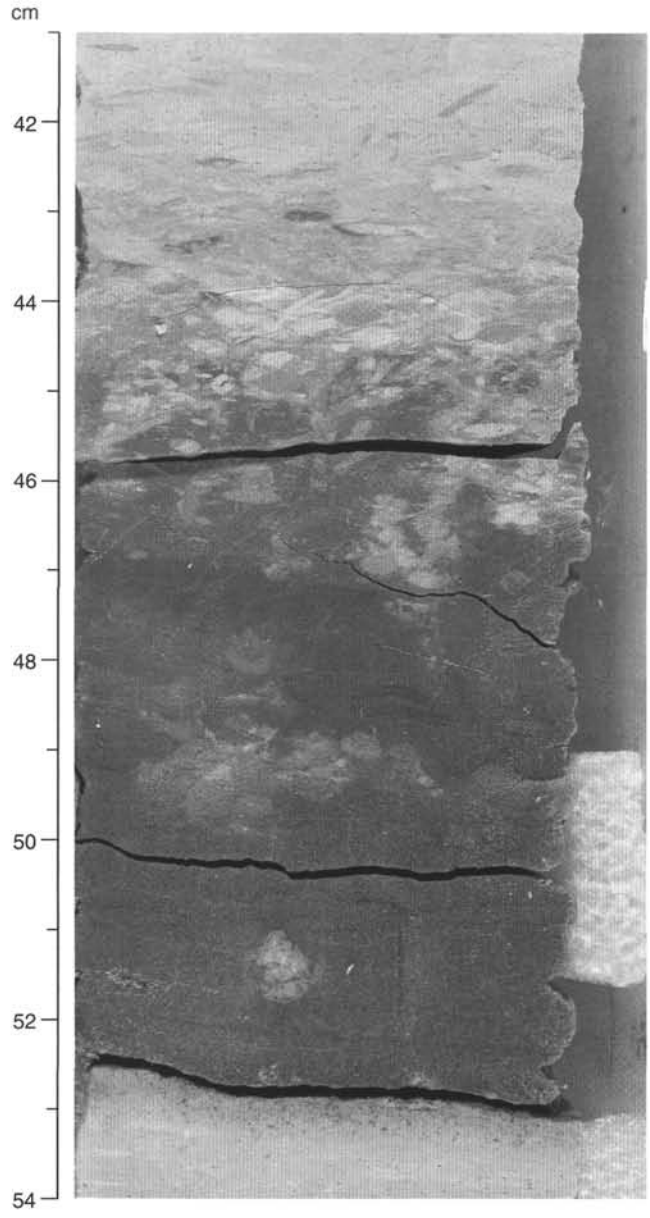

Figure 41. Partially altered early Oligocene volcanic ash fall layer in Section 165-998B-1R-7, 41–54 cm.

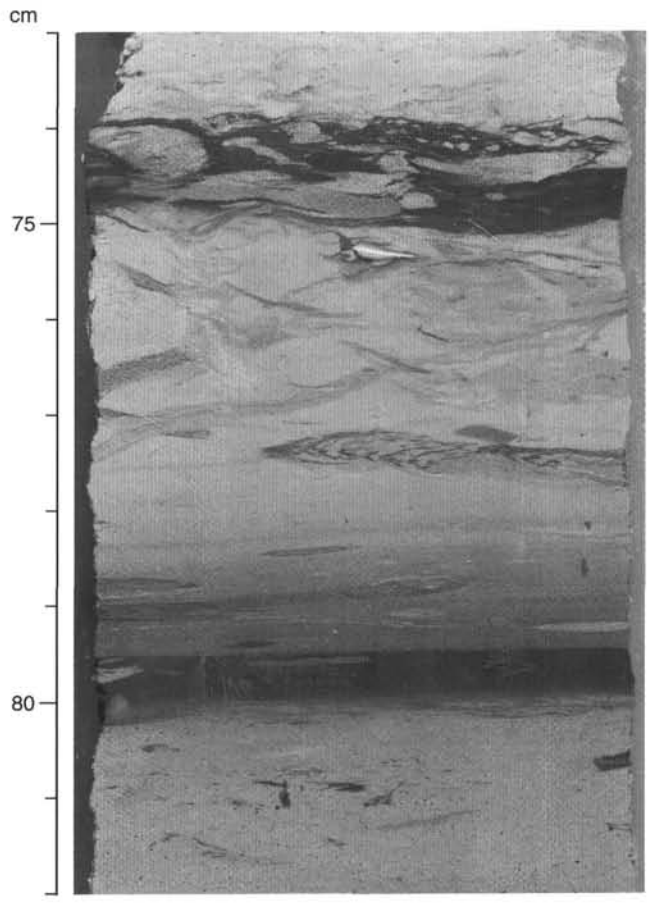

Figure 42. Altered Eocene volcanic ash fall layer in Section 165-998B-15R-1, 73–82 cm.

cence analyses. Most of the unaltered ash fall layers analyzed are of rhyolitic composition, with silica content ranging from 73% to 75% (Fig. 46). They are, however, notably high in potassium, with a Na_2O/K_2O ratio in the range from 0.46 to 0.63. The major element composition of the fresh Miocene silicic tephra is comparable to that of Miocene Central American volcanic ash layers recovered on DSDP Legs 66 and 67 in the Middle America Trench (Cadet et al., 1982a, 1982b; Rose et al., 1982). Detailed chemical comparisons are not possible, however, as the shipboard data are bulk analyses, whereas the Middle America Trench data is for electron microprobe analyses of glass shards only.

Some of the ash fall layers are largely altered to tri-octahedral smectite or other clay minerals, including the thickest layer recovered (Section 165-998A-14H-6), and this is reflected in their chemical composition (Fig. 47). The XRD patterns of samples from two of the layers (Sections 165-998A-13H-3, 28–30 cm, and 16H-4, 145–146 cm) show that smectite is the dominant mineral, with traces of quartz present. The altered layers, which retain a light gray to medium gray color, have an anomalously high MgO content (up to 7.35 wt%) and high alumina. Moreover, they are depleted in potassium and silica, compared with the other fresh tephra layers (Fig. 47). Their trace element concentration also reflects the effects of alteration and leaching, with depletion in Y, Ba, and Rb but enrichment in Sr, Ni, and Zr relative to the fresh rhyolitic tephra (Fig. 48). This leaching of silica, Rb, and K from the ash is clearly reflected in elevated concentrations of these components in the interstitial waters (see "Inorganic Geochemistry" section, this chapter). In terms of major oxides, the increase in MgO is probably the best index of the degree of alteration of the tephra, and this is accompanied by an enrichment in Ni. As shown in Figure 48, the downhole variation in Ni, and thus presumably the degree of ash alteration, is not systematic, and relatively fresh ash layers are encountered at various levels. The degree of alteration, as reflected by the nickel content, is also characterized by enrichment in some other trace elements in the ash, most notably Zr and Sr. These elements are not generally associated in geochemical processes, and we are unclear about the significance of this trend. The increase in Sr with alteration is, however, most likely a result of uptake of this element by the smectite, from the surrounding Sr-rich carbonates.

The major oxide and trace element composition of four early Eocene ash turbidites is also shown in Tables 14 and 15. The data also reflect the high carbonate content of the turbidites, composed of a mixture of volcanic glass (now altered to smectite), plagioclase, and, to a lesser extent, quartz crystal fragments and foraminifer tests. When the admixed carbonate content is taken into account, the bulk

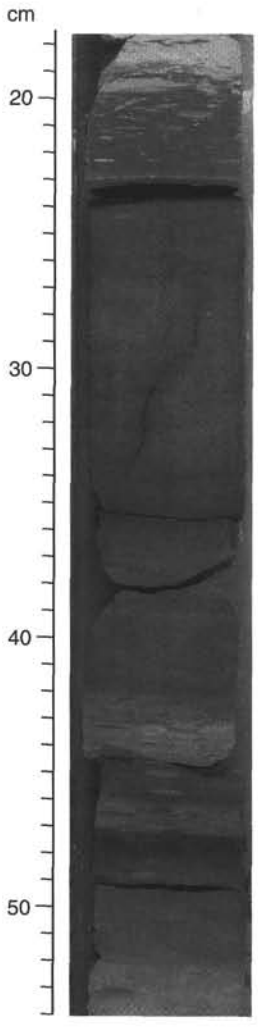

Figure 43. Volcaniclastic turbidite sequence in Section 165-998B-15R-4, 17.5–54 cm. The sequence consists of two thin basal units overlain by a thick stratified unit from 19 to 41 cm.

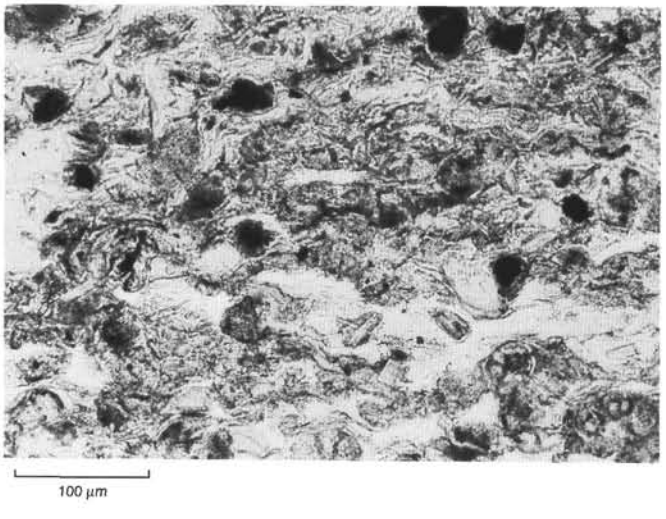

Figure 44. Photomicrograph of volcaniclastic turbidite layer in Section 165-998B-20R-4, 23–24 cm. The figure shows opaque grains of magnetite, angular to subrounded shards of feldspar and quartz (clear), and a matrix of smectite and other clay minerals (gray). The width of the field of view is 1.0 mm; plane-polarized light.

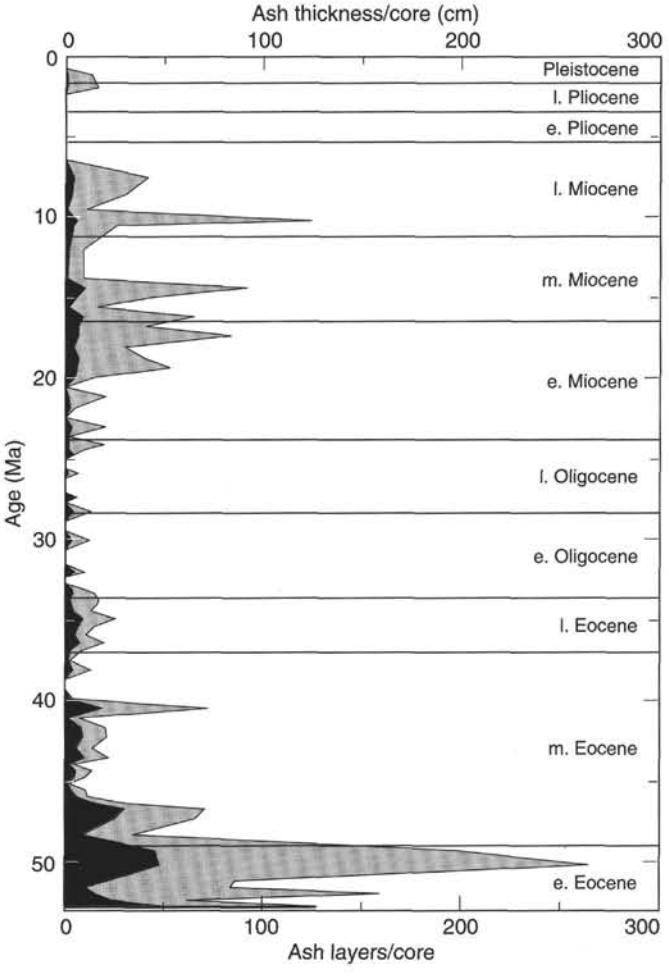

Figure 45. Number of volcanic layers (black) and total ash thickness per core in centimeters (shaded) as a function of age at Site 998.

composition of the turbidites is, in most respects, comparable to that of the silicic tephra fall layers.

Andesite

A 3-cm-long and solitary angular fragment of porphyritic andesite was found within the middle Eocene carbonate sediment (Sample 165-998B-21R-5, 48–49 cm). The rock is composed of a fine-grained groundmass of microlites of plagioclase, iron oxides, and pyroxene with an intersertal texture, with very common 2- to 5-cm-long euhedral and zoned phenocrysts of plagioclase. Pseudomorphs of smectite after pyroxene phenocrysts are also present, as well as iron oxide microphenocrysts. The lava fragment is vesicular and vesicles are filled with a zeolite with a radiating habit. We speculate that the rock fragment may have been transported to this part of the ocean by rafting in the roots of a floating tree trunk.

Discussion

Volcaniclastic material occurs as three components of the sedimentation at Site 998: ash fallout layers, volcaniclastic turbidites, and dispersed ash. As discussed in the "Inorganic Geochemistry" section (this chapter), the chemical composition of the background hemipelagic sediments at the site shows evidence of a dispersed ash component that ranges from 5% to 10% of the total sediment, reaching values as high as 40%. Discrete ash fallout layers and volcaniclastic turbidites make up a minimum of 2% of the drilled section. All of these

Table 14. Major element composition of volcanic ash layers in Site 998 sediments.

Core, section, interval (cm)	Depth (mbsf)	SiO_2	TiO_2	Al_2O_3	Fe_2O_3*	MnO	MgO	CaO	Na_2O	K_2O	P_2O_5	Total	LOI	Ma
Volcanic ash layers:														
165-998A-														
13H-3, 25–27	118	65.60	0.22	20.30	1.26	0.09	7.15	0.94	2.31	1.62	0.02	99.50	7.90	7.6
13H-5, 118–120	121	66.90	0.15	21.20	0.91	0.07	7.35	0.59	2.20	1.38		100.80	8.20	7.7
14H-6, 16–18	132	64.00	0.48	20.50	2.77	0.06	5.82	1.70	2.29	1.46	0.06	99.10	7.40	8.7
16H-4, 106–109	148	73.30	0.19	15.00	1.11	0.11	2.19	0.72	2.97	4.87	0.03	100.50	5.70	10.3
19X-3, 54–57	171	73.00	0.22	13.90	1.29	0.07	1.22	1.95	2.95	4.72	0.08	99.40	5.80	13.7
20X-2, 9–11	179	73.90	0.16	13.00	1.23	0.09	0.47	1.48	3.07	5.99	0.02	99.40	5.30	14.3
20X-CC, 32–33	183.5	75.00	0.11	13.10	1.44	0.04	0.38	1.46	2.79	6.05		100.40	5.40	14.4
28X-4, 123–125	259	74.70	0.09	12.90	1.33	0.06	0.25	1.84	3.23	5.97	0.01		4.90	19.4
31X-3, 129–131	286	70.50	0.20	15.20	2.01	0.05	1.62	2.11	3.48	4.75	0.05	99.90	5.90	21.2
37X-1, 142–144	341	59.80	0.22	16.80	3.19	0.01	4.09	9.27	2.59	1.68	0.00	97.70	13.30	24.4
165-998B-														
1R-7, 51–53	567	62.80	0.10	18.50	3.30	0.02	5.48	5.50	2.55	1.16	0.01	99.40	10.40	32.5
15R-4, 30–32	698	60.60	0.59	18.00	3.47	0.01	5.27	5.76	2.42	0.73	0.04		2.80	40.5
Ash turbidites:														
165-998B-														
31R-CC, 5–7	847.3	58.50	0.64	11.80	6.13	0.05	2.91	12.06	2.84	1.72	0.12		12.10	49.3
32R-4, 37–40	853	56.10	0.41	9.55	5.18	0.07	2.32	22.07	1.50	1.67	0.08		17.90	50.2
35R-5, 109–111	883	62.30	0.46	9.76	6.23	0.06	2.77	13.84	1.44	1.84	0.07		13.10	52.0
35R-6, 68–71	884	59.00	0.34	7.74	3.01	0.10	1.63	25.87	1.11	1.33	0.06			52.0

Notes: Shipboard XRF data given in weight percent. * = total iron reported as Fe_2O_3. LOI = loss on ignition. Ma = age of layers in millions of years. This entire table also appears on CD-ROM (back pocket).

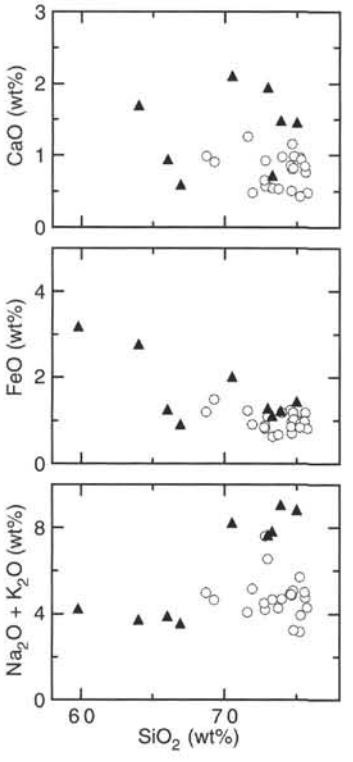

Figure 46. Plots of CaO, FeO, and $K_2O + Na_2O$ vs. SiO_2 for volcanic ash fall layers from Site 998 (solid triangles) and Legs 66 and 67 (open circles) (Cadet et al., 1982a).

volcanic components show large variations with time at the site. The pronounced Miocene maximum in ash fall layer frequency (Fig. 45) indicates two major episodes of silicic explosive volcanism in the circum-Caribbean area (early to middle Miocene and early late Miocene). A likely source area of this volcanism lies to the west of Site 998 along the Central American subduction zone. One way to evaluate the source area is from the grain size of the fall deposits. In general, the size of glass shards in ash fall deposits decreases systemati-

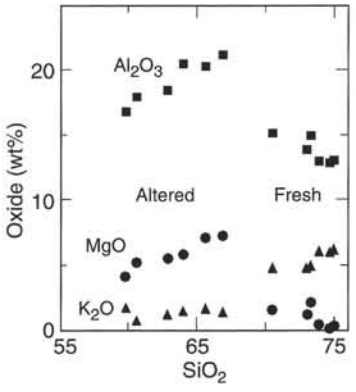

Figure 47. Subdivision of Site 998 volcanic ash falls into fresh and altered classes based on Al_2O_3 (squares), MgO (circles), and K_2O (triangles).

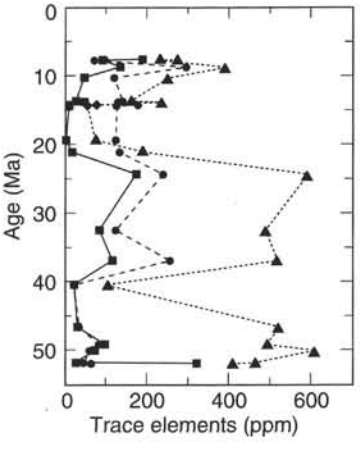

Figure 48. Variations of Ni (squares), Sr (triangles), and Zr (circles) in volcanic ash layers at Site 998 vs. age.

Table 15. Trace element composition of Site 998 volcanic ash layers.

Core, section, interval (cm)	Ma	Depth (mbsf)	Nb	Zr	Y	Sr	Rb	Zn	Cu	Ni	Cr	V	Ba
Ash layers:													
165-998A-													
13H-3, 25–27	7.6	118	9.9	95	1	273	24	49	1	187	18	507	165
13H-5, 118–120	7.7	121	7.6	70	1	230	17	22	1	90	1	31	86
14H-6, 16–18	8.7	132	12.9	293	1	392	21	69	23	134	1	47	500
16H-4, 106–109	10.3	148	16.1	118	22	250	149	29	3	46	1	13	917
19X-3, 54–57	13.7	171	5.8	140	16	158	92	40	7	26	1	12	721
19X-3, 54–57	13.8	171	4.5	128	11	235	78	51	10	47	1	20	600
20X-2, 9–11	14.3	179	12.3	177	39	76	130	42	6	9	1	4	660
20X-CC, 32–33	14.4	183.5	15.2	124	85	53	230	76	6	9	1	6	270
28X-4, 123–125	19.4	259	16.3	122	61	73	193	37	9	2	1	2	259
31X-3, 129–131	21.2	286	13.2	132	24	193	178	27	6	17	1	11	266
37X-1, 142–144	24.4	341	6.8	237	1	591	35	38	6	173	1	2	159
1R-7, 51–53	32.5	567	7.5	123	1	488	18	20	20	84	1	2	104
9R-4, 48–50	36.9	641	3.8	255	1	517	9	68	102	115	1	25	67
15R-4, 30–32	40.5	698	1	20	2	99	17	18	5	21	30	99	1173
28R-4, 53–55	46.7	815	0.8	33	8	522	17	39	28	30	22	30	187
Ash turbidites:													
165-998B-													
31R-CC, 5–7	49.3	847.3	1.9	81	8	489	35	61	199	97	83	151	325
32R-4, 37–40	50.2	853	1.5	59	6	609	37	48	75	72	48	92	480
35R-6, 68–71	52	884	0.6	45	5	460	26	40	30	25	41	70	370
35R-5, 109–111	52.1	883	1.9	63	6	408	44	46	45	319	59	131	195

Notes: Shipboard XRF data given in parts per million. Ma = age of layers in millions of years. This entire table also appears on CD-ROM (back pocket).

cally as a function of increasing distance from the volcanic source. The exact nature of this grain-size decrease is a function of eruption column height and the vertical gradient in wind direction and velocity, but air-borne tephra from major explosive eruptions is carried in the lower stratosphere and tropopause, at an elevation of about 15–20 km in the low-latitude regions. Glass shard diameters from coarse ash fall layers at Site 998 are on the order of 100–200 μm. In comparison with the grain size vs. downwind fallout distance relationship of some major explosive eruptions (Sigurdsson, 1990), these Miocene ash fall layers could be derived from sources at a distance of 1000–2000 km from the Cayman Rise. Presently, the site is about 1000 km northeast of the Central American silicic volcanic sources that were active in the Miocene on the Chortis block. This is a minimum distance, as the Chortis block has moved eastward since the Miocene, or toward the site, because of left-lateral strike-slip motion on the Cayman Trough Fracture Zone.

The potential source of this volcanism can be found in the middle to upper Miocene silicic welded and unwelded tuffs and flows of the Chalatenango Formation, which represents the most voluminous and wide-spread explosive volcanic episode in Central America (Wiesemann, 1975; Reynolds, 1980; Carr and Stoiber, 1990). The Chalatenango Formation makes up the high plateaus of El Salvador, southern Guatemala, southwestern Honduras, and central Nicaragua, as well as northwestern Costa Rica and central Panama. These areas are capped by vast deposits of rhyolitic ignimbrites, with an areal extent of over 10,000 km^2 and volumes on the order of thousands of cubic kilometers, with thicknesses up to 2 km locally (Williams and McBirney, 1969; McBirney and Williams, 1965). They include the Padre Miguel group of ignimbrites in southeastern Guatemala and in the Honduras (Dupre, 1970; Curran, 1980), which are up to 700 m thick (Donnelly et al., 1990). In Guatemala, the Padre Miguel Group contains silicic pumiceous tuffs or ignimbrites of middle to late Miocene age, equivalent to the Chalatenango Formation in El Salvador (Reynolds, 1980). It is underlain by the Morazan Formation of andesitic volcanics of Oligocene age. Biotites from welded tuffs in the Chalatenango Formation in Guatemala give K/Ar ages of 9.4 to 11.6 Ma, and similar ages are reported from central Honduras and Nicaragua.

Radiometric dating of the Central America igneous activity (F. McDowell in Donnelly et al., 1990) has shown that two main pulses of activity occurred around 14 and 18 Ma. This early to middle Miocene pulse of ignimbrite activity has been attributed to the subduction of the Farallon Plate beneath Central America, with ascending magmas from the subduction zone invading overlying continental crust. In the middle Eocene, development of the Middle American arc and subduction zone was initiated beneath the continental Chortis block. At about 25 Ma, a major reorganization of plate motion began in the Pacific region, with the breakup of the Farallon Plate into the Cocos and Nazca Plates (Atwater, 1989). This may have affected the style of subduction of the Cocos Plate into the Middle America Trench and had an impact on the zone of magma generation, with resulting increased magma ascent into the overlying continental lithosphere and crustal fusion to produce the rhyolitic magmas.

Miocene ash fall deposits corresponding to a similar age as the Site 998 ash fall maxima have also been recorded at Pacific Ocean DSDP sites. Cadet et al. (1982b) observed a distinction in the chemical composition of middle and early Miocene tephra derived from Central American sources, cored from the Pacific at DSDP Sites 495 to 497. The early Miocene tephra are generally lower in K than younger tephra, but middle Miocene tephra show a large range in K. The record shows a peak abundance of tephra in early to middle Miocene.

The early to middle Eocene sequence at Site 998 is characterized by a fundamentally different style of volcaniclastic sedimentation. During this interval, large amounts of volcaniclastic material was delivered to Site 998 by turbidity currents. The facies of this interval consists of a background flux of volcaniclastic mixed sediment, deposited under hemipelagic conditions, that was frequently interrupted by the emplacement of volcaniclastic turbidites and minor ash falls. The median thickness of turbidite deposits in this interval is between 5 and 10 cm, with the maximum thickness reaching 70 cm. Grain size in the turbidite deposits does not exceed coarse sand size. These characteristics suggest a deep-water depositional environment adjacent to a clastic volcanic source and is similar to volcaniclastic sequences described from both forearc and backarc basins in convergent margins (e.g., Sigurdsson et al., 1980). It is unlikely that turbidites of this type could be transported more than 200–300 km from their source, and thus we conclude that they are from Eocene arc volcanoes located on the Cayman Ridge. Dredging of the Cayman Ridge has revealed the presence of andesites, diorites, and granodiorite with arc affinities (Perfit and Heezen, 1978). The presence of coexisting ash fall layers indicates that at least some of these sources must have been subaerial. These findings are, however, somewhat at odds with the microfossil record of the sediments, as shallow-water benthic species are very rare in the Eocene part of the section, including the turbidites. The ash

fall deposits may have originated from subaerial sources that were more distal than the sources of the volcaniclastic material being delivered by the turbidites.

Volcaniclastic turbidites and ash fall layers in the middle and lower Eocene section of Site 998 indicate proximal volcanic sources on the Cayman Ridge, resulting in turbidite deposition in a basinal setting on the Cayman Rise. These findings must be viewed in the light of the tectonic setting of the Caribbean region. At the time of collision of the Cuban arc with the Bahamas platform (beginning in Late Cretaceous time and continuing into earliest Paleocene), subduction of Atlantic Ocean floor ceased beneath the Cuban arc (Pindell, 1993). At this time, a new north-dipping subduction zone may have been initiated in the present location of the Cayman Trench, giving rise to arc volcanism that built up the Cayman Ridge during the Paleocene and Eocene. Associated with this subduction was backarc rifting of the Yucatan Basin and extension of the Cayman Rise, receiving volcanic sediment components and volcaniclastic turbidites from the flanking Cayman Ridge arc to the south. The dominance of volcaniclastic turbidites and the low frequency of ash fall deposits at Site 998 during this period may reflect the east-west orientation of the arc relative to dominant atmospheric transport during this time. Sigurdsson et al. (1980) have shown that marked asymmetries in the proportion of ash falls vs. ash turbidites are the result of arc orientation relative to atmospheric (dominantly stratospheric) transport directions of fallout and differences in forearc and backarc morphologies.

The Eocene Cayman arc extended east to the Oriente Terrane of southeastern Cuba, and its activity is also recorded in Eocene volcanism in northern Hispaniola and Jamaica. In north Hispaniola, the Imbert Formation of dacitic tuffs and other volcanics are Paleocene–early Eocene in age, which is the last volcanism in the region of the north coast belt. The petrogenetic affinities of the Eocene volcanism in Hispaniola are unclear, but it probably coincides with the cessation of subduction (Lewis and Draper, 1990). During the early Eocene, calc-alkaline arc volcanism in Jamaica produced dacites and minor basalts associated with the Wagwater Formation (Lewis and Draper, 1990). At this time, the Nicaragua Rise terrane was located well to the west of its present position, and oceanic crust of Caribbean Plate affinity was most likely juxtaposed against the proposed Eocene Cayman Ridge arc. In most models of Caribbean tectonics, it is assumed that the physical properties of the Caribbean oceanic plateau prevented its subduction. Draper (1986) has, on the other hand, suggested that a north-dipping subduction zone existed beneath Jamaica at this time (Late Cretaceous–Paleogene), possibly a continuation of the proposed Cayman Ridge arc. The subduction zone of this Eocene arc was most likely quickly choked by the attempted subduction of the Caribbean Plate, leading to a change in the style of the North American–Caribbean Plate boundary from one of subduction at the Cayman Ridge, to one of east-west sinistral strike-slip motion with the opening of the Cayman Trench beginning in the late Eocene. Northern Hispaniola, Puerto Rico, and the Virgin Islands contain Greater Antilles arc-derived material that may have been transferred by strike-slip motion across the plate boundary associated with the opening of the Cayman Trough (Burke, 1988).

PHYSICAL PROPERTIES

The physical properties program at Site 998 included Multisensor Track (MST) and thermal conductivity measurements of whole-round cores as well as *P*-wave velocity, index properties, electrical resistivity, and vane shear strength measurements of split cores. Methods for these measurements are described in the "Physical Properties" section of the "Explanatory Notes" chapter (this volume). The high recovery at Site 998 allowed us to obtain a complete suite of physical properties data. MST magnetic susceptibility and GRAPE data were recorded at 1-cm intervals for Cores 165-998A-1H through 16H to a depth of about 151 mbsf; below this, measurements were made at 5-cm intervals in Holes 998A and 998B. MST *P*-wave velocity data were recorded at 1-cm intervals in Hole 998A to a depth of about 141 mbsf, but they were not recorded in the RCB-cored Hole 998B. MST natural gamma-ray measurements were made of all cores at 10-cm intervals. Thermal conductivity was measured on Sections 1, 3, and 5 of each core in Hole 998A to a depth at which induration prevented insertion of the needles (around 240 mbsf). On the split core, *P*-wave velocity was measured and samples for index properties were taken at a sampling interval of one per section in all cores, whereas one measurement per section of electrical resistivity and vane shear strength was taken in Hole 998A to the depth at which induration prevented insertion of the needles for electrical resistivity (around 200 mbsf) and the vane for shear strength (around 100 mbsf).

Multisensor Track

Data from the MST measurements are presented in Figure 49 and Tables 16, 17, 18, and 19. The magnetic susceptibility is high in the intervals rich in volcanic ash (see "Lithostratigraphy" section, this chapter), whereas the GRAPE data indicate an overall high density in the same intervals. As a rule, however, each single peak in magnetic susceptibility corresponds to a local low in GRAPE density. The GRAPE densities are close to those determined from index properties in Hole 998A, except in the uppermost 100 mbsf, where the high water content causes an overestimation of density by the GRAPE (no Boyce-correction for this phenomenon is included in the processing for Site 998). GRAPE densities are shifted to lower values relative to index property data in Hole 998B. This is to be expected because the cores in Hole 998B do not fill the liner, and the GRAPE processing assumes a core diameter corresponding to a filled liner. *P*-wave velocity data correspond well to the data collected on the split core (see below). Natural gamma radiation shows a general correlation with magnetic susceptibility, but the natural gamma radiation is generally low over the entire depth interval.

Thermal Conductivity

Thermal conductivity data were collected at the same locations where the velocity measurements were made (Table 20; Fig. 50). The thermal conductivity increases from around 0.9 W/(m·K) near the top of the cored interval, where porosities are about 78%, to around 1.2 W/(m·K) at 100 mbsf, where porosities have fallen to about 60% (see below). Downcore, the thermal conductivity remains roughly constant to depths of about 240 mbsf, the level of our last measurements.

P-Wave Velocity

Data from the velocity measurements on the split surface are presented in Table 21. The locations of measurement were chosen so as to avoid volcanic ash layers and basal coarse-grained layers of turbidites. Down to a depth of around 100 mbsf, the *P*-wave velocities were measured along the axis of the core as well as parallel to bedding by the digital sonic velocimeter (DSV). Between 100 and 740 mbsf, the sediments are more indurated. For this interval, the *P*-wave velocities were measured on split cores parallel to bedding by the Hamilton Frame. Below 740 mbsf, the Hamilton Frame was used for measuring *P*-wave velocities perpendicular to bedding on discrete samples. The three data sets indicate no significant difference between velocities along the core axis and parallel to bedding, and the change of measuring device at around 100 mbsf and around 740 mbsf seems to have no influence on the continuity of the data.

For comparison with logging velocities, the laboratory data were corrected to in situ stress (Table 21; Fig. 51) by the empirical relation derived by Urmos et al. (1993):

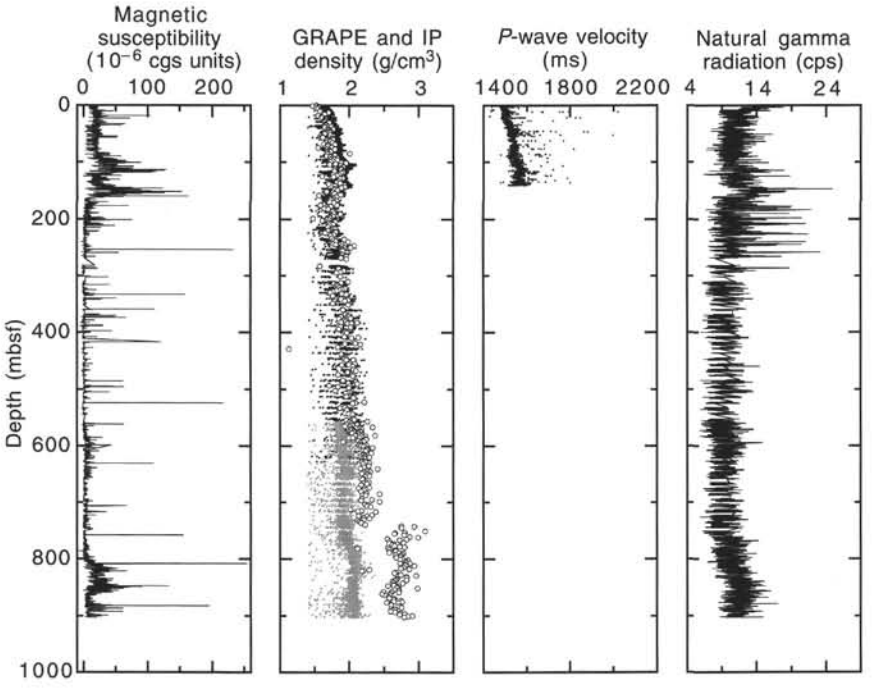

Figure 49. Multisensor track data showing magnetic susceptibility, GRAPE density for Holes 998A and 998B (solid and shaded, respectively), with index properties (IP) density (open circles) for comparison with GRAPE, *P*-wave velocity, and natural gamma radiation vs. depth.

Table 16. Magnetic susceptibility data for Site 998.

Core, section, interval (cm)	Depth (mbsf)	Raw mean susc. (10^{-6} cgs)	SD susc.	Drift corr.	DAQ period (s)
165-998A-					
1H-1, 5	0.05	6.4	0.320803	0	5
1H-1, 10	0.1	6.2	0.301289	0	5
1H-1, 15	0.15	6.8	0.235775	0	5
1H-1, 20	0.2	7.4	0.320803	0	5
1H-1, 25	0.25	9.2	0.301289	0	5
1H-1, 30	0.3	10.4	0.355295	0	5
1H-1, 35	0.35	12	0	0	5
1H-1, 40	0.4	13	0	0	5
1H-1, 45	0.45	16	0	0	5
1H-1, 50	0.5	17.05	0	–0.1	5

Notes: The data in this table differ from the raw data in that (1) all columns do not appear, (2) depths have been added, (3) columns have been labeled, (4) unsuccessful measurements have been deleted, and (5) magnetic susceptibility values have been averaged. susc. = susceptibility, SD = standard deviation, corr. = correction, DAQ = data acquisition.

Only part of this table is produced here. The entire table appears on CD-ROM (back pocket).

Table 17. Gamma-ray attenuation porosity evaluator (GRAPE) data for Site 998.

Core, section, interval (cm)	Depth (mbsf)	Raw counts	DAQ period (s)	Density (g/cm³)
165-998A-				
1H-1, 3	0.03		3	1.581
1H-1, 4	0.04		3	1.591
1H-1, 5	0.05		3	1.581
1H-1, 6	0.06		3	1.585
1H-1, 7	0.07		3	1.581
1H-1, 8	0.08		3	1.584
1H-1, 9	0.09		3	1.572
1H-1, 10	0.10		3	1.576
1H-1, 11	0.11		3	1.584
1H-1, 12	0.12		3	1.584

Notes: Raw counts are not reported for Hole 998A. DAQ = data acquisition. Density = bulk density, no Boyce correction applied. The data in this table differ from the raw data in that (1) all columns do not appear, (2) depths have been added, (3) columns have been labeled, and (4) unsuccessful measurements have been deleted.

Only part of this table is produced here. The entire table appears on CD-ROM (back pocket).

$$\Delta V_p = 0.646\,[1 - \exp(-0.00219Z)],$$

where ΔV_p is the correction (km/s) and Z is the depth (mbsf). The relation is derived on the Ontong Java Plateau and is expected to be valid down to 800 mbsf in a carbonate lithology. Comparison with log velocities (see "Downhole Measurements" section, this chapter) confirms this pattern. The corrected velocities show an overall agreement with the log data down to near 800 mbsf, below which depth the correction is too large, and the log data corresponds to the uncorrected laboratory data. No temperature correction was made. Data from Urmos et al. (1993) indicate that this correction should be between –30 and 15 m/s, and thus insignificant.

An overall increase in velocity with depth is seen from around 1500 m/s near the seafloor to around 3000 m/s at 900 mbsf, but two depths with a marked velocity increase were found (1) at around 190 mbsf, where velocity shifts from 1600 to 1700 m/s; and (2) between 750 and 800 mbsf, where velocity shifts from 2400 to 3400 m/s. These velocity breaks correlate with changes in index properties. The velocity shift around 750 mbsf correlates with the onset of silicification (see "Lithostratigraphy" and "Inorganic Geochemistry" sections, this chapter). Single velocity spikes above this depth correspond to local silicified intervals.

Index Properties

Index properties samples were taken from split cores at those locations where the velocity measurements were made. Wet and dry weights and wet and dry volumes were measured and used to calculate wet-bulk density, grain density, water content, porosity, and dry-bulk density (see "Explanatory Notes," this volume). Table 22 presents the index properties for Site 998. Figure 52 presents wet-bulk

Table 18. Multisensor track *P*-wave data for Site 998.

Core, section, interval (cm)	Depth (mbsf)	*P*-wave velocity (m/s)	Raw mean time	Raw SD time	Raw mean displ.	Raw SD displ.	Mean signal level	DAQ period (s)
165-998A-								
1H-1, 4	0.04		30.4	0.0374	51	0	05	5
1H-1, 5	0.05		30.4	0.08	50	0	05	5
1H-1, 6	0.06		42.2	8.0858	50	0	285	5
1H-1, 7	0.07	1503.80	51.2	0.02	50	0	1075	5
1H-1, 8	0.08	1503.50	51.2	0.0245	50	0	1275	5
1H-1, 9	0.09	1505.90	51	0	47	0	1815	5
1H-1, 10	0.1	1503.60	51	0	46	0	1815	5
1H-1, 11	0.11	1502.30	51	0.02	46	0	1835	5
1H-1, 12	0.12	1503.30	51	0.02	46	0	1825	5
1H-1, 13	0.13	1505.30	50.9	0	46	0	1795	5

Notes: SD = standard deviation, displ. = displacement, DAQ = data acquisition. The data in this table differ from the raw data in that (1) all columns do not appear, (2) depths have been added, (3) columns have been labeled, and (4) unsuccessful measurements have been deleted.

Only part of this table is produced here. The entire table appears on CD-ROM (back pocket).

density and porosity data. Porosity decreases from about 78% near the seafloor to around 22% at a depth of 900 mbsf.

Electrical Resistivity

Electrical resistivity data were collected at the same locations where the velocity measurements were made. The electrical resistivity data are presented in Table 23 and Figure 53. The electrical resistivity increases from around 0.35 Ωm near the seafloor to around 0.75 Ωm at 70 mbsf, below which depth a cyclic variation is suggested. The resistivity varies from 0.5 to 1.1 Ωm at 40 m scale to 200 mbsf, where the last data were collected. The formation factor, F, corresponding to the resistivity was calculated from $F = R_o/R_w$, where R_o is the resistivity of the sediment and R_w is the resistivity of the pore water. The pore-water resistivity was assumed to be that of seawater at 20°C (0.206 Ωm). The porosity, Ø, was calculated from the formation factor by Archie's equation, $F = a/(Ø)^m$, under the assumption of $a = 1$ and $m = 2$. The resulting porosity data are plotted on Figure 53. The Archie porosity is above the one determined from index properties for Ø > 65% and below for Ø < 65%.

Vane Shear Strength

The ODP motorized minivane was used to measure undrained shear strength in split-core sections. The measurements were made at the depths also used for *P*-wave velocity determination. The results are presented in Table 24 and Figure 54. An overall increase in shear strength with depth is evident.

DOWNHOLE MEASUREMENTS

Operations

On 2 January 1996, after reaching a total depth of 904.8 mbsf, Hole 998B was swept of sediment during a complete wiper trip using seawater circulation. The pipe was placed at 200.3 mbsf for the beginning of each logging run and raised approximately 28 m to a depth of 172.3 mbsf while logging uphole. The first of four logging runs began at Hole 998B at 1100 UTC on 2 January 1996, and all logging runs were completed at 2000 UTC on 3 January, corresponding to a total logging time of 33 hr (Table 25).

The Quad combo tool string (see "Downhole Measurements" section, "Explanatory Notes" chapter, this volume) included, from top to bottom, the telemetry cartridge, natural gamma spectrometry, long-spaced sonic, compensated neutron, lithodensity, dual induction resistivity, and the Lamont temperature tool (TLT). These tools were strung together into a tool string 33.99 m long. The Quad combo tools were run down to the level of the drill-pipe opening and held stationary for 3 min to obtain a bottom-water calibration point for the TLT. Excellent quality data were recorded as the tool string moved uphole at 300 m/hr from the bottom of the hole and into the drill pipe (Figs. 55, 56, 57). A 91-m repeat section was logged from 309.3 to 218.3 mbsf. As the tools were pulled upward, the depth to the end of pipe was measured at 171.3 mbsf, which is 1 m shallower than the depth as calculated by the driller. Finally, another bottom-water temperature calibration point for the TLT was obtained at the drill-pipe opening.

The geochemical tool string ("Downhole Measurements" section, "Explanatory Notes" chapter, this volume), which included telemetry, natural gamma spectrometry, aluminum activation clay, and induced gamma-ray spectrometry tools, was strung together to create a tool string 17.13 m long. Logging data were recorded from 904.7 to 132.3 mbsf as the tool string moved uphole at 200 m/hr (Figs. 56, 57). A 65-m repeat section was logged from 327.3 to 232.3 mbsf.

The Formation MicroScanner (FMS), which included telemetry, natural gamma spectrometry, and FMS sections, was the third toolstring run in the hole. An obstruction, possibly a ledge or bridge, was encountered at 430.3 mbsf, preventing further penetration of the borehole. FMS data were recorded uphole at 260 m/hr from 420 to 294.5 mbsf. During the first upward logging pass, the wireline heave compensator (WHC) shut down unexpectedly. The unit was quickly restarted and a short overlapping run was recorded from 327.5 to 197 mbsf. The cause of the shutdown has not yet been determined. An uninterrupted repeat section was run from 425 to 192 mbsf.

The same obstruction at 430.3 mbsf, first encountered by the FMS, also prevented passage of the Geological High-Sensitivity Magnetic Tool (GHMT) logging string during the final logging run at Hole 998B. Excellent quality GHMT data were collected, however, from 425.3 to 222.8 mbsf. A repeat section between 426.4 and 205.8 mbsf was logged to insure accuracy and repeatability of the data. Because of deteriorating hole conditions, the drill pipe was not raised by 28 m, as was done for the three previous tool strings.

Log Quality

In general, the data from all four tool strings appear to be of high quality and rarely were the data degraded by borehole washouts. The sonic log in particular displayed no cycle skipping and values for both near- and far-spaced receivers are nearly identical. In addition, resistivity values from the ILD, ILM, and SFL, which range in depth of penetration from 1.5 to 0.38 m ("Downhole Measurements" section, "Explanatory Notes" chapter, this volume), show identical responses throughout the logged interval indicating uniform borehole conditions without significant invasion of the formation by seawater (Figs. 55, 56, 57). The data recorded from the gamma-ray spectrometry tool will require post-cruise processing; references made here to silicon, calcium, and iron are only broadly qualitative. In contrast, the natural gamma-ray spectrometry tool produces reliable values for the concentration of potassium, thorium, and uranium, and the aluminum activation clay log is generally little improved through post-cruise processing. The FMS data have undergone preliminary shipboard image processing, resulting in an interpretable record.

Consistent depths for each of the logging runs was accomplished by correlating the natural gamma-ray logs and depth shifting relative to the Quad combo tool string. The depth to the end of pipe determined by wireline measurement was 1 m shallower than that given by drill-pipe measurement. All logs were depth shifted from meters below rig floor to meters below seafloor by subtracting 3190.7 m. These preliminary depth shifts will be replaced by depth shifts accomplished post cruise at the borehole research facility, Lamont-Doherty Earth Observatory.

Table 19. Natural gamma-ray (NGR) data for Site 998.

Core, section, interval (cm)	Depth (mbsf)	GR (cps)	Win 1	Win 2	Win 3	Win 4	Win 5	DAQ period (s)
165-998A-								
1H-1, 5	0.05	13.45	7.6	3.8	1.4	0.4	0.25	20
1H-1, 15	0.15	12.45	6.75	3.9	1.35	0.25	0.2	20
1H-1, 25	0.25	13.25	7.15	4.05	1.5	0.4	0.15	20
1H-1, 35	0.35	15.1	7.35	5.1	2.05	0.4	0.2	20
1H-1, 45	0.45	13.2	7.25	4.2	0.95	0.4	0.4	20
1H-1, 55	0.55	13.1	6.2	4.5	1.1	0.5	0.8	20
1H-1, 65	0.65	14.9	7.35	4.8	1.65	0.55	0.55	20
1H-1, 75	0.75	13.4	7.35	3.85	1.4	0.4	0.4	20
1H-1, 85	0.85	12.35	6.75	3.25	1.35	0.6	0.4	20
1H-1, 95	0.95	11.7	6.55	3.45	1.1	0.35	0.25	20

Notes: Win 1 through Win 5 = counts per second in each of five energy windows, corresponding to Schlumberger practice for spectral natural gamma-ray logs. DAQ = data acquisition. The data in the table differ from the raw data in that (1) all columns do not appear, (2) depths have been added, (3) columns have been labeled, and (4) unsuccessful measurements have been deleted.

Only part of this table is produced here. The entire table appears on CD-ROM (back pocket).

Table 20. Thermal conductivity measured on whole-round core sections for Site 998.

Core, section, interval (cm)	Depth (mbsf)	Thermal conductivity (W/[m·K])
165-998A-		
1H-2, 31–31.1	1.81	0.9977
1H-6, 31–31.1	7.81	1.0212
2H-1, 31–31.1	9.11	0.968
2H-5, 31–31.1	15.11	1.0912
3H-1, 31–31.1	18.61	1.0696
3H-3, 31–31.1	21.61	1.1310
3H-5, 31–31.1	24.61	1.1255
4H-1, 31–31.1	28.11	0.9660
4H-3, 31–31.1	31.11	1.1566
4H-5, 31–31.1	34.11	1.1762

Only part of this table is produced here. The entire table appears on CD-ROM (back pocket).

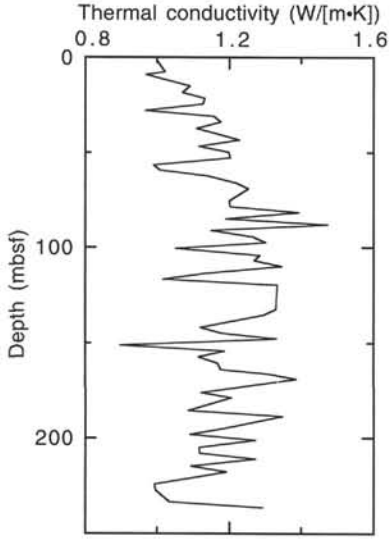

Figure 50. Thermal conductivity vs. depth measured on whole cores.

Table 21. DSV (DSV1 and DSV2) and Hamilton Frame (DSV3) velocities measured at discrete intervals for Site 998.

Core, section, interval (cm)	Depth (mbsf)	DSV1 (km/s)	DSV2 (km/s)	DSV3 (km/s)	Urmos correction (km/s)	Corrected velocity (m/s)
165-998A-						
1H-2, 111–111.1	3.24		1.493		0.005	1498
1H-3, 30.4–30.5	3.304	1.542			0.005	1547
1H-3, 30.4–30.5	3.304		1.53		0.005	1535
1H-4, 31.1–31.2	4.811	1.528			0.007	1535
1H-4, 31.3–31.4	4.813		1.525		0.007	1532
1H-5, 31.1–31.2	6.312	1.539			0.009	1548
1H-5, 31.1–31.2	6.311		1.534		0.009	1543
1H-6, 31.1–31.2	7.811	1.533			0.011	1544
1H-6, 31–31.1	7.81		1.514		0.011	1525
2H-1, 31–31.1	9.11	1.524			0.013	1537

Only part of this table is produced here. The entire table appears on CD-ROM (back pocket).

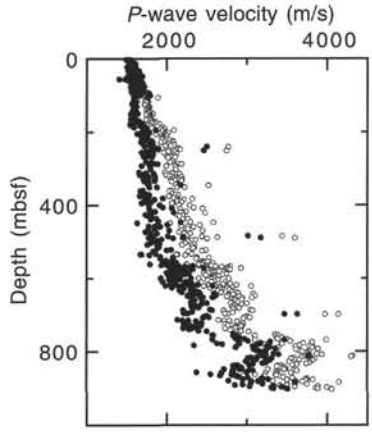

Figure 51. *P*-wave velocities. DSV measurements and Hamilton Frame measurements are marked by solid circles. Open symbols refer to depth-corrected values. Below 800 mbsf, this depth correction is too large (see text).

Table 22. Index properties measured at discrete intervals for Site 998.

Core, section, interval (cm)	Depth (mbsf)	Water content (bulk wt%)	Water content (dry wt%)	Bulk density (g/cm^3)	Grain density (g/cm^3)	Dry density (g/cm^3)	Porosity (%)
165-998A-							
1H-1, 30–32	0.30	52.24	109.40	1.53	2.83	0.73	78.11
1H-1, 115–117	1.11	54.43	119.43	1.47	2.73	0.67	78.32
1H-2, 30–32	1.80	51.02	104.15	1.53	2.68	0.75	76.01
1H-2, 110–112	2.60	49.01	96.10	1.56	2.72	0.80	74.71
1H-3, 30–32	3.30	47.36	89.98	1.57	2.68	0.82	72.39
1H-4, 30–32	4.80	50.03	100.12	1.53	2.67	0.76	74.61
1H-5, 30–32	6.30	48.59	94.51	1.56	2.71	0.80	73.94
1H-6, 30–32	7.80	48.15	92.86	1.59	2.79	0.83	74.93
2H-1, 30–32	9.10	46.16	85.72	1.60	2.80	0.86	71.91
2H-2, 29–31	10.60	46.08	85.44	1.59	2.67	0.86	71.38

Only part of this table is produced here. The entire table appears on CD-ROM (back pocket).

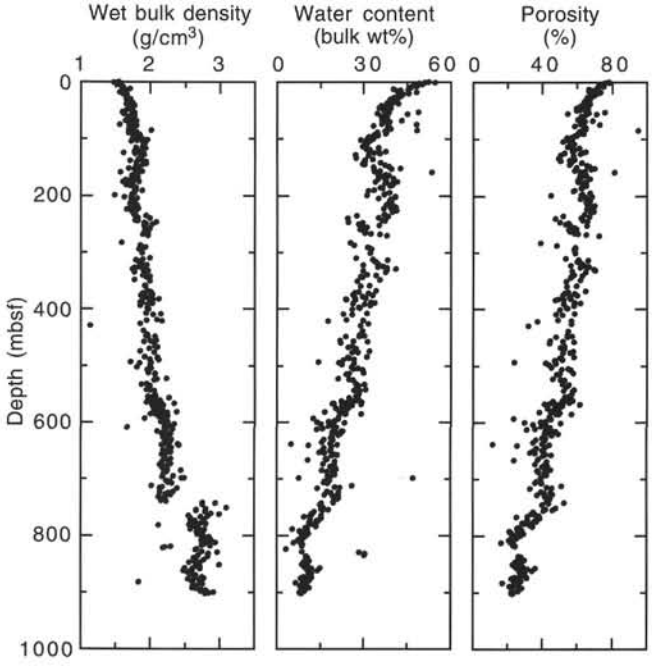

Figure 52. Wet bulk density, water content, and porosity vs. depth.

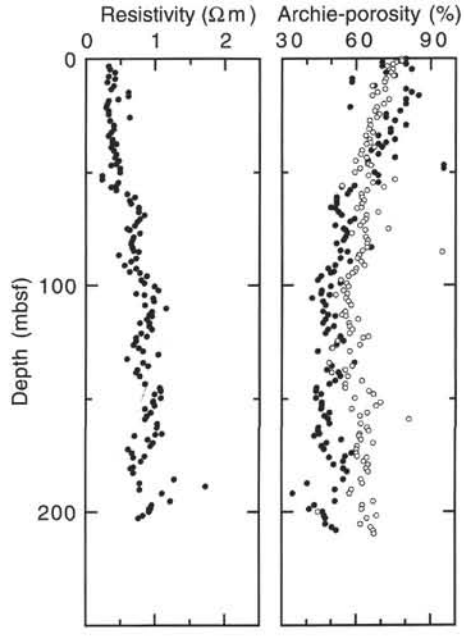

Figure 53. Electrical resistivity vs. depth and a comparison of Archie porosity (solid circles) and index property porosity (open circles).

Table 23. Electrical resistivity measured at discrete intervals for Hole 998A.

Core, section, interval (cm)	Depth (mbsf)	Resistivity (Ωm)
165-998A-		
1H-3, 30–32	3.295	0.323
1H-4, 30–32	4.802	0.342
1H-5, 30–32	6.302	0.418
1H-6, 30–32	7.802	0.323
2H-1, 30–32	9.101	0.418
2H-2, 30–32	10.60	0.304
2H-3, 31–33	12.11	0.399
2H-4, 30–32	13.60	0.361
2H-5, 31–33	15.11	0.608
2H-6, 30–32	16.60	0.608

Only part of this table is produced here. The entire table appears on CD-ROM (back pocket).

Table 24. Undrained and residual shear strength from miniature vane shear measurements for Site 998.

Core, section, interval (cm)	Depth (mbsf)	Undrained shear strength (kPa)	Residual shear strength (kPa)
165-998A-			
1H-1, 111–111.2	1.11	2.1	0.4
1H-2, 30.1–30.2	1.804	2.3	0.7
1H-3, 31–31.2	3.311	3.8	1.2
1H-4, 31–31.3	4.812	1.9	2.5
1H-5, 31–31.2	6.311	3.3	1.1
1H-6, 31–31.1	7.81	3.6	0.6
2H-1, 31–31.2	9.111	2.7	0.7
2H-2, 31–31.1	10.61	3.8	0.6
2H-3, 31–31.1	12.11	8.3	0.8
2H-4, 31.1–31.2	13.611	3.5	4.7

Only part of this table is produced here. The entire table appears on CD-ROM (back pocket).

Logging Units

Five logging units were identified in Hole 998B (Figs. 55, 56, 57) based on log response and analyses of recovered cores; these should not be confused with the lithologic units defined earlier (see "Lithostratigraphy" section, this chapter). The boundaries between adjacent logging units were placed at significant inflection points resulting from simultaneous variations on at least several of the logs (Figs. 55, 56, 57). These units display consistent log responses or distinct overall trends.

Core recovery was relatively high throughout the logged interval (average recovery = 69.1%). The lithologies for unrecovered intervals can be inferred from the logs based on the broad assumption that

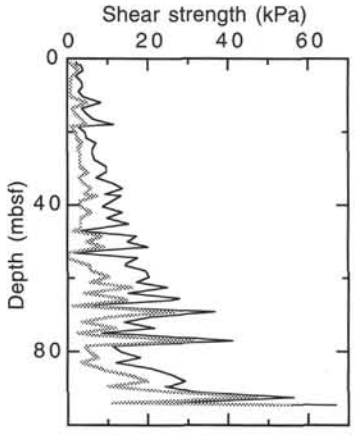

Figure 54. Undrained shear strength (solid line) and residual shear strength (shaded line) vs. depth.

the logging tools respond to varying proportions of the primary constituents in samples actually recovered (e.g., carbonate, pelagic clay, volcanic ash, altered volcanogenic material, biogenic silica) and to their relative porosity.

Logging Unit 1 (180–280 mbsf)

Logging Unit 1 is distinguished by the relatively high and extremely variable concentrations of potassium, uranium, and thorium; the relatively high and variable aluminum concentrations; and the relatively low and variable photoelectric effect (PEF) values. Concentrations of potassium, uranium, and thorium covary with aluminum concentrations, and maxima in these four elements correspond to large minima in PEF values. This unit is also characterized by the lowest average sonic velocity (1.927 km/s) and bulk density (1.7 g/cm^3) and an interval of relatively low resistivity (<1 Ωm) from 204 to 228 mbsf, followed by an interval where resistivities are uniformly above 1 Ωm (FMS and SFL) extending to the bottom of logging Unit 1. The lower boundary of this unit, at 280 mbsf, is marked by the change to higher and less variable values for PEF, lower aluminum concentrations, a decrease in the frequency of extreme gamma-ray maxima (i.e., K, Th, U), and slight increases in velocity, density and resistivity accompanied by a subtle shift to lower values of the lithology indicator ratio (LIR) [Si/(Si+Ca)]. The LIR is used to assess the relative amounts of carbonate and silica. Decreases in LIR suggest a relative increase in carbonate (decrease in silica) below 280 mbsf (Fig. 56). The iron indicator ratio (IIR), Fe/(Si+Ca), is used to identify iron-rich clay intervals. The IIR remains relatively low and constant throughout much of the logged section, suggesting little change in concentrations of altered (clay) volcanogenic material.

The extreme variability and general trends in logging responses appear to correlate with the presence of abundant and distinct "fresh" volcanic ash fall layers within nannofossil chalk ("Lithostratigraphy" section, this chapter). The logging response indicates that the contribution of volcanic ash is greatest in the interval above 280 mbsf (logging Unit 1), which agrees with the reported increase in number of ash beds per core at this depth ("Igneous Petrology and Volcanology" section, this volume).

Logging Unit 2 (280–540 mbsf)

Logging Unit 2 is characterized by an interval of nearly constant velocity (~2.0 km/s) and relatively low resistivity (<1 Ωm) from 280 to 340 mbsf followed by a subtle but distinct increase in velocity (2.2 km/s) and an interval of relatively high resistivity (>1 Ωm) from 340 to 360 mbsf. Below 340 mbsf, there is a very gradual and uniform increase in velocities (2.2–2.4 km/s) and densities (~1.75–2.0 g/cm^3), and uniformly low resistivities (0.92–0.94 Ωm), aluminum concentrations, and total gamma-ray counts (<10 API). The PEF values are higher and less variable than those observed in logging Unit 1. The above logging response is associated with the least variable and highest carbonate concentrations in the entire logged interval ("Lithostratigraphy" section, this chapter). A marked change in sediment mass accumulation rates near the Oligocene/Miocene boundary corresponds to the change in velocity at 340 mbsf.

The top of logging Unit 2 down to 340–360 mbsf is also distinguished by the continuation of the elevated and highly variable gamma-ray counts that characterized logging Unit 1. Potassium, thorium, and uranium all exhibit extreme variations in concentration down to 310 mbsf, at which depth concentrations become uniformly low and are punctuated only by maxima in the Th/U value. Thorium concentrations in volcanic ash are typically high relative to uranium and potassium; therefore, increases in Th/U can be used to discriminate ash layers from nonvolcanogenic clays (Fig. 57). The logging response at the top of logging Unit 2 argues for continued but increasingly less frequent volcanic ash layers downhole. The isolated maxima in thorium, uranium, and aluminum concentrations and minima in PEF occurring at 305–308 and 358 mbsf indicate ash layers. These anomalies are notable because they illustrate the utility of logging response for examining nonrecovered intervals or for placing distinct horizons in their correct stratigraphic position within partially recovered cores.

Logging Unit 3 (540–782 mbsf)

Logging Subunit 3A (540–670 mbsf)

The boundary between logging Unit 2 and Subunit 3A is defined by a distinct and consistent rise in the rate of downhole increases in velocity, density, and resistivity (i.e., a change in slope on these logs). Gamma-ray counts remain generally low (<10 API) with episodic maxima occurring in the Th/U value. For example, several large maxima in Th/U occur between 571 and 581 mbsf where numerous ash layers were recovered ("Igneous Petrology and Volcanology" section, this chapter). Interestingly, there are no corresponding excursions in the PEF or aluminum values at this depth.

The abrupt covarying decrease in velocity, density, and increase in resistivity at 540 mbsf is caused by an enlargement of the borehole to a diameter of over 18 in (see caliper log, Fig. 55) and is not a criterium used to place the upper boundary of logging Subunit 3A. Maximum values for density (2.2 g/cm^3), resistivity (2 Ωm), and PEF are attained near the base of this logging unit at approximately 650 mbsf, and velocity reaches a maximum (~2.85 km/s) at the base of logging Subunit 3A (670 mbsf).

The general trends in logging data within this unit correlate to a consistent decrease in carbonate concentration, increased lithification (decrease porosity), and a uniformly low ash component. The absolute maximum values in resistivity, density, and velocity in Subunit 3A from 650 to 670 mbsf, followed by nearly constant values for these logs down to approximately 750 mbsf, correlates to the final transition from chalk to limestone within lithologic Unit III ("Lithostratigraphy" section, this volume).

Logging Subunit 3B (670–782 mbsf)

Logging Subunit 3B is characterized by a small unidirectional shift to uniformly lower velocity (2.75–2.80 km/s), density (2.1 g/cm^3), and resistivity values (1.7 Ωm) from 670 to 740 mbsf. This interval is punctuated by a distinct anomaly recorded by all the logs at 702 mbsf. The caliper log indicates a change to smaller hole diameter (12 in) at this depth, which rapidly enlarges to 18 in just below this level. The anomaly is defined by maxima in potassium, Th/U, resistivity, aluminum, Si/(Si+Ca), and Fe/(Si+Ca) and a minimum PEF value (Figs. 55, 56, 57). The sonic and density logs display a sinusoidal anomaly (relative minima followed by maxima). This anomaly probably correlates to several thick (30 cm), altered volcanic ash layers (see core descriptions in Section 4) recovered within Core 165-998B-15R. At approximately 740–750 mbsf, a rapid increase in velocity, resistivity, and density occurs. Velocity levels off from 750 to 782 mbsf, whereas re-

Table 25. Time schedule (UTC) for logging operations at Hole 998B, including a listing of the tools used during each logging run.

Time (UTC)	Activity
2–3 Jan 1996	
0030	Last core on deck Hole 998B. Begin wiper trip. Drop bit. Raise pipe to 200.3 mbsf.
1100	Make up cable. Quad combo assembled and prepared for logging.
1200	Run in hole with Quad combo (TLT/DIT/HLDT/CNT/SDT/NGT/TCC/LEH-QT).
1330	Begin pass 1 (904.8–25.8 mbsf). Drillers pull pipe up 28 m to 172.3 mbsf. Repeat 91-m section (309.3–218.3 mbsf).
1745	Quad combo pulled out of drill string.
1945	Quad combo disassembled and removed from rig floor.
1945	GLT assembled and prepared for logging.
2030	GLT lowered into the drill string.
0145	Begin pass 1 (904.7–157.3 mbsf). Drillers pull pipe up 28 m. Repeat 95-m section between (327.3–232.3 mbsf).
0500	GLT pulled out of drill string.
0630	GLT disassembled and removed from rig floor.
0630	FMS assembled and prepared for logging.
0715	RIH with FMS. Obstruction encountered (430.3 mbsf). Not able to penetrate borehole any further.
0900	Begin FMS pass 1 (420–294.5 mbsf). When WHC stops compensating, restart WHC and continue logging pass 2 (327.5–197 mbsf). Pull pipe up 28 m. Run full repeat section (425–192 mbsf).
1215	FMS pulled out of drill string.
1330	FMS disassembled and removed from rig floor.
1330	GHMT assembled and prepared for logging.
1415	RIH with GHMT. Obstruction encountered (430.3 mbsf). Attempt to penetrate obstruction at (430.3 mbsf). No success.
1545	Begin GHMT pass 1 (425.3–202.8 mbsf). Run full repeat section (426.4–205.8 mbsf).
1730	GHMT pulled out of the drill string.
1900	GHMT disassembled and removed from rig floor.
2000	End logging operations.

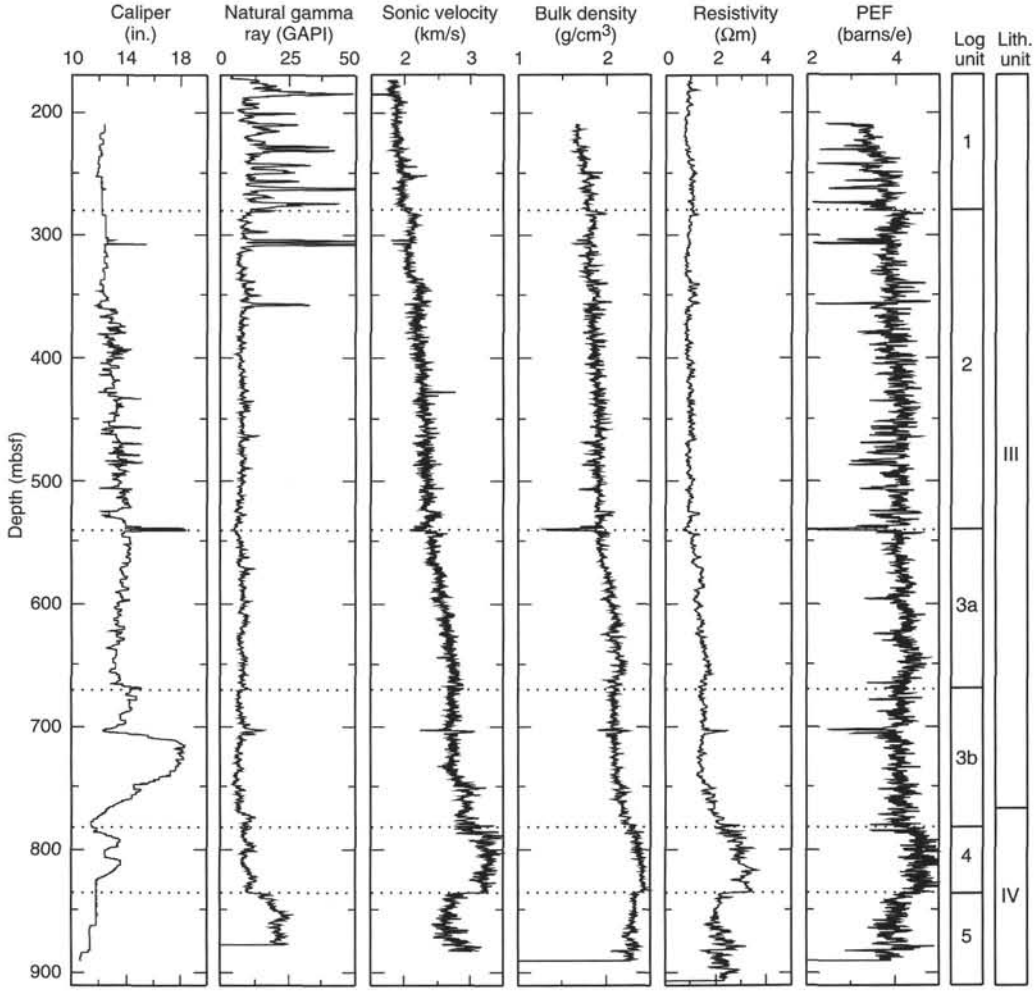

Figure 55. Selected downhole logs from the Quad combo tool string for Hole 998B: caliper, total gamma ray, sonic velocity, bulk density, resistivity, and photoelectric effect (PEF). Depth intervals of logging units are marked by dotted lines. Sonic velocity, resistivity, and density reflect the porosity of the formation and therefore the degree of lithification or cementation. In general, sections with high concentrations of volcanogenic material correspond to relative minima in velocity, density, resistivity, PEF, and maxima in gamma ray.

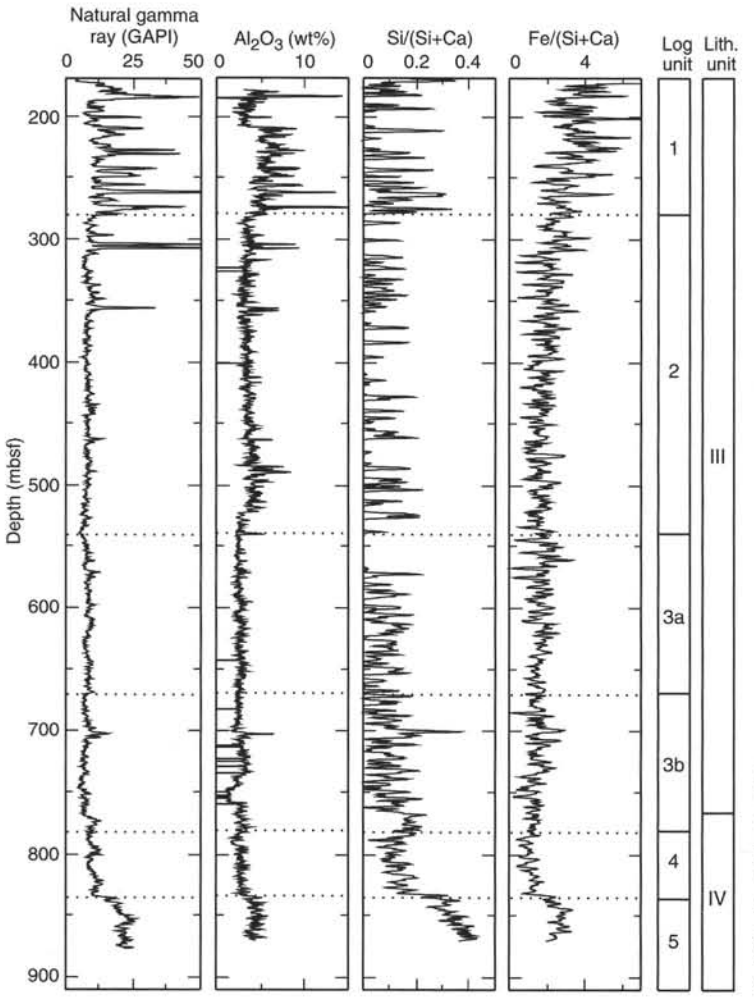

Figure 56. Selected downhole logs from the geochemical tool string for Hole 998B: total gamma ray, Al_2O_3, and Si/(Si+Ca) and Fe/(Si+Ca), known as the lithology indicator ratio (LIR) and iron indicator ratio (IIR), respectively. Depth intervals of logging units are marked by dotted lines. The relative abundances of the elements Ca, Si, Al, and Fe serve to identify the primary constituents that distinguish the major lithologies recovered from Holes 998A and 998B (e.g., carbonate, pelagic clay, and volcanogenic material including clay).

sistivity and density continue to increase over this interval. In addition, Si/(Si+Ca) and Fe/(Si+Ca) ratios and aluminum concentrations steadily increase from 750 mbsf to the base of logging Subunit 3B (782 mbsf), and gamma-ray counts abruptly increase at 770 mbsf and remain relatively high.

The logging response from 740 to 782 mbsf characterizes the boundary chosen for lithologic Unit III to Unit IV at 766 mbsf and indicates a transition in dominant lithologies occurring over tens of meters. This interval broadly corresponds to the reported change in lithology from limestone to limestone with turbidites and altered volcanic ash in turbidites with altered volcanic ash that defines lithologic Unit IV ("Lithostratigraphy" section, this chapter).

Logging Unit 4 (782–835 mbsf)

A dramatic and distinct logging response marks the top of logging Unit 4. Covarying step increases in velocity, density, resistivity, and PEF occur at 782 mbsf and these properties remain consistently high throughout Unit 4. The absolute maximum values of velocity (3.2 km/s), density (2.4 g/cm^3), resistivity (3.5 Ωm), and PEF (5 barns/e) within the entire logged interval are recorded in Unit 4. Covarying decreases in Si/(Si+Ca) and Fe/(Si+Ca) values and aluminum concentrations also characterize this unit. Maxima in Th/U near the top of this unit indicate that discrete altered ash layers are still present. This distinct logging response correlates to much more indurated calcareous limestone with turbidites and altered ashes with lower volcanogenic components than the immediately surrounding intervals.

Logging Unit 5 (835 to >880 mbsf)

Logging Unit 5 extends from 835 mbsf to the total depth for logging operations at Site 998, which typically were initiated at 880 mbsf. Logging Unit 5 is defined by abrupt increases in gamma-ray counts (primarily from potassium and thorium), aluminum, Si/(Si+Ca), and Fe/(Si+Ca), all of which remain uniformly high throughout this interval. Logging Unit 5 is also marked by a sharp decrease in velocity (2.7 km/s), density (2.3 g/cm^3), resistivity (2.4 Ωm), and PEF (<4.0 barns/e).

These dramatic logging responses correlate to an increase in porosity (less lithified), a marked increase in volcanic ash turbidites and altered volcanic ash (as opposed to "fresh" discrete ash layers), and a decreasing carbonate concentration reported for this interval ("Lithostratigraphy" section, this chapter). The sudden change in log character at 835 mbsf is consistent with the observation of marked lithologic change occurring within Core 165-998B-30R.

Acoustic Velocities

The sonic log from Hole 998B was integrated over the depth interval sampled by the LSS tool (180–880 mbsf) to produce a plot of TWT vs. depth (Fig. 58). The seafloor appears at 4.184 s TWT on single-channel seismic Line EW9417-13 ("Underway Geophysics and Pre-Site Surveys" section, "Explanatory Notes" chapter, this volume, and "Seismic Stratigraphy" section, this chapter), and velocities were linearly interpolated between 1.5 km/s at the seafloor to the first log

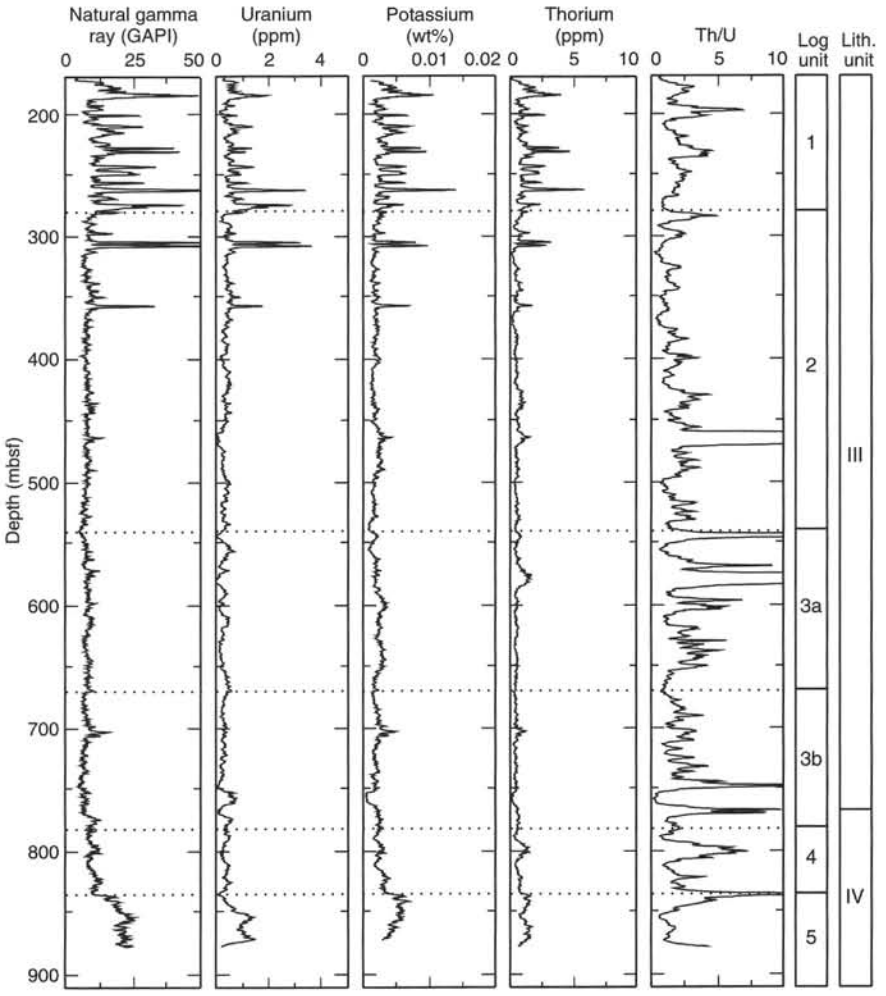

Figure 57. Downhole logs from the natural gamma-ray spectrometry tool on the Quad combo tool string for Hole 998B: total gamma ray, uranium, potassium (wt%), thorium, and thorium-uranium ratio. Depth intervals of logging units are marked by dotted lines. At Site 998, maxima in the above elements and elemental ratios correlate with discrete ash fall layers and other intervals with a relatively high volcanogenic component.

velocity of 1.8 km/s at 180 mbsf. The resultant traveltime vs. depth below seafloor curve (Fig. 58) is used to tie the cored sequences at Site 998 to the seismic reflection data over the site. A summary of these correlations is shown in Figure 64 and is discussed in the "Summary and Conclusions" section (this chapter).

Geological High-Sensitivity Magnetic Tool (GHMT-A)

Total induction and magnetic susceptibility were recorded, respectively, by the scalar magnetometer (NMRS) and the susceptometer (SUMS). A detailed review of these sensors and principles of magnetic logging are provided in the "Explanatory Notes" chapter (this volume). During the time interval that the GHMT-A recorded data, the measured total field and susceptibility logs can be affected by such time-dependent factors as transient variations in the Earth's field and temperature drift. A repeat pass of the GHMT-A tool permitted analysis of the time-dependent components of the borehole magnetic environment that affect the measurement of magnetization of the surrounding formation. The time-invariant components of the measured field (magnetic mineral concentration, remanent magnetization) can then be examined. Post-cruise data processing will further isolate and quantify both time-dependent and time-invariant factors, and may provide results on the orientation of the paleomagnetic field. We discuss the quality of magnetometer and susceptometer data in the following sections.

Total Induction Log

We removed the contribution of the Earth's magnetic field (Br) using the IGRF value of 42,725 nT from the total field B measured

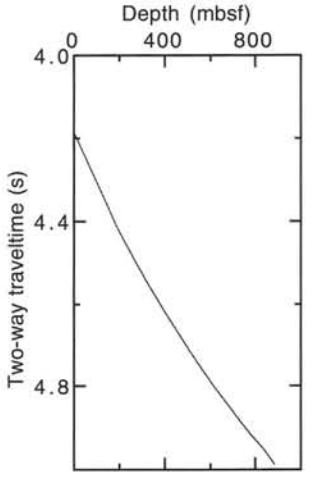

Figure 58. Two-way traveltime vs. depth below seafloor calculated from the long-spaced sonic log in Hole 998B.

by the magnetometer. Figure 59 shows the remaining "local" field for the two runs (B1 and B2), which contains only local effects, that is, $B1(z) = Bf(z) + Ba(z) + Bt1(z,t)$ and $B2(z) = Bf(z) + Ba(z) + Bt2(z,t)$.

Two different magnetic signatures are observed. First, high values are observed between 200 and 300 mbsf for both runs owing to the highly magnetic bottom-hole assembly (BHA). Second, apart from

sharp positive peaks, the data show little magnetic variation downhole, with the average values of the "local" fields B1 and B2 being only slightly lower than zero. The true value of Bf, the magnetization component of the formation, can be obtained by evaluating the anomaly field Ba and the transient fields Bt1 and Bt2.

Analysis of the Components of the Magnetic Induction

Data from the two runs B1 and B2 are quite similar (Fig. 59) and indicate that no significant temporal changes are present in the external Earth's field. The remaining "local" B field for the first run after correction for pipe effect (B1 corrected) is shown on Figure 59. This drill-pipe perturbation can usually be removed, assuming a dipolar effect, and allows for data recovery up to about 10 m beneath the BHA. Only low-frequency variations ($\leq 5 \times 10^{-3}$ Hz, or ≥30 m interval) can affect the recorded values (skin effect) as the measurements were performed under more than 3000 m of conductive seawater. An overall negative value of the remaining "local" field (B1 corrected) is observed, centered around –20 nT.

Analysis of Susceptibility Records

The magnetic susceptibility data in Hole 998B appear to be of good quality (Fig. 60). There is a good correlation between the records, indicating that there were few measurement errors and little thermal drift of the measurement coils. A depth difference of about 1 m is observed between these two runs, which may be the result of the cable stretching during log acquisition. As the core recovery is low in the logged interval (60%), the depth correlation between core susceptibility measurements and logging susceptibility records is not easy, but some correlations can be observed for the strongest susceptibility peaks between both sets of data. Moreover, lab measurements have a finer vertical resolution as a result of the difference in sampling volume that each tool measures. Core data is derived from a small volume of material. In contrast, the GHMT-A's susceptibility sensor integrates a much larger volume of sediment, which lowers resolution (vertical resolution of the tool is related to its depth of investigation).

As magnetic susceptibility and gamma-radiation are both lithologic indicators, it is interesting to compare these two curves (Fig. 60). The correlations between the susceptibility and the gamma-ray measurements are generally because of the proportion of clay minerals. Our data show correlations between these two logs for some of the ash layers present in the cores (e.g., at 255, 263, 273, 306, and 355 mbsf). These correlations are due to the occurrence of clay minerals resulting from the alteration of volcanogenic material.

Comparison of Total Field and Susceptibility Logs

A comparison of the "local" B field, obtained from the first magnetometer run (B1 corrected), with the induced magnetization field (Bfi) is shown in Figure 61. The induced magnetization field is calculated from the susceptibility recorded during the first run using the relation: $Bfi = Br \cdot k \cdot [1–3 \cdot \sin^2(I)]/2$, where k is the susceptibility, and Br and I are the intensity and the inclination of the actual Earth's field, respectively. Bfi corresponds to the susceptibility effect on the total field. These two logs show correlations and anticorrelations that may be prove useful with further post-cruise processing for determining polarity reversals and establishing a magnetostratigraphy for the logged interval.

SUMMARY AND CONCLUSIONS

Site 998 is located on the Cayman Rise, between the Cayman Trough to the south, and the Yucatan Basin to the north. Because of its location, the site provides an opportunity to evaluate paleoceanographic connections between the Caribbean and the Gulf of Mexico throughout much of the Cenozoic, as well as the nature and origin of the Cayman Ridge and Cayman Rise. Lithologic variations in the

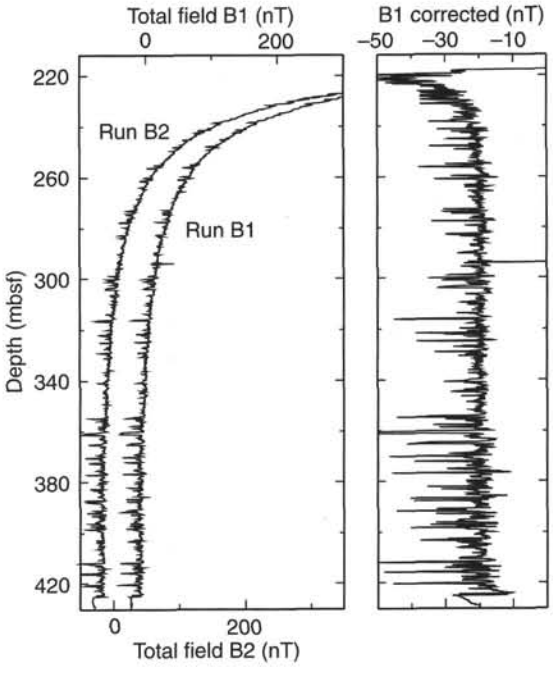

Figure 59. "Local" total magnetic induction for the two runs (B1 and B2) and the resulting induction after correction for pipe effect (B1 corrected). Part of the total induction has been obtained by correcting the total induction for the main dipolar field. The scale shift between runs is 50 nT.

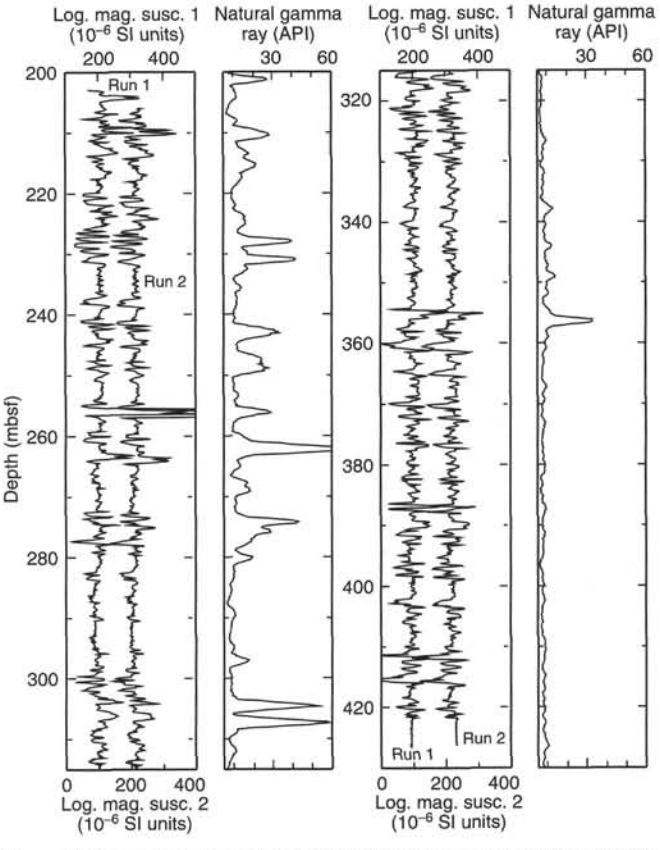

Figure 60. Downhole magnetic susceptibility (two runs shifted by 0.0001 uSI) and natural gamma-ray log for the interval logged by GHMT.

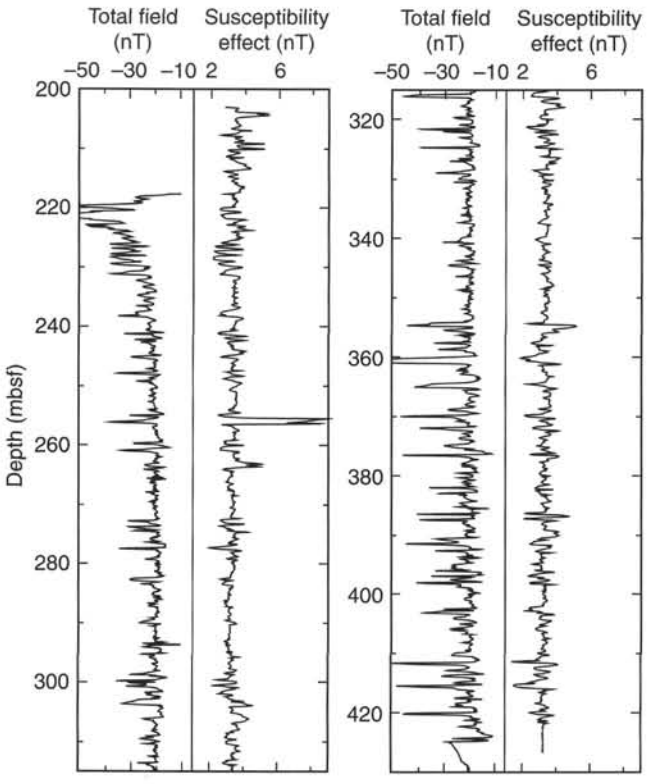

Figure 61. "Local" total induction after correction for pipe effect (B1 corrected) and downhole induction caused by the susceptibility effect.

904.8 m of cored lower Eocene to recent section are the result of input from distinct sedimentary sources (pelagic carbonate and biosiliceous particles, terrigenous clay, and volcanic ash) and varied depositional processes (volcanic ash falls, pelagic and volcaniclastic turbidites, contour currents; Fig. 62).

Two episodes of tectonic and volcanic activity, one during the Miocene and the other during early to middle Eocene times, impart a distinct character to the sedimentary record cored at Site 998. A Miocene interval containing numerous pelagic turbidites and thick ash fall deposits originating from distant silicic volcanoes in Central America separates Pliocene–Pleistocene nannofossil ooze and Oligocene chalk. The lower part of the sequence consists of Eocene chalk and limestone with numerous thin turbidites of redeposited ash from a proximal volcanic arc. A major oceanographic event, the late Miocene carbonate crash, known from the central and eastern equatorial Pacific, is well developed on the Cayman Rise. This event, too, may owe its origin, in part, to changing tectonics in the Central America–Caribbean region.

Turbidite deposition is a major feature of sedimentation at Site 998. Two intervals of turbidite deposition characterize the Eocene–Pleistocene section: (1) a Miocene turbidite maximum, characterized by thick (10–110 cm) pelagic turbidites, derived predominantly from bathyal sources; and (2) a middle–lower Eocene turbidite maximum, characterized by more frequent but thinner deposits of graded foraminiferal and/or radiolarian sands and redeposited volcanic ash and clay. Preliminary benthic foraminiferal evidence suggests that most of the pelagic turbidites examined in the Oligocene–Pleistocene interval originate from bathyal depths. However, two turbidites examined from the upper Miocene contain a size-sorted mixture of neritic and bathyal taxa, suggesting a shallower source (Sections 165-998A-16H-4 and 17H-5; 146.6 and 157.7 mbsf, respectively). The presence of fragments of larger benthic foraminifers suggests a shallow-water origin (carbonate platform?) for some of the Eocene turbidites (e.g., Section 165-998B-5R-CC; 605.2 mbsf), although most of these pelagic and volcaniclastic turbidites also appear to be derived from bathyal sources. Further reworking of sediments by bottom currents is a common feature of the middle Eocene part of the section (upper part of lithologic Unit IV).

Turbidity currents can be triggered in a variety of ways, including seismic activity, redistribution of sedimentary load with changing eustatic sea level, high sedimentation rates and slope instability, and scour by currents and oversteepening of slopes. Given the proximity of the Cayman Rise to the Cayman Trough and the strike-slip fault zone that defines the northern boundary of the Caribbean Plate, it seems likely that the record of turbidite deposition at Site 998 largely reflects regional tectonic activity. For example, an episode of turbidite deposition in mid-Oligocene time coincides with the major reorganization of spreading in the Cayman Trough, when the rift axis jumped westward by about 50 km (Rosencrantz and Sclater, 1986). One of the turbidites from the upper Oligocene (Section 165-998A-42X-3; 390.91 mbsf) contains clasts of mica schist and quartzite. Perfit and Heezen (1978) dredged a diverse suite of rock types along the Cayman Ridge/north wall of the Cayman Trough that included micaceous schists, amphibolites, and gneisses associated with plutonic rocks.

The rate of sedimentation varied by approximately a factor of three through the lower Eocene–Pleistocene section at Site 998. Based on our shipboard biostratigraphy and magnetostratigraphy, the section appears to be nearly complete, with the exception of several suspected minor breaks in the Pliocene–Pleistocene. Silicification of Eocene chalks and limestones was expected, but the characteristic chert horizons thought to be responsible for the middle Eocene A″ seismic reflector are poorly developed in this part of the Caribbean and core recovery was very good. Early to middle Eocene sedimentation rates averaged about 15 m/m.y. during the deposition of mixed volcaniclastic turbidites and carbonates and then increased to 24 m/m.y. during late Eocene through Oligocene time with the deposition of limestone and chalk (Figs. 21, 22). Rates decreased to approximately 16 m/m.y. during early and middle Miocene times of continued chalk deposition. A similar pattern of high carbonate mass accumulation rates in the Oligocene and lower rates in the Miocene has been observed in other tropical regions of the Indo-Pacific and Atlantic (van Andel, et al., 1975; Theyer et al., 1989; Kroenke, Berger, Janecek, et al., 1991; Peterson et al., 1992; Curry, Shackleton, Richter, et al., 1995).

A sharp reduction in sedimentation rates is associated with the carbonate crash in the middle/late Miocene boundary interval at Site 998. This late Neogene event is well documented from the central and eastern equatorial Pacific (e.g., van Andel, et al., 1975; Mayer, Theyer, Thomas, et al., 1985; Lyle et al., 1995). Its prominent development in the northern Caribbean has important tectonic and oceanographic implications including the timing and geographic extent of the event, circulation and the nature of gateways and sills, and water mass source and chemistry. An average sedimentation rate of approximately 8 m/m.y. characterizes the late Miocene deposition of carbonate-poor clays, followed by carbonate recovery with the accumulation of nannofossil ooze and mixed sediments. In the eastern equatorial Pacific, the carbonate crash was followed by an episode of enhanced carbonate and biosiliceous productivity (Farrell et al., 1995; Pisias et al., 1995). A marked increase in carbonate mass accumulation rates also occurs widely in the tropical Indo-Pacific region at this time (e.g., Peterson et al., 1992; Berger et al., 1993; Farrell et al., 1995) and is also subtly recorded on the Ceara Rise in the western equatorial Atlantic (Curry, Shackleton, Richter, et al., 1995). At Site 998, a marked recovery in carbonate mass accumulation rates did not occur until about 5.5 Ma (Figs. 23, 24). Nannofossil ooze has been the dominant sediment at Site 998 since latest Miocene time and has accumulated at an average rate of nearly 19 m/m.y.

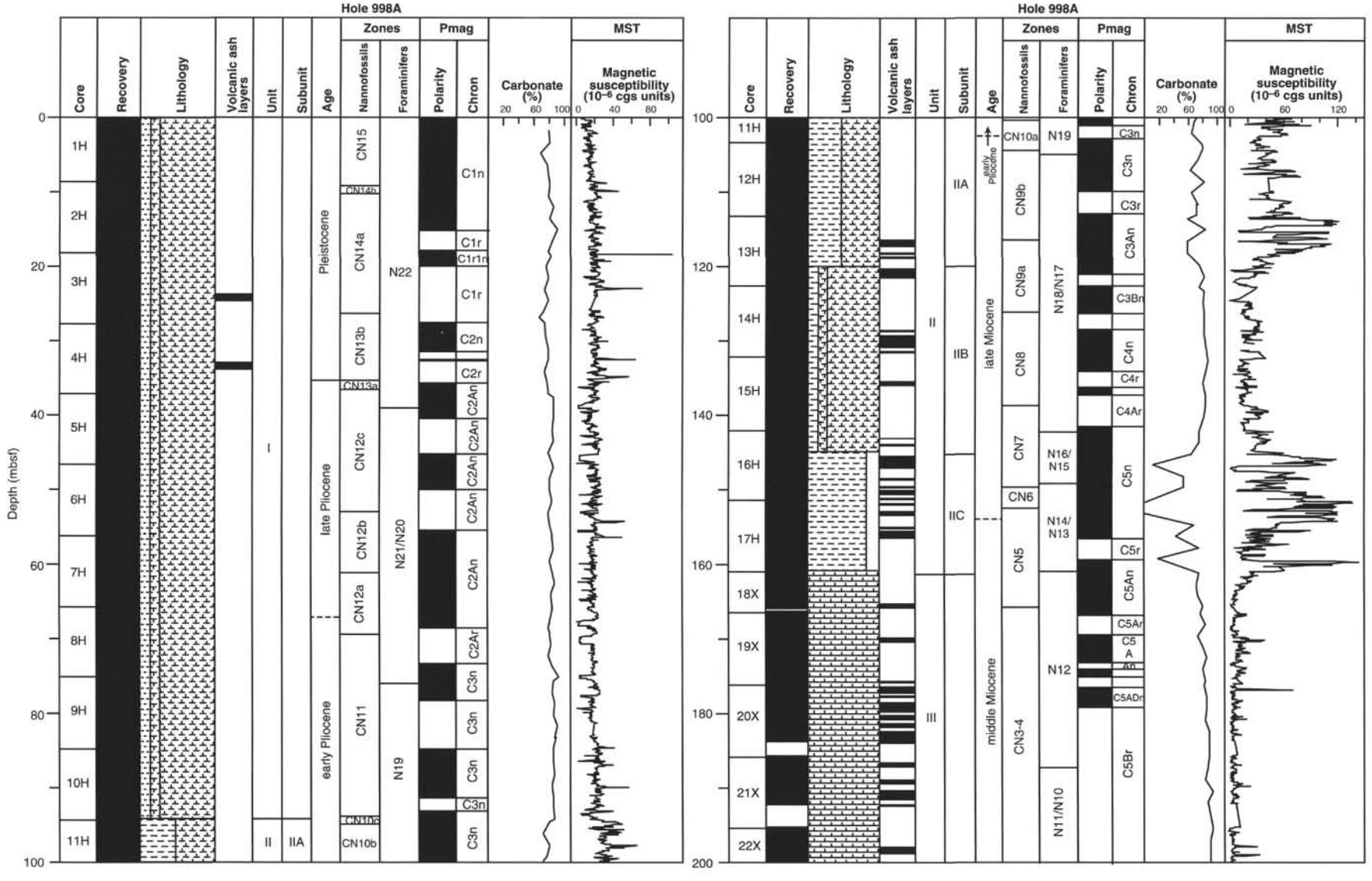

Figure 62. Site 998 summary column for core recovery, lithology, volcanic ash layer occurrence, lithologic unit and subunit boundaries, ages, nannofossil and foraminifer datum boundaries, magnetic reversal boundaries with interpreted chron correlations, carbonate percentages, MST magnetic susceptibilities, and, for Hole 998B, *P*-wave velocities from downhole measurements.

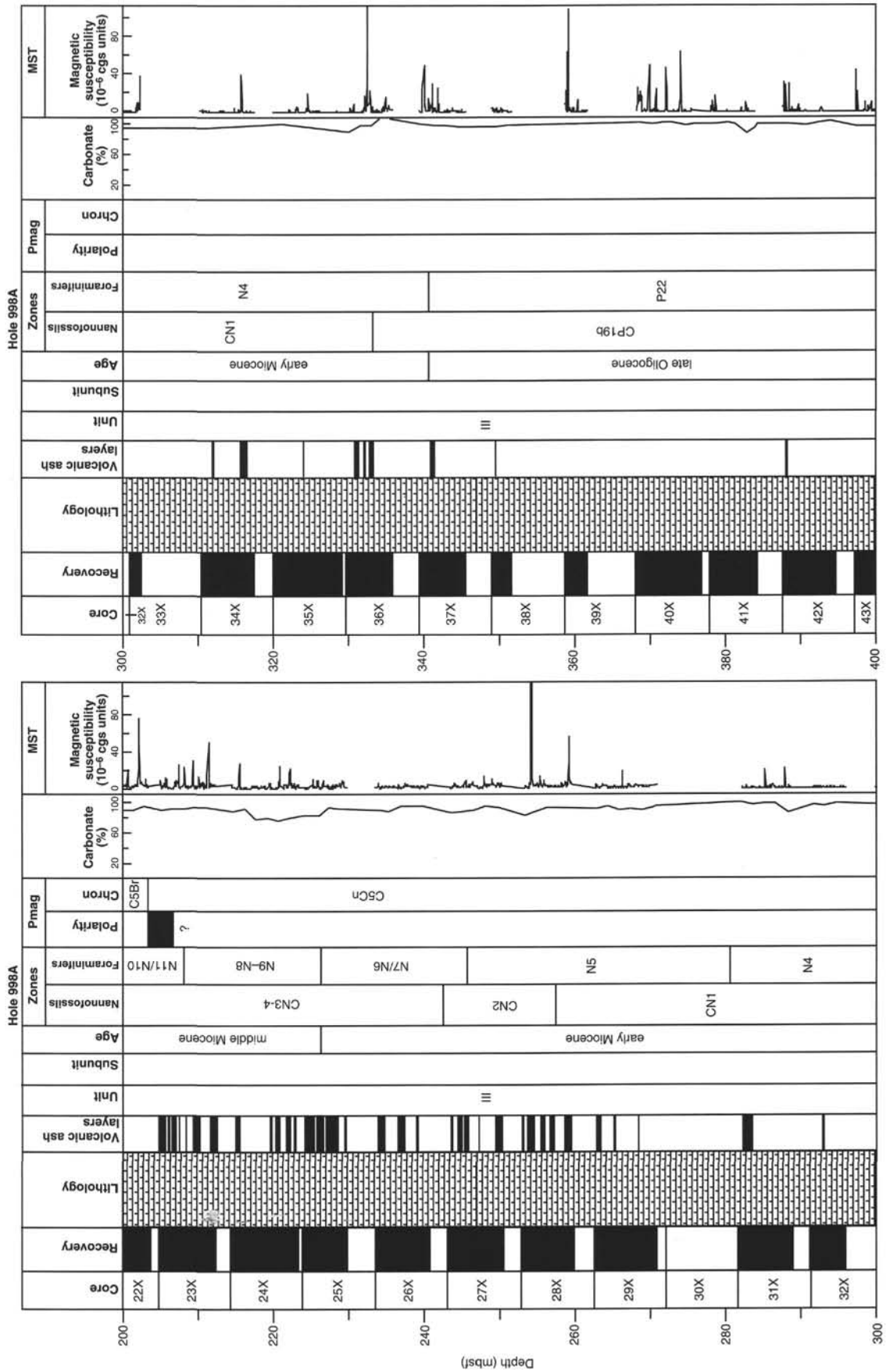

Figure 62 (continued).

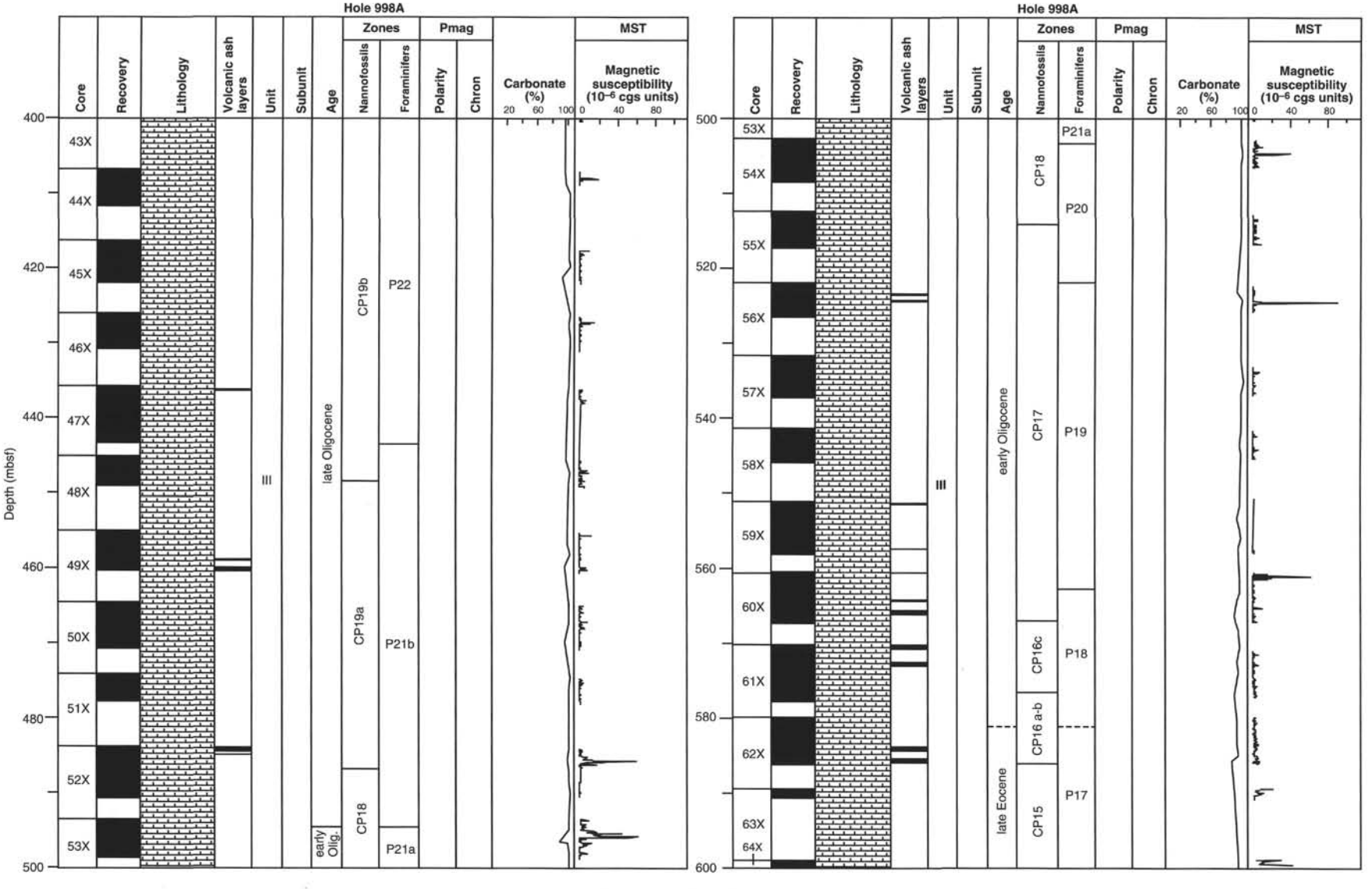

Figure 62 (continued).

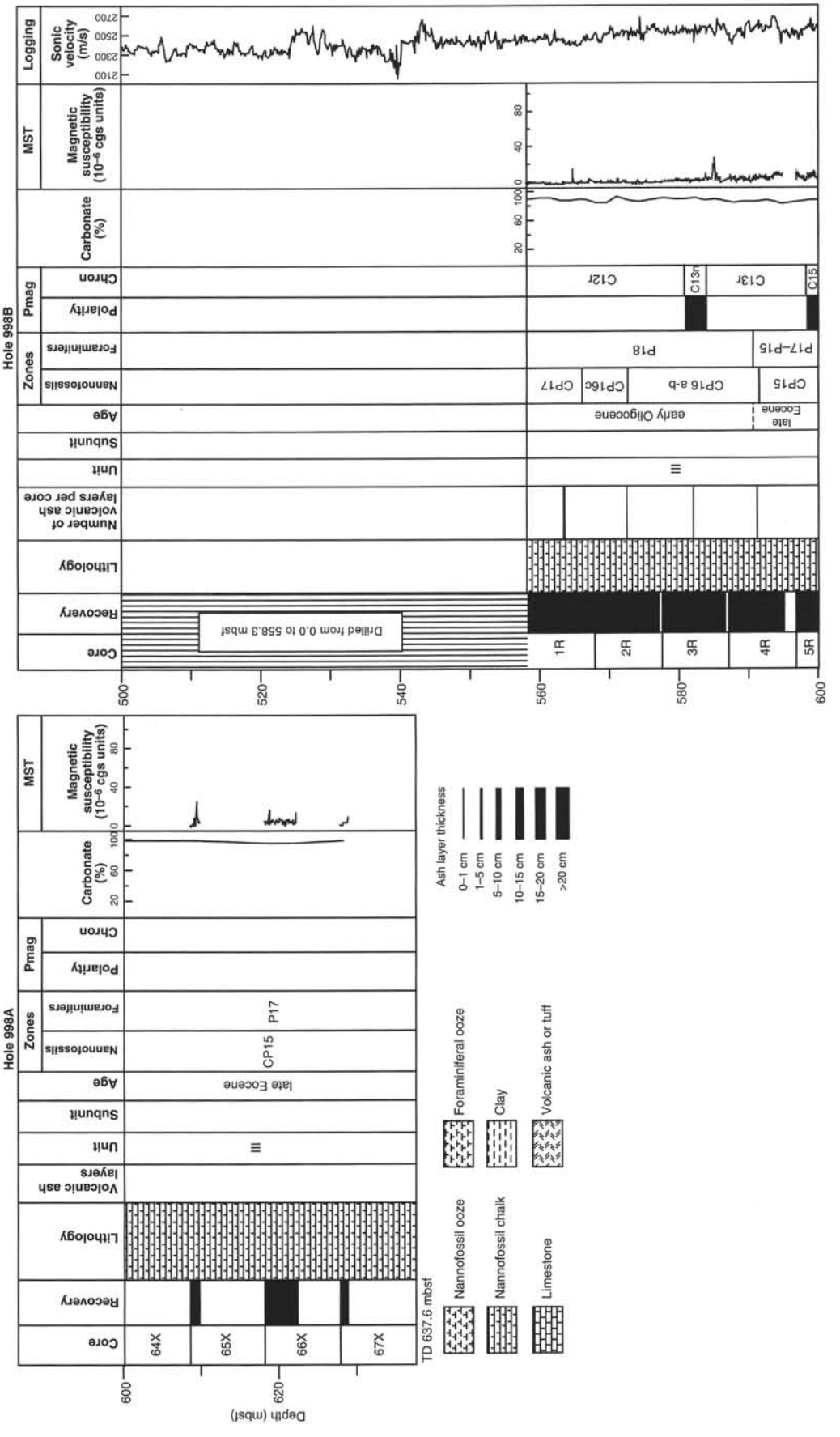

Figure 62 (continued).

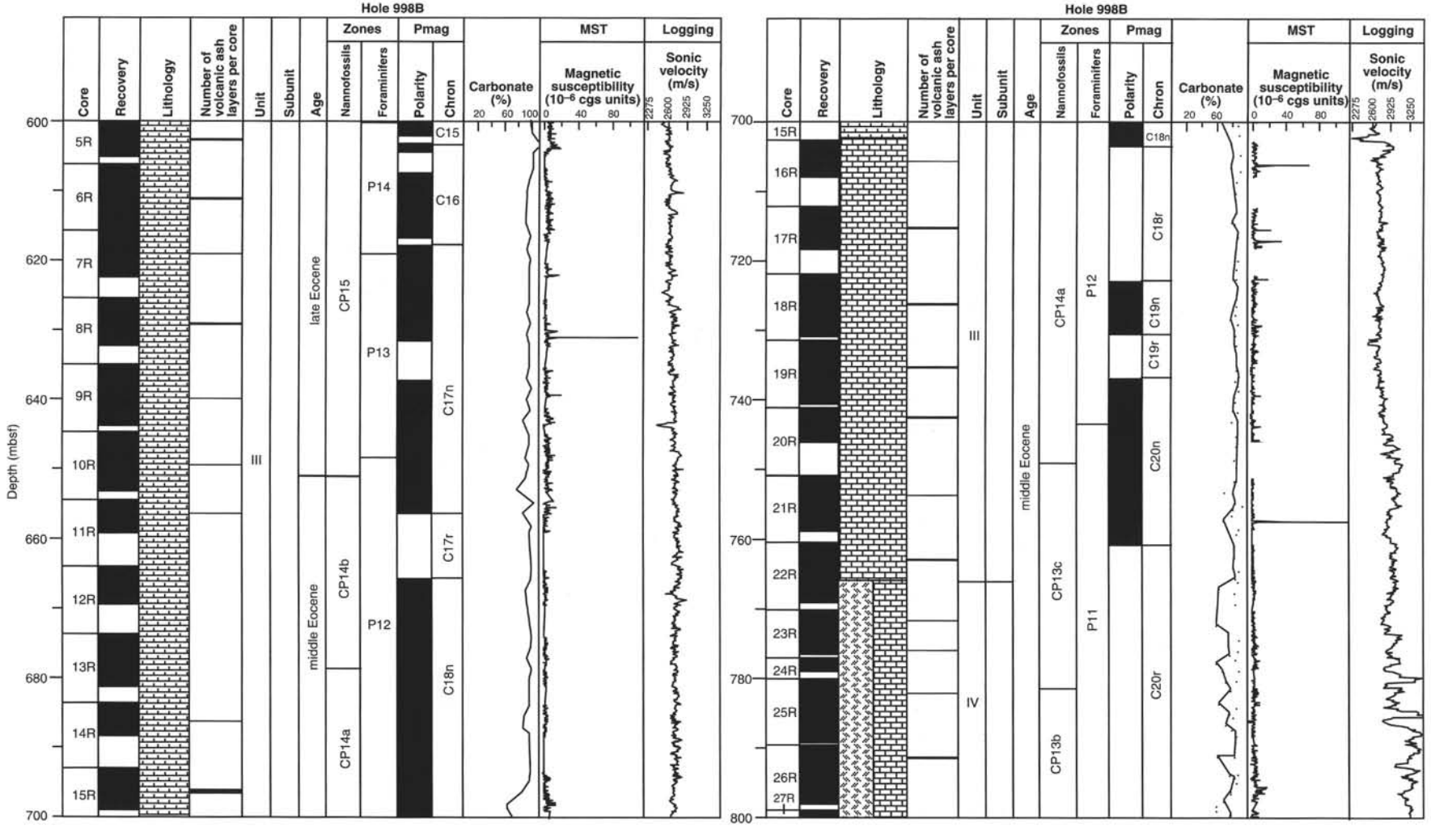

Figure 62 (continued).

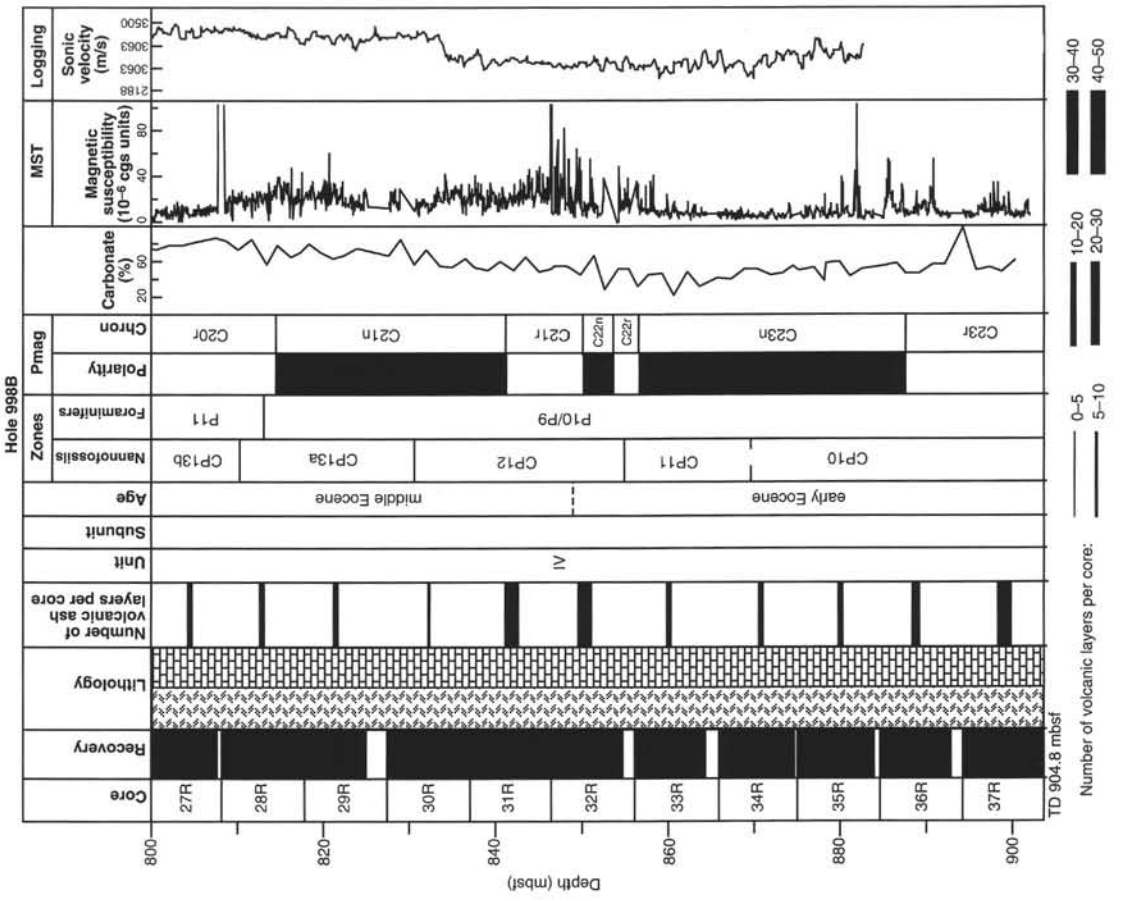

Figure 62 (continued).

An unexpected amount of volcaniclastic sediment was recovered at Site 998, especially in the Miocene and Eocene. The volcaniclastic material is present as three components: discrete ash fallout layers, volcaniclastic turbidites, and dispersed ash. Although highly conspicuous, the ash fallout and turbidite layers represent only about 2% of the total drilled section, whereas the dispersed ash material, which is observed in smear slides and quantified on the basis of sediment geochemistry (see "Inorganic Geochemistry" section, this chapter), represents about 7%–10% of the total sediment at this site (Fig. 62). This volcanic component has had a major impact on both the sediment geochemistry and interstitial water chemistry at this site, as discussed below.

The volcaniclastic material indicates that two prominent episodes of volcanism are recorded at Site 998. One of these is during the Miocene, when a number of thick and discrete silicic ash fallout layers were deposited ("Igneous Petrology and Volcanology" section, this chapter). These massive layers have all the petrographic and chemical characteristics of distal co-ignimbrite ash fallout from large ignimbrite-forming eruptions (Fig. 63). Their source is most likely to be found in the major episode of Miocene silicic volcanism in Central America, principally in Guatemala, Honduras, El Salvador, and Nicaragua, where the ignimbrites on land represent an up to 2-km-thick formation (Reynolds, 1980; Weyl, 1980). On the basis of the biostratigraphic record, the Miocene volcanic episode observed at Site 998 begins at about 20 Ma and terminates by 7 Ma with two pulses of activity about 19–14 Ma and 10 Ma (Fig. 45). In Central America, the initiation of the Miocene ignimbrite episode has been dated by the K/Ar method at 19 Ma, with vigorous activity persisting to less than 10 Ma (Donnelly et al., 1990).

The discovery of Eocene ash fallout layers and associated volcaniclastic turbidites at Site 998 has important implications for the origin and evolution of the Cayman Ridge. Taken together, these types of volcaniclastic deposits indicate a relatively local, and at least in part subaerial, volcanic source, whereas the petrography and geochemistry supports an arc source. The stratigraphic distribution of Eocene ash layers indicates that the rate of local island arc volcanism increases downhole into the lower Eocene (Fig. 45), and most likely extends at least into the Paleocene in this region. Thus, it is likely that the seismic reflector, which we identify as basement at a depth between 1100 and 1130 mbsf at this site (see "Seismic Stratigraphy" section, this chapter), represents volcanic rocks overlain by interbedded volcaniclastics and pelagic-hemipelagic sediments. Support for a volcanic arc origin of the Cayman Ridge comes from both geophysical studies and dredging (Bowin, 1968; Perfit and Heezen, 1978).

The tectonic and petrogenetic model that best fits the evidence from Site 998 and dredging from the north wall of the Cayman Trough indicates an arc origin for the Cayman Ridge, with subaerial volcanic islands present into the Eocene (Fig. 63). If the Yucatan Basin is formed by backarc spreading (Hall and Yeung, 1980; Pindell and Barrett, 1990), then the age relations indicate that its spreading occurred behind the Cayman arc, as the Cuban arc was already extinct at this time (Iturralde-Vinent, 1994). The fundamental question regarding the Cayman arc relates to its polarity of subduction. Its relationship to the Yucatan Basin would support a north-dipping subduction zone, due to the subduction of the leading edge of the Caribbean Plate. We hypothesize that when the thicker portion (oceanic plateau) of this plate choked off the Cayman subduction zone in the middle Eocene, the plate motion along this boundary changed to one of strike-slip, with the formation of the Cayman Trough. Before the cessation of subduction and volcanic activity, the occurrence of volcaniclastic turbidites and ash fallout indicates subaerial volcanic sources on the arc. Subsidence of the Cayman Ridge and Cayman Rise must have occurred, therefore, during the post-middle Eocene. This is generally consistent with the proposal of Wadge and Burke (1983) that subsidence to abyssal depths of at least the volcanic sources occurred in the Oligocene.

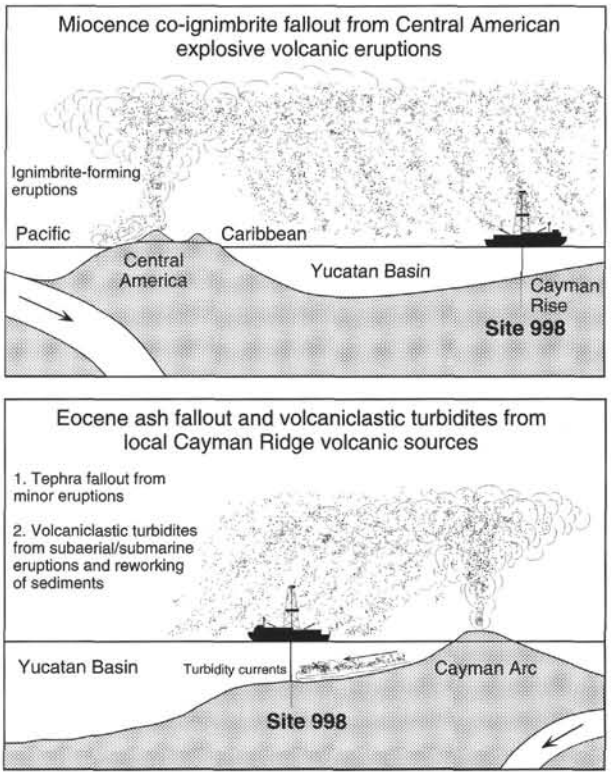

Figure 63. Schematic cross-section of the tectonic setting of the Cayman Rise in the middle Miocene and Eocene. Ash transport to Site 998 was by ash fallout from distal sources and ash turbidite transport from a local source.

The geochemistry of the volcanic ash layers, interstitial waters, and sediments at Site 998 is interwoven in a complex manner, largely driven by the alteration of volcanic glass in the tephra layers and dispersed tephra to smectite. The dominant effect of this process is to deplete the ash in silica and potassium and enrich it to a high degree in MgO and Al_2O_3. The uptake of magnesium is accompanied by enrichment of nickel in the smectite by two orders of magnitude above that in fresh rhyolitic glass, or up to levels of 300 ppm. This unusual enrichment of nickel must be attributed to uptake from seawater and interstitial fluids in the sediment, implying an extremely high water-rock ratio in the smectite-forming reaction. Concomitant with these enrichments is a depletion in the ash of leachable components, including K, Rb, and Si. This is matched in a remarkable manner by their enrichment in the interstitial pore waters at the site, with the peak in pore-water concentration of these constituents coinciding with the peak accumulations of volcanic ash downcore. The sediment geochemistry shows that the background sediment contains a high dispersed ash component, typically on the order of 7% of the total sediment (Fig. 34). In addition, the discrete volcanic ash layers at the site constitute at least 2% of the total sediment. Thus, volcaniclastic sedimentation is about one tenth of the total sediment thickness.

Downhole measurements of both physical properties and geochemical parameters in Hole 998B reveal two zones with unusual characteristics that correlate well with the abundance of volcaniclastic material in the sediment. For example, logging Unit 1 (180–280 mbsf) shows extremely variable concentrations of Th, K, U, and Al, which are consistent with the high abundance of early to middle Miocene volcanic ash fallout layers in this unit (Fig. 64). Similarly, in logging Unit 5 (835–880 mbsf), there is an abrupt increase in K and Th, as well as in silica and iron, which corresponds to a great increase in the abundance of early to middle Eocene volcaniclastic turbidites and ash fallout layers at this level (Fig. 65).

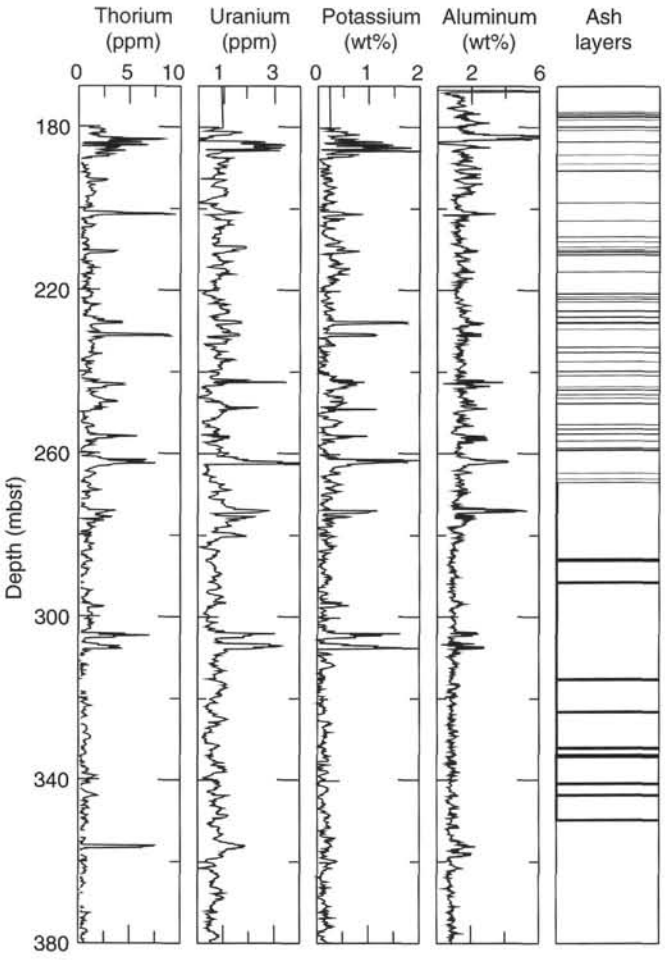

Figure 64. Comparison of ash layer occurrence with Th, U, K, and Al logs from the upper to middle part of Hole 998B.

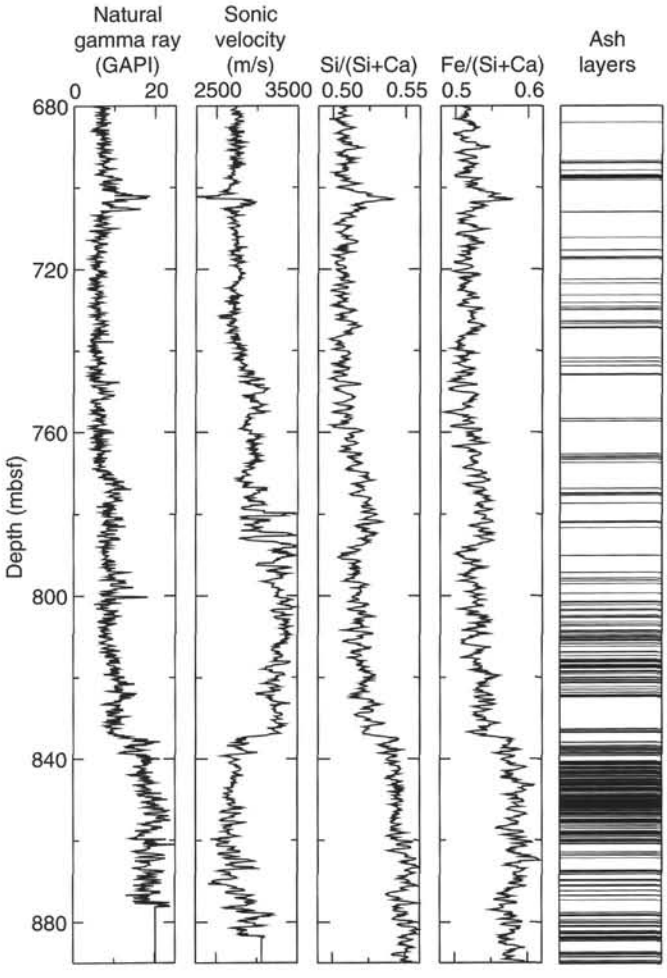

Figure 65. Comparison of ash layer occurrence with natural gamma-ray counts, sonic velocity, lithology indicator ratio, and iron indicator ratio logs for the lower part of Hole 998B.

A plot of TWT vs. depth below seafloor (Fig. 58) was used to tie the cored section at Site 998 to seismic reflection data over the site. Because reflectors apparent on the seismic records may result from interference patterns owing to the impedance effects of many thin beds, our interpretations are tentative (Fig. 66). More detailed correlations will be done post cruise using synthetic seismograms.

The acoustic basement reflection at 5.15 s TWT is interpreted as the top of a volcanic arc of unknown age (volcanic basement). Within the region surveyed during EW9417, volcanic basement displays irregular relief and varies in depth by approximately 300 m over a 3 km range in the immediate vicinity of Site 998 ("Seismic Stratigraphy" section, this chapter). The total depth at Hole 998B of 904.8 mbsf corresponds to 5.0 s TWT, approximately 210 m above volcanic basement if average velocities recorded at the bottom of the hole are extended to 5.15 s TWT.

The seismic interval (seismic Unit C) immediately overlying volcanic basement is observed to fill basement depressions and to thin over or onlap onto basement highs (Fig. 3, "Seismic Stratigraphy" section, this chapter). The distinctive high-amplitude, continuous reflection (reflection 4 in Fig. 3) marking the boundary between seismic Unit C and the overlying seismic Unit B at 4.94 s TWT is correlated to logging Unit 4 within lithologic Unit IV. Logging Unit 4 is characterized by a 53-m interval of the highest velocity and density values recorded at this site and is located between intervals of significantly lower velocity and density. The corresponding portion of lithologic Unit IV contains an interval of well indurated calcareous limestone turbidites with altered ash in between less indurated intervals characterized by a larger altered volcanogenic component.

Seismic Unit B extends up to 4.72 s TWT, where another continuous high-amplitude reflection exists across the EW9417 survey area (reflection 3 in Fig. 3). This reflection correlates to the interval between 518 and 540 mbsf in lithologic Unit III, approximately the boundary between logging Unit 2 and Subunit 3A. Chert layers have been reported within this interval, and the logging boundary is characterized by gradual increases downhole in velocity and density. The caliper log also indicates an isolated washout at 540 mbsf. All of these factors are consistent with a change in the physical properties of the sediment that could produce the impedance contrasts that create this reflection.

Seismic Unit A extends from 4.72 s TWT to the seafloor and consists primarily of low-amplitude, flat-lying, semicontinuous reflections and two separate sets of high-amplitude reflections that can be traced throughout the survey region. Reflection 2 (Fig. 3) at 4.47 s TWT correlates to 244 mbsf within lithologic Unit III and logging Unit 1. This interval of the section is characterized by numerous and distinct volcanic ash fall layers within nannofossil chalk, and the first reported occurrence of chert within Core 165-998A-27X (143–153 mbsf). Increases in GRAPE and index properties density values as well as in sonic log velocities are recorded at approximately 250 mbsf.

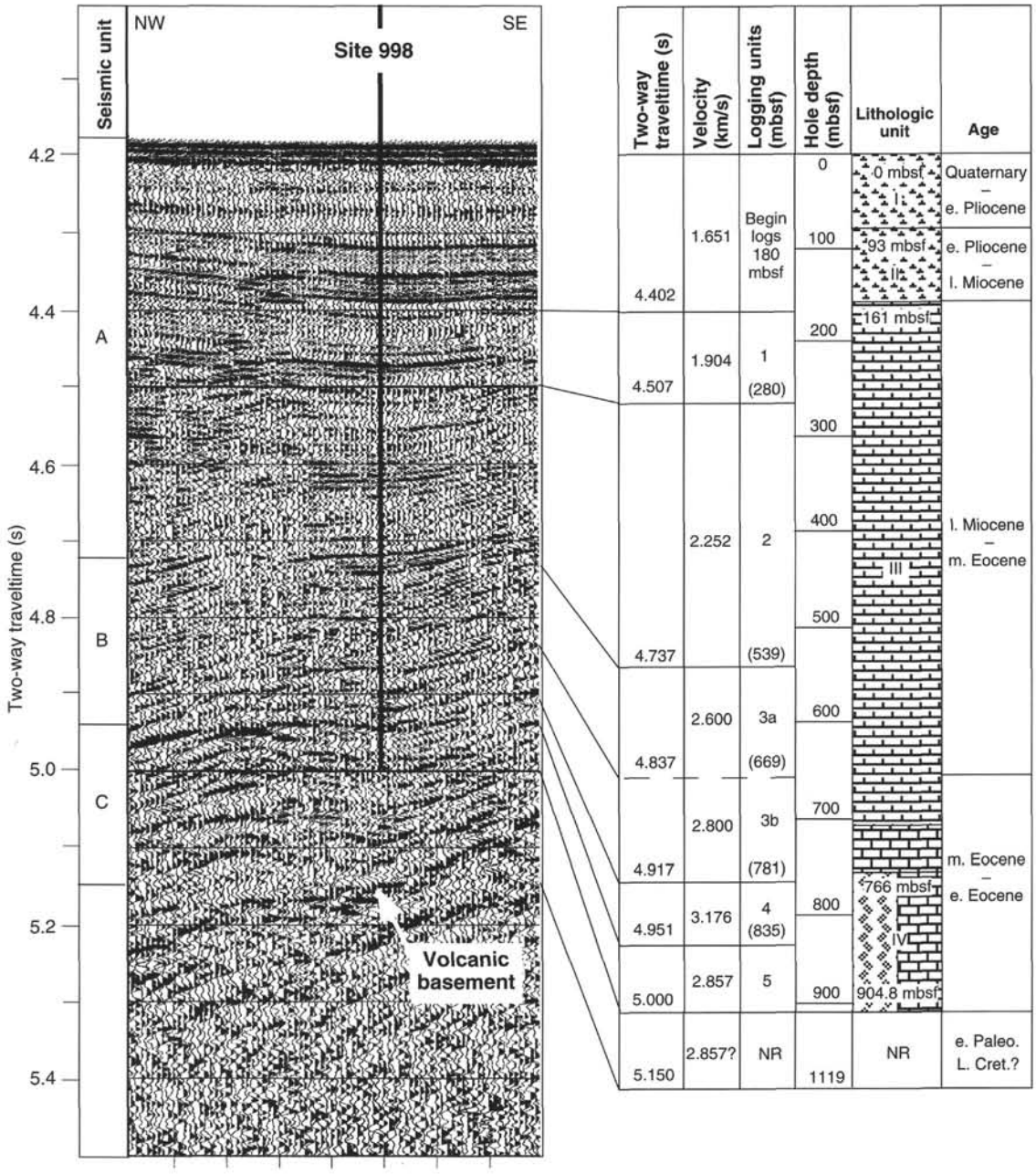

Figure 66. Summary of correlations between seismic stratigraphy, depths, logging units, lithologic units, and ages at Site 998. Correlations with the reflection seismic record were constrained by calculations of two-way traveltime vs. depth derived from downhole sonic velocity measurements (see Fig. 58 in "Downhole Measurements" section, this chapter). Velocities shown are averages derived from the sonic velocity tool within each logging unit. The 1.65 km/s velocity is an average of 1.5 km/s at the seafloor and the first log velocity of 1.8 km/s at 180 mbsf. Although total depth at Hole 998B is 904.8 mbsf, logging Unit 5 is only defined to 880 mbsf. The bottom of Hole 998B at 904.8 mbsf corresponds to 5 s TWT and volcanic basement lies at 5.15 s TWT. A 2.6-km portion of EW9417 SCS Line 13 is displayed ("Seismic Stratigraphy" section, this chapter). NR = no recovery.

The set of parallel, high-amplitude reflections (reflection 1 in Fig. 3) between 4.32 and 4.39 s TWT correspond to a depth of 112–170 mbsf within lithologic Units II and III. This depth interval includes the carbonate crash as well as abundant volcanic ash fall layers.

Although neither the K/T boundary nor basement objectives were achieved at Site 998, the cored interval yielded an abundance of geological and geophysical information about the Cayman Rise and the surrounding region. In particular, three key observations have intriguing implications for tectonic and paleoceanographic studies. First, the distribution, abundance, and type of ash deposits provide a means to date regional volcanic events accurately and are indicative of the tectonic setting of the region. For example, the volcaniclastic turbidites and ash fall layers in the Eocene sequence testify to a local source, which leads us to propose that the Cayman Ridge was an active volcanic arc at this time. Second, the timing, frequency, and thicknesses of turbidite deposits through time may be closely linked to the development and evolution of the Cayman Trough and the depositional environment of the Cayman Rise. Finally, the carbonate crash observed at Site 998, marked by a precipitous decrease in carbonate as well as anomalies in a variety of other data sets, extends a similar signature observed in the central and eastern Pacific to regional scale. Defining the extent and timing of this event should prove im-

portant in constraining the influence of paleoceanographic and tectonic events that have affected the region.

REFERENCES

Atwater, T., 1989. Plate tectonic history of the northeast Pacific and western North America. *In* Winterer, E.L., Hussong, D.M., and Decker, R.W. (Eds.), *The Eastern Pacific Ocean and Hawaii.* Geol. Soc. Am., Geol. of North America Ser., N:21–72.

Aubry, M.-P., 1989. *Handbook of Cenozoic Calcareous Nannoplankton* (Book 3): *Ortholithae (Pentaliths and Others). Heliolithae (Fasciculiths, Sphenoliths, and Others):* New York (Micropaleontology Press).

Backman, J., and Hermelin, J.O.R., 1986. Morphometry of the Eocene nannofossil *Reticulofenestra umbilicus* lineage and its biochronological consequences. *Palaeogeogr., Palaeoclimatol., Palaeoecol.,* 57:103–116.

Backman, J., and Shackleton, N.J., 1983. Quantitative biochronology of Pliocene and early Pleistocene calcareous nannofossils from the Atlantic, Indian and Pacific oceans. *Mar. Micropaleontol.,* 8:141–170.

Berger, W.H., Leckie, R.M., Janecek, T.R., Stax, R., and Takayama, T., 1993. Neogene carbonate sedimentation on Ontong Java Plateau: highlights and open questions. *In* Berger, W.H., Kroenke, L.W., Mayer, L.A., et al., *Proc. ODP, Sci. Results,* 130: College Station, TX (Ocean Drilling Program), 711–744.

Bishop, J.K.B., 1988. The barite-opal organic carbon association in oceanic particulate matter. *Nature,* 332:341–343.

Blow, W.H., 1969. Late middle Eocene to Recent planktonic foraminiferal biostratigraphy. *In* Brönnimann, P., and Renz, H.H. (Eds.), *Proc. First Int. Conf. Planktonic Microfossils, Geneva, 1967:* Leiden (E.J. Brill), 1:199–422.

Bolli, H.M., and Premoli Silva, I., 1973. Oligocene to Recent planktonic foraminifera and stratigraphy of the Leg 15 sites in the Caribbean Sea. *In* Edgar, N.T., Saunders, J.B., et al., *Init. Repts. DSDP,* 15: Washington (U.S. Govt. Printing Office), 475–497.

Bolli, H.M., and Saunders, J.B., 1985. Oligocene to Holocene low latitude planktonic foraminifera. *In* Bolli, H.M., Saunders, J.B., and Perch-Nielsen, K. (Eds.), *Plankton Stratigraphy:* Cambridge (Cambridge Univ. Press), 155–262.

Bowin, C.O., 1968. Geophysical study of the Cayman Trough. *J. Geophys. Res.,* 73:5159–5173.

Bralower, T.J., and Mutterlose, J., 1995. Calcareous nannofossil biostratigraphy of Site 865, Allison Guyot, Central Pacific Ocean: a tropical Paleogene reference section. *In* Winterer, E.L., Sager, W.W., Firth, J.V., and Sinton, J.M. (Eds.), *Proc. ODP, Sci. Results,* 143: College Station, TX (Ocean Drilling Program), 31–74.

Burke, K., 1988. Tectonic evolution of the Caribbean. *Annu. Rev. Earth Planet. Sci.,* 16:201–230.

Cadet, J.-P., Thisse, Y., Pouclet, A., Bardintzeff, J.M., and Stephan, J.F., 1982a. Tephra from Deep Sea Drilling Project Leg 66: Middle American Trench Transect (Southern Mexico). *In* Watkins, J.S., Moore, J.C., et al., *Init. Repts. DSDP,* 66: Washington (U.S. Govt. Printing Office), 687–698.

Cadet, J.-P., Pouclet, A., Thisse, Y., Bardintzeff, J.M., and Azéma, J., 1982b. Middle America Neogene explosive volcanism and ash layers: evidence from the Middle America trench transect, Deep Sea Drilling Project Leg 167. *In* Aubouin, J., von Huene, R., et al., *Init. Repts. DSDP,* 67: Washington (U.S. Govt. Printing Office), 475–491.

Carr, M.J., and Stoiber, R.E., 1990. Volcanism. *In* Dengo, G., and Case, J.E. (Eds.), *The Caribbean Region.* Geol. Soc. Am., Geol. of North America Ser., H:375–391.

Curran, D.W., 1980. Geology of the Siguatepeque quadrangle, Honduras, Central America. [M.S. thesis], State Univ. of New York, Binghampton.

Curry, W.B., Shackleton, N.J., Richter, C., et al., 1995. *Proc. ODP, Init. Repts.,* 154: College Station, TX (Ocean Drilling Program).

Dehairs, F., Chesselet, R., and Jedwab, J., 1980. Discrete suspended particles of barite and the barium cycle in the open ocean. *Earth Planet. Sci. Lett.,* 49:528–550.

Donnelly, T.W., Beets, D., Carr, M.J., Jackson, T., Klaver, G., Lewis, J., Maury, R., Schellenkens, H., Smith, A.L., Wadge, G., and Westercamp, D., 1990. History and tectonic setting of Caribbean magmatism. *In* Dengo, G., and Case, J.E. (Eds.), *The Caribbean Region.* Geol. Soc. Am., Geol. of North Am., H:339–374.

Draper, G., 1986. Blueschists and associated rocks in eastern Jamaica and their significance for Cretaceous plate-margin development in the northern Caribbean. *Geol. Soc. Am. Bull.,* 97:48–60.

Dupre, W.R., 1970. Geology of the Zambrano quadrangle, Honduras. [M.S. thesis]. State Univ. of New York, Binghampton.

Dymond, J., Suess, E., and Lyle, M., 1992. Barium in deep-sea sediment: a geochemical proxy for paleoproductivity. *Paleoceanography,* 7:163–182.

Edgar, N.T., Saunders, J.B., et al., 1973. *Init. Repts., DSDP,* 15: Washington (U.S. Govt. Printing Office).

Emerson, S., and Bender, M., 1981. Carbon fluxes at the sediment-water interface of the deep-sea: calcium carbonate preservation. *J. Mar. Res.,* 39:139–162.

Farrell, J.W., Raffi, I., Janececk, T.R., Murray, D.W., Levitan, M., Dadey, K.A., Emeis, K-C., Lyle, M., Flores, J-A., and Hovan, S., 1995. Late Neogene sedimentation patterns in the eastern equatorial Pacific Ocean. *In* Pisias, N.G., Mayer, L.A., Janecek, T.R., Palmer-Julson, A., and van Andel, T.H. (Eds.), *Proc. ODP, Sci. Results,* 138: College Station, TX (Ocean Drilling Program), 717–756.

Francois, R., Honjo, S., Manganini, S.J., and Ravizza, G.E., 1995. Biogenic barium fluxes to the deep sea: implications for paleoproductivity reconstruction. *Global Biogeochem. Cycles,* 9:289–303.

Froelich, P.N., Klinkhammer, G.P., Bender, M.L., Luedtke, N.A., Heath, G.R., Cullen, D., Dauphin, P., Hammond, D., Hartman, B., and Maynard, V., 1979. Early oxidation of organic matter in pelagic sediments of the eastern equatorial Atlantic: suboxic diagenesis. *Geochim. Cosmochim. Acta,* 43:1075–1090.

Gieskes, J.M., 1983. The chemistry of interstitial waters of deep-sea sediments: interpretation of deep-sea drilling data. *In* Riley, J.P., and Chester, R. (Eds.), *Chemical Oceanography* (Vol. 8): London (Academic), 222–269.

Hall, S.A., and Yeung, T., 1980. A study of magnetic anomalies in the Yucatan Basin. *Trans. 11th Carib. Geol. Conf.,* 35:1–13.

Iturralde-Vinent, M.A., 1994. Cuban geology; a new plate-tectonic synthesis. *J. Petrol. Geol.,* 17:39–69.

Kennett, J.P., and Srinivasan, M.S., 1983. *Neogene Planktonic Foraminifera: A Phylogenetic Atlas:* Stroudsburg, PA (Hutchinson Ross).

Kroenke, L.W., Berger, W.H., Janecek, T.R., et al., 1991. *Proc. ODP, Init. Repts.,* 130: College Station, TX (Ocean Drilling Program).

Leckie, R.M., Farnham, C., and Schmidt, M.G., 1993. Oligocene planktonic foraminifer biostratigraphy of Hole 803D (Ontong Java Plateau) and Hole 628A (Little Bahama Bank), and comparison with the southern high latitudes. *In* Berger, W.H., Kroenke, L.W., Mayer, L.A., et al., *Proc. ODP, Sci. Results,* 130: College Station, TX (Ocean Drilling Program), 113–136.

Lewis, J.F., and Draper, G., 1990. Geology and tectonic evolution of the northern Caribbean margin. *In* Dengo, G., and Case, J.E. *(Eds.) The Caribbean Region.* Geol. Soc. Am., Geol. of North Am. Ser., H:77–140.

Lyle, M., Dadey, K.A., and Farrell, J.W., 1995. The late Miocene (11–8 Ma) eastern Pacific carbonate crash: evidence for reorganization of deep-water circulation by the closure of the Panama Gateway. *In* Pisias, N.G., Mayer, L.A., Janecek, T.R., Palmer-Julson, A., and van Andel, T.H. (Eds.), *Proc. ODP, Sci. Results,* 138: College Station, TX (Ocean Drilling Program), 821–838.

Martens, C.S., and Berner, R.A., 1974. Methane production in the interstitial waters of sulfate-depleted marine sediments. *Science,* 185:1167–1169.

Mayer, L.A., Pisias, N.G, Janecek, T.R., et al., 1992. *Proc. ODP, Init. Repts.,* 138: College Station, TX (Ocean Drilling Program).

Mayer, L.A., Theyer, F., Thomas, E., et al., 1985. *Init. Repts. DSDP,* 85: Washington (U.S. Govt. Printing Office).

McBirney, A.R., and Williams, H., 1965. *Volcanic History of Nicaragua:* Berkeley (Univ. California Press).

Millero, F.J., and Sohn, M.L., 1992. *Chemical Oceanography:* Boca Raton (CRC Press).

Mix, A.C., Rugh, W., Pisias, N.G., Veirs, S., Leg 138 Shipboard Sedimentologists (Hagelberg, T., Hovan, S., Kemp, A., Leinen, M., Levitan, M., Ravelo, C.), and Leg 138 Scientific Party, 1992. Color reflectance spectroscopy: a tool for rapid characterization of deep-sea sediments. *In* Mayer, L., Pisias, N., Janecek, T., et al., *Proc. ODP, Init. Repts.,* 138 (Pt. 1): College Station, TX (Ocean Drilling Program), 67–77.

Okada, H., and Bukry, D., 1980. Supplementary modification and introduction of code numbers to the low-latitude coccolith biostratigraphic zonation (Bukry, 1973; 1975). *Mar. Micropaleontol.,* 5:321–325.

Perfit, M.R., and Heezen, B.C., 1978. The geology and evolution of the Cayman Trench. *Geol. Soc. Amer. Bull.,* 89:1155–1174.

Peterson, L.C., Murray, D.W., Ehrmann, W.U., and Hempel, P., 1992. Cenozoic carbonate accumulation and compensation depth changes in the

Indian Ocean. *In* Duncan, R.A., Rea, D.K., Kidd, R.B., von Rad, U., and Weissel, J.K. (Eds.), *Synthesis of Results from Scientific Drilling in the Indian Ocean.* Geophys. Monogr., Am. Geophys. Union, 70:311–333.

Pindell, J.L., 1993. Regional synopsis of Gulf of Mexico and Caribbean evolution. *Proc.—GCSSEMP Found. 13th Annu. Res. Conf.,* 251–274.

Pindell, J.L., and Barrett, S.F., 1990. Geologic evolution of the Caribbean region: a plate-tectonic perspective. *In* Dengo, G., and Case, J.E. (Eds.), *The Caribbean Region,* Geol. Soc. Am., Geol. North. Am. Ser., H:405–432.

Pisias, N.G., Mayer, L.A., and Mix, A.C., 1995. Paleoceanography of the eastern equatorial Pacific during the Neogene: synthesis of Leg 138 drilling results. *In* Pisias, N.G., Mayer, L.A., Janecek, T.R., Palmer-Julson, A., and van Andel, T.H. (Eds.), *Proc. ODP, Sci. Results,* 138: College Station, TX (Ocean Drilling Program), 5–21.

Reynolds, J.H., 1980. Late Tertiary volcanic stratigraphy of northern Central America. *Bull. Volcanol.,* 43:601–607.

Rose, W.I., Jr., Bornhorst, T.J., and Drexler, J.W., 1982. Preliminary correlation of Quaternary volcanism and ash layers: evidence from the Middle America Trench Transect, Deep Sea Drilling Project Leg 67. *In* Aubouin, J., von Huene, R., et al., *Init. Repts. DSDP,* 67: Washington (U.S. Govt. Printing Office), 67:493–495.

Rosencrantz, E., 1990. Structure and tectonics of the Yucatan Basin, Caribbean Sea, as determined from seismic reflection studies. *Tectonics,* 9:1037–1059.

Rosencrantz, E., and Sclater, J.G., 1986. Depth and age in the Cayman Trough. *Earth Planet. Sci. Lett.,* 79:133–144.

Sato, T., Kameo, K., and Takayama, T., 1991. Coccolith biostratigraphy of the Arabian Sea. *In* Prell, W.L., Niitsuma, N., et al., *Proc. ODP, Sci. Results,* 117: College Station, TX (Ocean Drilling Program), 37–54.

Schmitz, B., 1987. Barium, equatorial high productivity, and the northward wandering of the Indian continent. *Paleoceanography,* 2:63–77.

Sigurdsson, H., 1990. Assessment of the atmospheric impact of volcanic eruptions. *Pap.—Geol. Soc. Am. Sp.,* 247:99–110.

Sigurdsson, H., Sparks, R.S.J. , Carey, S.N., and Huang, T.C., 1980. Volcanogenic sedimentation in the Lesser Antilles arc. *J. Geol.,* 88:523–540.

Takayama, T., and Sato, T., 1987. Coccolith biostratigraphy of the North Atlantic Ocean, Deep Sea Drilling Project Leg 94. *In* Ruddiman, W.F., Kidd, R.B., Thomas, E., et al., *Init. Repts. DSDP,* 94 (Pt. 2): Washington (U.S. Govt. Printing Office), 651–702.

Taylor, S.R., and McLennan, S.M., 1985. *The Continental Crust: Its Composition and Evolution:* Oxford (Blackwell Scientific).

Theyer, F., Vincent, E., and Mayer, L.A., 1989. Sedimentation and paleoceanography of the central equatorial Pacific. *In* Winterer, E.L., Hussong, D.M., and Decker, R.W. (Eds.), *The Eastern Pacific Ocean and Hawaii.* Geol. Soc. Am., Geol. of North Am. Ser., N:347–372.

Urmos, J., Wilkens, R.H., Bassinot, F., Lyle, M., Marsters, J.C., Mayer, L.A., and Mosher, D.C., 1993. Laboratory and well-log velocity and density measurements from the Ontong Java Plateau: new in-situ corrections to laboratory data for pelagic carbonates. *In* Berger, W.H., Kroenke, L.W., Mayer, L.A., et al., *Proc. ODP, Sci. Results,* 130: College Station, TX (Ocean Drilling Program), 607–622.

van Andel, T.H., Heath, G.R., and Moore, T.C., Jr., 1975. Cenozoic history and paleoceanography of the central equatorial Pacific Ocean: a regional synthesis of Deep Sea Drilling Project data. *Mem.—Geol. Soc. Am.,* 143.

Wadge, G., and Burke, K., 1983. Neogene Caribbean Plate rotation and associated Central American tectonic evolution. *Tectonics,* 2:633–643.

Walter, L.M., and Burton, E.A., 1986. The effect of orthophosphate on carbonate mineral dissolution rates in seawater. *Chem. Geol.,* 56:313–323.

Westbrook, G., 1990. Gravity anomaly map of the Caribbean region. *In* Dengo, G., and Case, J.E. (Eds.), *The Caribbean Region.* Geol. Soc. Am., Geol. of North Am. Ser., H: back pocket.

Weyl, R., 1980. *The Geology of Central America:* Berlin (Gebruder Borntraeger).

Wiesemann, G., 1975. Remarks on the geologic structure of the Republic of El Salvador. *Mitt. Geol.-Palaeontol. Inst. Univ. Hamburg,* 44:557–574.

Williams, H., and McBirney, A.R., 1969. *Volcanic History of Honduras:* Berkeley (Univ. California Press).

Ms 165IR-103

NOTE: Core-description forms ("barrel sheets") and core photographs can be found in Section 4, beginning on page 403. Forms containing smear-slide data can be found in Section 5, beginning on page 821. Thin-section descriptions are given in Sections 6 and 7, beginning on page 851. See Table of Contents for material contained on CD-ROM.

SHORE-BASED LOG PROCESSING
HOLE 998B

Bottom felt: 3190.7 mbrf (used for depth shift to seafloor)
Total penetration: 904.8 mbsf
Total core recovered: 287.9 m (83.1%)

Logging Runs

Logging string 1: DIT/SDT/HLDT/CNTG/NGT
Logging string 2: ACT/GST/NGT
Logging string 3: FMS/GPIT/NGT (2 passes)
Logging string 3: GHMT/NGT (2 passes)

Wireline heave compensator was used to counter ship heave.

Bottom-Hole Assembly

The following bottom-hole assembly depths are as they appear on the logs after differential depth shift (see "Depth shift" section) and depth shift to the seafloor. As such, there might be a discrepancy with the original depths given by the drillers on board. Possible reasons for depth discrepancies are ship heave, use of wireline heave compensator, and drill string and/or wireline stretch.

DIT/SDT/HLDT/CNTG/NGT: Bottom-hole assembly at ~173 mbsf.
ACT/GST/NGT: Bottom-hole assembly at ~173 mbsf.
FMS/GPIT/NGT: Did not reach bottom-hole assembly (2 passes).
GHMT/NGT: Did not reach bottom-hole assembly (2 passes).

Processing

Depth shift: Original logs have been interactively depth shifted with reference to NGT from DIT/SDT/HLDT/CNTG/NGT run, and to the seafloor (–3190.7 m).

Gamma-ray processing: Data have been processed to correct for borehole size and type of drilling fluid.

Acoustic data processing: Because of the good quality of the acoustic logs, no processing has been performed.

Geochemical processing: The elemental yields recorded by the GST tool represent the relative contribution of only some of the rock-forming elements (iron, calcium, chlorine, silicon, sulfur, hydrogen, gadolinium, and titanium—the last two ones computed during geochemical processing) to the total spectrum. Because other rock-forming elements are present in the formation (such as aluminum, potassium, etc.), caution is recommended in using the yields to infer lithologic changes. Instead, ratios are more appropriate to determine changes in the macroscopic properties of the formation.

List of oxide factors used in geochemical processing:
SiO_2 = 2.139
$CaCO_3$ = 2.497
FeO* = 1.358
TiO_2 = 1.668
K_2O = 1.205
Al_2O_3 = 1.889

FeO* = computed using an oxide factor that assumes a 50:50 combination of Fe_2O_3 and FeO factors.

Quality Control

The quality of the neutron porosity data is low throughout most of the hole because of an intermittent detector problem and borehole conditions; for this reason, no data is shown in the log summary figures. Only the following intervals show valid data: 546–565, 569–621, 642–677, 678–730, 740–755, 757–838, and 842–885 mbsf.

Data recorded through bottom-hole assembly, such as the gamma-ray data above 173 mbsf, should be used qualitatively only because of the attenuation on the incoming signal.

The hole diameter was recorded by the hydraulic caliper on the HLDT tool (CALI) and the caliper on the FMS string (C1 and C2).

FACT = quality control curve in geochemical processing. Accuracy of the estimates is inversely proportional to the magnitude of the curve.

Details of standard shore-based processing procedures are found in the "Explanatory Notes" chapter (this volume). For further information about the logs, please contact:

Cristina Broglia
Phone: 914-365-8343
Fax: 914-365-3182
E-mail: chris@ldeo.columbia.edu

Zhiping Tu
Phone: 914-365-8336
Fax: 914-365-3182
E-mail: ztu@ldeo.columbia.edu

Hole 998B: Natural Gamma Ray Logging Data

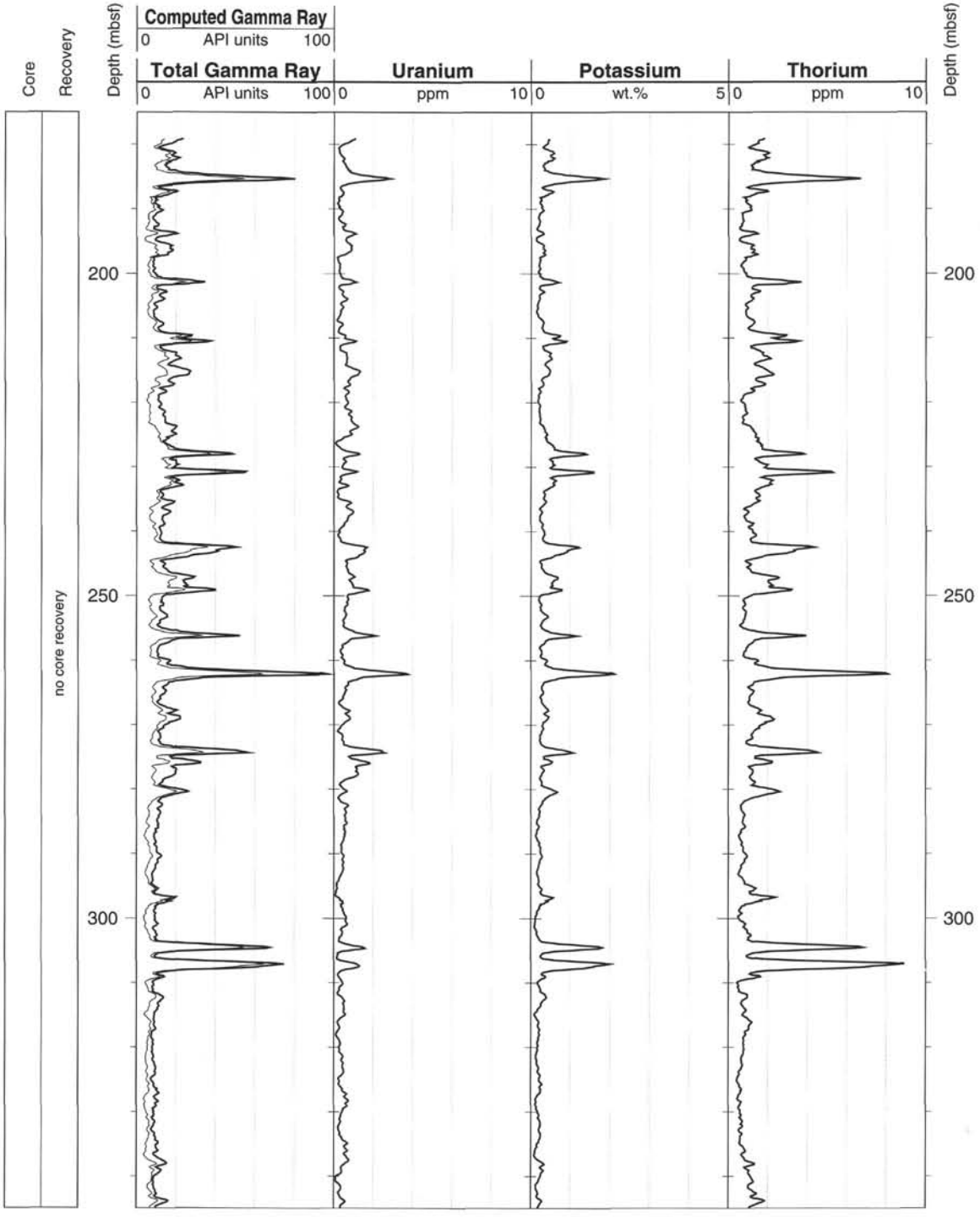

Hole 998B: Natural Gamma Ray Logging Data (cont.)

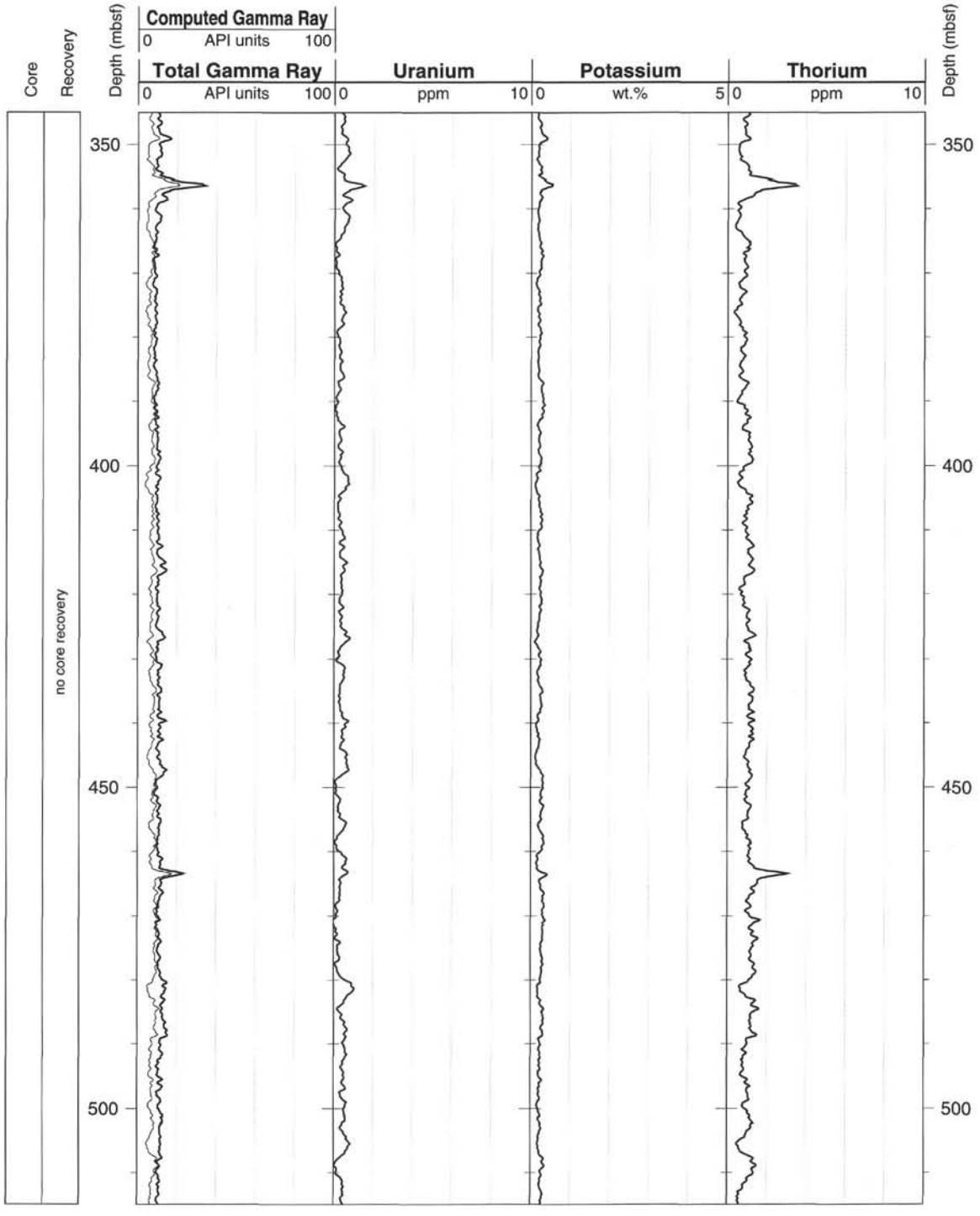

Hole 998B: Natural Gamma Ray Logging Data (cont.)

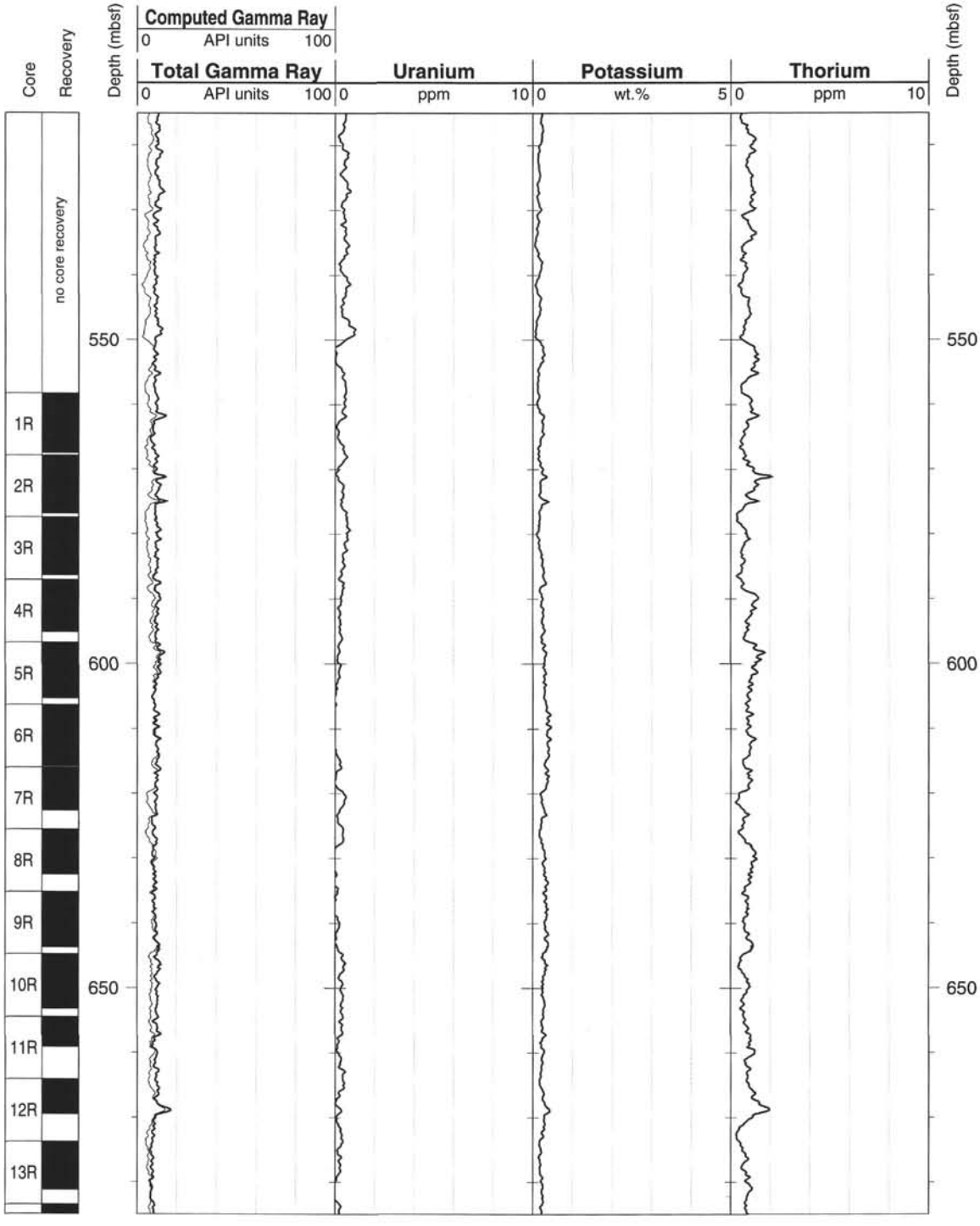

Hole 998B: Natural Gamma Ray Logging Data (cont.)

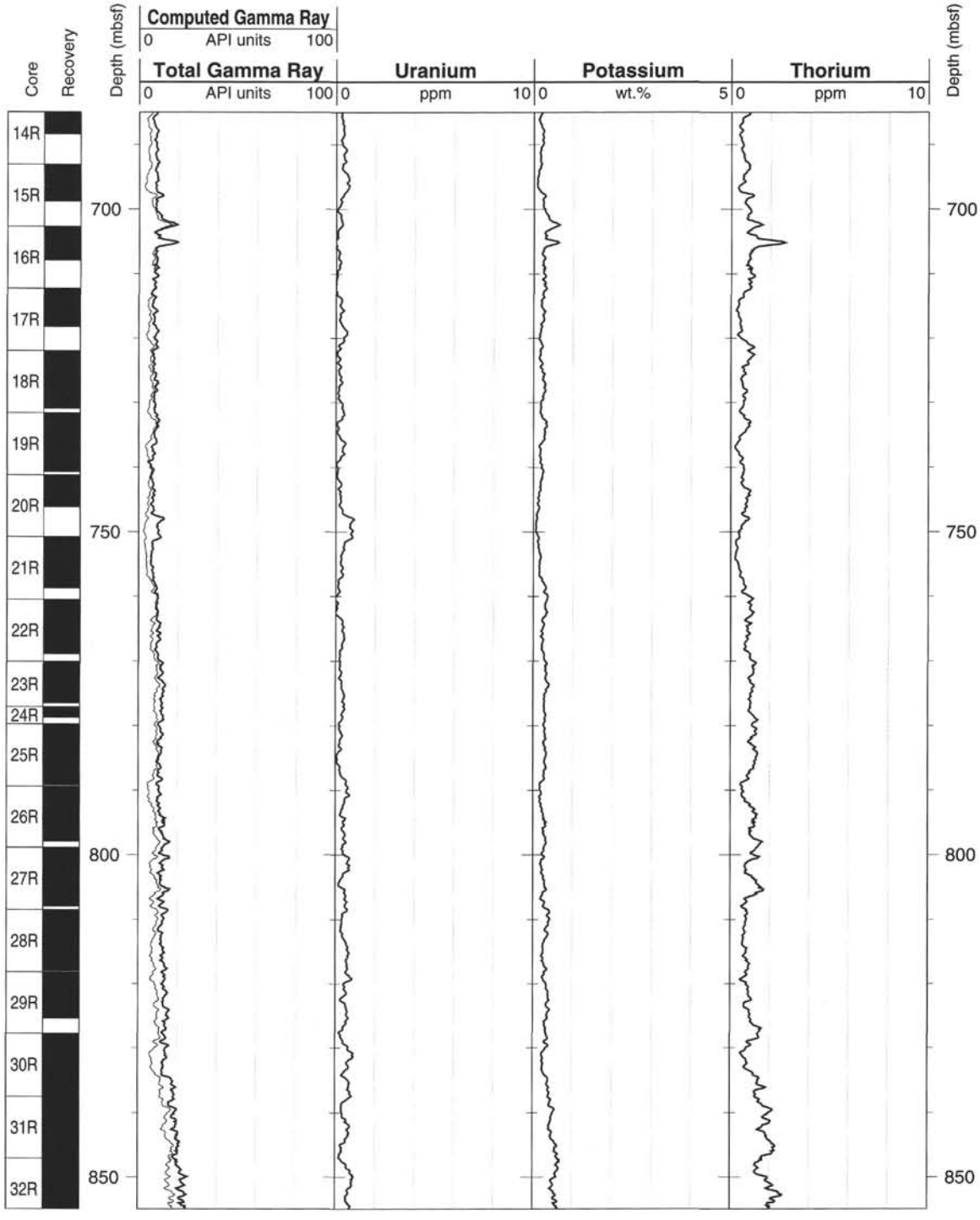

Hole 998B: Natural Gamma Ray Logging Data (cont.)

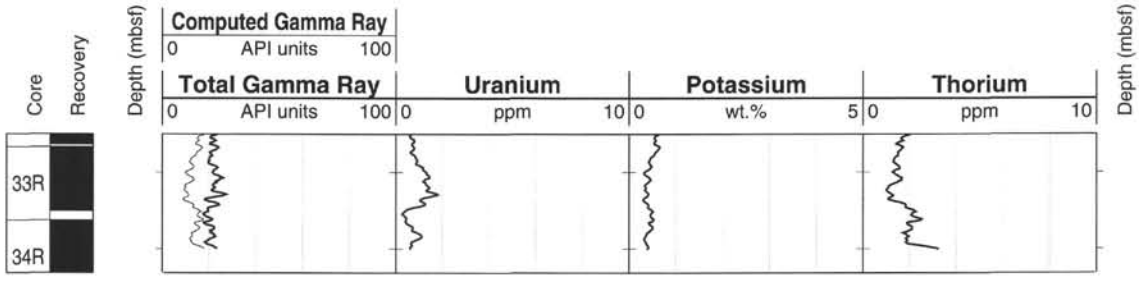

Hole 998B: Natural Gamma Ray-Density Logging Data

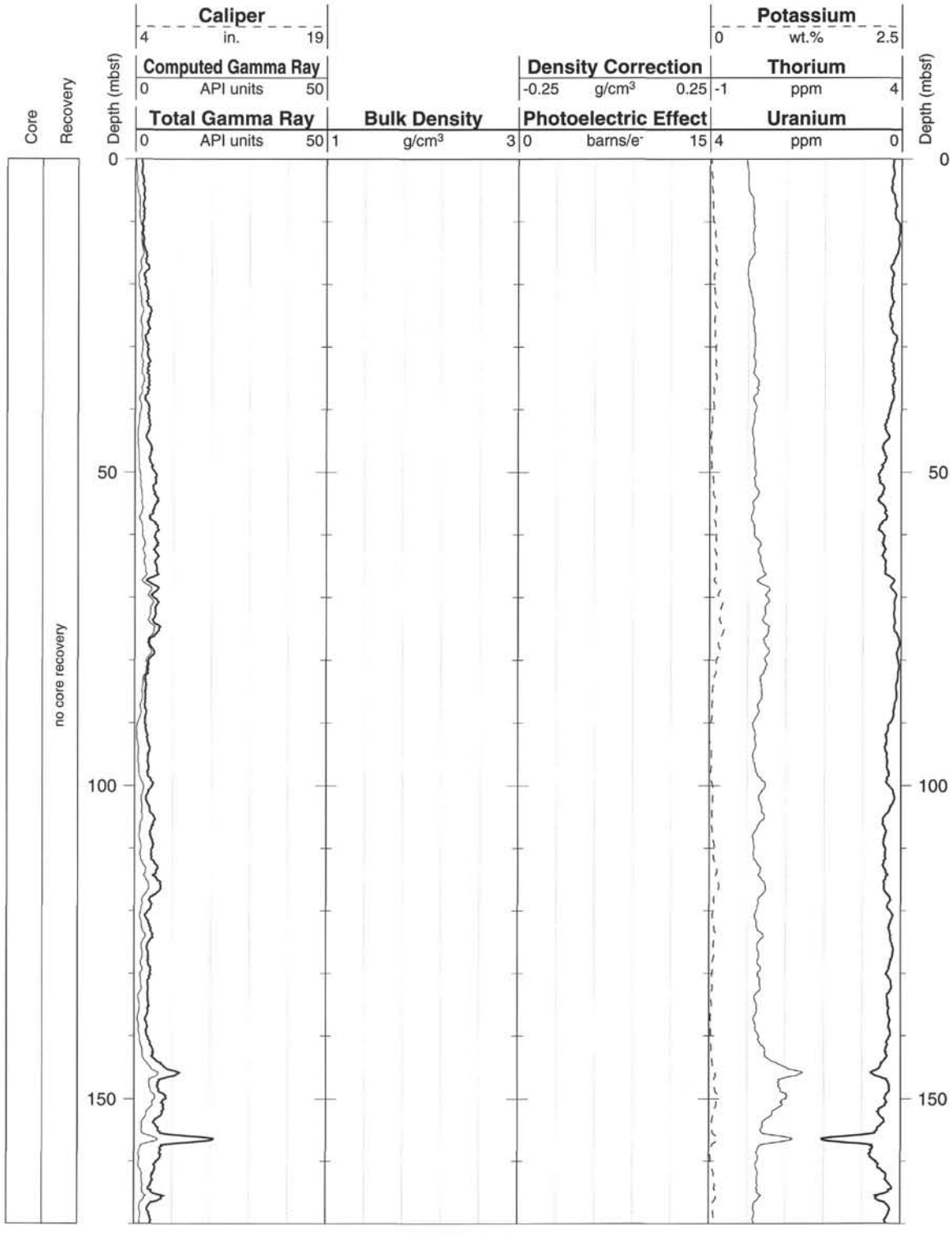

Hole 998B: Natural Gamma Ray-Density Logging Data (cont.)

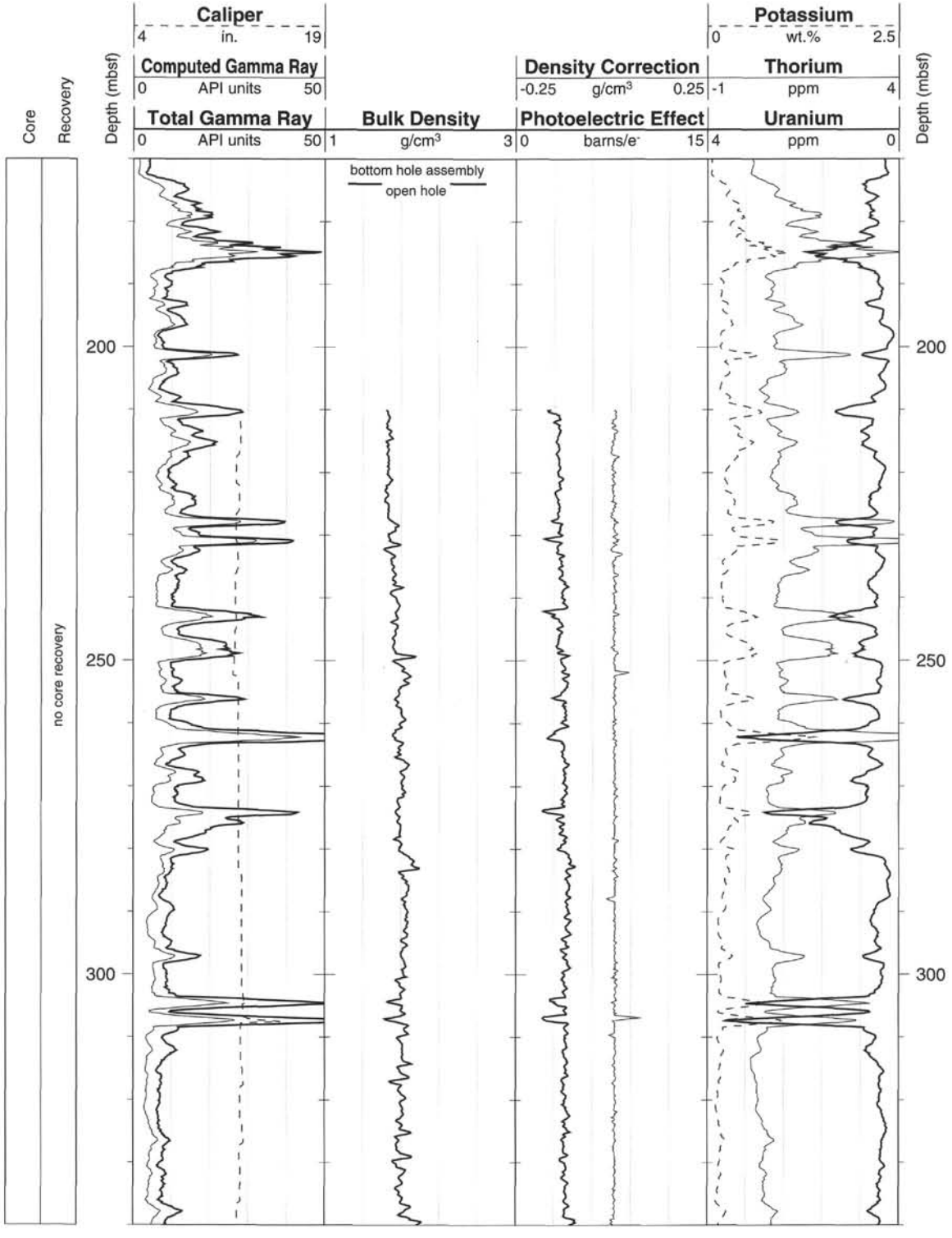

Hole 998B: Natural Gamma Ray-Density Logging Data (cont.)

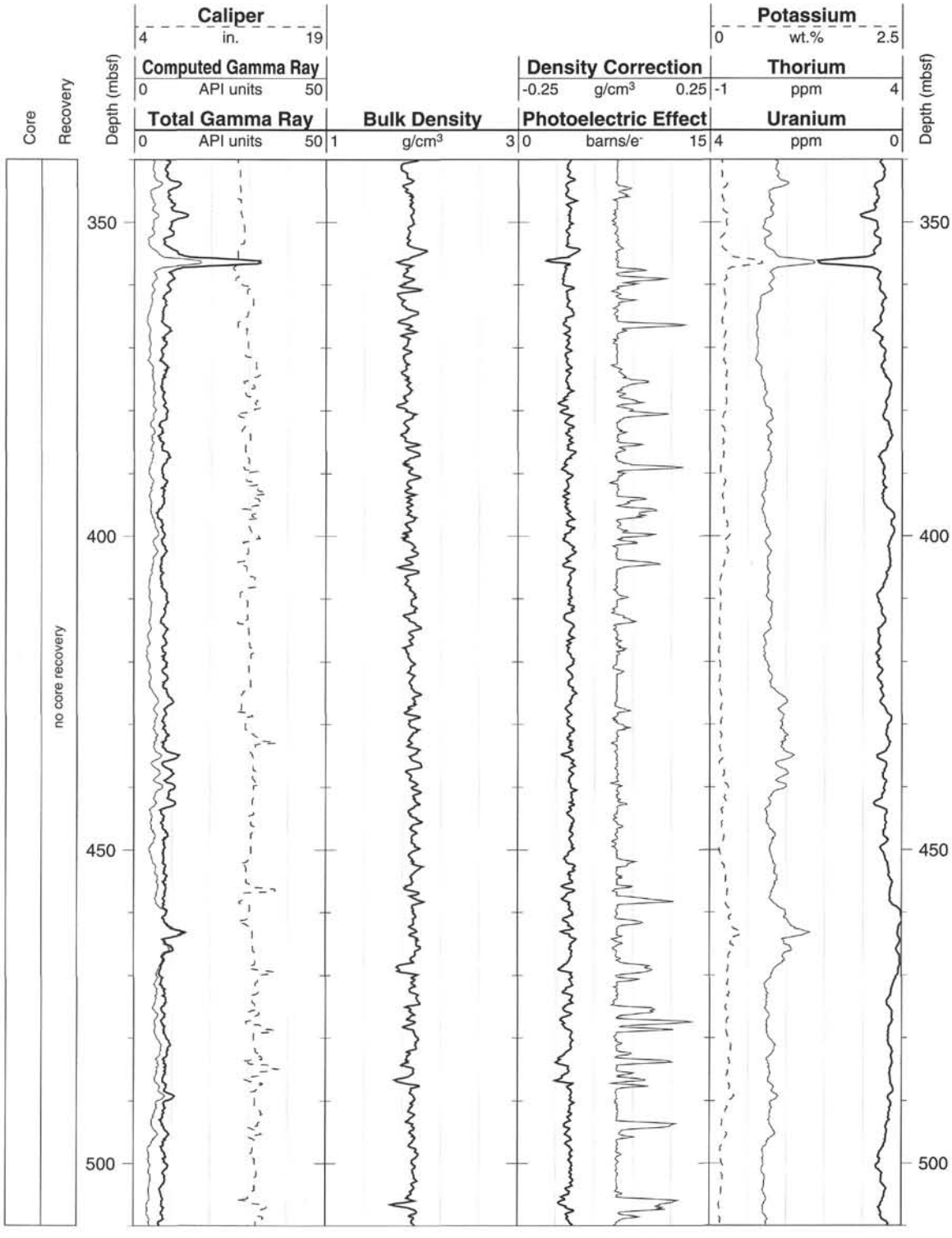

Hole 998B: Natural Gamma Ray-Density Logging Data (cont.)

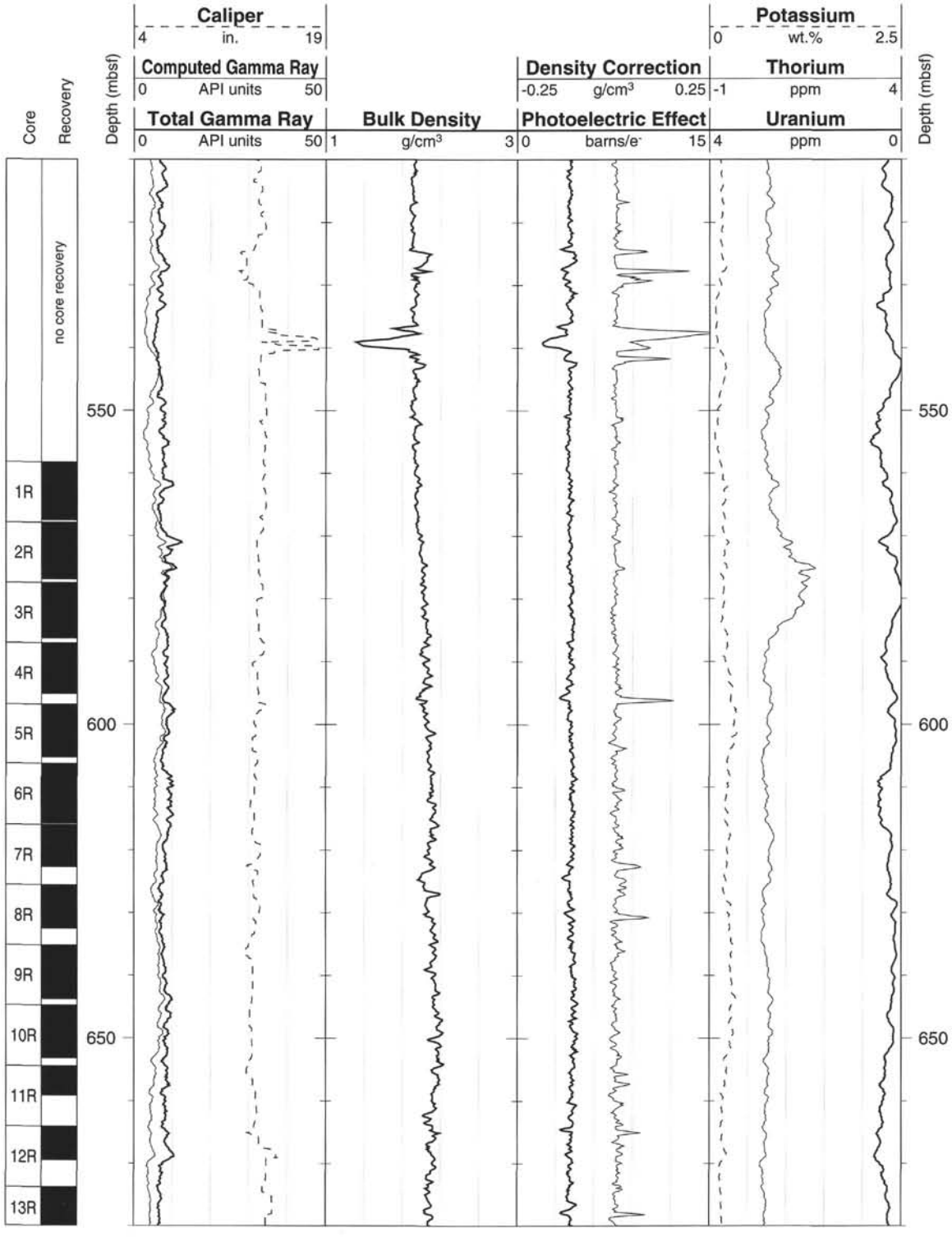

Hole 998B: Natural Gamma Ray-Density Logging Data (cont.)

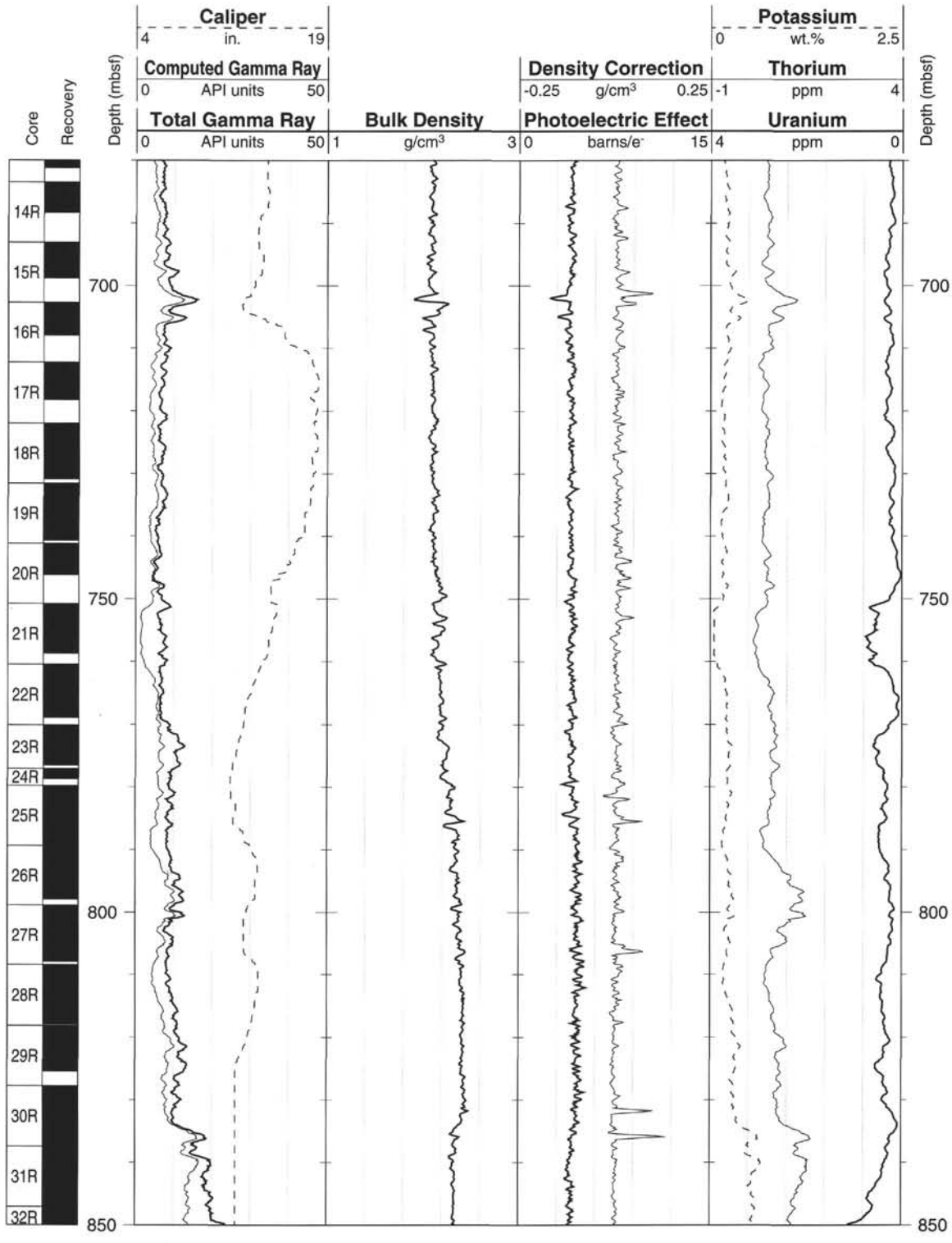

Hole 998B: Natural Gamma Ray-Density Logging Data (cont.)

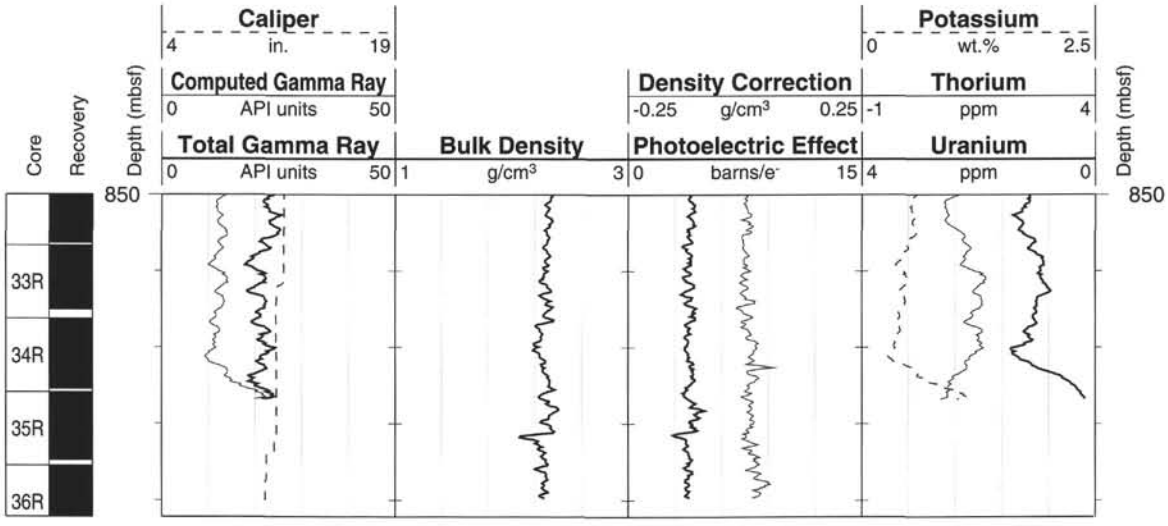

Hole 998B: Natural Gamma Ray-Resistivity-Sonic Logging Data

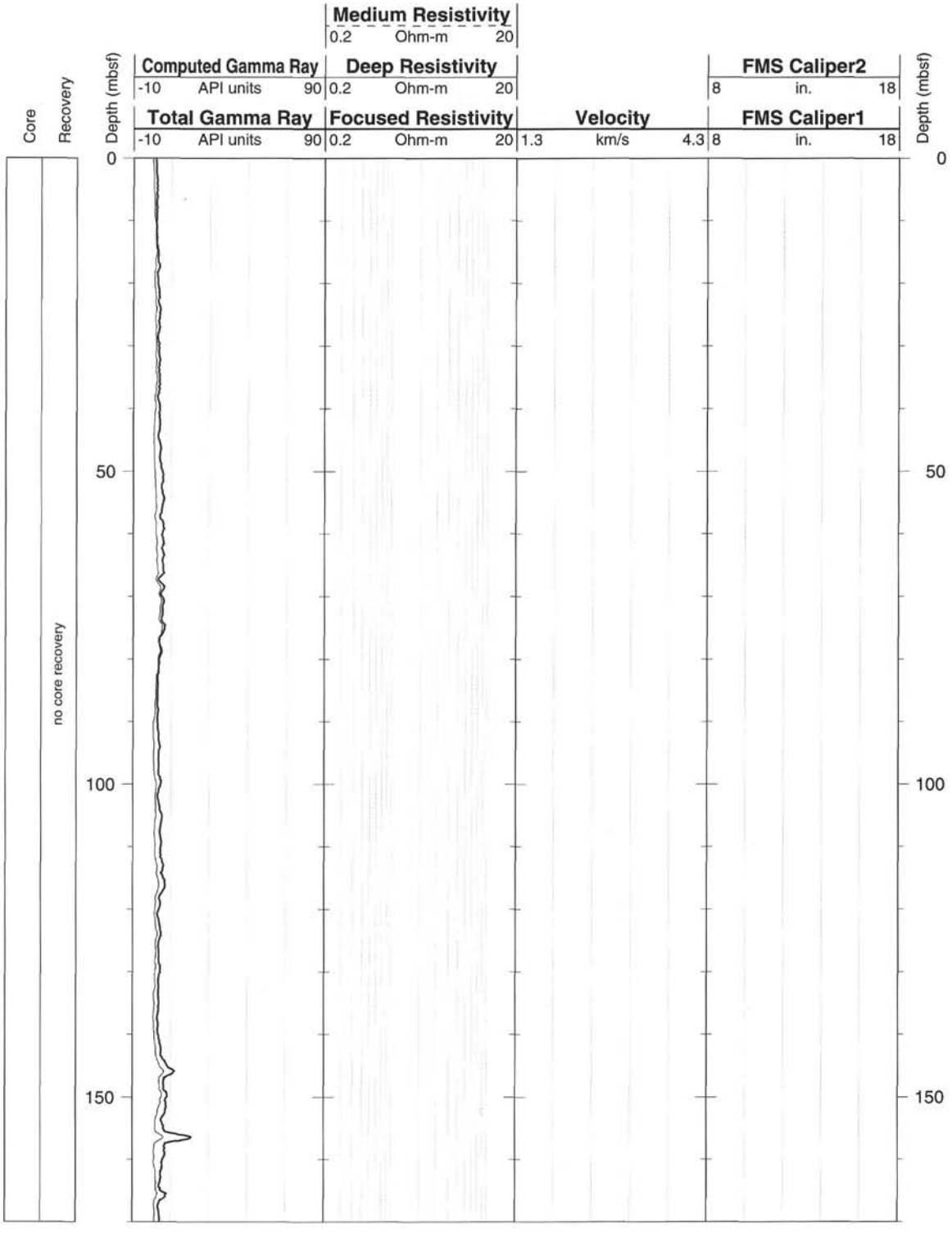

Hole 998B: Natural Gamma Ray-Resistivity-Sonic Logging Data (cont.)

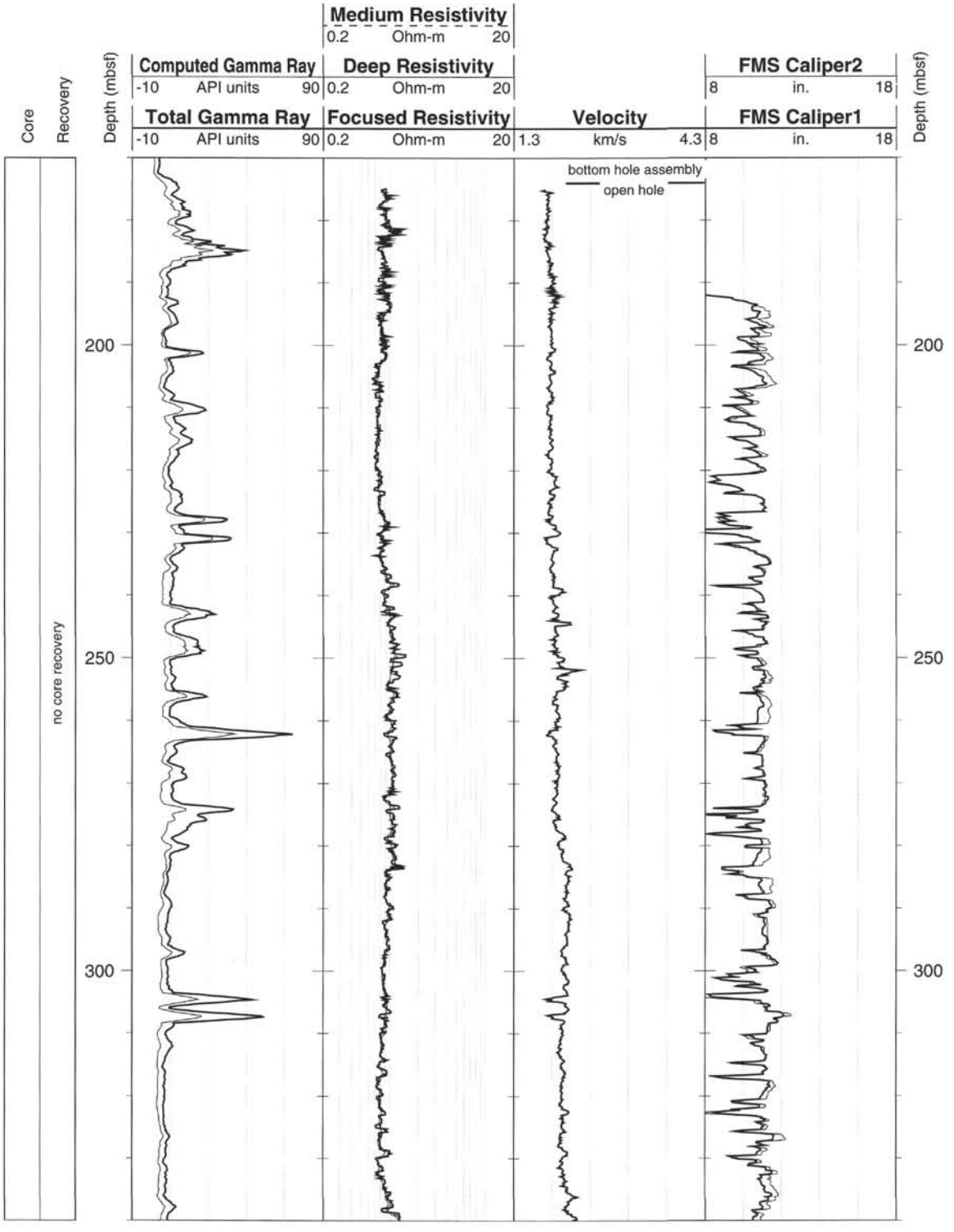

Hole 998B: Natural Gamma Ray-Resistivity-Sonic Logging Data (cont.)

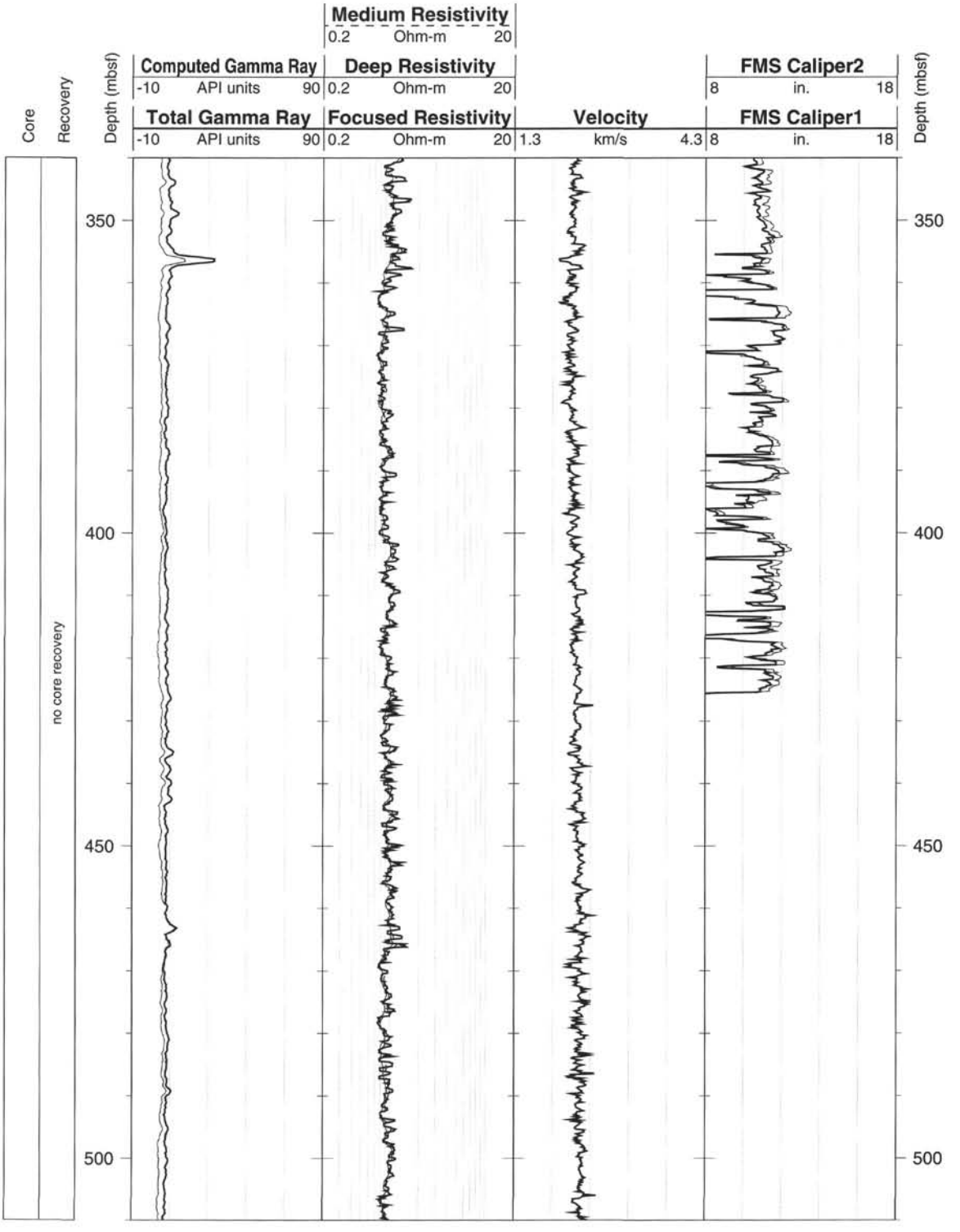

Hole 998B: Natural Gamma Ray-Resistivity-Sonic Logging Data (cont.)

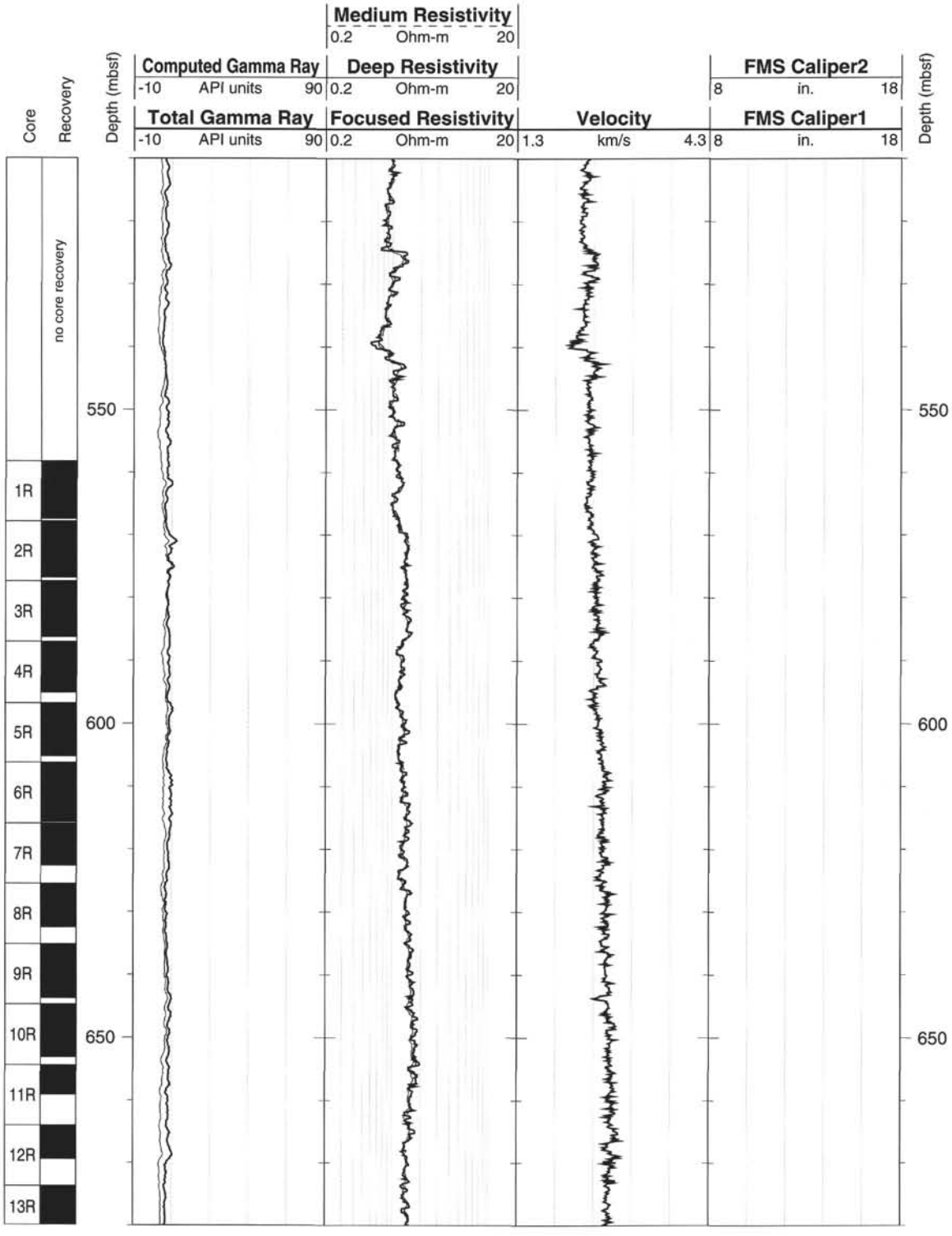

Hole 998B: Natural Gamma Ray-Resistivity-Sonic Logging Data (cont.)

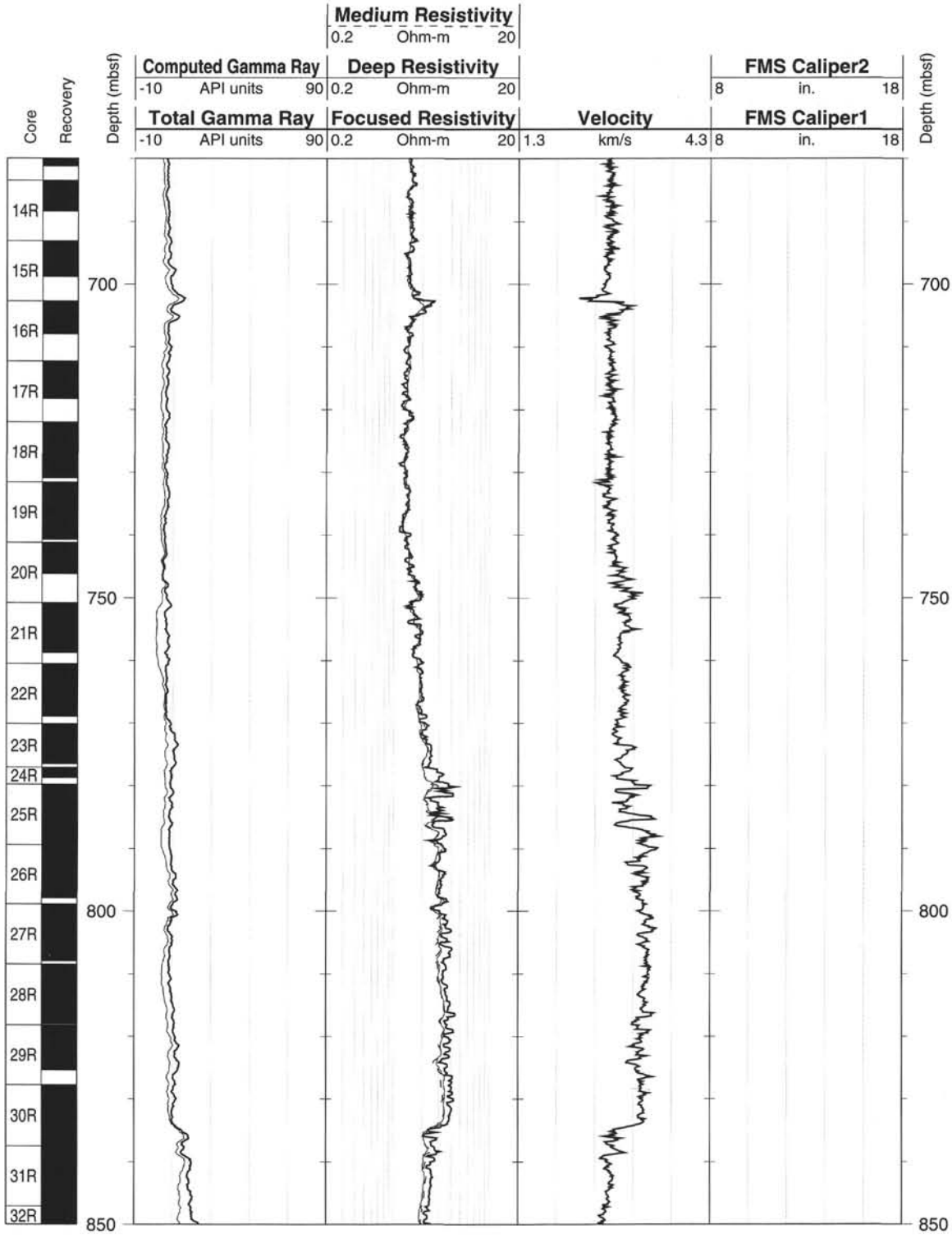

Hole 998B: Natural Gamma Ray-Resistivity-Sonic Logging Data (cont.)

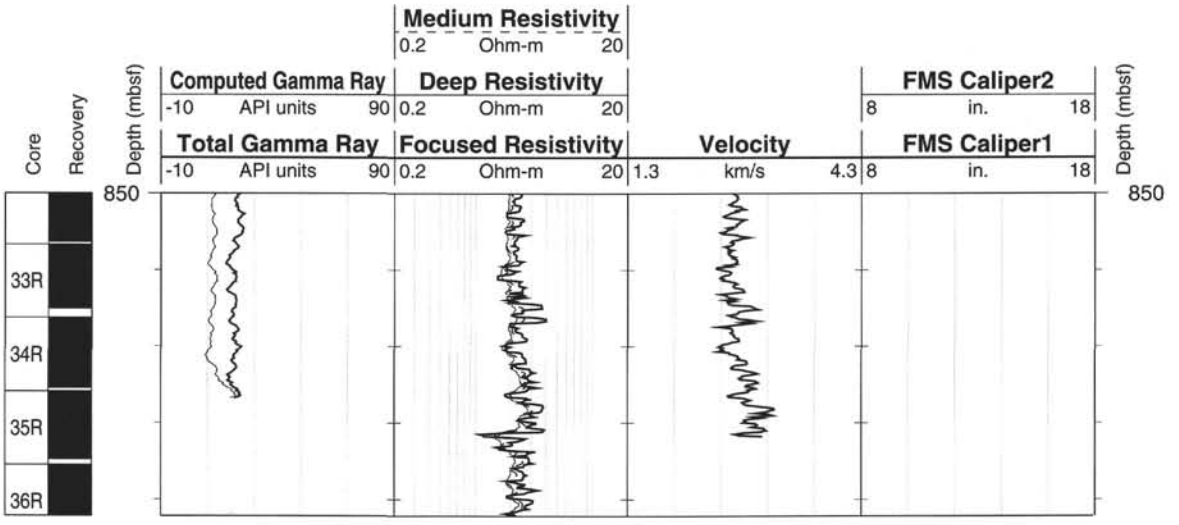

Hole 998B: Geochemical Logging Data

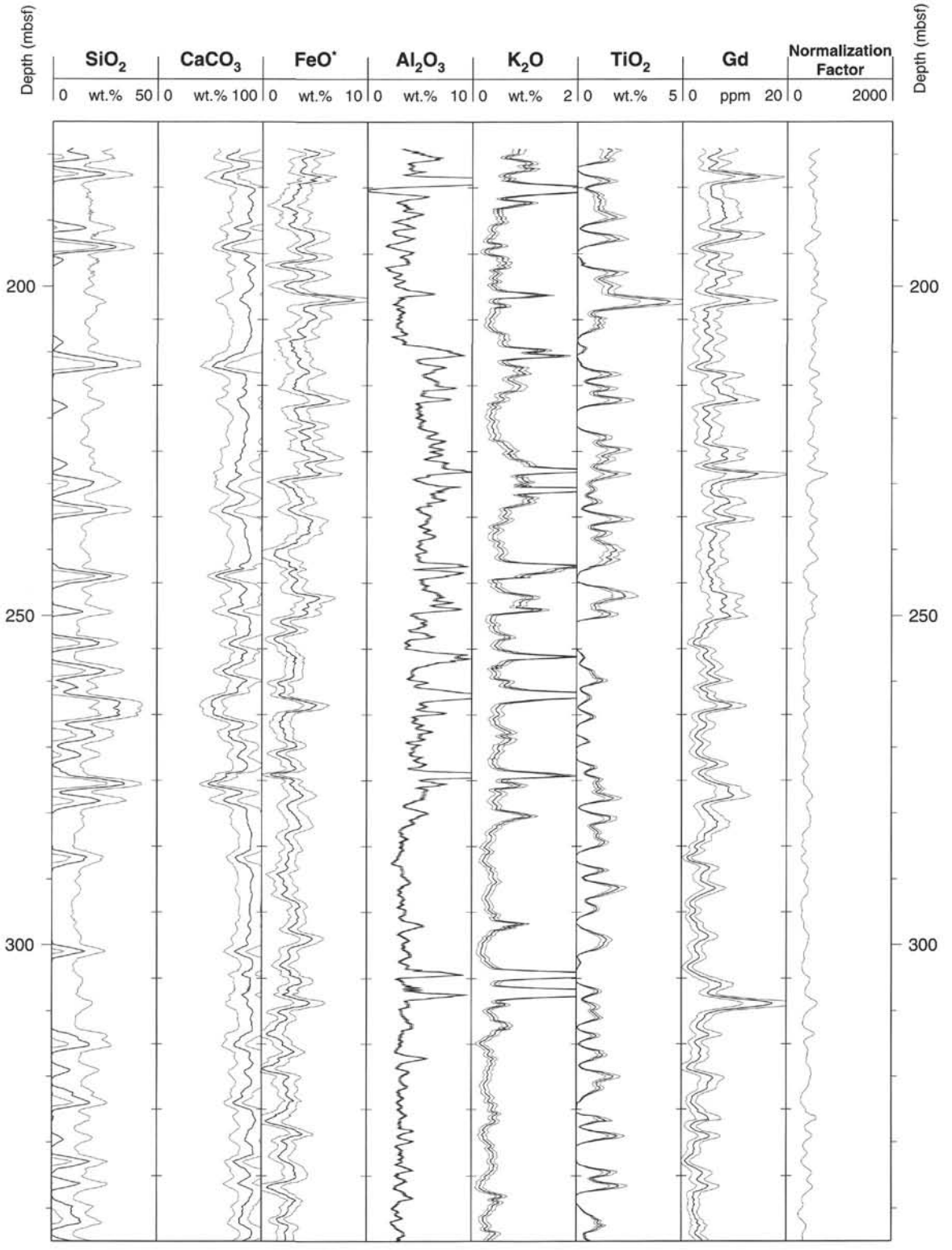

Hole 998B: Geochemical Logging Data (cont.)

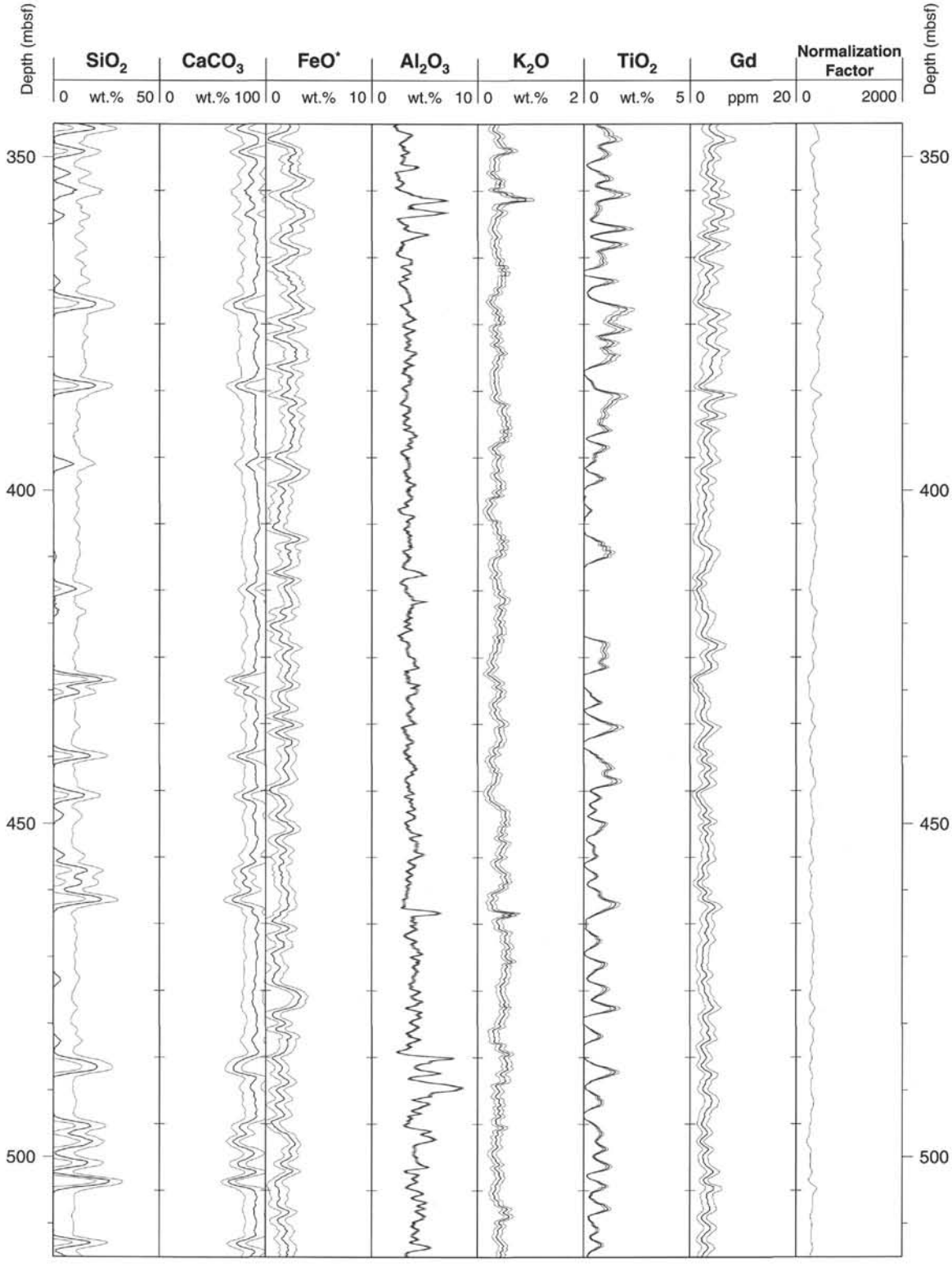

Hole 998B: Geochemical Logging Data (cont.)

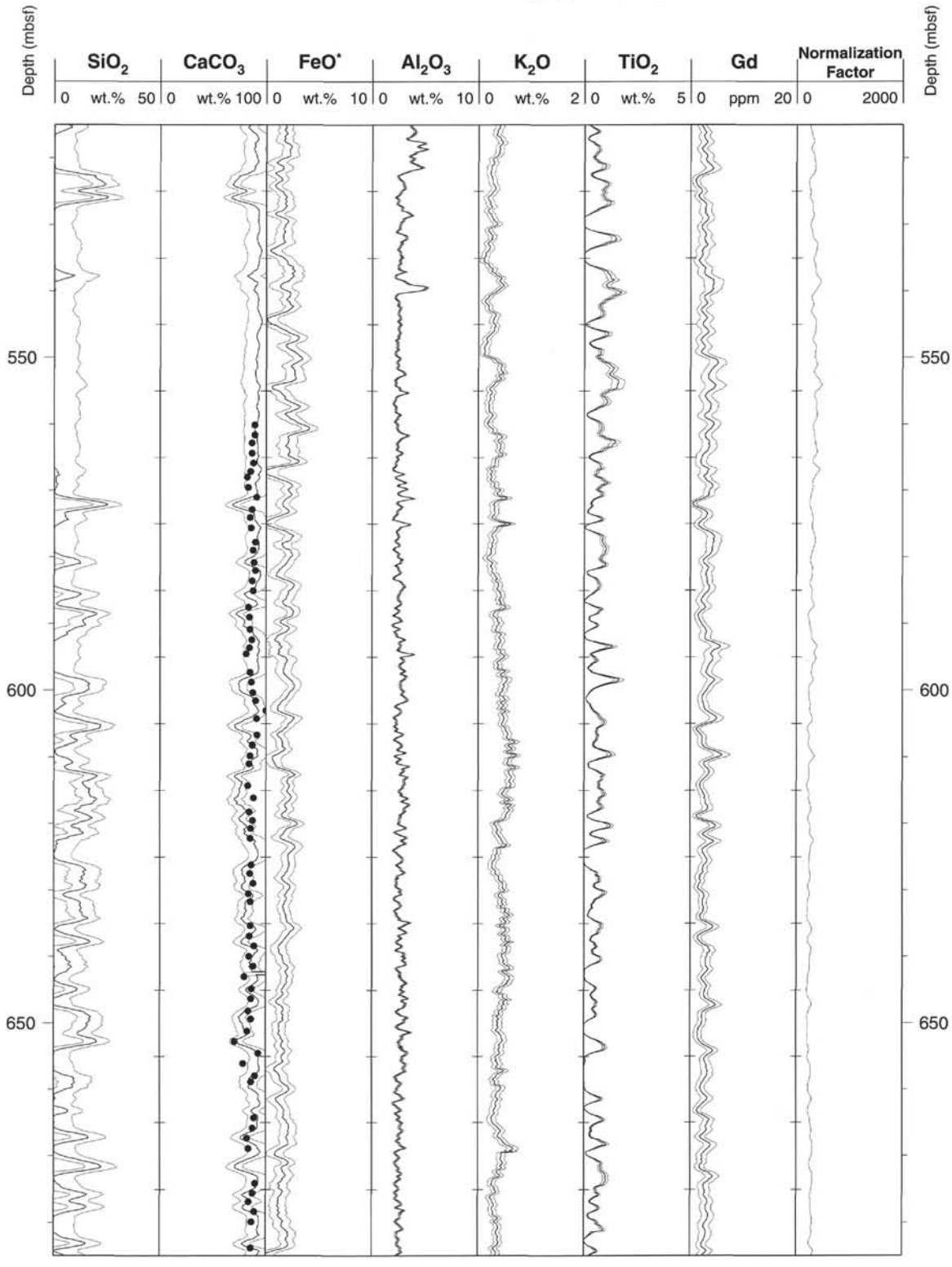

Hole 998B: Geochemical Logging Data (cont.)

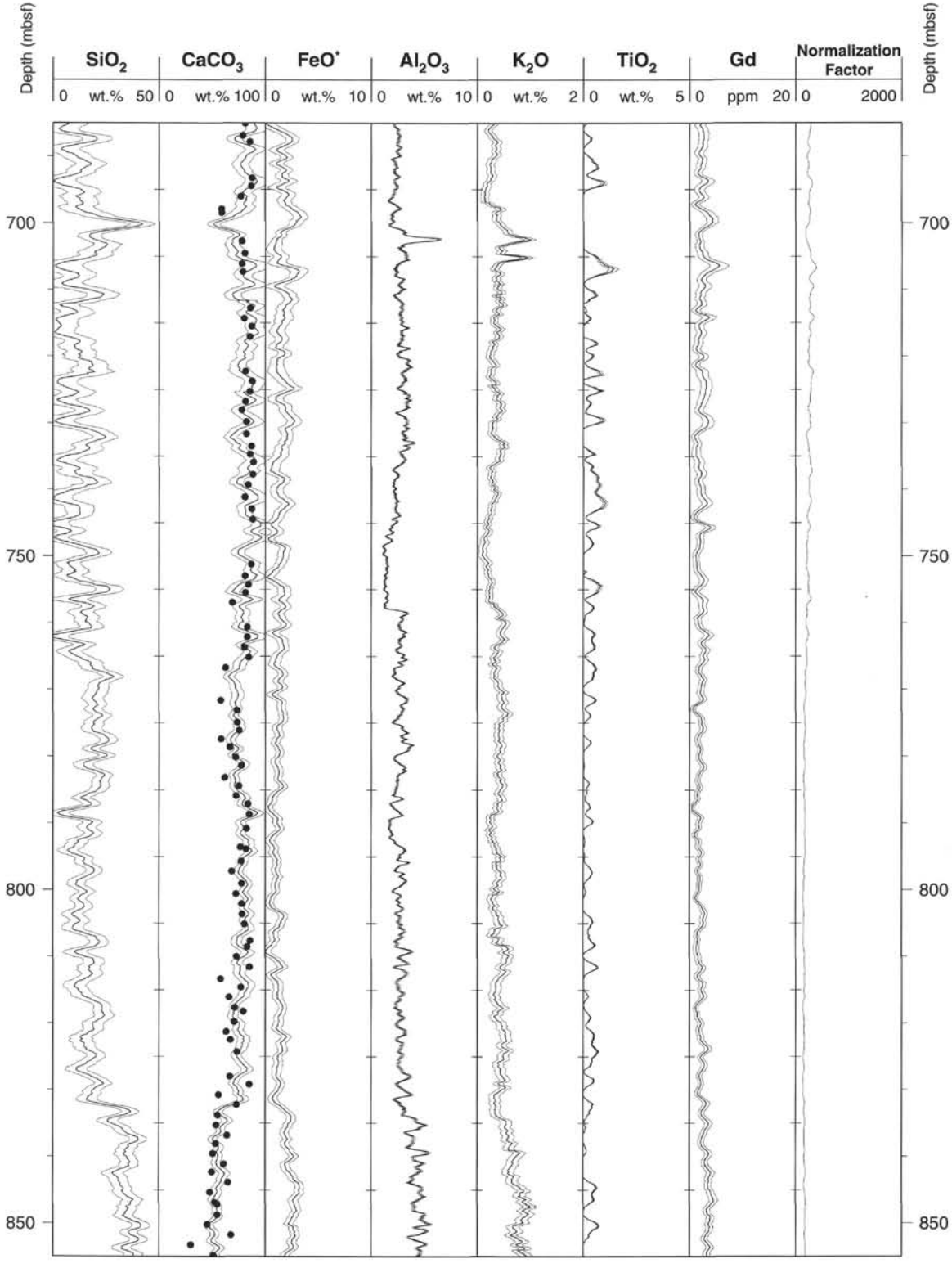

Hole 998B: Geochemical Logging Data (cont.)